Bursty Bulk Flows and Substorm-Time Magnetotail Dynamics

Colin Forsyth

Radio and Space Plasma Physics Group
Department of Physics and Astronomy
University of Leicester

*A thesis submitted to the University of Leicester
for the degree of Doctor of Philosophy*

September 2008

Declaration

I, Colin Forsyth, hereby declare that the work contained within this thesis is my own. I acknowledge the sources of my data and reference any material which is reproduced.

Sections of this thesis have been previously published, or submitted for publication, in the following:

Forsyth, C., Lester, M., Milan, S. E., Grocott, A., Frey, H. U., Lucek, E., Reme, H., and Watermann, J.: Observations of tail dynamics using ground and space based instruments during a period of multiple substorm events, in Proceedings of the Eighth International Conference on Substorms (ICS-8), edited by Syrjäsuo and Donovan, pp. 65–70, University of Calgary, Alberta, Canada, 2007

Forsyth, C., Lester, M., Cowley, S. W. H., Dandouras, I., Fazakerley, A. N., Fear, R. C., Frey, H. U., Grocott, A., Kadokura, A., Lucek, E., Rème, H., Milan, S. E., and Watermann, J.: Observed tail current systems associated with bursty bulk flows and auroral streamers during a period of multiple substorms, *Ann. Geophys.*, **26**, 167–184, 2008a

Forsyth, C., Lester, M., Lucek, E., Dandouras, I., Fazakerley, A. N., Fear, R. C., Singer, H., and Yeoman, T. K.: Solar wind and substorm excitation of the wavy neutral sheet, *Ann. Geophys.*, **submitted**, 2008b

Bursty Bulk Flows and Substorm-Time Magnetotail Dynamics

Colin Forsyth

Abstract

I present three studies of magnetospheric tail dynamics associated with bursty bulk flows (BBFs) and substorms, concentrating on observations of the current systems of the BBFs and the dynamics of magnetotail current sheet waves.

From a case study, I show that the observed magnetospheric current system of a BBF consisting of two flow bursts matched the current system predicted by Sergeev *et al.* (1996), and that the currents were consistent with previous studies. I also show that the particle signatures of the BBF were similar to the particle signatures in the PSBL prior to the BBF observations, demonstrating that the BBF was produced by the reconnection of lobe magnetic field-lines.

From a survey of 628 BBF events, I show that BBF occurrence is highest during the recovery phase of substorms and lowest during non-substorm times and substorm growth phases. Using a subset of 211 BBF encounters that were sufficiently far from the magnetotail current sheet to determine the field-aligned currents, I show that the current magnitude is larger during the expansion and recovery phases of substorms than during the growth phase. Furthermore, the current magnitude is larger in the pre-midnight sector on large scale sizes.

Utilising data from ground- and space-based observatories, I investigate an interval of current sheet wave activity following a solar wind pressure pulse and two substorms. By comparing the propagation of aurora and tail dipolarization signatures and the neutral sheet waves, I conclude that the propagation of these features is controlled by the same mechanism. I test two models of neutral sheet wave propagation and find that the model of Erkaev *et al.* (2008) gives a good fit to the data.

Acknowledgements

I would like to pay thanks to the following people for aiding me in the creation of this thesis:

Contents

List of Figures

List of Tables

Chapter 1

Plasma Physics and Solar-Terrestrial Physics

According to Empedocles, the Criterion of Truth is not Sense but Right Reason
"The True Intellectual System of the Universe ", Cudworth (1678)

Solar system science concerns itself with the study of the interconnected solar-planetary systems. Within this field, solar-terrestrial physics (STP) investigates the effect of the particles and magnetic fields emanating from the Sun and impinging on the near-Earth space and the dynamics of the terrestrial magnetic environment. In this thesis, I investigate three related dynamic features of the magnetosphere; substorms, bursty bulk flows and current sheet waves. These features are important for transporting energy and momentum in the magnetotail and between the magnetotail and the ionosphere

This chapter gives an overview of the fundamental physics involved in the dynamics of the magnetosphere and some of the basic concepts of STP relevant to this thesis. I consider both single particle and fluid treatments of plasmas and show how these lead to the frozen-in flux approximation and give rise to current systems. I then discuss the basic properties of the solar wind and the magnetosphere and the magnetospheric and ionospheric current systems. Finally, I give a first order treatment of magnetic reconnection and show how this applies to the magnetotail.

1.1 Plasma physics

In order to understand the dynamics of the magnetosphere, one must have an understanding of the underlying physics involved. The following describes two different treatments of plasma physics to highlight various properties of magnetised plasmas. Results from these two different approaches are used throughout this thesis to describe and explain the dynamical processes of the magnetosphere.

1.1.1 Single particle plasma physics

The simplest consideration of plasma physics deals with the motion of individual charged particles in an electromagnetic field. This description of plasma physics shows that, to a first approximation, particles gyrate about magnetic field-lines, although variations in the field give rise to particle drifts.

The particle motions are governed by the Lorentz and Coulomb forces and Maxwell's Equations;

$$F = q\left(\mathbf{E} + \mathbf{v} \times \mathbf{B}\right) \tag{1.1}$$

$$\nabla.\mathbf{B} = 0 \tag{1.2}$$

$$\nabla.\mathbf{E} = \frac{\rho_q}{\epsilon_0} \tag{1.3}$$

$$\nabla \times \mathbf{B} = \mu_0 \mathbf{j} + \mu_0 \epsilon_0 \frac{\partial \mathbf{E}}{\partial t} \tag{1.4}$$

$$\nabla \times \mathbf{E} = -\frac{\partial \mathbf{B}}{\partial t} \tag{1.5}$$

$$\tag{1.6}$$

In the case of space plasmas, it is generally assumed that any variations in the electric field occur over long periods, such that $\mu_0\epsilon_0\partial\mathbf{E}/\partial t$ is negligible, which is true as long as the propagation of electromagnetic waves is ignored.

A simple treatment of Eqn. 1.1 for a particle moving in a non-varying magnetic field with no electric field shows that the force on a charged particle due to its motion is perpendicular to the particle motion and the magnetic field

$$\mathbf{F} = \pm ne(\mathbf{v} \times \mathbf{B}) \tag{1.7}$$

Differentiating Eqn. 1.7 with respect to time, it can be shown that the particles orbit or gyrate about the magnetic field-line at the Larmor (or gyro) frequency, ω_L and Larmor (or gyro) radius, r_L,

$$\omega_L = \frac{neB}{m}; r_L = \frac{mv_\perp}{neB} \tag{1.8}$$

Since the force acts perpendicular to the magnetic field and particle velocity it does not increase the kinetic energy of the particles. Furthermore, particle motion along the field-line is unaffected, hence a particle with a finite velocity along the field will describe a helix. The angle between the particle's gyratory motion and it's motion parallel to the magnetic field is the particle's pitch angle.

Introducing an electric field brings an extra term to the force equation, such that Eqn. 1.1 is regained. Taking the simple case that $\mathbf{B} = B_X$ and $\mathbf{E} = E_Y$, Eqn. 1.1 becomes

$$\frac{dv_X}{dt} = 0 \tag{1.9}$$

$$\frac{dv_Y}{dt} = \frac{q}{m}(E_Y + B_X v_Z) \tag{1.10}$$

$$\frac{dv_Z}{dt} = -\frac{q}{m}v_Y B_X \tag{1.11}$$

Differentiating these equations with respect to time, and substituting in the relevant acceleration expressions gives

$$\frac{d^2 v_Y}{dt} = -\frac{q}{m}v_Y B_X^2 \equiv -\omega_L^2 v_Y \tag{1.12}$$

$$\frac{d^2 v_Z}{dt} = -\left(\frac{q}{m}\right)^2 (B_X E_Y + B_X^2 v_Z) \equiv -\omega_L^2 \left(\frac{E_Y}{B_X} + v_Z\right) \tag{1.13}$$

These equations shows that the particle motion is the sum of the gyratory motion perpendicular to the magnetic field and the velocity due to the electric field,

$$\mathbf{v}_E = \frac{\mathbf{E} \times \mathbf{B}}{B^2} \tag{1.14}$$

The additional motion due to the electric field is often referred to as the guiding centre drift, where the guiding centre of the particle motion (i.e. the field-line about which the particle gyrates) moves. As such, one might consider that introducing an electric field causes motion of the magnetic field-lines.

This summation of velocities can be further extended to any force acting on the particle, such that the particle motion is the sum of velocities due to the forces acting,

$$\mathbf{v}_F = \frac{1}{q}\frac{\mathbf{F} \times \mathbf{B}}{B^2} \tag{1.15}$$

This indicates that any force that does not contain a multiple of the particle charge must cause a current to flow since the velocity will be in opposite directions for ions and electrons.

Of particular interest to magnetotail physics (and an application of Eqn. 1.15) is the effect of curved field-lines. As a particle moves along the field-line it experiences a centripetal force

$$\mathbf{F}_c = \frac{mv_\parallel^2}{R_c}\mathbf{r}_c \equiv \frac{mv_\parallel^2}{R_c^2}\mathbf{R}_c \tag{1.16}$$

where m is the mass of the particle, $v_\parallel$ is the velocity of the particle along the field-line, R_c is the radius of curvature and $\mathbf{r}_c$ is the unit vector in the direction of the radius of curvature. This then gives a velocity of

$$\mathbf{v}_c = \frac{mv_\parallel^2}{q}\frac{\mathbf{R}_c \times \mathbf{B}}{R_c^2 B^2} \tag{1.17}$$

A further drift component is due to the gradient in the magnetic field. From a simple sketch, it can be seen that as a charged particle gyrates into an area of increasing magnetic field, its Larmor radius decreases and as it returns to an area of lower magnetic field, it's Larmor radius increases. The resultant motion gives the particle a net velocity perpendicular to the magnetic field and its gradient.

Assuming that the scale length of the magnetic field variation is greater than the particle gyro-radius, then the magnetic field can be expanded using a Taylor expansion

$$\mathbf{B} = \mathbf{B}_0 + (\mathbf{r}.\nabla)\mathbf{B}_0 + \frac{1}{2}(\mathbf{r}^2.\nabla^2)\mathbf{B}_0 + \dots \tag{1.18}$$

where $\mathbf{B}_0$ is the magnetic field at the gyro-centre and $\mathbf{r}$ is the gyro-radius. Taking the first order differentials and substituting this into Eqn. 1.7 gives

$$\mathbf{F} = q\left(\mathbf{v} \times \mathbf{B}_0 + \mathbf{v} \times (\mathbf{r}.\nabla)\mathbf{B}_0\right) \tag{1.19}$$

Using Eqn. 1.15, the velocity due to this force is

$$\mathbf{v} = \frac{-1}{B_0^2}\left(\mathbf{B}_0 \times \mathbf{v} \times \mathbf{B}_0 + \mathbf{B}_0 \times \mathbf{v} \times (\mathbf{r}.\nabla)\mathbf{B}_0\right) \tag{1.20}$$

where the first term on the right hand side is the gyro-motion of the particle and the second is the motion due to the magnetic field gradient. This second term is perpendicular to the magnetic field direction and the direction of the magnetic field gradient and has a magnitude of $vr/B^2 \equiv mv^2/qB^3$ such that the velocity due to the magnetic gradient can be written

$$\mathbf{v}_\nabla = -\frac{mv^2}{qB^3}(\mathbf{B} \times \nabla\mathbf{B}) \tag{1.21}$$

1.1.2   Magnetohydrodynamics (MHD)

Unlike single particle plasma physics, which looks at the motion of each particle in the plasma, magnetohydrodynamics considers the bulk properties of the plasma. Since the ions in a plasma are at least three orders of magnitude more massive than the electrons, electrostatic forces will accelerate the electrons to much higher velocities than the ions. The electrons move quickly into areas of positive charge abundance and away from areas of positive charge depletion, preventing any charge build up. As such, the plasma is considered to be an electrically neutral, perfectly conducting fluid. In the case of the magnetotail, there are effectively no sources or sinks of ions and electrons, such that mass is conserved. This is given by

$$\frac{\partial \rho}{\partial t} + \nabla \cdot (\rho \mathbf{v}) = 0 \tag{1.22}$$

where ρ is the density of particles and $\mathbf{v}$ is there bulk velocity. Particles are also subject to the Lorentz force, the $\mathbf{j} \times \mathbf{B}$ force (where $\mathbf{j} = nq\mathbf{v}$) and, given that the plasma is a fluid, a pressure force. However, since the fluid is considered to be quasi-neutral, the Lorentz forces on the individual species cancel, such that the resultant forces on the fluid are

$$\rho \frac{d\mathbf{v}}{dt} = \mathbf{j} \times \mathbf{B} - \nabla p \tag{1.23}$$

where ∇p is the pressure gradient. Using Ampére's law (Eqn. 1.4) and the convective derivative, this can be rewritten as

$$\rho \frac{\partial \mathbf{v}}{\partial t} + \rho (\mathbf{v} \cdot \nabla) \mathbf{v} = \frac{1}{\mu_0} (\mathbf{B} \cdot \nabla) \mathbf{B} + \nabla p_B + \nabla p \tag{1.24}$$

where∇p_B is the gradient in the magnetic pressure.

Ohm's Law is given by

$$\mathbf{j} = \sigma \mathbf{E} \tag{1.25}$$

where σ is the conductivity of the medium through which the current is flowing. From Eqn. 1.1, it can be seen that for a particle travelling in a magnetic field, the total electric field it experiences is $\mathbf{E} + \mathbf{v} \times \mathbf{B}$, giving

$$\frac{\mathbf{j}}{\sigma} = \mathbf{E} + \mathbf{v} \times \mathbf{B} \tag{1.26}$$

Taking the curl of equation 1.26, and substituting Ampére's Law and Faraday's Law (equations 1.4 and 1.5) then gives

$$\frac{\partial \mathbf{B}}{\partial t} = \nabla \times \mathbf{v} \times \mathbf{B} - \frac{1}{\mu_0 \sigma} \nabla \times \nabla \times \mathbf{B} \tag{1.27}$$

from which follows

$$\frac{\partial \mathbf{B}}{\partial t} = \nabla \times \mathbf{v} \times \mathbf{B} + \frac{1}{\mu_0 \sigma} \nabla^2 \mathbf{B} \tag{1.28}$$

The first term on the right hand side of equation 1.28 is a convective term and the second term is a diffusive term. In the limit of a perfectly conducting plasma ($\sigma = \infty$), then Eqn. 1.28 dictates that the field moves with the plasma. This is known as the frozen-in flux condition. If the conductivity of the plasma is finite, i.e. the plasma is collisional, then the field will diffuse through the plasma to some extent. The extent to which the plasma is convective or diffusive can be expressed as the magnetic Reynolds number,

$$R_m = \frac{|\nabla \times \mathbf{v} \times \mathbf{B}|}{|\nabla^2 \mathbf{B}/\mu_0\sigma|} \equiv \mu_0 \sigma v L \tag{1.29}$$

where L is the scale length of the variation of the magnetic field. Plasmas with Reynolds numbers greater (less) than 1 are predominantly convective (diffusive).

In a collisional plasma, a further term must be introduced to Eqn. 1.1 to account for the loss of momentum due to collisions. This gives

$$\mathbf{F} = q(\mathbf{E} + \mathbf{v} \times \mathbf{B}) - m\nu_c\mathbf{v} \tag{1.30}$$

where ν_c is the collision frequency. For a static ($\mathbf{F} = 0$) fluid in a region of no magnetic field, this becomes

$$\mathbf{E} = \frac{m}{q}\nu_c\mathbf{v} \tag{1.31}$$

Substituting in $\mathbf{j} = qn\mathbf{v}$ gives

$$\mathbf{E} = \frac{m\nu_c}{nq^2}\mathbf{j} \equiv \frac{\mathbf{j}}{\sigma} \tag{1.32}$$

which is Ohm's Law, giving that the plasma conductivity is $nq^2/m\nu_c$. Substituting this expression for the plasma conductivity into equation 1.28 shows that, for low density plasmas such as those in the magnetotail, the conductivity is low and hence the plasma is approximately "frozen" to the magnetic field.

It should be noted that this treatment does not consider additional forces, such as those due to gradients and the curvature of the magnetic field and is consistent with the treatment of Eqn. 1.1 in Section 1.1.1. As such, the convective term is equivalent to the Larmor (gyratory) motion of the particles about the magnetic field and the motion due to the guiding centre drift. The diffusive term did not appear in the single particle treatment since collisions between particles were not considered so is in addition to the drift mechanisms discussed in the single particle approach. As such, both descriptions have their merits in describing the behaviour of plasmas.

Since plasmas are fluids, they exert a pressure on objects and interfaces that the plasma comes into contact with. However, unlike unmagnetized fluids, the pressure a plasma exerts is a combination of the ram pressure (pressure due to the bulk motion of the plasma), particle pressure (due to the thermal motion of the particles) and magnetic pressure (due to the magnetic field energy density). For plasmas with a slow bulk motion, in which the ram pressure is negligible, it is often useful to quantify which of the remaining

pressures is dominant, particularly in identifying plasma regimes. To this end, I introduce the plasma β, which is the ratio of the particle pressure to the magnetic pressure,

$$\beta = \frac{nkT}{\mu_0 B^2} \tag{1.33}$$

High β plasmas are dominated by the particle pressure, whereas low β plasmas are dominated by the magnetic field pressure.

1.2 Solar-Terrestrial Physics

1.2.1 The Sun and the solar wind

The Sun is the star at the heart of the solar system. Consisting predominantly of ionic hydrogen and helium, it is the primary source of energy in the solar system. Processes within the Sun generate a large magnetic field that interacts with the solar ions and electrons such that the Sun's constituents make up a magnetised plasma.

Observations of comet tails in the 1950s (e.g. Biermann, 1951, 1952, 1957) led to the theory that particles streamed away from the Sun. The momentum and continuity equations for a hot gas around a large gravitating body are

$$\rho(r)v(r)\frac{dv(r)}{dr} = -\frac{dp(r)}{dr} - \rho(r)\frac{GM}{r^2} \tag{1.34}$$

$$\frac{1}{r^2}\frac{d}{dr}\rho(r)v(r)r^2 = 0 \tag{1.35}$$

where v is the gas velocity, ρ is the gas density, p is the thermal gas pressure and GM/r^2 is the acceleration due to gravity. Parker (1958) showed that solving these equations of for $v = 0$ gave a far greater pressure at infinity than was needed to balance with the interstellar medium. Instead, Parker suggested that Eqn. 1.35 should be solved in the limit

$$\rho(r)v(r)r^2 = \rho_0 v_0 r_0 \tag{1.36}$$

where ρ_0 and v_0 are the values of ρ and v at a radial distance r_0. It can then be shown that the Eqn. 1.34 comes to

$$\frac{dv}{dr}\left(v - \frac{2kT(r)}{mv}\right) = \frac{4kT(r)}{mr} - \frac{2k}{m}\frac{dT}{dr} - \frac{GM}{r^2} \tag{1.37}$$

where k is Boltzmann's constant, m is the average mass of the gas particles, T is the gas temperature which has some radial dependance and G is the gravitational constant.

In the isothermal approximation, the middle term on the right-hand side vanishes.

The remaining terms show that when r is small, i.e. locations close to the Sun, the plasma is gravitationally bound to the Sun but as distance increases, particles begin to flow away from the Sun. At some point, known as the critical radius, the right-hand side goes to 0. This gives several solutions for v. Firstly, dv/dr can go to zero, indicating that v reaches a maximum or minimum at this point. Alternatively, the particle velocity can reach the sound speed at this point ($v^2 = 2kT/m$). Observations of coronal emission lines have shown that the coronal velocity is slower than the sound speed, whereas spacecraft observations at Earth have shown that the solar wind is supersonic at 1 AU. As such, the solar wind solution indicates that the particle velocity is initially low, becomes supersonic at the critical radius, then continues to increase to a finite value as r tends to infinity.

The above solution ignores the solar magnetic field. Parker (1958) also addressed this issue. He noted that, due to the frozen-in flux condition, if plasma was flowing radially outward from the Sun, then it would carry the solar magnetic field with it. If the Sun was a non-rotating body, then this field would be point radially outwards. However, since a given magnetic field-line threads through all of the plasma emitted from the same point on the Sun, and the Sun rotates round, the magnetic field forms an Archimedean spiral, now known as the Parker spiral. The magnetic field drawn away from the Sun is termed the interplanetary magnetic field (IMF).

At 1 AU, the solar wind encounters the Earth. The average properties of the solar wind at this distance are given in Table 1.1 (Kivelson and Russell, 1995).

Ion number density	6.85 cm^{-3}
Electron number density	7.1 cm^{-3}
Solar wind speed	450 km/s
Temperature	~100-150 kK
Magnetic Field Strength	7 nT
Thermal pressure	25 pPa
Magnetic Pressure	10 pPa
Ram pressure	5 nPa

Table 1.1: Table of solar wind properties at 1 AU

1.2.2 Earth's magnetosphere

That the Earth has a significant magnetic field as been known for centuries. However, it is only in the light of the discovery of the solar wind that its importance has been realised.

In the absence of the solar wind and IMF, the Earth's field would be dipolar (to a first approximation). However, since the solar wind and the IMF exert pressures, the Earth's magnetic field is compressed by the action of the solar wind. Due to the frozen-in condition, the solar wind and the terrestrial magnetic field remain separate (again, to first order approximation). Given that the solar wind magnetic field is low (Table 1.1)
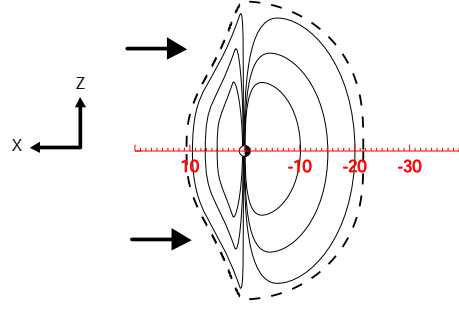
Figure 1.1: Schematic of a model of the closed magnetosphere in the XZ plane (Y=0). The solid lines show the magnetic field-lines in the magnetosphere; the dashed lines indicate the magnetopause; the arrows indicate the motion of the incoming solar wind.

compared with the terrestrial magnetic field at the equator and that without the solar wind, the Earth's magnetic field would be dipolar, then the "residual" dipole field must be removed from the solar wind. This is done by a current sheet that separates the solar wind and the terrestrial field, known as the Chapman-Ferraro current sheet (after Chapman and Ferraro (1930)). This current sheet "adds" an additional magnetic field which cancels out the dipole field on one side (the solar wind side) and approximately doubles the magnetic field on the other (the Earth side). As such, the Earth's magnetic field strength is

$$\mathbf{B} = 2\mathbf{B}_{dipole} \equiv 2\mathbf{B}_{eq}\frac{1}{r^3}\sqrt{1 + 3\cos^2\theta} \tag{1.38}$$

where B_{eq} is the equatorial magnetic field, r is in planetary radii and θ is the angle from the dipole direction.

The solar wind compresses the terrestrial magnetic field until the ram pressure of the solar wind is balanced by the magnetic pressure of the terrestrial magnetic field. Given that the ram pressure is $2\rho\left(V\cos\chi\right)^2$ (the change in momentum multiplied by the flux of particles), where χ is the angle between the normal to the boundary and the direction of the solar wind and p_{sw} is the solar wind thermal pressure, pressure balance on the Sunward side occurs at

$$R_{mp}^3 = \frac{\mathbf{B}_{eq}^2}{\mu_0\rho\left(V\cos\chi\right)^2 + p_{sw}/2}\left(1 + 3\cos^2\theta\right) \tag{1.39}$$

This boundary is known as the magnetopause and defines the limit of the cavity in the solar wind caused by the Earth's magnetic field known as the magnetosphere. R_{mp} is the magnetopause stand-off distance, in planetary radii. Figure 1.1 shows a schematic of the magnetosphere under these conditions. As all the magnetic field-lines remain solely connected to the Earth, this is known as the closed magnetosphere model.

Dungey (1961) revisited a suggestion by Hoyle (1949) that suggested aurora were excited by the acceleration of particles by neutral points caused by the reconnection of magnetic field-lines. This led to the possibility of the magnetosphere being "open" to solar wind particles. In the closed magnetosphere model, the particles did not cross from the
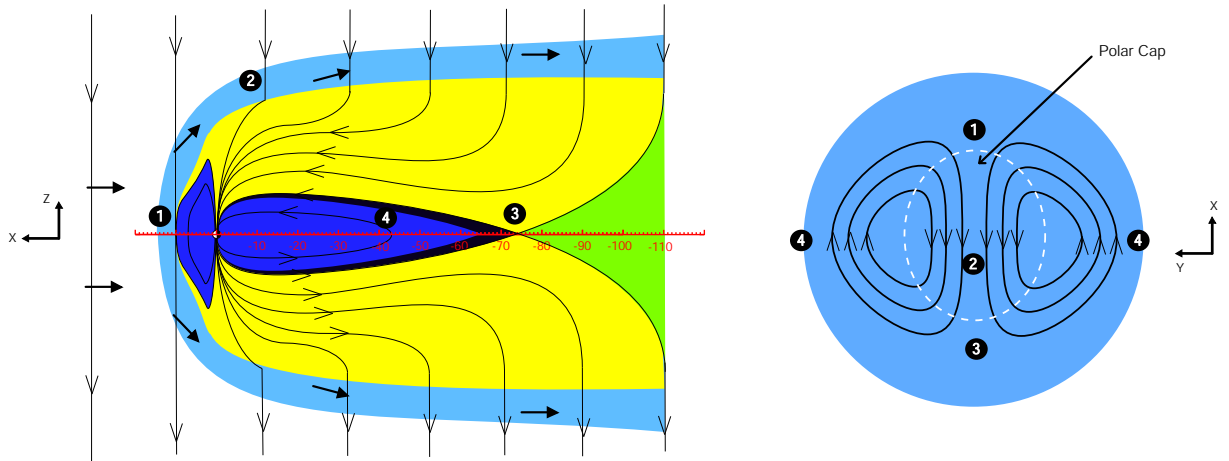
Figure 1.2: Schematic of a model of the open magnetosphere in (a) the XZ plane (Y=0) and (b) looking down into the ionosphere. The black lines in (a) represent the magnetic field-lines. The arrows indicate the motion of the solar wind and IMF. The light blue region depicts the magnetosheath; the dark blue region depicts the closed field region in the magnetosphere; the yellow region depicts the open field-line region (the lobes); the green region indicates the "disconnected tail" (Milan *et al.*, 2006b). In panel (b), the black lines represent the paths of the footprints of the magnetic field-lines in the ionosphere; the white dashed line represents the open-closed field-line boundary (OCB) at the limit of the polar cap. The numbers indicate the evolution of a magnetospheric field-line through the Dungey cycle.

solar wind onto the Earth's magnetic field-lines. In Dungey's model, the terrestrial and solar wind magnetic field-lines became joined at the sub-solar point (1 in Fig. 1.2), hence solar wind particles could enter into the magnetosphere. Dungey further proposed that the magnetic field-lines of the Earth were then transported anti-sunward across the polar cap (2 in Fig. 1.2) and reconnected on the anti-sunward side of the Earth (3 in Fig. 1.2). The reconnected magnetic field-lines then convect round the flanks of the magnetosphere back to the dayside (4 in Fig. 1.2). This process is now known as the Dungey cycle. Figure 1.2a shows a schematic of this process in the magnetospheric XZ GSM plane. In this figure I have included another plasma regime which results from the supersonic nature of the solar wind; the magnetosheath (light blue area). When the supersonic solar wind encounters the magnetosphere it is shocked; the flow speeds are retarded and the plasma heated. The outer limit of this region is known as the bow shock. Figure 1.2b shows the flow streamlines (black) of the convection of the footpoints of magnetic field-lines in the ionosphere. The white dotted line indicates the boundary between open and closed field-lines (OCB). Field-lines opened at the dayside magnetopause cross the OCB into the polar cap and convect across to the tail. They are then reconnected and return to the dayside at lower latitudes.

Figure 1.3 shows the output from the Map Potential Model (Ruohoniemi and Baker, 1998), which combines data from the SuperDARN radars to derive the ionospheric flow patterns in the polar regions. This is overlaid on an image from FUV-WIC on-board the IMAGE spacecraft. The black lines represent the ionospheric flow patterns, the coloured vectors represent the direction of the flow determined by the model from the SuperDARN input. The blue line is an estimation of the OCB, based on the FUV-WIC image. This snapshot of the polar ionospheric flows shows a pattern of flows similar to the pattern
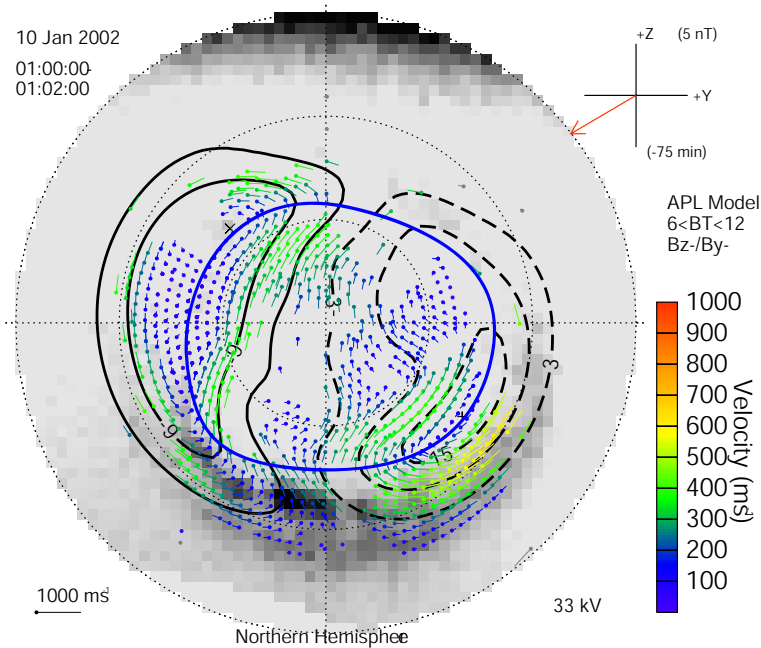
Figure 1.3: Ionospheric flows determined using the Map Potential Model overlaid on a grey-scale FUV-WIC image of the aurora. The vector colours indicate the flow speeds. The thick black lines (solid and dashed) show the equipotentials in the ionospheric electric field, equivalent to the global ionospheric flow pattern.

from Dungey (1961) for southward IMF.

1.2.3   The magnetotail

The region of field-lines anti-sunward of the Earth shown in Fig. 1.2 constitutes the magnetotail. It is this region that is the focus of this thesis. The open field-line regions (yellow) are the tail lobes. These are populated by a mixture of captured solar wind plasma and ionospheric-origin plasma. Generally, the particle density in the lobes is low (<0.1 cm^{-3}), although this increases towards the solar wind density with distance downtail (Cowley, 1984). The ionospheric footpoints of the open field-lines lie within the dim region of the polar cap inside the auroral oval. The magnetic field strength in the lobes can be found by equating the flux through the polar cap and the magnetic flux through a single lobe. Approximating the lobe as a half cylinder gives the lobe magnetic flux as $\phi_l = \pi R_l^2 B_l / 2$. Then, assuming the polar cap is circular and that the magnetic field at the surface of the Earth is constant, the flux through the polar cap is $\phi_{pc} = \pi \left(R_E \cos\theta \right)^2 B_E$, where θ is the latitude of the OCB. Taking the OCB latitude as 70°, the magnetic field at the Earth to be 62,000 nT and the width of the tail to be 40 R$_E$ based on the closed magnetosphere model, this gives a lobe magnetic field strength of 35 nT. This is in general agreement with more sophisticated magnetospheric models (Baker and Pulkkinen, 1998).

The black region on the Earthward side of the tail X-line is the plasma sheet boundary layer (PSBL); a transition region between the low density lobes and the plasma sheet. This

is populated by recently reconnected plasma which forms bidirectional field-aligned beams with particle energy increasing with distance from the central plane of the magnetotail (see below for details). Inside the PSBL is the plasma sheet (blue). The plasma in this region is on closed field-lines. As the field-lines are convected away from the X-line, they contract leading to an increase in the plasma density to between $0.1-1$ cm^{-3}. To maintain pressure balance with the lobes, in which the magnetic field pressure is dominant, the magnetic field strength in the plasma sheet is lower than in the lobes. As such, the plasma β is higher in the plasma sheet than in the PSBL or the lobes. This has lead to the definition that the inner central plasma sheet is that region where $\beta > 0.5$ (e.g. Baumjohann *et al.*, 1989; Angelopoulos *et al.*, 1992), which I adopt in this thesis.

It is worth noting at this point that although the magnetotail regimes connected to the polar cap constitute the majority of the magnetotail volume, they are connected to the Earth via a relatively small area. The volume connected to the remaining area (equatorward of the polar caps) is not generally involved in the convective cycle that dominates the rest of the magnetosphere. This region, known as the plasmasphere, consists of a dense plasma, relative to the plasma sheet, on dipolar field-lines and that approximately co-rotates with the Earth.

1.2.4   Magnetospheric and ionospheric current systems

Currents occur throughout the magnetosphere-ionosphere system. They are important in separating various plasma regimes, such as the magnetosphere and solar wind (Chapman-Ferraro current, discussed earlier), and support the distortion of the magnetotail away from a dipolar configuration. Other current systems arise due to particle drifts or the diversion of existing current systems. These current systems are important for transferring energy and momentum between the magnetosphere and the Earth and for energising or de-energising the different plasma regimes.

In the magnetotail, the dominant current is the cross-tail current that supports the oppositely directed magnetic fields in distended tail. This current flows in a duskward direction across the tail and is closed by the currents across the magnetopause (which flow from dusk to dawn). A first approximation of this current can be made using the value for the lobe magnetic field calculated above. Approximating the system as two regions of anti-parallel magnetic field separated by an infinitely thin current sheet and using the integral form of Ampére's Law gives

$$\oint \mathbf{B}.d\mathbf{l} = \mu_0 \int \mathbf{j}.d\mathbf{A} \tag{1.40}$$

$$\Rightarrow 2\mathbf{B}_l l = \mu_0 I \tag{1.41}$$

gives the current per unit length of the current sheet. Using the lobe field strength

(B_l) from section 1.2.3, this gives the cross-tail current as 55 A km^{-1} or 0.35 MA R$_{\mathrm{E}}^{-1}$. However, the current sheet in the magnetotail is not infinitely thin due to the gyrations of the charge carriers. Determining the current perpendicular to the magnetic field from Eqn. 1.23 gives

$$\mathbf{j}_{perp} = \frac{\mathbf{B} \times \nabla p}{B^2} - \rho \frac{d\mathbf{v}}{dt} \times \mathbf{B} \frac{1}{B^2} \tag{1.42}$$

where ∇p is the particle pressure gradient. In the limit that the plasma is not accelerating ($d\mathbf{v}/dt = 0$), the current is only dependant on the pressure gradient. In the magnetotail, the pressure gradient is approximately in the Z direction away from the central plane of the tail and the magnetic field is in the X direction hence the pressure gradient supports the cross-tail current.

In the inner magnetosphere, the opposing directions of the gradient-curvature drifts of trapped ions and electrons produce a westward current known as the ring current. The magnetic field associated with this current is in opposition to the Earth's dipole inside of the ring current region so acts to reduce the equatorial magnetic field at the Earth's surface. The injection of large fluxes of particles into the inner magnetosphere during storms and substorms can enhance this current. The resultant depression of the magnetic field is detectable in ground-based magnetometer data.

A number of the magnetospheric current systems are connected to ionospheric current systems through field-aligned currents. As these currents pass through the ionosphere they heat the ionospheric neutral particles via Joule heating, thus transferring energy and momentum from the magnetosphere into the ionosphere. The most significant of these ionospheric currents are the auroral electrojets. Charged particle precipitation in the auroral oval increases the conductivity of the ionosphere there, hence increasing the magnitude of the currents that can flow. Hall currents, which flow perpendicular to the electric and magnetic fields flow from the dayside round to the nightside via dawn and dusk. Pedersen currents, which flow in the direction of the electric field, flow in a poleward/anti-poleward direction across the auroral oval. Both close in the magnetosphere through field aligned current systems, known as the Region 1 and Region 2 currents. Region 1 currents flow into and out of the ionosphere on the poleward side of the auroral oval, closing along the PSBL, whereas the Region 2 currents flow into and out of the ionosphere on the equatorward edge of the auroral oval, closing in the ring current.

1.2.5   Magnetic reconnection in the magnetotail

The merging of magnetic field-lines, termed magnetic reconnection, is at the heart of the interaction of the solar wind with the Earth's magnetosphere. The micro-physics of this problem are still to be fully understood, although the large scale effects can be understood through basic plasma physics, as described by Cowley (1984). The following describes the process of plasma acceleration due to a curved magnetic field-line and the associated
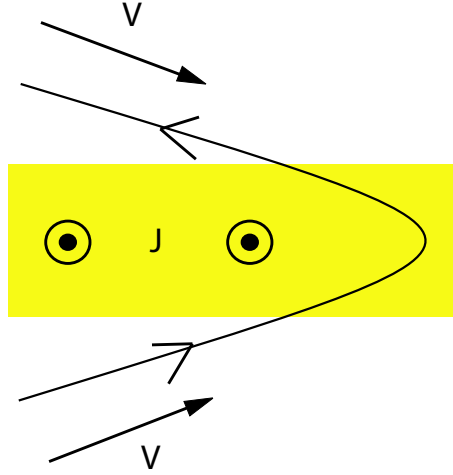
Figure 1.4: Schematic of a curved magnetic field-line passing through a current sheet

current sheet. The speed of the particles required to support a curved magnetic field is derived in the frame of reference of the magnetic field. Using frame transformations, this is then applied to the magnetotail situation in which lobe field-lines populated by slow moving plasma are reconnected at an X-line.

In the following, it is assumed that charged particles (ions and electrons) travel along the field-lines such that $V_{X,Z}/V = B_{X,Z}/B$, that B_Z is constant throughout and that B_X is varies with Z inside the current sheet. Particle gyrations about the field-lines are ignored for simplicity. Under these assumptions

$$\mathbf{j} = j_y = \frac{1}{\mu_0}\frac{dB_X}{dz} \tag{1.43}$$

Shown in Fig. 1.4 is a diagram of a curved magnetic field-line passing through a current sheet with properties as described above. The frame of reference has been chosen such that there is no electric field and the field-line is stationary. The total force acting on the plasma particles associated with the field-line as they pass through the current sheet (and hence the force supporting the curved magnetic field line) is

$$\mathbf{F} = \int_{-d}^{d}\mathbf{J}\times\mathbf{B}dz \tag{1.44}$$

where $\mathbf{J}$ is the total current flowing in the current sheet and d is the current sheet half-thickness. Assuming the current density, $\mathbf{j}$, is known, the force per unit area of the current sheet is

$$\mathbf{P} = \int_{-d}^{d}\mathbf{j}\times\mathbf{B}dz = \frac{2B_Z B_X}{\mu_0}\hat{\mathbf{x}} \tag{1.45}$$

Since there is no force in the Z direction, V_Z remains constant. The force per unit area equates to the rate of change of momentum of the particles per unit area of the current
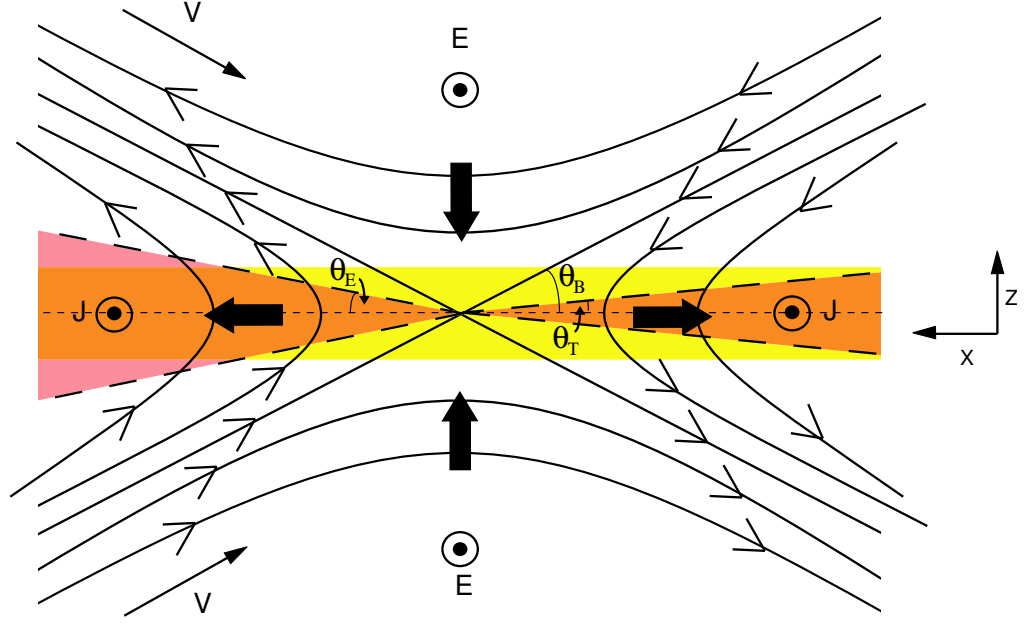
Figure 1.5: Schematic of a reconnection X-line. The solid black lines represent the magnetic field-lines; the large black arrows indicate the motion of the magnetic field-lines; the thin arrow indicate the incoming particle velocity; the red shaded region limited by the dashed lines represents the particle outflow regions. The Electric field and cross tail current are indicated by dotted circles.

sheet. Since the particles continue to travel along the field-lines and V_Z is constant, the change in momentum is $2mV_X \equiv 2mV B_X/B$. The rate of change of momentum is given by the momentum change multiplied by the flux of particles into the current sheet, $2nV_Z$ or $2nV B_Z/B$, giving

$$\frac{2B_X B_Z}{\mu_o} = \frac{4mnV^2 B_X B_Z}{B^2} \tag{1.46}$$

$$\Rightarrow V = \frac{B}{\sqrt{2\mu_0 \rho}} \equiv \frac{V_A}{\sqrt{2}} \tag{1.47}$$

Hence, in the stationary equilibrium state, the particle inflow and outflow speeds are approximately V_A, the Alfvén velocity of the plasma just outside the current sheet. Alternatively, it can be considered that the curved magnetic field line moves with the Alfvén velocity in the rest frame of the plasma.

The process of reconnection creates highly curved field-lines. Figure 1.5 shows a schematic of a reconnection X-line. The black lines represent the magnetic field-lines and the yellow area represents the current sheet, with the current out of the page. The electric field is represented by the dotted circles above and below the X-line. As this scenario is not in the rest frame of the reconnected magnetic field-lines, there is an electric field to drive their motion. The large black arrows indicate the movement of the magnetic field-lines due to the electric field.

The electric field causes the magnetic field to diffuse across the current sheet from both
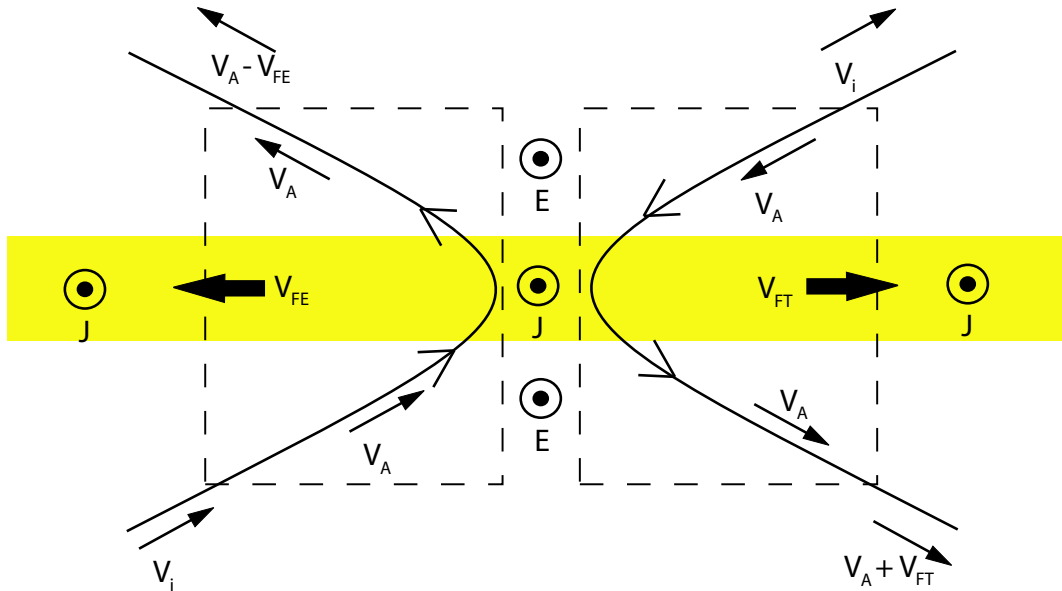
Figure 1.6: Schematic diagram of a two reconnected magnetic field-lines. The large arrows indicate the motion of charged particles along the field-lines. The velocities inside the dashed frames are indicative of velocities in the frame of reference moving with the field-line. Arrows outside of the dashed frames are indicative of the particle velocities in the fixed frame, e.g. the frame of reference of the Earth.

directions at the rate $\mathbf{E} \times \mathbf{B}/B^2$. When two anti-parallel field-lines meet, they reconnect such that instead of having two field-lines separated in the Z-direction, there are two highly curved field-lines separated in the X-direction. The electric field then forces these reconnected field-lines in the +X and -X directions.

The closed field-lines of the magnetotail plasma sheet are created by the reconnection of open lobe field-lines by a tail X-line (e.g. Dungey Cycle or near-Earth neutral line). In these situations, the field-lines are not stationary in the frame of reference of the Earth. As such, the simple stationary field-line situation has to be adapted. This is done by transforming the above scenario to a reference frame in which the magnetic field-lines are non-stationary. It is assumed that initially, the plasma is flowing away from the Earth on the lobe magnetic field-lines. In a reference frame moving with the reconnected field-line (i.e. transformed to remove the electric field), the particle inflow and outflow from the plasma sheet is at V_A (as shown above). However, in the frame of reference of the Earth

$$V_i = V_A \mp V_f \tag{1.48}$$

$$V_o = V_A \pm V_f \tag{1.49}$$

for the field-lines moving towards and away from the Earth respectively, where V_i, V_o and V_f are the inflow, outflow and reference frame velocities respectively. For example, consider that the inflowing particle on the Earthward travelling field-line is already travelling in the same direction as the stationary example, the frame only has to add the extra velocity to get the particle to be travelling at the Alfvén velocity, whereas for the field-line moving away from the Earth, the frame of reference has to catch up with the particle, then travel faster than it by the Alfvén velocity. Figure 1.6 shows the two frames
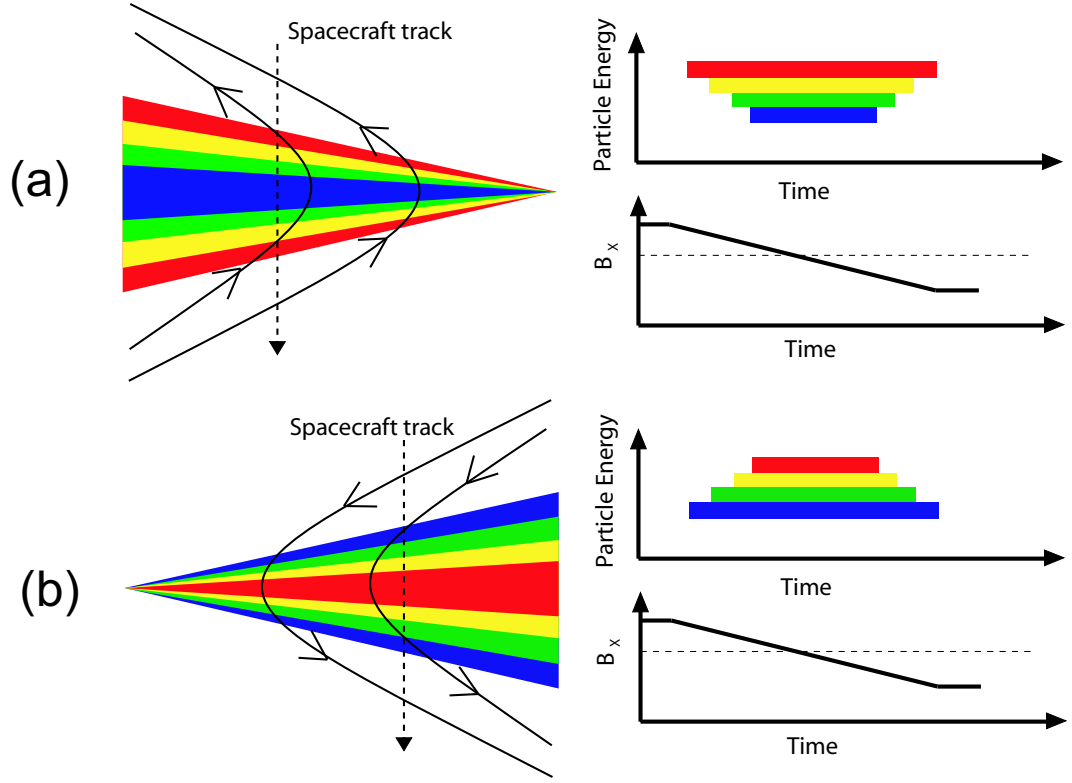
Figure 1.7: Diagram indicating the particle distribution functions that would be detected by spacecraft passing Earthward and tailward or a reconnection X-line. Panel (a) shows the spacecraft's path through the regions, with the coloured regions indicating where different energy particles would be observed. Panel (b) shows the magnetic field B_X component and the particle energy spectrograms (particle distribution functions).

of reference moving in opposite directions, and the various particle velocities in the Earth (stationary), Earthward moving and tailward moving frames. Note that particles are only shown inflowing from one side of the X-line for each magnetic field-line, although approximately equal numbers of particles flow in from either side. If V_i is known, then

$$V_o = 2V_A \mp V_i \qquad (1.50)$$

for the field-lines moving towards and away from the Earth respectively. Note that particles moving towards the Earth are accelerated to a lower speed than those travelling away from the Earth, leading to anti-symmetric particle beams.

In the stationary frame of reference, it was assumed that the particles remain fixed to the field-line, such that $V_Z/V_= B_Z/B$. Since none of these variables change when the frame of reference changes, the relationship is equally applicable in the Earth's frame of reference. The angle of the particle velocity to the X-direction is then given as

$$\tan \theta_{E,T} = \frac{V_A B_Z}{B(2V_A \mp V_i)} \equiv \frac{V_A}{(2V_A \mp V_i)} \sin \theta_B \qquad (1.51)$$

which, using the low angle approximation gives

$$\theta_{E,T} = \frac{V_A}{(2V_A \mp V_i)}\theta_B \qquad (1.52)$$

Hence, the particles form a beam that is close to, but not, field-aligned. Note that as particle energy (and thus velocity) increases, the angle that the particles flow out at tends towards the angle of the field on the Earthward side. This then gives a signature of reconnection; higher energy particles are seen in beams that are approximately field aligned further from the centre of the current sheet, with particle energy dropping with decreasing $|Z|$ on the Earthward side of the X-line. On the tailward side,the inverse is true. Figure 1.7 shows the particle energy spectra and magnetic field B_X as a spacecraft crosses across the particle out-flow region of an X-line on the Earthward and tailward sides.

It is also interesting to note that the speed of the field-lines is determined only by the particle inflow velocity and the Alfvén velocity. Considering that the speed of the field-lines is due to the electric field,

$$\frac{E_Y}{B_Z} = V_A \mp V_i \qquad (1.53)$$

Since V_A and V_i are not determined by the rate of reconnection, E_Y and B_Z must vary coherently. As such, an increased rate of reconnection produces more dipolar field-lines and vice versa.

It should be noted that this description does not describe all of the physics associated with particle acceleration due to reconnection, or deal with reconnection itself. Introducing particle gyrations introduces complications such as the demagnetisation of ions and electrons at different distances from the X-line due to their differing Larmor radii. However, observations of magnetotail regions such as the plasma sheet boundary layer (PSBL), which consists of recently reconnected plasma, match the predictions of this treatment of the problem to first order.

Chapter 2

Literature Review

> *And by that destiny, to perform an act whereof*
> *What's past is prologue; what to come,*
> *In yours and my discharge*
> William Shakespeare, "The Tempest", Act 2 Scene 1

In this chapter I provide an overview of previous work on magnetospheric physics with particular relevance to this thesis. The concepts of substorms, bursty bulk flows (BBFs) and the wavy current sheet, the prominent dynamical features of the magnetosphere that I study in this thesis, are introduced. I give a brief overview of the substorm cycle and the features of each phase of the substorm, as well as discussing the how substorms affect the global magnetospheric system. Also discussed are some of the features of BBFs and how these phenomena have been related to dynamical activity in the tail, such as substorms. Finally, I discuss the wavy current sheet; a type of large scale magnetospheric activity.

2.1   Substorm Observations and Models

In order to further understand the underlying physics of substorms, observations of the dynamical processes involved have been combined in the framework of various phenomenological models. Baumjohann *et al.* (1988, 1989) noted that these models were generally developed to account for distinct observed dynamical features, as opposed to accounting for previously observed features. As spacecraft instrument technology has improved and further observations have been taken, these models have become more sophisticated.

It is generally considered that there are two major competing substorm models; the current disruption (CD; Lui, 1991, 1996, 2000, and references therein) and near-Earth neutral line (NENL; McPherron *et al.*, 1973; Baker *et al.*, 1996; Lui, 2000, and references therein) models. In their most basic forms, these models account for the majority of the

observed substorm phenomena (as is necessary for a successful model). However, they vary in their implied causality of various features, such as the expansion phase onset (see Fig. 2.1). There are also numerous theories on the causes of substorms, such as triggering by northward turnings of the IMF (Lyons *et al.*, 1997) or when the energy state of the magnetosphere reaches a critical level (Freeman and Morley, 2004). Although the question of triggering is an interesting area of research, I leave this to be discussed by other authors.

Substorms nominally consist of three phases; growth phase, expansion phase (which traditionally begins with the substorm onset), and recovery phase (e.g. Akasofu, 1964; McPherron, 1970; McPherron *et al.*, 1973). These phases are not always unambiguous, especially in the case of a series of substorms or substorms with multiple expansion phase onsets. Due to historical reasons, the substorm onset is considered to be the start of the expansion phase. Early observations of substorms were made from the ground (e.g. Akasofu, 1964), where the growth phase signature may not be particularly strong (McPherron *et al.*, 1973). As such, the onset was considered to be the time of the auroral breakup, which is now known to be related to the start of the expansion phase in the magnetotail. This terminology is retained.

The growth phase starts with a southward turning of the IMF. Under these conditions, reconnection occurs at the sub-solar point, eroding the Earth's dayside magnetic field. It is anticipated that the rate of reconnection at the dayside would not be matched by reconnection in the tail as there is no apparent mechanism for the near instantaneous transfer of information about the reconnection rates, hence the amount of open flux in the magnetosphere increases. This manifests itself as an increase in the size of the polar cap. The newly opened field-lines are moved across the polar cap via their connection with the solar wind and added to the magnetotail lobes. This addition of flux to the tail increases the flaring of the magnetosphere (Milan *et al.*, 2004), increasing the angle of attack of the solar wind ram pressure and causing the plasma sheet to thin and cross tail current to increase (McPherron, 1979). The magnetotail becomes stretched and less dipolar (e.g. Fairfield and Ness, 1970; Kokubun and McPherron, 1981; Nagai, 1982). At the ground, the growth phase can be associated with a gradual increase in the AE index (McPherron, 1970).

The expansion phase onset is still the subject of much debate since the features that cause or are related to the onset and their locations provide the fundamental differences between the CD and NENL models. For the CD model, a current disruption occurs in the inner magnetosphere (<10 R_E) causing the cross tail current to be diverted along the magnetic field-lines and the disruption region to become dipolarized (Lui, 1991; Lui *et al.*, 1991; Lui, 1996). A rarefaction wave then propagates downtail, eventually initiating reconnection further downtail. For the NENL model, the tail current sheet thins with the addition of flux into the lobes during the growth phase. At some point, the sheet becomes so thin that reconnection begins, firstly on closed field-lines and rapidly expanding to open

1) Electric field associated with an auroral arc enhances current density when ions become unmagnetized, leading to onset of a current-driven instability (current disruption occurs)

2) The most equatorward auroral arc, associated with the largest cross-tail current, is the most likely location of auroral breakup

7) An X-type magnetic neutral line develops from a CD site and causes a major plasma sheet recovery

3) Current disruption (CD) causes substorm injection of energetic particles

4) CD causes further thinning of mid-tail plasma sheet, leading to CD spreading tailward

5) Multiple CD sites occur within the thin current sheet

6) Turbulence in CD causes efficient plasma and magnetic flux transport

dipolar and tail like field (10-20 R_E)

4) field-aligned current of the substorm current wedge

5) Initial brightening of aurora

3) Pileup of magnetic field

2) High-speed ion flow in the neutral sheet (10-20 R_E)

1) X-type reconnection (20-30 R_E)

3) Dawnward inertia/pressure current

5) Pi2 pulsation

4) compressional pulse

5) Particle injection at 6.6 R_E

Figure 2.1: Schematics of the phenomenology of the current disruption (top figure) and near-Earth neutral line (bottom figure) models, after Lui (2000).

field-lines (Baker *et al.*, 1996). Following the expansion phase onset, the tail magnetic field topology becomes more dipolar, especially at geosynchronous orbit, coupled with the diversion of the cross tail current into the ionosphere via the substorm current wedge (McPherron *et al.*, 1973; Rostoker, 1974; Nagai, 1982). This dipolarization of the field is initially localised and then expands azimuthally (Kokubun and McPherron, 1981; Nagai, 1982) and can extend over several R_E downtail (Nakamura *et al.*, 2005b). The azimuthal propagation of the dipolarization at geosynchronous orbit has been associated with the azimuthal expansion of the substorm auroral bulge (Liou *et al.*, 2002). Furthermore, it has been shown that the expansive motion of the auroral bulge is determined by the polarity of the IMF B_Y component if it is fairly steady, although the speed of the expansion is only moderately correlated with the magnitude of the IMF B_Y (Liou *et al.*, 2006). Liou and Ruohoniemi (2006a,b) used two case studies to show that the direction of the expansion of the auroral bulge was dependent on the plasma convection flows at the location of the auroral breakup. On the ground, the expansion phase results in the rapid formation of magnetic bays (negative excursions in the northward magnetic field component), related to the formation of the substorm electrojets. Furthermore, an auroral bulge forms and expands polewards. Substorm expansion phases can close large amounts of magnetic flux in the magnetotail, in some cases up to 80% of the open flux in the magnetosphere prior to the substorm onset (Milan *et al.*, 2006a), and as such are a major dynamic process within the magnetosphere.

The recovery phase begins at the end of the expansion phase, when the expansion of the aurora reaches it maximum poleward excursion. At the ground, the recovery phase is also identified by the recovery of magnetic bays or a maximum in the AE index. In the tail, the recovery phase begins when the near-Earth neutral line begins to retreat downtail (Hones, 1984; Baker *et al.*, 1996). At this point, the rate of retreat of the centre of the plasmoid exceeds the rate at which new flux is being added to it. However, it should be noted that there can be a disparity between the ground and tail signatures (Baker *et al.*, 1994).

2.2 Bursty Bulk Flows

The Dungey Cycle (Dungey, 1961) and its associated ionospheric convection (see Figs. 1.2 and 1.3) imply that plasma is transported Earthwards and towards the flanks of the magnetosphere. In the simplest case, the cross-tail electric field would drive the plasma Earthwards at a steady rate through the plasma sheet. Statistical studies of plasma flows in the plasma sheet showed that the average ion speed in the central plasma sheet was low ($\sim$50 km s^{-1}) leading to the conclusion that high speed plasma flows were statistically insignificant (Huang and Frank, 1986, 1987). However, the selection criterion that flows of $V_i > 150$ kms^{-1} detected at $|Z| > 1.5$ R$_E$ were PSBL flows and therefore not considered in their study, was somewhat limiting and likely removed a significant proportion of plasma

sheet high speed flows from the results. Baumjohann *et al.* (1990) later showed that high speed flows with $V_i > 400 \, \text{km s}^{-1}$, identified using AMPTE/IRM, occurred with almost equal frequency in the PSBL and central plasma sheet, predominantly near midnight in the central plasma sheet and with increasing frequency with distance downtail. They also showed that the majority of these central plasma sheet fast flows were perpendicular to the magnetic field direction, indicating flux transport, as opposed to the PSBL fast flows, which tended to be parallel to the magnetic field. This, together with the result of Baumjohann *et al.* (1989) that the fast flows were directed Earthwards, hinted at the importance of fast flows to the transport of plasma through the magnetotail.

Angelopoulos *et al.* (1992) provided an analysis of several quiet time (AE<100 nT) fast flow events and coined the terminology now commonly used to describe them. They noted that the flow velocity was highly variable, arranged in sporadic, uncorrelated bursts of high speed flows ($V_i > 400 \, \text{km s}^{-1}$) lasting of the order of 1 min (flow bursts or FBs) embedded within longer period velocity enhancements of about 10 min duration (bursty bulk flows or BBFs). Echoing the results of Baumjohann *et al.* (1989, 1990), they showed that the FBs were predominantly directed Earthwards, whereas flows at other times had arbitrary directions, and were often directed at >45° to the local magnetic field. They also noted that these flows were associated with transient dipolarizations of the magnetic field, shown most clearly in their superposed epoch analysis of the flow bursts (see their Fig. 6, reproduced in Fig. 2.2). Furthermore, they derived the electric field and Earthward energy flux density for a particular event to show that, given sufficient size or occurrence frequency, BBFs were capable of transporting the necessary levels of energy, magnetic flux and mass to meet the requirements of the Dungey Cycle.

The definitions of BBFs and FBs by Angelopoulos *et al.* (1992) were arbitrary and not based upon a physical quantity or model (as noted by the authors). Although various other criteria have be used to define BBFs and FBs (see Cao *et al.*, 2006), these have been developed to emphasise particular properties of the flows, such as the flux transport, and were also not based upon physical models of the flow. Although it is useful to use these in large, automated studies of the magnetotail, one should be prepared to use these criteria as guidance in individual case studies (e.g. Forsyth *et al.*, 2008a, or Chapter 5).

Spacecraft studies have determined approximate sizes for BBFs. The results of Angelopoulos *et al.* (1992) showed that BBFs could be an important transport mechanism within the magnetosphere, given a sufficient size. Sergeev *et al.* (1996) used the two ISEE spacecraft (separated by 0.3 R_E) to estimate the width of a series of BBFs. Using minimum variance analysis (see Chapter 4) to determine the orientation of the fronts of the flows (the point at which the spacecraft first encountered the flow) at both spacecraft, and assuming that the front side of the flow was semi-circular. They determined that the width of the BBF was between 1 and 3 R_E. Nakamura *et al.* (2001b) performed a statistical analysis of 20 BBFs using plasma data from Geotail and auroral data from Polar. From this, they estimated the azimuthal size of BBFs based on mapping their auroral

INNER CPS FLOWS
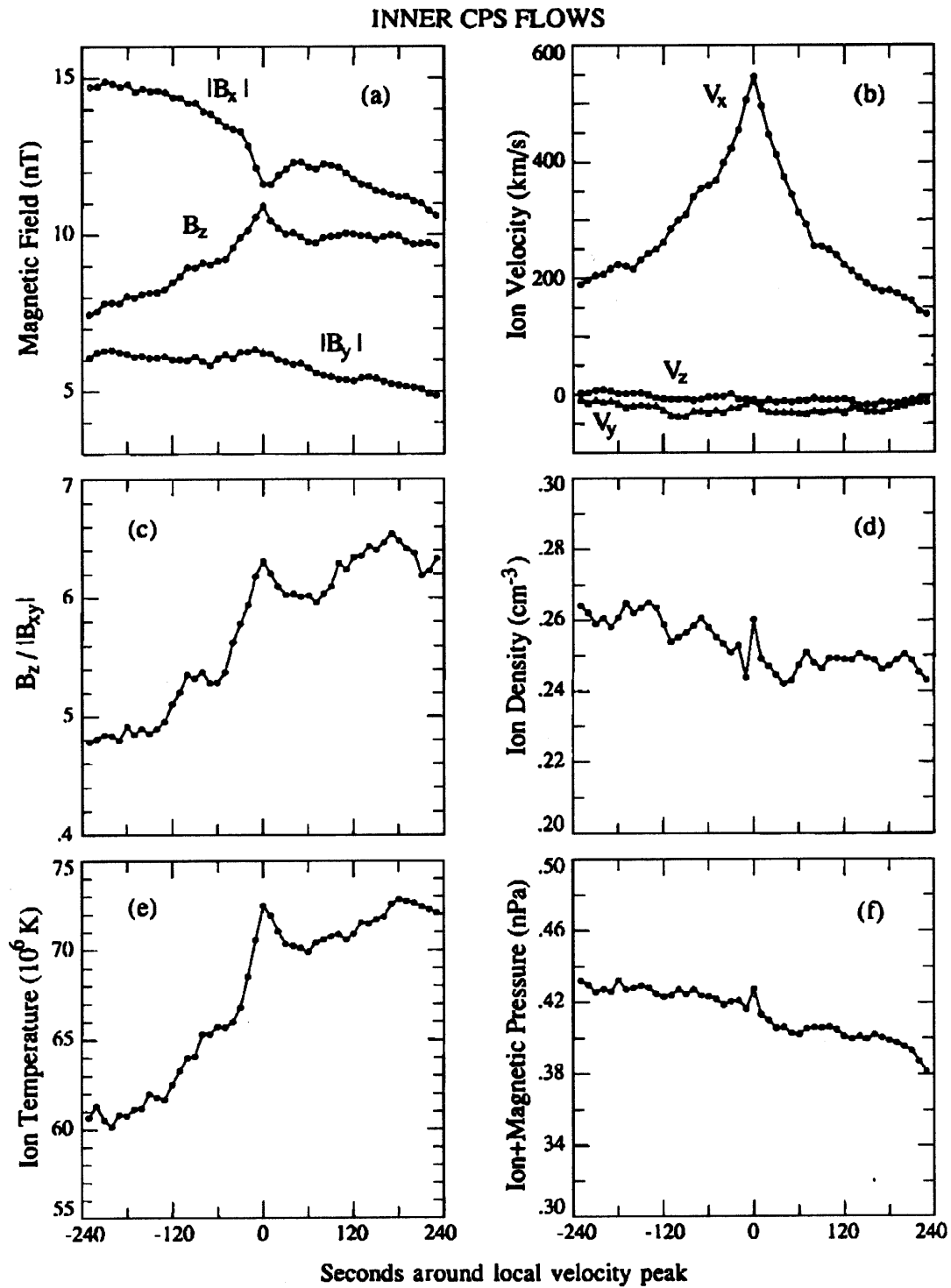
Figure 2.2: Results of superposed epoch analysis of central plasma sheet flow bursts taken from Angelopoulos *et al.* (1992). Plasma and magnetic field data from AMPTE-IRM were averaged over ±4 min of the velocity peak of a flow burst.

manifestations into the magnetosphere. Following on from Nakamura *et al.* (2001a), who showed that BBFs at different radial distances down the tail related to different auroral signatures, Nakamura *et al.* (2001b) showed that BBFs associated with small expansions of the aurora (often referred to as pseudo-breakups) were associated with BBFs with a width of 4-5 R_E at an average distance of 13 R_E down tail, whereas BBFs associated with auroral streamers had a width of 3-4 R_E at an average distance of 23 R_E down tail. Amm and Kauristie (2002) suggested that BBFs had a radial length of greater than 10 R_E but provided no direct evidence of this. However, a quick calculation based on the cut-off speed for the detection of BBFs (taken to be 100 $\mathrm{km\,s^{-1}}$) and the period over which they are observed (10 min) gives an length of approximately 10 R_E . By the same argument, flow bursts with a speed of 400 $\mathrm{km\,s^{-1}}$ and lasting for 1 min are approximately 4 R_E long. Sergeev *et al.* (2000) used a fortuitous conjunction of five spacecraft to study a BBF over 17 R_E of the tail. Based on the energy dispersion of the ions detected by one of the spacecraft (Interball), they determined that the BBF initiated at 40 R_E and implied that the flow had significant length in the tail, although again provided no quantitative estimate of the flow length.

Models of the magnetosphere under steady convection suggested that, due to adiabatic drift, $pV^{5/3}$ is constant along the drift path of the flux tubes (Wolf, 1983), where p is the particle pressure and V is the flux tube volume. However, observations of the magnetotail and observation-based models of the magnetic field showed that the gradients in p and V were inconsistent with this theory. This inconsistency was termed the "pressure crisis". Chen and Wolf (1993) showed that, based on the Tsyganenko (1987) magnetic field model, the pressure in a flux tube moved from X=-30 R_E to X=-14 R_E was an order of magnitude larger than the observed pressure. Pontius and Wolf (1990) suggested that flux tubes that were depleted of plasma compared to the local plasma conditions, or "bubbles", could solve this "pressure crisis". They suggested that these flux tubes would have a lower particle pressure than the surrounding flux tubes, hence a higher magnetic field strength, and that these flux tubes would move Earthwards with large velocities. Chen and Wolf (1993) showed that, if the depleted flux tubes were more dipolar than the surrounding flux tubes, then the ratio of $pV^{5/3}$ between the depleted flux tube and the surrounding flux tubes would decrease with distance from the cross-tail current sheet, such that the particle pressure within the flux tube could be higher than the surrounding plasma, yet the flux tube was still depleted of plasma (see their Table 1 and Fig. 4, reproduced in Fig. 2.3 and Table 2.1). This model was consistent with the observations of Angelopoulos *et al.* (1992), who showed through superposed epoch analysis that the ion temperature increased during flow bursts, whilst the ion density remained approximately constant. BBFs associated with a drop in plasma pressure and density have been observed (e.g. Sergeev *et al.*, 1996; Forsyth *et al.*, 2008a, and Chapter 5) and that these are not in violation of the Chen and Wolf (1993) model.

Chen and Wolf (1993) failed to discuss the effect of the change in the $pV^{5/3}$ ratio along
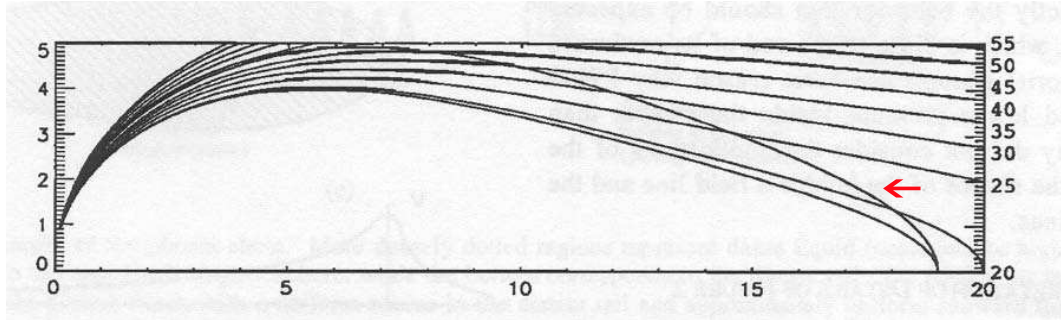
Figure 2.3: Magnetic field model used by Chen and Wolf (1993) to determine the flux tube volume of a more dipolar flux tube (indicated by the red arrow).

	Equatorial crossing point, R_E	p	V	$pV^{5/3}$
Bubble	19	1237.2	1.387	2135
Medium	19	1239.6	1.378	2115
Medium	20	1230.1	1.497	2410
Medium	25	1189.4	2.033	3880
Medium	30	1154.2	2.468	5202
Medium	35	1121.3	2.835	6367
Medium	40	1089.6	3.163	7425

Table 2.1: Comparison of bubble properties with neighbouring flux tubes from Chen and Wolf (1993)

the length of the flux tubes with regards to the "buoyancy" of the flux tube. The authors suggest that the interchange instability drives the flux tubes into the inner magnetosphere towards regions of comparable $pV^{5/3}$. However, near the equatorial plane, $pV^{5/3}$ is approximately balanced with the surroundings in their calculations, such that the portions of the flux tube further from the current sheet would be convecting at a higher velocity than those nearer the current sheet.

As BBFs are small scale, dynamical, non-stationary features in the magnetotail, it is almost impossible to follow their evolution and propagation using spacecraft. Birn *et al.* (2004), furthering the work of Chen and Wolf (1999), used a 3-dimensional MHD code to investigate the propagation of depleted flux tubes through the magnetotail by imposing pressure and density depletions on localised flux tubes. They found that reductions in the flux tube entropy ($S = \int p^{1/\gamma} ds/B$) controlled the evolution of the flux tube and was important in a number of factors. Firstly, non-depleted flux tubes given an initial Earthward velocity did not propagate into the inner magnetosphere, unlike those with a reduced entropy. Secondly, the entropy reduction controlled the speed with which the flux tubes propagated into the magnetosphere, such that flux tubes given an initial Earthward velocity reached similar final velocities as those that were initially stationary. In contrast to Chen and Wolf (1993), who assumed that the particle pressure along a mature depleted flux tube was constant, Birn *et al.* (2004) modelled the effect of the depletion of a flux tube and showed that along the flux tube pressure balance was not maintained such that neither the pressure nor the pressure gradient along the flux tube were constant.
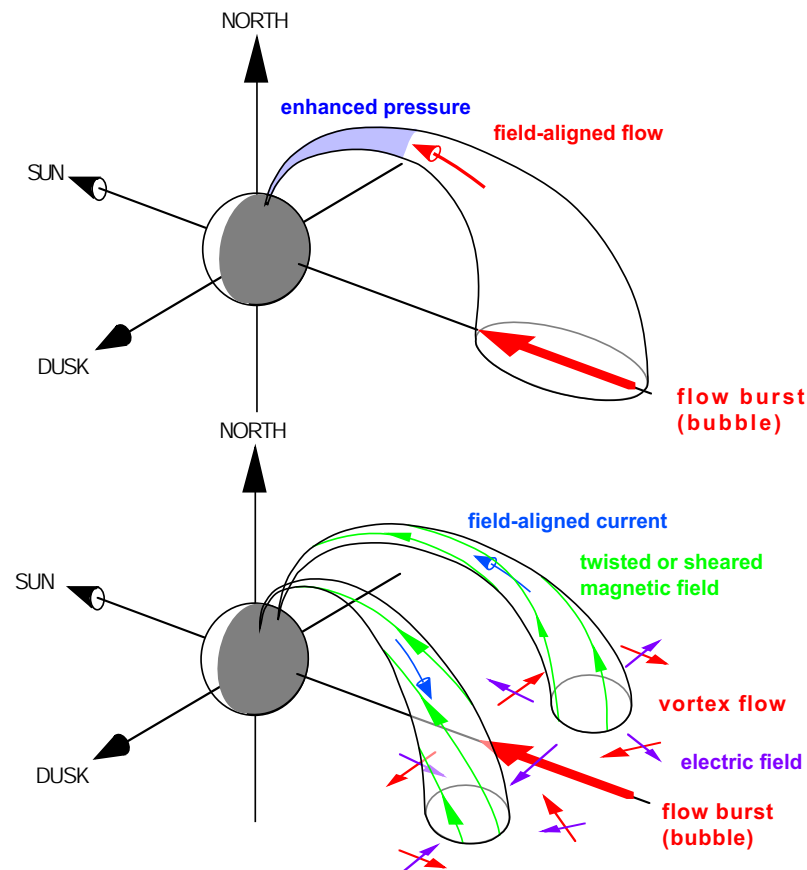
Figure 2.4: Schematic of the results from the MHD model of Birn *et al.* (2004). Reproduced from their Fig. 19.

Birn *et al.* (2004) noted that their model was limited by the initial perturbation applied to the model flux tube. Whereas their model solely reduced the pressure (or density), models of reconnection reduce the volume of flux tubes, and hence their entropy (Birn *et al.*, 1996). These can then also give density reductions and temperature increases, as have been associated with BBFs (Angelopoulos *et al.*, 1992; Sergeev *et al.*, 1996, e.g.). However, under the right initial perturbations (of density rather than pressure), the model might still be considered valid given that it is the reduction in entropy that is important.

2.2.1   BBF as mangetotail phenomena

Since their discovery, BBFs and FBs have been implicated in many magnetotail dynamical processes, most notably the formation of the substorm current wedge (Birn and Hesse, 1996; Shiokawa *et al.*, 1997, 1998a,b; Birn *et al.*, 1999). As such, BBFs are seen as crucial in the substorm cycle. Proponents of the NENL model have adapted the model such that fast flows into the inner magnetosphere, generated by reconnection at the near-Earth neutral line, cause the formation of the substorm current wedge and current disruption in the inner magnetosphere. On the other hand, proponents of the CD model proposed that fast flows from localised bursts of reconnection would propagate into the inner tail,
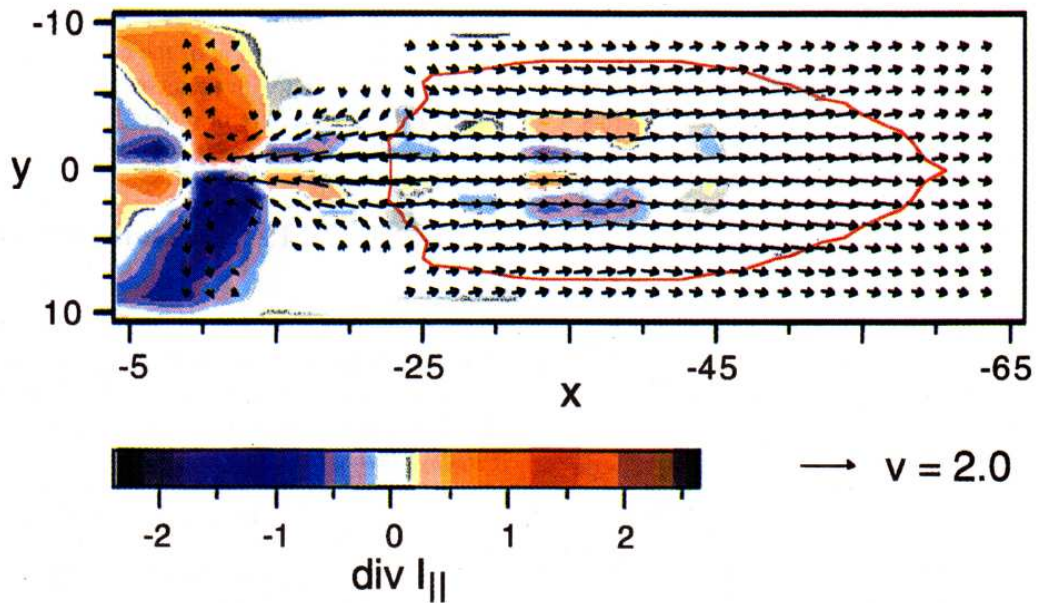
Figure 2.5: Divergence of the parallel currents and flow vectors from the model of Birn *et al.* (1999), showing the generation of a substorm current wedge due to fast flows generated by a reconnection X-line (red line in the figure). From Birn *et al.* (1999), Plate 1.

providing the conditions for current disruption to take place.

Birn and Hesse (1996) simulated the effect of high-speed flows on the inner magnetosphere (X< -5 R$_E$) following a current disruption in the inner magnetosphere. Their results showed that the braking of fast flows in the inner magnetosphere could generate currents comparable to those seen in the substorm current wedge. However, Haerendel (1992) and Shiokawa *et al.* (1997, 1998b) showed that the inertial currents and currents due to pressure balance were insufficient to drive the substorm current wedge. Birn *et al.* (1999) revisited the work of Birn and Hesse (1996) to investigate this inconsistency by considering the various components of the current. They found that their simulations predicted that the majority of the field-aligned current was due to an azimuthal pressure gradient caused by the injection of plasma in the midnight sector from the reconnection X-line, rather than the inertial currents of the fast flows. Furthermore, they showed that the pressure gradient currents outlasted the duration of the fast flows, whereas the inertial currents only lasted as long as the flow bursts. This was in keeping with Shiokawa *et al.* (1998b), who used data from the AMPTE/IRM spacecraft and the plasma sheet definitions of Baumjohann *et al.* (1989) to show that there was a pressure gradient within 30° azimuth of the midnight line, although their data was limited to 3 data points in either direction. Interestingly, the model of Birn *et al.* (2004) showed that as depleted flux tubes evolve a pressure gradient from the ionosphere to the tail builds up in conjunction with a reduction in the Earthward velocity of the particles, although they did not discuss whether or not the pressure within the depleted flux tubes is still reduced with respect to the surrounding flux tubes.

Since the initial studies into BBFs, many authors have implied a connection between BBFs and reconnection (e.g. Angelopoulos *et al.*, 1992; Chen and Wolf, 1993; Sergeev *et al.*, 1996, and others). Models of the magnetosphere have shown the creation of fast flow channels following the onset of reconnection (Birn and Hesse, 1996; Birn *et al.*, 1999). However, their localised nature means that the creation of BBFs does not close as much flux as larger substorm events. Milan *et al.* (2006a) studied the flux closure and reconnection rates associated with 14 reconnection events, including nine substorms and one event during northward IMF that was related to a BBF (Grocott *et al.*, 2004, 2007, see below). Milan and co-authors showed that the substorm events in their study closed, on average, 0.5 GWb of open magnetic flux with a flux closure rate of between 50 and 100 kV, whereas the BBF event only closed 0.15 GWb of flux associated with a flux closure rate of 30 kV. This flux closure rate is similar to, but larger than, the values reported by Grocott *et al.* (2004, 2007) (10 and 25 kV respectively). However, the flux transport reported by Milan *et al.* (2006a) was somewhat higher than the flux transport associated with individual BBFs Angelopoulos *et al.* (1994), given that they are expected to have a cross-tail size of 3-5 R_E . Grocott *et al.* (2007) explained this by suggesting that the reconnection rate observed in the ionosphere consisted of the reconnection due to a number of localised BBFs.

The difficulty in determining the flux closure associated with BBFs should be noted. Firstly, unambiguously determining the flux closure associated with a BBF from the ionosphere during substorm expansion phases is difficult due to the underlying electro-dynamics occurring during the expansion phase. Secondly, the majority of spacecraft observations of BBFs in the magnetosphere cannot instantaneously determine the size of the BBF since the shape and limits of the flow may not be determined.

More recently, Sergeev *et al.* (2006) implied that BBFs and FBs might be connected to the generation of current sheet flapping waves. These waves propagate azimuthally across the current sheet with a relatively low propagation speed, large wavelength and a large tilt in the current sheet in the YZ plane (Zhang *et al.*, 2002; Runov *et al.*, 2003; Sergeev *et al.*, 2003, 2004a; Zhang *et al.*, 2005; Sergeev *et al.*, 2006). In particular, Sergeev *et al.* (2006) provided circumstantial evidence that the occurrence rate of the current sheet flapping waves detected by Geotail was similar to the occurrence rate of fast flows ($V_X >$400 $\mathrm{km\,s^{-1}}$) in the radial direction, although the correspondence was not as good in the azimuthal direction.

2.2.2   Ionospheric counterparts of BBFs

As noted by Sergeev *et al.* (2000), the study of BBFs necessitates the investigation of ionospheric and auroral features associated with the flows to aid the determination of their global impact. Multi-spacecraft studies using closely separated spacecraft may enable the
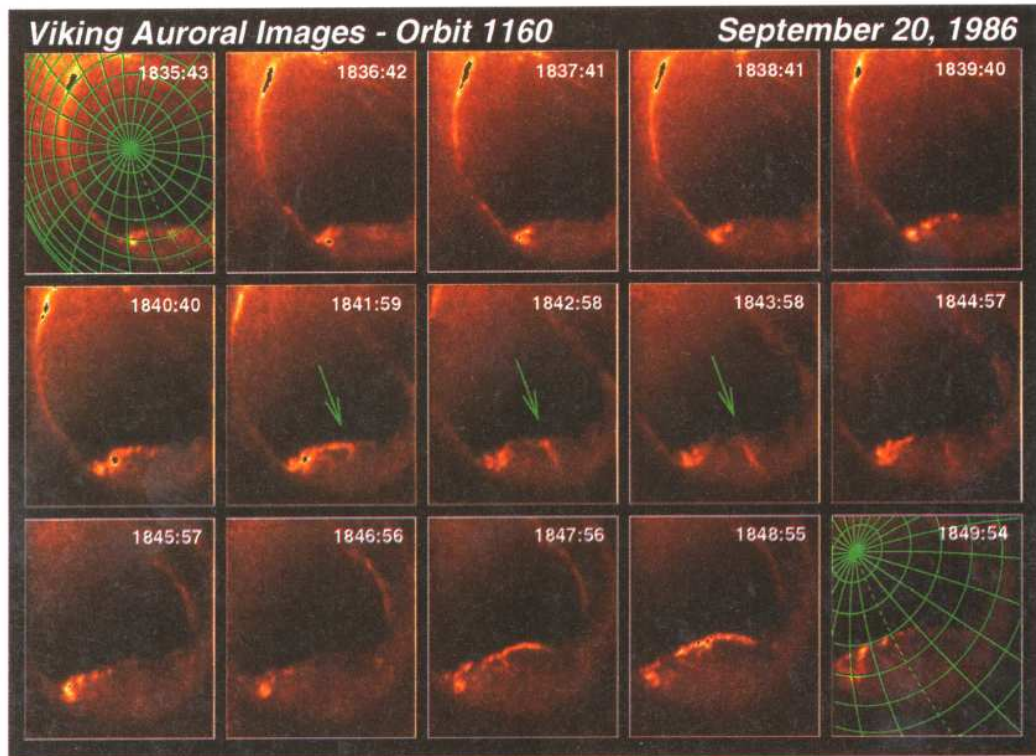
Figure 2.6: Auroral images of a substorm taken by the Viking spacecraft and presented in Henderson *et al.* (1998), Fig. 2. An auroral streamer was evident (indicated by the arrows between 1841 UT and 1844 UT). Henderson *et al.* related these auroral phenomena to BBFs.

determination of features such as the propagation of the flow and the currents associated with it, but on a global scale represent a point measurement, whereas without ionospheric observations, there is no way to unambiguously confirm that a BBF observed by multiple spacecraft separated by large distances (i.e. several R_E) are the same feature.

Henderson *et al.* (1998) attempted to relate BBFs to auroral streamers using circumstantial evidence rather than direct observations of the flow. Subsequent studies, however, were able to relate BBFs and auroral activity in a more quantitative manner (Lyons *et al.*, 1999; Sergeev *et al.*, 2000; Nakamura *et al.*, 2001a; Grocott *et al.*, 2004). Nakamura *et al.* (2001a) studied the relationship between flow bursts, their mapped ionospheric locations and auroral activations for 31 flow bursts detected by Geotail. They found a one-to-one correlation between their flow bursts and auroral activations near the footpoint of the spacecraft, leading them to conclude that all FBs are associated with auroral activity. Also, using event-orientated magnetic field modelling, they found that the Geotail footpoints at the times of the flow were close to the auroral activity. We note, however, that Nakamura *et al.* (2001a) used a somewhat restrictive selection criteria (flux transfer rate greater than 2 mV m^{-1} for no more than 10 min separated from all other events by more than 5 min). This criteria would remove a significant number of events consisting of multiple flow bursts. The authors themselves noted that their study did not include any events from large substorm events during which time the accuracy of magnetic field-line mapping may be reduced and distinct auroral features may be obscured.

More recent observations of auroral streamers have provided new insight into their generation mechanisms. White-light All-Sky Imagers deployed in Canada to coincide with the launch of NASA's THEMIS spacecraft provided high time and spatial resolution images of the auroral zone over much of the North American continent. Studies using space-borne auroral imagers were restricted due to the relative low temporal and spatial resolutions. Liu *et al.* (2008) provided a case study of a series of quiet time auroral streamers using these imagers. From these data, they showed that the equatorward evolution of a poleward boundary intensification into an auroral streamer was very rapid ($\sim$10 s) after a "gestation" period of approximately 1 min. Also, the streamer width was somewhat narrower than previously reported. Furthermore, they suggested that the apparent poleward motion of some streamers was because the auroral enhancement was due to Alfvén waves emanating from a moving source.

Ground-based magnetometer observations of auroral streamers and near the footpoints of BBFs (Amm *et al.*, 1999; Kauristie *et al.*, 2000; Amm and Kauristie, 2002; Grocott *et al.*, 2004) have shown these features to be associated with a distinct signature in the magnetic field data. Amm *et al.* (1999) identified the magnetic signature of an auroral streamer to be a minimum in the Z (downward) component of the magnetic field associated with the equatorward (duskward) edge of the streamer, whereas the Y component (eastward) showed a distinct sawtooth-like feature. A similar feature in the Y component can be seen in the data presented by Grocott *et al.* (2004, Fig. 4). This signature can be understood by considering that ground-magnetometers detect the divergence-free ionospheric current associated with the field-aligned currents within the feature (Untiedt and Baumjohann, 1993; Amm and Kauristie, 2002). During quiet times, one might expect to see a similar feature in the X (northward) component (in fact, one is visible in Grocott *et al.* (2004)), although during more disturbed periods, such as substorms, the prevailing elecrojet currents may mask such a feature. A further magnetic signature of BBFs has been shown to be an increase in Pi2 wave activity (Lyons *et al.*, 1999; Amm and Kauristie, 2002; Grocott *et al.*, 2004).

Coherent scatter radars, such as the SuperDARN radars (Greenwald *et al.*, 1995; Lester *et al.*, 2004; Chisham *et al.*, 2007) facilitate the observation of large swathes of the polar and auroral ionosphere. Grocott *et al.* (2004) used these radars to investigate the ionospheric convection signatures associated with a BBF observed by Cluster during a substorm growth phase. They showed that enhanced convection flows (500-1000 m s^{-1}) occurred near the footpoint of the Cluster spacecraft at the time they detected the BBF in conjunction with an auroral brightening and an increased polar cap potential. Using the Map Potential Model (Ruohoniemi and Baker, 1998) and the method of McWilliams *et al.* (2001), Grocott and co-authors showed that the auroral brightening was associated with a region of upward field aligned current. Grocott *et al.* (2007) later showed that bursts of high speed convective return flow related to tail reconnection during extended intervals of northward IMF with no substorm signature (coined "tail reconnection during IMF
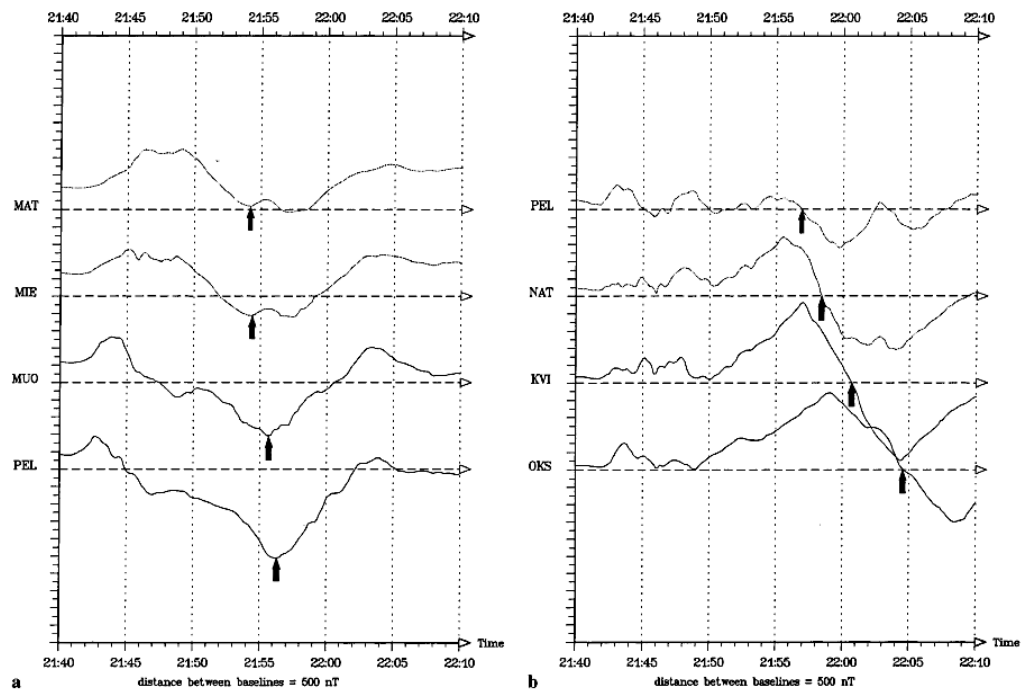
Figure 2.7: Ground magnetometer data in (a) the Z (positive downwards) direction and (b) the Y (eastwards) direction from various stations in the Scandinavian Magnetometer Array at the during the passage of an auroral streamer. From Amm *et al.* (1999), Fig. 4.
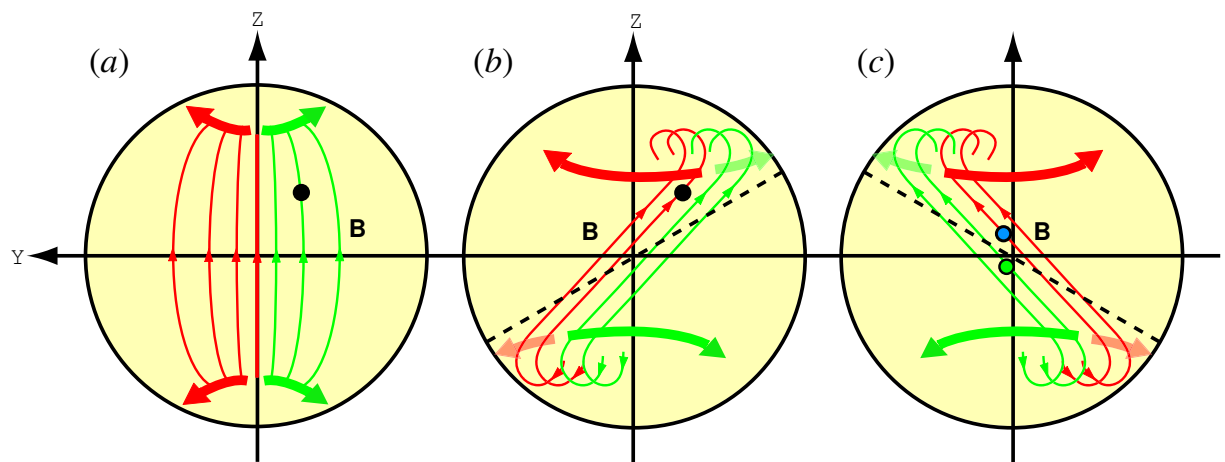
Figure 2.8: Schematic of the twisting of closed magnetotail field-lines due to the IMF B_Y, looking towards the Earth from the tail. The red and green curves represent closed BBF magnetic field-lines, with the thick arrows indicating the TRINNI flow directions in the ionosphere. Green (red) lines represent field-lines reconnected pre- (post-) midnight. The three panels indicate the situation for (a) IMF B_Y 0, (b) IMF $B_Y < 0$ and (c) IMF $B_Y > 0$. Figure taken from Grocott *et al.* (2007).

northward, non-substorm intervals", or TRINNIs, by Milan *et al.* (2005)) were associated with BBFs. In particular, they showed that under the influence of a steady IMF B_Y, the magnetotail would twist and that the convection signatures of BBFs in opposite hemispheres would be in opposite directions (see their Fig. 6, reproduced in Fig. 2.8).

2.2.3 BBF current systems

Magnetospheric current systems are of fundamental importance to the dynamics of the magnetosphere, and the currents associated with BBFs are no different. Field aligned currents that run along the edges of the flow (Sergeev *et al.*, 1996) support the dipolarized magnetic field within them, allow the flow to penetrate into the inner magnetosphere and transfer energy from the magnetosphere to the ionosphere through Joule heating and auroral excitation (e.g. Henderson *et al.*, 1998; Nakamura *et al.*, 2001a,b; Forsyth *et al.*, 2008a).

The superposed epoch analysis by Angelopoulos *et al.* (1992) showed that FBs were associated with a transient dipolarization of the magnetic field, resulting in a shear in the magnetic field between the FB and the surrounding plasma. Sergeev *et al.* (1996), based on the depleted flux tube model of Chen and Wolf (1993), formalised the expected current system and plasma signatures of BBFs. Considering the reduced plasma pressure within the depleted flux tube, Sergeev and co-authors suggested that the cross-tail current within the bubble would be reduced, and that field aligned currents in the form of a current wedge or intertidal currents would maintain the current continuity. Further, they suggested that a shear in the plasma flows would be present at the edges of the BBF, pushing the surrounding flux tubes aside and allowing the BBF to penetrate into the inner magnetosphere.

Previous studies have provided evidence of the current system suggested by Sergeev *et al.* (1996). Amm *et al.* (1999) used ground-based magnetometers and ionospheric radars to determine the current system associated with an auroral streamer. Although these narrow, north-south aligned auroral forms were proposed to be the ionospheric counterpart to BBFs given their small azimuthal size and the association with field-aligned currents (Henderson *et al.*, 1998), and have since been shown to be closely correlated with BBFs (Nakamura *et al.*, 2001a,b), Amm *et al.* (1999) provided no direct evidence of the association with a BBF. Amm and co-authors found that the bright, duskward edge of the auroral streamer was associated with a narrow region of large upward field-aligned current and that the diffuse aurora to the dawnward side of the steamer were associated with a region of smaller downward field-aligned currents. This current system was in keeping with the expected ionospheric currents required to close the BBF magnetospheric current system. Nakamura *et al.* (2005a) expanded upon this and confirmed the results of Amm *et al.* (1999) using the magnetometers of the IMAGE magnetometer network to determine the current associate with a BBF detected by the Cluster spacecraft when their footprints were located near to the magnetometers (see their Fig. 11b, reproduced in Fig. 2.9).

The first published quantitative study of the magnetospheric currents associated with BBFs was by Snekvik *et al.* (2007), who used the Cluster spacecraft to study the in-situ
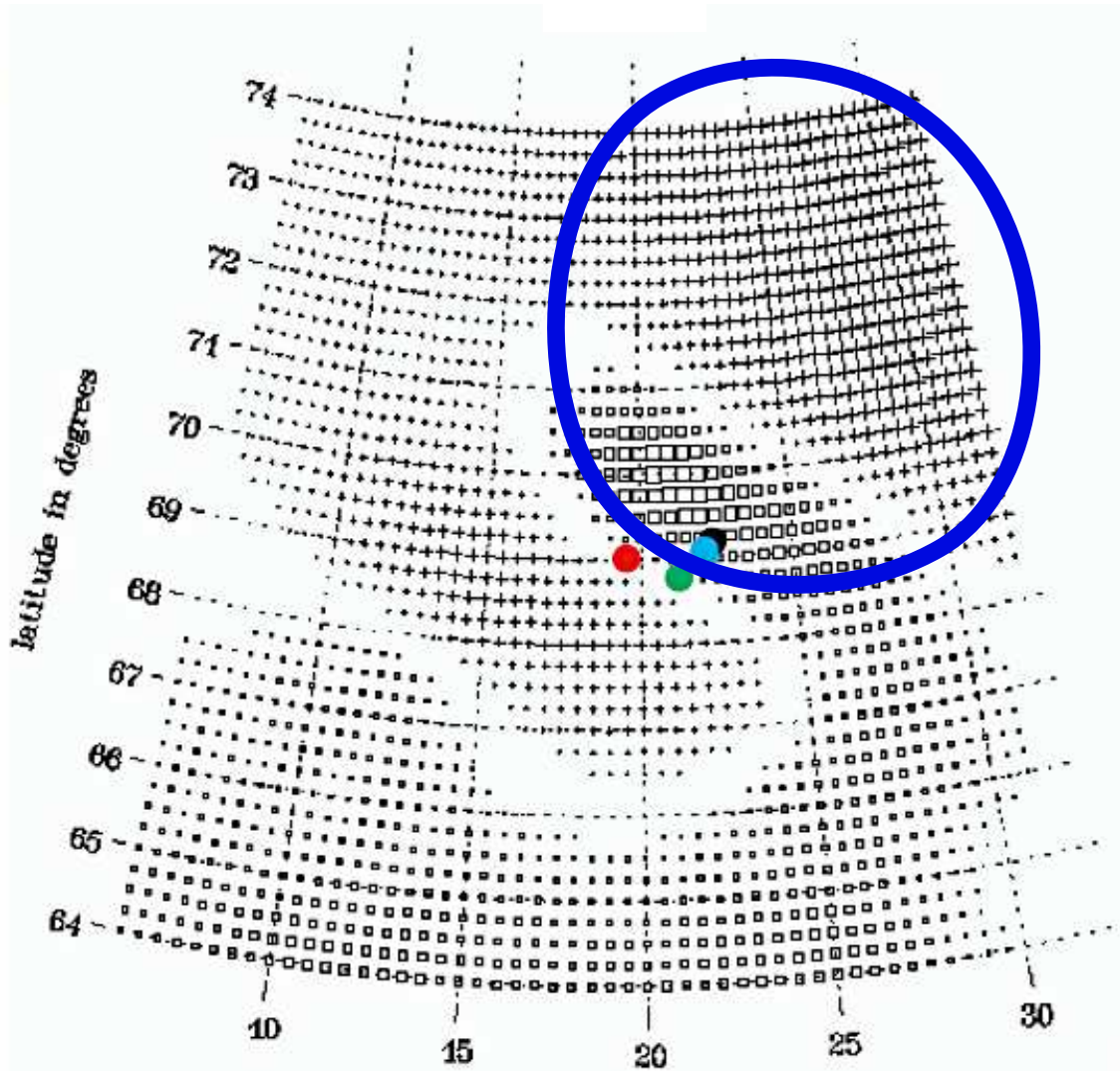
Figure 2.9: The ionospheric current system associated with a BBF determined by data from the IMAGE magnetometer array and EISCAT radars. The BBF associated current system has been highlighted by the blue ring. The coloured dots indicate the footpoints of the Cluster spacecraft. Squares indicate upward field-aligned current and crosses indicate downward field-aligned currents. Figure taken from Nakamura *et al.* (2005a).

current system. Using data from the Cluster spacecraft to reconstruct the Grad-Shafranov MHD equilibrium equation (Hau and Sonnerup, 1999; Hasegawa *et al.*, 2005), Snekvik *et al.* (2007) determined the field-aligned current system along the dawnward edge of a BBF. They found that the current system was approximately 0.3 R_E thick and that the currents determined by the Grad-Shafranov reconstruction were a good match for the results of the curlometer technique, although their assertion that $|div\mathbf{B}|/|curl\mathbf{B}| < 1$ indicates valid curlometer results was quite relaxed (see Chapter 4).

Studies of the current systems associated with BBFs have been based during times of differing geomagnetic activity. Amm *et al.* (1999) reported that their event occurred during a particularly disturbed period and shortly after a substorm expansion phase onset. Nakamura *et al.* (2005a) reported that their event occurred 1 hr before a major substorm expansion phase, during a period of steady southward IMF, indicating that the event was

during the growth phase of a substorm. Similarly, Grocott *et al.* (2004) reported on the currents associated with an event observed during a period of almost steady southward IMF, although unlike Amm *et al.* (1999) and Nakamura *et al.* (2005a), Grocott and co-authors determined the ionospheric field-aligned current associated with their BBF using the method of McWilliams *et al.* (2001) to determine the curl of the ionospheric electric field as detected by the SuperDARN radars. These authors found ionospheric currents ranging from 0.2 A km^{-2} (Grocott *et al.*, 2004) to 25 A km^{-2} (Amm *et al.*, 1999).

Estimations of the total current associated with BBFs have been made and are re-markably similar. In terms of true total current determination, these suffer from the un-certainty in the area of the BBF (more correctly, the area perpendicular to the magnetic field) and a lack of knowledge of the current variation over that area, although they can provide useful estimates for comparison with other current features in the magnetosphere-ionosphere system. Grocott *et al.* (2004) and Snekvik *et al.* (2007) estimated the total field-aligned current associated with a BBF to be 0.1 MA from the two different methods discussed above. From their model, Birn *et al.* (2004) found the total currents in the BBFs they tested were between 0.01 and 0.1 MA. Despite the similarity between these results, one should be cautious about assigning a given current to be driven by BBFs. Both Grocott *et al.* (2004) and Birn *et al.* (2004) studied quiet time events (Birn *et al.* (2004) artificially depleted their flux tubes within a model of the plasma sheet that was otherwise quiet). Snekvik *et al.* (2007) made no mention of the prevailing magnetospheric conditions, although an examination of the AU and AL indices suggests that their event was detected during a substorm expansion phase.

2.3   The wavy current sheet

The magnetotail current sheet is the separatrix of the two regions of approximately anti-parallel magnetic flux which make up the magnetotail and has been extensively studied since spacecraft technology allowed for in-situ measurements to be made. These in-situ measurements have shown that the current sheet often has a flapping or wavy motion (e.g. Speiser and Ness, 1967; Sergeev *et al.*, 2006) which is not only an interesting dynamical feature, warranting its own investigation (e.g. Zhang *et al.*, 2002), but also facilitates the further investigation of the current sheet structure (e.g. Sergeev *et al.*, 2003).

Early studies of the current sheet motion were restricted to single spacecraft observa-tions and as such, the motion of current sheet waves could not be determined unambigu-ously. Speiser and Ness (1967) reported that during several orbits, the IMP 1 spacecraft crossed the current sheet several times (indicated by a reversal of the magnetic field in the Sun-Earth direction). They dismissed the hypothesis that the spacecraft crossed multiple current sheets based on that fact that single crossings were also observed for some orbits, instead suggesting that the current sheet moved back and forth over the spacecraft. This
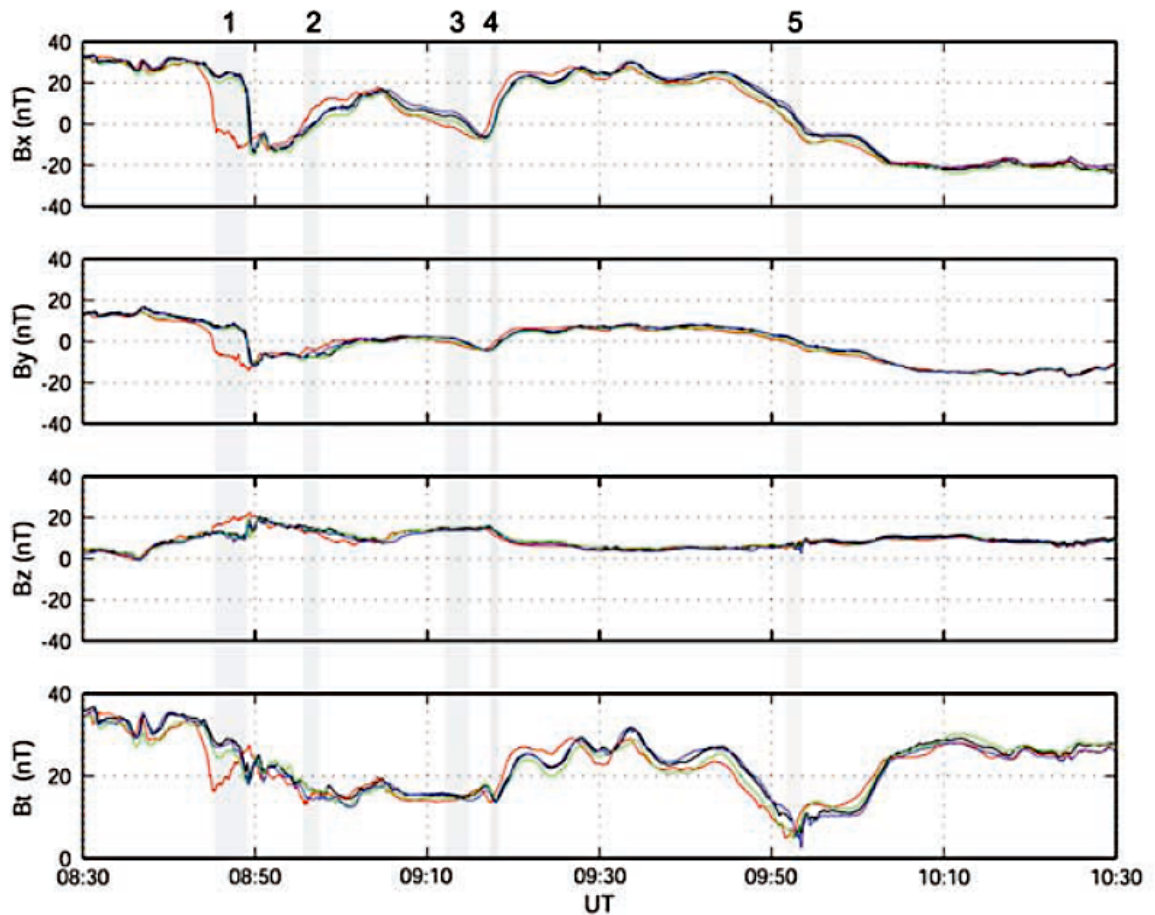
Figure 2.10: Cluster FGM data indicating the wavey current sheet taken from Zhang *et al.* (2002). Five current sheet crossings are labelled. Data is shown from Cluster 1 (black), 2 (red), 3 (green) and 4 (blue).

motion, they noted, would be superimposed on the motion of the current sheet due to the dipole tilt. It is interesting to note that recent studies (e.g. Runov *et al.*, 2003; Sergeev *et al.*, 2003) have used intervals of wavy current sheet activity to probe the current sheet and report on the occurrence of a bifurcated current sheet, which Speiser and Ness (1967) dismissed.

Nakagawa and Nishida (1989) furthered the idea of Speiser and Ness (1967) using data from IMP 6. Nakagawa and Nishida suggested that, with a significant B_Y component through the current sheet, a wave propagating through the current sheet would cause the B_Y and B_Z components to vary, such that a spacecraft might encounter a southward pointing magnetic field at various times. Using this model, they determined that current sheet waves observed by IMP 6 had a significant velocity in the dusk-dawn direction.

The limitations of single spacecraft studies meant that the unambiguous motion of the current sheet waves could not be determined. Observations made by the multi-spacecraft Cluster mission have since removed this ambiguity. Zhang *et al.* (2002) provided the first observations of the wavy current sheet using Cluster (see their Fig. 1, reproduced in

Fig. 2.10). Their case study showed that, in the presence of a current sheet wave, the current sheet was highly tilted in the YZ direction, in keeping with the results of Nakagawa and Nishida (1989), and that the wave propagated out of the central tail towards dawn. Furthermore, they showed that the wave propagation was relatively slow ($\sim 20\ \mathrm{km\,s^{-1}}$) and that the wavelength was long ($\sim 4\ R_E$). Statistical studies (Runov *et al.*, 2005; Sergeev *et al.*, 2006) have shown that during periods in which the Cluster spacecraft crossed the current sheet several times, the current sheet tended to be highly tilted in the YZ plane and exhibited transient features in the dusk/dawn direction away from the centre of the tail. Runov *et al.* (2005) used multi-spacecraft analysis techniques to show that the motion of the current sheet was not up-down, but rather a corrugation of the current sheet, as suggested by Nakagawa and Nishida (1989). Using Cluster data to investigate the validity of the minimum variance analysis technique for the determination of the normal to the current sheet (and hence the tilt of the current sheet), Sergeev *et al.* (2006) used Geotail data to confirm the results of Runov *et al.* (2005) using a larger dataset. Sergeev *et al.* (2006) also showed that the occurrence rate of current sheet flapping with radial and cross tail location was comparable to the occurrence rate of BBFs and that superposed epoch analysis of the AE index at the time of current sheet flapping suggested that current sheet flapping was likely during substorm expansion phases. This lead them to suggest that BBFs and substorms might be a source of current sheet waves. This was in agreement with previous studies (e.g. Bauer *et al.*, 1995; Sergeev *et al.*, 1998). Zhang *et al.* (2005) used a conjunction of the Cluster and Double Star satellites to expand upon earlier studies that used Geotail or Cluster and show that the wavy current sheet could be detected across $5\ R_E$ of the tail. Zhang and co-authors suggested that the whole of the near-Earth current sheet might be driven to oscillate outside the magnetotail hinge region.

Various models have been proposed to describe the motion of the current sheet under current sheet waves and explain its large scale motion. Early MHD models that tended to treat the current sheet as a Harris current sheet (Harris, 1962) over-estimated the wave velocity and models suggesting that an ion drift mechanism failed to account for the motion of waves in both the duskward and dawnward directions (see Sergeev *et al.*, 2004b). Recently, two competing models have been developed which both consider a scenario in which the plasma is contained on curved magnetic field-lines, as opposed to the 1D Harris sheet approximation in which there are two anti-parallel field-line regions.

Golovchanskaya and Maltsev (2005) related the problem to a similar problem in describing the motion of substorm absorption bays in riometer data that moved in east/west directions. Using the dispersion relation for the ballooning instability for small perturbations, Golovchanskaya and Maltsev (2005) determined the group velocity of the flapping waves in the Y direction by assuming that the wave was a standing wave in the X direction. However, as noted by Golovchanskaya and Maltsev, and subsequently by other authors (Erkaev *et al.*, 2008), the method used to derive their dispersion relation implies
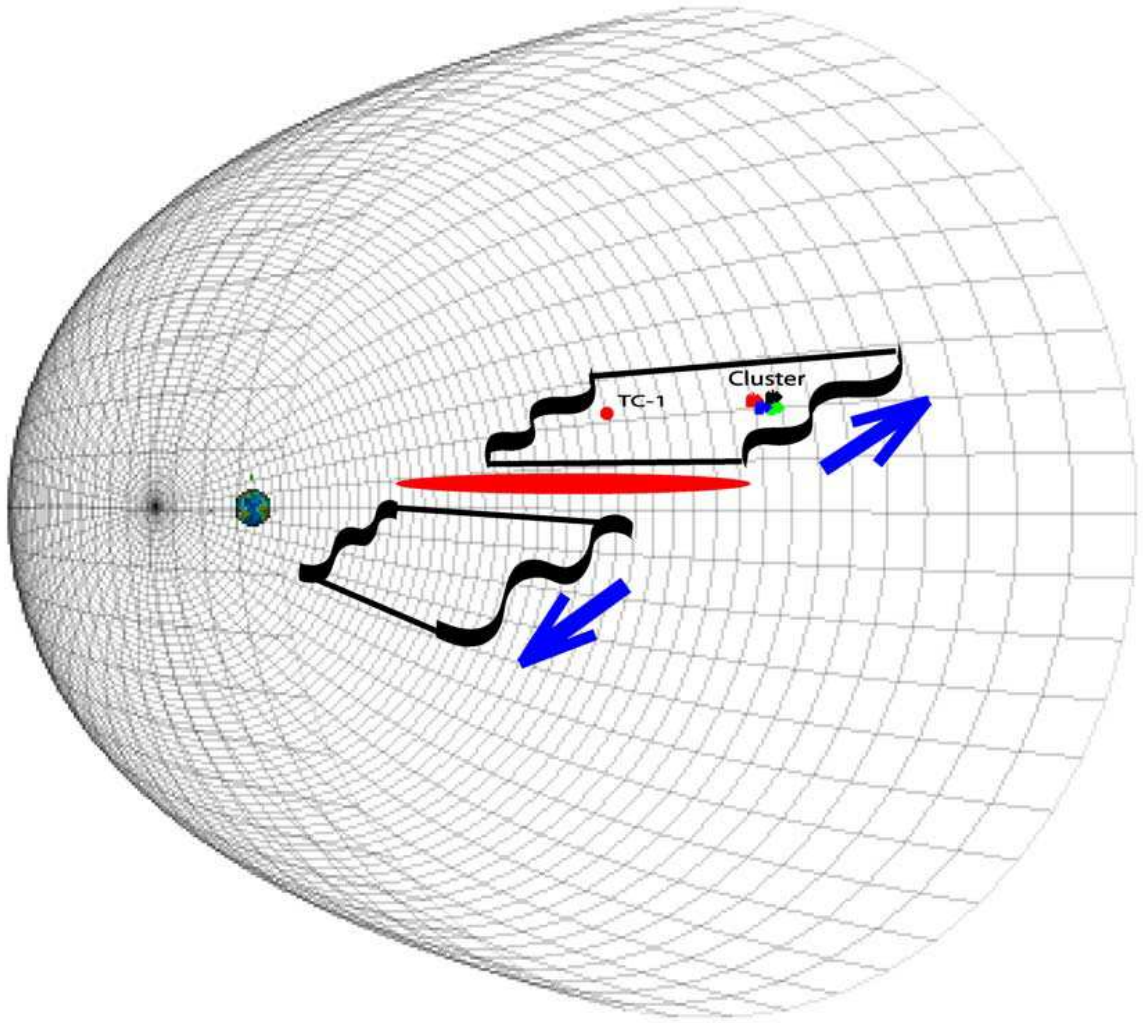
Figure 2.11: Schematic of the wavy current sheet. Figure taken from Zhang *et al.* (2005).

small scale perturbations with respect to the background variations, which clearly is not the case for waves with amplitudes of ~ 1 R_E or greater in the current sheet. Also, the results of Golovchanskaya and Maltsev (2005) imply that both kink and sausage mode perturbations (Fig. 2.12) are equally possible. However, the majority of observations of the current sheet report kink link oscillations, identified as multiple crossings of the current sheet.

Erkaev *et al.* (2008) linearised the equations of incompressible, ideal MHD under the assumption that there was no background velocity, that the magnetic field varied as $\mathbf{B} = (B_X(Z), 0, B_Z(X))$ and that perturbations in the velocity, pressure and magnetic field varied proportional to $\exp(i\omega t - iky)$. These equations were then solved in a piecewise manner, similar to Golovchanskaya and Maltsev (2005) for a non-varying region of magnetic field coupled with a region in which the B_X component varies with Z. Their results give, with reasonable values for the current sheet thickness and scale length of the variations of the magnetic field, group speeds and frequencies comparable with the observed values. Furthermore, their results show that the sausage mode of oscillation can
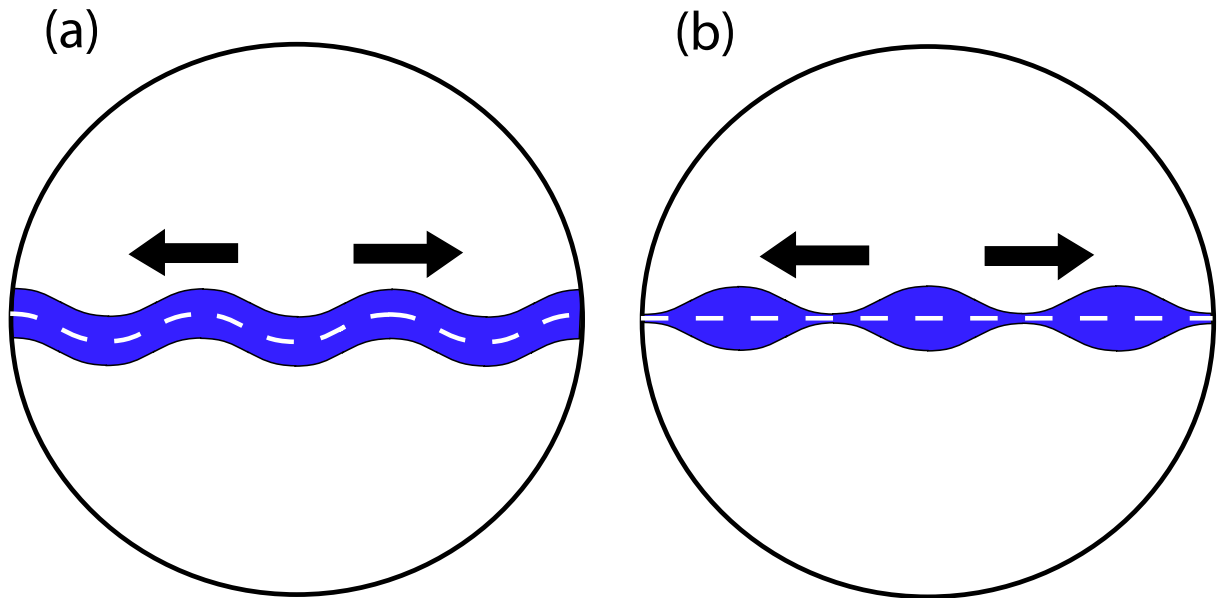
Figure 2.12: Schematic of (a) the kink and (b) the sausage modes of current sheet waves looking towards the Earth from down the tail. The blue areas indicate the current sheet and the dashed white lines indicate the separatrix ($B_X = 0$ crossing).

occur, but the growth rate of the kink mode was far greater.

2.4   Outstanding issues

Although there have been many studies of BBFs and their effects on the dynamics of the magnetosphere, there are still a number of questions that remain. In order to truly investigate the importance of BBFs to the substorm cycle and large scale magnetospheric dynamics, it is necessary to consider the relationship between BBFs and substorm phase. Although Angelopoulos *et al.* (1994) showed that the occurrence rate of BBFs increases with AE, individual values of AE are not an indicator of substorm phase. A more pertinent relationship maybe BBF occurrence rate to substorm phase. Equally, the limited number of studies of the ionospheric currents associated with BBFs during different levels of geomagnetic activity show that the currents can vary by two orders of magnitude (Amm *et al.*, 1999; Nakamura *et al.*, 2005a; Grocott *et al.*, 2004), suggesting that there is some relationship between the BBF currents and substorm phase.

In order to determine how BBFs might affect large scale dynamical features, such as the wavy current sheet, it is useful to determine a usable model of these large scale phenomena and how features associated with these large scale dynamics related to other transient features within the magnetosphere.

In this thesis I investigate BBFs, and more specifically their current systems, and the wavy current sheet. In Chapter 5 I present a case study of a BBF observed during a

substorm expansion phase. In this case study I investigate the magnetospheric current system associated with the BBF using the Cluster spacecraft and relate this current to ionospheric features, including an auroral streamer. This allows for a comparison with the previous studies mentioned above and provides proof of concept for using the curlometer to accurately determine the currents associated with BBFs. Expanding upon this study, I provide a statistical analysis of BBFs detected by the Cluster spacecraft between 2001 and 2004 in Chapter 6, considering the current systems with respect to position and substorm phase. This statistical survey also provides an insight into the importance of BBFs during the various substorm phases based on their occurrence rates. Finally, in Chapter 7 I provide a case study of the wavy current sheet, providing strong evidence of a link between the propagation mechanism of current sheet waves and the dipolarization of the magnetotail following two substorms. Using data from the Cluster and Polar spacecraft, I compare the models of Golovchanskaya and Maltsev (2005) and Erkaev *et al.* (2008) and show that the model of Erkaev *et al.* (2008) gives a more physically reasonable fit to the data.

Chapter 3

Instrumentation

Had our instruments permitted it, we might have seen the gathering trouble
"The War of the Worlds", Wells (1898)

In this chapter I provide an overview of the various instruments that have contributed data presented in this thesis and their deployment as either ground stations or on board spacecraft. For an overview of the basic operation of some of these instruments, see Appendix B

3.1   Cluster II

The European Space Agency's Cluster II mission [1] consists of four identically equipped spacecraft. It was designed to facilitate multi-point analysis of small scale plasma structures in various regions of the near-Earth space environment such as the magnetotail.

The Cluster mission was launched in the summer of 2000 and declared operational in February of 2001. Cluster orbits the Earth in a polar orbit with an apogee of 19 R_E and a perigee of 4 R_E and an orbital period of 57 hour (Escoubet *et al.*, 2001). Figure 3.1a shows complete Cluster orbits starting at 00:00 UT on the 1st March, 1st June, 1st September, 1st December 2001 in the XY GSM plane. The orbits of the spacecraft are manipulated such that the spacecraft are in a tetrahedral formation when they pass through a specified region of interest. These orbits are fixed in inertial space, hence the plane of the orbit rotates in the XY GSM plane. This results in four 'seasons' per year in which the spacecraft apogee is either on the dayside near the magnetopause and bow shock, in the magnetotail, or close to one of the flanks of the magnetosphere. The tail

---

[1]Cluster II is commonly referred to as Cluster following the destruction of the original Cluster I satellites in 1996
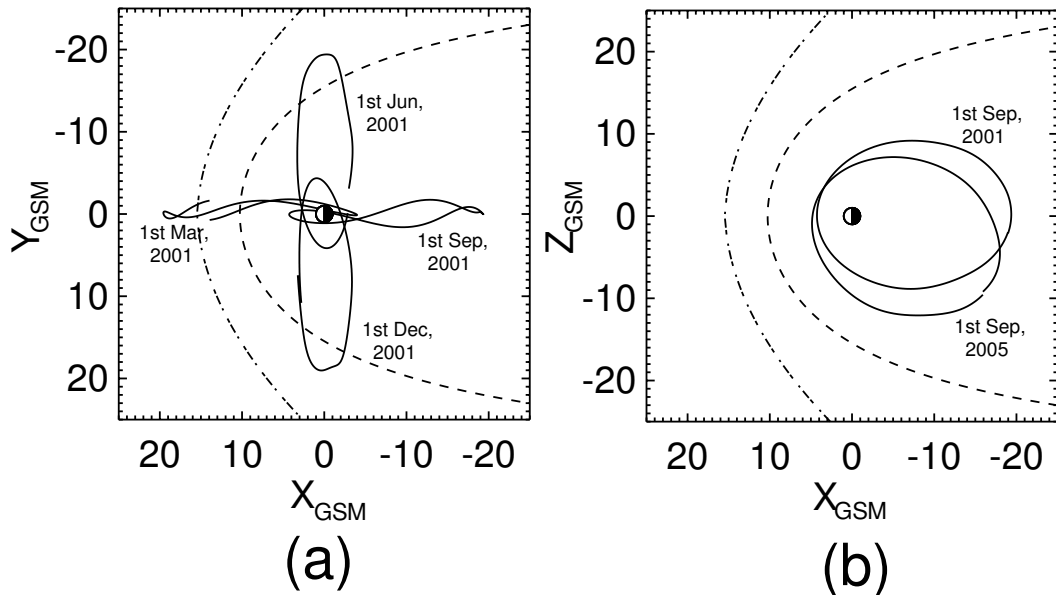
Figure 3.1: Complete Cluster orbits starting at 00:00 UT (a) 1st March, 1st June, 1st September, 1st December 2001 in the XY GSM plane and (b) 1st September 2001 and 2005 in the XZ plane. The dashed lines represents the magnetopause and the dot-dashed lines represents the bow shock determined from the T96 magnetic field model with no IMF component inputs, solar wind dynamic pressure of 2 nPa, solar wind proton density of 2 cm^{-3} and solar wind velocity of 400 km s^{-1}.

season nominally lasts from three months centred on 1st September (day 244, or 245 for a leap year).

As with any polar orbiting satellite, the orbit of the Cluster spacecraft has precessed over time so that the semi-major axis of the orbit is inclined to the GSM XY plane. As such, the distance downtail that the Cluster spacecraft sample the plasma sheet (taken as a first approximation to be centred on $Z_{GSM}=0$) has decreased since launch. This is demonstrated in Fig. 3.1b, which shows complete Cluster orbits starting at 00:00 UT on the 1st September 2001 and 2005 in the XZ GSM plane.

Throughout this thesis, data are extensively employed from the Fluxgate Magnetometer (FGM; Balogh *et al.* (2001))and the Cluster Ion Spectrometer (CIS; Rème *et al.* (2001)). Data are also presented from Plasma Electron And Current Experiment (PEACE; Johnstone *et al.* (1997)). PEACE data are presented with the spacecraft potential from the Electric Fields and Waves instrument (EFW; Gustafsson *et al.* (2001)) to facilitate the isolation of plasma populations created around the spacecraft due to spacecraft charging, often referred to as photo-electrons.

3.1.1 Cluster Fluxgate Magnetometer

The Cluster FGM (Balogh *et al.*, 2001; Brown *et al.*, 2008) consist of two tri-axial fluxgate magnetometers and a data processing unit. The magnetometers are mounted on a 5.2 m radial boom; one at the end of the boom (outboard or OB sensor) and one 1.5 m from the

end of the boom (inboard or IB sensor). This configuration aids in removing the magnetic background from the spacecraft. The default configuration designates the outboard sensor as the primary sensor, although this can be changed by ground commands. Data from both sensors are acquired simultaneously, although data from the secondary sensor is acquired at a lower frequency. This data is telemetered to the ground and distributed to other instruments on-board the spacecraft.

In normal operating modes, the FGMs sample the magnetic field vector at 201.793 Hz. This data stream is then filtered and telemetered to the ground. The number of vectors telemetered to the ground is dependant on the spacecraft operating mode, although the most commonly used modes transmit vectors at 22 and 67 Hz. This is then commonly averaged to 5 Hz and spin ($\sim$4 s) resolution. An additional data collection mode was created to improve data coverage from periods during which there was no telemetry acquisition, known as FGM Extended Mode (FGMEXT). During these periods, spin averaged magnetic field data from the primary sensor is stored in memory that is usually allocated to storing short periods of high resolution data. In this thesis I employ full resolution, 5 Hz and FGMEXT data for analysis. The data are then filtered as appropriate for the required analysis.

3.1.2   Cluster Ion Spectrometer

The Cluster Ion Spectrometer (Rème *et al.*, 2001) consists of two detectors; the Hot Ion Analyser (HIA) and the Composition and Distribution Function (CODIF) sensor. HIA is a quadrispherical "top hat" detector as described in Section B.2, whereas CODIF is a rotationally symmetric toroidal electrostatic analyser, although the properties of both are similar. Both detectors are mounted on the side of the spacecraft such that they acquire a full 3D particle distribution once per spacecraft spin.

Due to the large range of ion fluxes the Cluster spacecraft encounter, both the HIA and CODIF detectors are divided into two 180° sections with slightly varying geometries. This allows one side of the detector to give meaningful results in the various plasma populations encountered. The small or low geometry sides are predominantly used for detecting the solar wind and will not be discussed further here. The high geometry side of the HIA detector consists of 16 anodes covering 11.25° each, whereas the high geometry side of the CODIF detector consists of 8 anodes covering 22.5°. Both detectors apply a high voltage to the inner plate in order to select particles with a given energy per charge. For HIA, the observable energy range is 5 eV e^{-1}-32 keV e^{-1}. For CODIF, the observable energy range is 0-38 keV e^{-1}. This energy range is covered once per 62.5 ms and once per 125 ms for HIA and CODIF respectively, giving a 2D particle distribution in that time. 3D particle distributions are acquired once per spin.

The CODIF sensor includes a time of flight (TOF) analyser after the electrostatic

analyser. By applying a known voltage along the particles trajectory for a given energy-charge ratio (as selected by the electrostatic analyser), the mass-charge ratio of the incident particles can be computed based on the time they take to traverse a fixed distance. As such, the CODIF sensor can differentiate between particle species detected.

Although 2D and 3D particle distributions allow for detailed examination of the plasma environment, the bulk properties of the plasma are sometimes required. Further information on the plasma properties are obtained by reducing the data to moments of the particle distribution. Data from the CIS instruments allows for the density, velocity vector, heat flux tensor and momentum flux tensor to be calculated once per spin. Although the spacecraft calculate these moments on-board, these often have to be recalculated to take into account changes in calibration.

3.1.3 Plasma Electron And Current Experiment

The Plasma Electron and Current Experiment (Johnstone *et al.*, 1997; Fear, 2006) consists of two detectors; the High Energy Electron Analyser (HEEA) and the Low Energy Electron Analyser (LEEA). Both detectors are "top hat" detectors, similar to the CIS HIA sensor, although unlike CIS the PEACE sensors are mounted "side-on" to the spacecraft, with one detector on either side. Also similar to the CIS instrument, the major difference between the two detectors is a lower geometric factor on LEEA, for the same reasons as discussed above.

Both PEACE sensors have an energy range of 0.59 eV to 26.4 keV and a polar angular resolution of 15°. As the spacecraft spins, the detectors sample through varying azimuths. As such, the azimuthal angular resolution depends on the number of energy ranges sampled and the time taken to perform a full sweep through the energy range. The two detectors have independent energy ranges, such that two energy ranges can be covered simultaneously.

3.2 Imager for Magnetopause-to-Aurora Global Exploration (IMAGE)

NASA's Imager for Magnetopause-to-Aurora Global Exploration (IMAGE; Gibson *et al.*, 2000; Burch, 2000) mission was designed to provide global images of magnetospheric plasma in order to determine the magnetospheric response to variations in the solar wind. IMAGE was launched on 25th March 2000, and the mission was terminated on 18th December 2005, ending after communication with the spacecraft was lost. The spacecraft was injected into a polar orbit at an inclination of 40° to the ecliptic, with an apogee
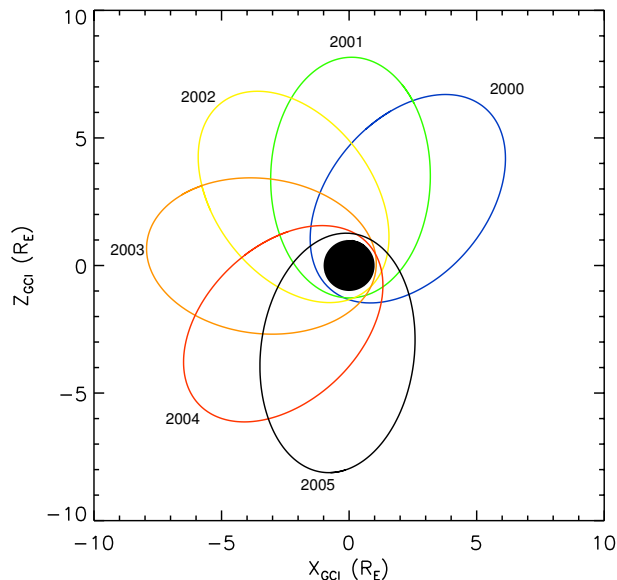
Figure 3.2: Complete IMAGE orbits starting at 00:00 UT on 1 June 2000 to 2005 in XZ GCI coordinates. Separate orbits are colour coded and labelled.

of $7R_E$ and perigee of 1000 km. The orbit precessed such that after 1 year apogee was above the north pole and by 2004, the spacecraft was predominantly imaging the southern auroral oval. Figure 3.2 shows complete orbits of the IMAGE observatory on 1 June in the years 2000 to 2005. The spacecraft spun with a nominal period of 2 minutes. The spin axis of the spacecraft was aligned perpendicular to the orbital plane such that each instrument pointed Earthwards once per spin.

3.2.1 Far UltraViolet Wideband Imaging Camera (FUV-WIC)

Previous missions showed that imaging the aurora in far-ultraviolet significantly reduces contamination of the image by scattered sunlight from the ground and clouds and allows the aurora to be distinguished from day-glow in the auroral region. The Wideband Imaging Camera (Mende *et al.*, 2000b,a, FUV-WIC) was designed to image the aurora over a broad band to enable high spatial and temporal resolution as opposed to the Spectrographic Imager (Mende *et al.*, 2000c, FUV-SI) which was designed to observe specific proton and electron excited aurora.

FUV-WIC consists of a Cassegrain Burch type mirror (Burch, 1947) which focuses the incident photons onto a photo-cathode. The emitted photo-electrons are accelerated and multiplied through a microchannel plate (MCP) onto a phosphor. Photons emitted by the phosphor are then channelled along fibre optics to the charge-couple detector (CCD). Various baffles and windows are employed to reduce the scattered light and restrict the wavelength of the incident light to the FUV band.

FUV-WIC had a 17° × 17° processed field of view, comparable to the angular size of

the Earth at apogee (16°) made up of 256×256 pixels, giving a pixel size of 92×92 km at apogee and 1.2×1.2 km at perigee. In order to maximise the data obtained whilst the aurora were in the field of view of FUV-WIC, the data obtained by the instrument were processed on-board the spacecraft using Time Delay Integration (TDI). This technique reduces the blurring caused by the rotation of the spacecraft by summing the data from pixels with given look angles in successive images in a memory area of pixels with fixed look angles for a given spin, whilst maximising the amount of data acquired whilst the Earth was within the field of view of the instrument.

3.3 Geostationary Operational Environmental Satellite

The National Oceanic and Atmospherics Administration's (NOAA) Geostationary Operational Environmental Satellites (GOES) are primarily designed as weather monitors, although they also carry a Space Environment Monitor suite of instruments. As the name implies, these satellites are deployed in geostationary orbit, such that they are always located over the same point on the Earth's surface. Nominally, there are two operational satellites at any time. For details of the GOES spacecraft, see the "GOES I-M Databook" (1997). The GOES spacecraft are equipped with two FGMs as part of the Space Environment Monitor (SEM). These provide three component magnetic field vectors at 1.95 Hz, with a resolution of ± 0.03 nT. This data is then averaged down to 1 min resolution.

3.4 Polar

The National Aeronautics and Space Administration's NASA Polar satellite was launched in 1996 in order to investigate the high and low altitude plasmas in the near-Earth space environment. Initially, Polar's apogee was above the north pole, but as with any polar orbiting satellite, the apogee has precessed round such that in 2007, the apogee moved above the south pole. For further details on the Polar spacecraft, see Acuña *et al.* (1995). The Magnetic Field Experiment (MFE; Russell *et al.*, 1995) on board the Polar spacecraft provides three component magnetic field vectors.

3.5 Advanced Composition Explorer

The Advanced Composition Explorer (ACE; Stone *et al.*, 1998) is primarily designed to measure the relative compositions of the energetic particles in the interplanetary medium.

Launched in 1997, ACE orbits the L1 point, the point at which the gravitational forces of the Sun and Earth are balanced and which orbits the Sun once per year, approximately 240 R_E from Earth. The spacecraft is fitted with two instruments of interest to this study; the Magnetic Fields Experiment (MAG; Smith *et al.*, 1998) and the Solar Wind Electron Proton Alpha Monitor (SWEPAM; McComas *et al.*, 1998). These provide real-time solar wind data, which can be lagged, using various techniques (e.g. Khan and Cowley, 1999; Volwerk *et al.*, 2004), to the magnetosphere to give an indication of the local solar wind conditions.

3.6   Ground Magnetometers

Global magnetometer chains, such as those described below, can be used to monitor current systems in the ionosphere and magnetosphere through variations in the magnetic field detected at the Earth's surface. As the magnitude of the Earth's magnetic field is large compared to the variations in the field caused by magnetotail activity, it is usual to remove a "quiet" level from the magnetometer data such that the data presented is the deviation of the magnetic field from the "quiet" level. The "quiet" level is usually taken as a mean over a period of more than 24 hour during which magnetic activity is low. In all cases presented in this thesis, the magnetometer data has also had the daily mean removed. For stations which have previously had a "quiet" level removed, this should be a relatively small change. However for those stations that have not had a "quiet" level removed, this will bring the values of the magnetic field presented into line with those of the "quiet" level removed stations.

3.6.1   CANOPUS and CARISMA Magnetometer Chains

The Canadian Array for Realtime Investigations of Magnetic Activity (CARISMA) is an extension of the Canadian Auroral Network for the OPEN Program Unified Study (CANOPUS) magnetometer chain in Canada. CARISMA consists of 13 fluxgate magnetometers deployed throughout Canada, seven of which lie approximately along the 332° magnetic meridian (the "Churchill Line") and five of which lie approximately at 65° MLAT across 4 hrs of MLT (with the station at Gillam common to both). The station locations are given in Table A.1 and shown in Fig. 5.2.

Data from the CANOPUS magnetometers had a temporal resolution of 5 s, whereas the upgraded CARISMA magnetometers have a temporal resolution of 1 s. For further details of the CANOPUS and CARISMA arrays, see `http://www.cgsm.ca/documents.html`.
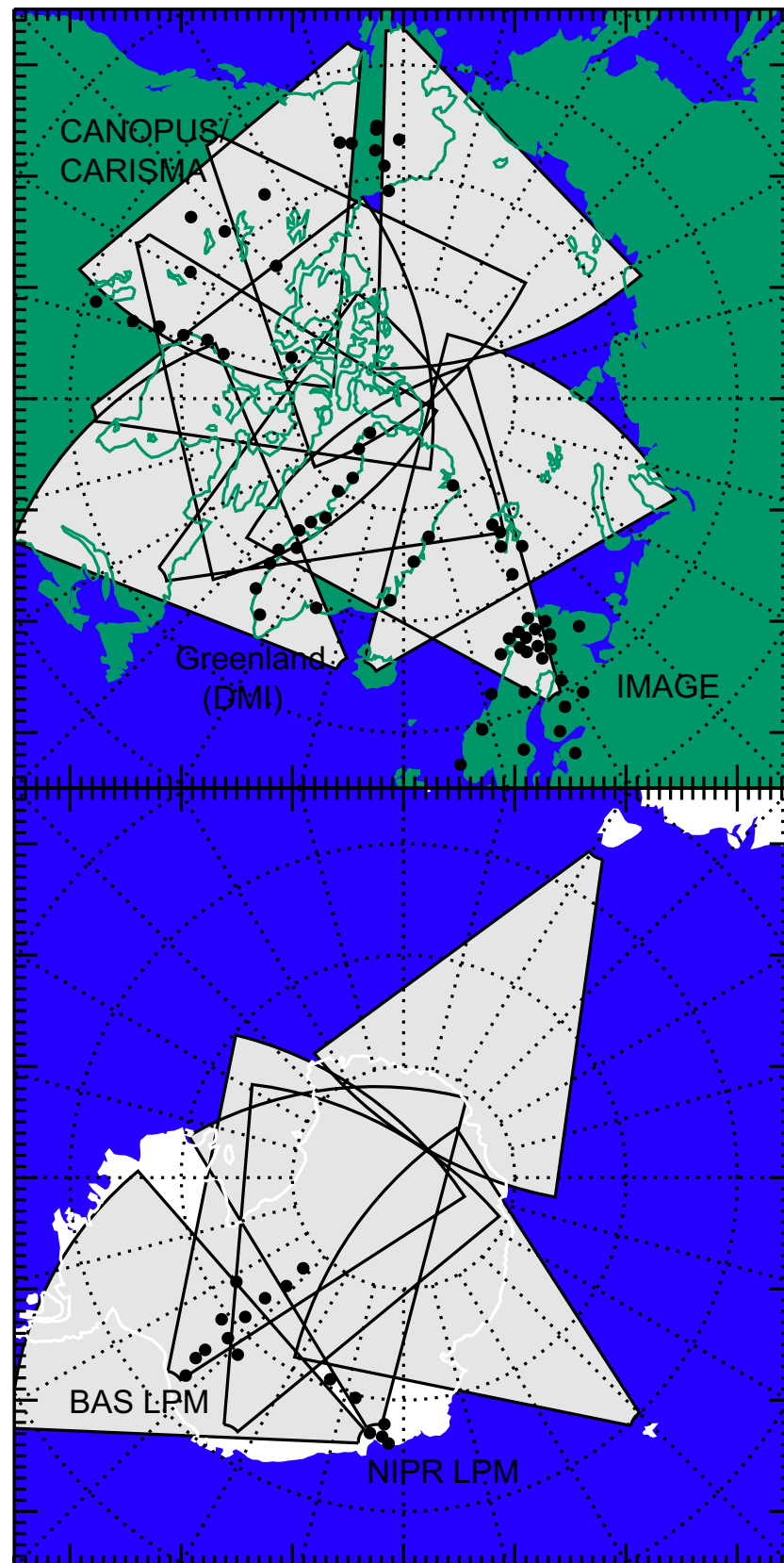
Figure 3.3: Maps of the northern and southern hemisphere polar regions in magnetic coordinates (AACGM) showing the location of the magnetometer stations of the CARISMA, Greenland, IMAGE, BAS LPM and NIPR LPM magnetometer chains as calculated of 00:00 UT on 1st January 2005. Shown in grey are the fields of view of the SuperDARN radars.

3.6.2   Greenland Magnetometer Chain

The Greenland magnetometer chain, operated by the Danish Meteorological Institute, is comprised of 17 magnetometer stations; 5 on the east coast of Greenland and 12 on the west coast of Greenland, stretching across 20° magnetic latitude and 74° magnetic longitude. The station locations are given in Table A.3 and A.2 and shown in fig. 3.3. Each station consists of a three-axis linear core fluxgate magnetometer. The magnetometer axes are orientated to magnetic north (H), magnetic east (D) and vertically down (Z). From 1991 until 2002, field was sampled with a 20 s period. From 2002 onwards, the field was sampled at 1 and 20 s periods. The magnetic field is sampled at 0.1 nT resolution, although the final resolution of the data is 0.25 nT for 20 s data and 0.125 nT for 1 s data. The "quiet" or reference levels are set shortly after the end of the calendar year. For more details, see `http://dmiweb.dmi.dk/fsweb/projects/chain/`.

3.6.3   Antarctic Low Power Magnetometer Chains

The British Antarctic Survey (BAS) and Japanese National Institute of Polar Research (NIPR) have built and deployed low power magnetometers (LPMs) in Antarctica that are able to maintain over 405 days of unattended operations under extreme conditions. Each LPM consists of a three-axis fluxgate magnetometer. On deployment, the Z-axis is orientated to point upwards and the X- and Y- axes are pointed in arbitrary directions. The H (northwards) direction is found during data processing, defined as the mean direction of the magnetic field perpendicular to Z on the quietest day of the year. The quietest day is defined as the 24 hour with the smallest change in the field vector. The magnetic field is nominally sampled for 150 ms every 60 s. The data resolution 1 nT.

The locations of the LPMs used in this thesis are given in Table A.4 and Table A.5 and shown in Fig. 3.3. For further information on LPM deployment, the interested reader is directed to the NIPR and BAS websites (`http://www.nipr.ac.jp/~uap-mon/NIPR_LPM.html`, `http://www.antarctica.ac.uk/bas_research/instruments/lpm.php`)

3.6.4   International Monitor for Auroral Geomagnetic Effects

The International Monitor for Auroral Geomagnetic Effects (IMAGE) is a chain of 30 magnetometers in Scandinavia and northern Europe operated by a number of institutes, having expanded from the 7 stations in the EISCAT magnetometer cross, which it succeeded. These stations measure the magnetic field in geographic XYZ coordinates (North, West, vertically down) with a resolution of 1 nT and a temporal resolution of 10 s.

The IMAGE magnetometer stations used in this thesis are listed in Table A.6. The

locations of all the stations in the IMAGE magnetometer array are shown in Fig. 3.3. For further information, the interested reader is directed to the IMAGE website (`http: //www.ava.fmi.fi/image/`).

3.7 The Super Dual Auroral Radar Network, Super-DARN

Coherent scatter radars, such as those in the Super Dual Auroral Radar Network (Super-DARN) facilitate the observation of large areas of the ionosphere. These radars transmit high frequency pulses (8 to 20 MHz, Lester *et al.* (2004)) into the ionosphere. These pulses are Bragg scattered by density irregularities in the ionospheric plasma which have a **k** vector that is twice that of the radar emission. By determining the Doppler shift of the returned pulse, the line-of-sight velocity of ionospheric field-lines can be determined, along with further parameters (spectral width, backscatter power). SuperDARN is a chain of these radars whose fields of view overlook the auroral magnetosphere in the northern and southern hemispheres. The fields of view are shown in Fig. 5.2.

The SuperDARN radars generally consist of 16 dipole antennae that make up a log-periodic array (length and separation increase logarithmically). Each antenna transmits and receives the radar pulses and the backscattered signal. By phasing the signal from the antennae relative to another, the transmitted signal forms a beam that can be pointed in one of 16 directions within the field of view of the radar, with each beam covering 3.2°İn their normal operating mode, the SuperDARN radars transmit a pulse sequence of seven 300 ms pulses. From the start of the transmission, the radars transmit and receive on the same beam for 7 s, moving through the 16 beams in sequence in 2 min.The normal pulse sequence results in a 45 km resolution between 180 and over 3000 km along the beam. The measured velocities and spectral widths have a resolution of 10 m s^{-1} between $\pm 3000 \text{ m s}^{-1}$.

A major development in the use of coherent scatter radar data was the Map Potential Model (Ruohoniemi and Baker, 1998). This technique combines the data from all the radars in a single hemisphere and determines the ionospheric electric field pattern and associate ionospheric field-line motion. The model uses the average flow patterns of Ruohoniemi and Greenwald (1996) to constrain the flows. This then gives a global view of the footpoints of the magnetic field-lines involved in the Dungey cycle and other magnetospheric processes.

Chapter 4

Analysis techniques

In God we trust, all others bring data
W. Edwards Denning

The following describes some of the analysis techniques used within this thesis. All are documented in the literature. I describe those analysis techniques that are unique to multi-spacecraft missions in which the spacecraft orbit in a 3-dimensional formation, such as Cluster, in particular the curlometer and four-spacecraft timing analysis. Furthermore, I investigate the results of the curlometer technique from different current systems moving across a tetrahedron of spacecraft. I also include a description of minimum variance analysis, which is based on single-point measurements. These and other multi-spacecraft analysis techniques are covered at length in Paschmann and Daly (1998,2000) and references therein.

4.1   Four-Spacecraft Timing

Variations in the magnetic field and particle signatures observed in the magnetosphere can be the result of either temporal variations, spatial structures or some combination of the two. A spacecraft taking single point measurements is unable to differentiate between spatial and temporal variations, although, in principle, multiple spacecraft can. By comparing magnetic field or particle signatures (normally magnetic field signatures due to the higher temporal resolution of magnetic field data) across four spacecraft that have a non-coplanar distribution, the orientation of a structure that doesn't vary temporally can be determined.

For the purposes of this technique, it is assumed that a magnetic field structure has a distinct discontinuity between the structure and the ambient magnetic field, and that this discontinuity can be approximated as a plane on the scale of the spacecraft separation.

As such, the plane has a unit normal $\hat{\mathbf{n}}$ and this plane moves along the direction of the normal with a velocity V. The time taken for the discontinuity to pass from one reference spacecraft to the remaining spacecraft is then the projection of $\hat{\mathbf{n}}$ onto the separation of the spacecraft divided by the velocity of the structure

$$(\mathbf{r_s} - \mathbf{r_{ref}}).\frac{\hat{\mathbf{n}}}{V} = t_s - t_{ref} \tag{4.1}$$

where $\mathbf{r_s} - \mathbf{r_{ref}}$ is the relative separation of spacecraft s from an arbitrary reference spacecraft and $t_s - t_{ref}$ is the relative timing of signature between the two spacecraft (Harvey, 1998).

Using four spacecraft gives three timing separations and three vector projections. From these, a 3×3 matrix, $\mathbf{R}$, and 1×3 array, $\mathbf{T}$ are constructed such that

$$\mathbf{R} = (\mathbf{r_1} - \mathbf{r_3}, \mathbf{r_2} - \mathbf{r_3}, \mathbf{r_4} - \mathbf{r_3}) \tag{4.2}$$

$$\mathbf{r_a} - \mathbf{r_b} = \begin{pmatrix} r_{ax} - r_{bx} \\ r_{ay} - r_{by} \\ r_{az} - r_{bz} \end{pmatrix} \tag{4.3}$$

$$\mathbf{T} = \begin{pmatrix} t_1 - t_3 \\ t_2 - t_3 \\ t_4 - t_3 \end{pmatrix} \tag{4.4}$$

Combining these in the form of Eq. 4.1, it can be seen that

$$\frac{\hat{\mathbf{n}}}{V} = \mathbf{R}^{-1}\mathbf{T} \tag{4.5}$$

where R^{-1} is the inverse matrix of R, and hence the normal to the plane of the discontinuity can be determined, along with the velocity of the discontinuity in the direction of the normal.

It can be seen that the values of $\hat{\mathbf{n}}$ and V determined are reliant on the accuracy in the determination of the spacecraft position and the timing of the discontinuity signature across the four spacecraft. In practice, the uncertainty in a spacecraft's position can be well defined. However, the accuracy in the determination of the timing of the signature may be less well defined. For the purposes of this thesis, the following method to determine the timing of a signature across the four spacecraft was used:

1) The signature to be tested was identified in the data from each spacecraft,

3) The data were smoothed to remove any small period variations

2) Data from the reference spacecraft (Cluster 3, in this case) were cross correlated with data from the remaining spacecraft to give a first estimate of the lag between the reference spacecraft and each of the other spacecraft,

3) Data from the reference spacecraft were plotted against data from the other spacecraft with the lags removed, such that the data traces should be aligned,

4) The lags were adjusted by eye until the traces were aligned.

For further details on this analysis technique, see Russell *et al.* (1983); Harvey (1998); Schwartz (1998).

4.2   Minimum Variance Analysis

As described above, spatial magnetic structures are separated from the surrounding ambient magnetic field by a discontinuity. From Gauss's Law, it can be shown that, in the ideal situation, the magnetic field component across the discontinuity is constant. Take, for example, a 1-D layer in which the magnetic field varies solely with position in the z direction ($\mathbf{B} = (B_x(z), B_y(z), B_z(z))$). In this case, Gauss's Law for magnetic fields ("no monopoles" law) gives

$$\nabla.\mathbf{B} = 0 \tag{4.6}$$

$$\frac{\partial B_x(z)}{\partial x} + \frac{\partial B_y(z)}{\partial y} + \frac{\partial B_z(z)}{\partial z} = 0 \tag{4.7}$$

$$\Rightarrow \frac{\partial B_z(z)}{\partial z} = 0 \tag{4.8}$$

As such, the magnetic field component in the z direction does not change. In practice, observations of the magnetic field do not lend themselves to this simple picture. In order to determine the non-varying direction, observations of the magnetic field need to be made on either side of the discontinuity. Observations made by a single spacecraft must be temporally separated, therefore any temporal variation in the structure may result in the magnetic field appearing to vary across the discontinuity. The direction normal to the discontinuity is thus estimated as the direction of minimum variance in the magnetic field.

From Sonnerup and Scheible (1998), the variance of the magnetic field along a direction $\hat{\mathbf{n}}$ is given by

$$\sigma^2 = \frac{1}{M} \sum_{a=1}^{M} \left| \left(\mathbf{B}^{(a)} - \langle \mathbf{B} \rangle \right) . \hat{\mathbf{n}} \right|^2 \tag{4.9}$$

The condition that $|\hat{\mathbf{n}}|^2 = 1$ can then be used to constrain the minimisation of this function

using a Lagrange multiplier, such that

$$\nabla \sigma^2 = \lambda \nabla \left(|\hat{\mathbf{n}}|^2 - 1 \right) \tag{4.10}$$

$$\frac{\partial}{\partial n_x} \left(\sigma^2 - \lambda \left(|\hat{\mathbf{n}}|^2 - 1 \right) \right)$$

$$\frac{\partial}{\partial n_y} \left(\sigma^2 - \lambda \left(|\hat{\mathbf{n}}|^2 - 1 \right) \right) \tag{4.11}$$

$$\frac{\partial}{\partial n_z} \left(\sigma^2 - \lambda \left(|\hat{\mathbf{n}}|^2 - 1 \right) \right)$$

where the differential is done along the components of the vector $\hat{\mathbf{n}}$ for simplicity. These equations can be written in matrix form as

$$\sum_{b=1}^{3} M_{ab} n_b = \lambda n_a$$

$$M_{ab} = \langle B_a B_b \rangle - \langle B_a \rangle \langle B_b \rangle \tag{4.12}$$

where M_{ab} is the covariance matrix of $\mathbf{B}$ and b=1,2,3 represent the three Cartesian coordinates. As such, λ represents a set of eigenvalues of the covariance matrix and the corresponding eigenvectors give the directions of maximum, intermediate and minimum variance. The variance in the direction of the eigenvectors is given by the corresponding eigenvalue. In order to determine the quality of the minimum variance analysis, the variances along the minimum and intermediate directions are compared. Throughout this thesis I will consider a ratio of $\lambda_2/\lambda_3 > 10$ to be a good result (Eastwood *et al.*, 2005). It is worth considering that, unlike the four spacecraft timing analysis described in Section 4.1, minimum variance analysis does not determine the motion of the structure. Also, since the minimum variance direction is an eigenvector of the covariance matrix, the vector in the opposite direction (rotated by 180°) is equally applicable.

For further details on this analysis technique, see Sonnerup and Cahill (1967); Sonnerup and Scheible (1998).

4.3   Current Density Analysis or the Curlometer

During the tail season, the Cluster spacecraft are manoeuvred into orbits such that the spacecraft form the vertices of a tetrahedron. Under the assumption that the magnetic field varies linearly between the spacecraft, the current density through the faces of the tetrahedron can be estimated. Combining the current density through three of the faces provides an estimate of the vector current density within the spacecraft tetrahedron.
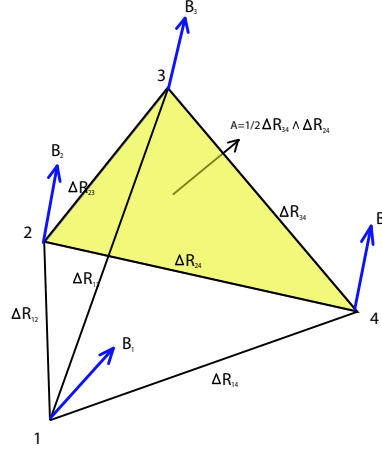
Figure 4.1: Schematic of the curlometer

Ampere's Law states that

$$\mu_0 \left(\mathbf{J} + \epsilon_0 \frac{\partial \mathbf{E}}{\partial t} \right) = \nabla \times \mathbf{B} \tag{4.13}$$

which, in the low frequency approximation, where $\mathbf{E}$ is approximately temporally constant, becomes

$$\mu_0 \mathbf{J} = \nabla \times \mathbf{B} \tag{4.14}$$

hence, given the spatial variation of the magnetic field, one can calculate the associated current density. Alternatively, using Stokes' theorem, this can be described as

$$\mu_0 \int_A \mathbf{J}.d\mathbf{A} = \int_S \mathbf{B}.d\mathbf{S} \tag{4.15}$$

where $\mathbf{S}$ is the closed path around the area $\mathbf{A}$. Assuming that the field varies linearly between any three points, the current density through the triangle enclosed by the points can be calculated. Taking the position of the points to be $\mathbf{R}_{a,b,c}$, the magnetic field at those locations to be $\mathbf{B}_{a,b,c}$ (see Fig. 4.1) then the area through which the current is flowing is

$$\mathbf{A} = \frac{1}{2}(\triangle \mathbf{R}_{ab} \times \triangle \mathbf{R}_{ac}) \tag{4.16}$$

Also, the right hand side of Eq. 4.15 becomes

$$\int_S \mathbf{B}.d\mathbf{S} \equiv (\mathbf{R}_b - \mathbf{R}_a).\frac{\mathbf{B}_a + \mathbf{B}_b}{2} + (\mathbf{R}_c - \mathbf{R}_b).\frac{\mathbf{B}_b + \mathbf{B}_c}{2} + (\mathbf{R}_a - \mathbf{R}_c).\frac{\mathbf{B}_c + \mathbf{B}_a}{2} \tag{4.17}$$

Taking one of the points as a reference point such that $\mathbf{R_{b,c}} - \mathbf{R_a} = \triangle\mathbf{R_{b,c}}$ and $\mathbf{B}_{b,c} = \mathbf{B}_a + \triangle\mathbf{B}_{b,c}$, Eq. 4.17 becomes

$$\mu_0 \mathbf{J}.(\triangle\mathbf{R}_b \times \triangle\mathbf{R}_c) = \triangle\mathbf{R}_c.\triangle\mathbf{B}_b - \triangle\mathbf{R}_b.\triangle\mathbf{B}_c \tag{4.18}$$

If a=1 then b,c=2,3,4 then by cycling through b and c, three independent components of

J can be determined in the directions of the normals to the three faces of the tetrahedron with spacecraft 1 at a vertex. These three simultaneous equations can then be solved for the three components of **J**

Given the assumptions used to determine the current density, any values determined by this technique may only be considered as an estimate to the true current density. Assuming a linear variation in the field between the spacecraft is the simplest approach without prior knowledge of the field variations. Throughout this thesis I determine the divergence of the magnetic field through the tetrahedron using a similar technique to the above. Any measured magnetic field divergence is a departure from Gauss's Law ($\nabla.B = 0$) due to a combination of the assumption made in applying this technique and the uncertainties in the data. By comparing the magnitudes of the curl and divergence of the magnetic fields I can infer the quality of the curlometer technique. A small ratio is taken to indicate that the current is reliable, although this is discussed in more detail later.

Gauss's Theorem tells us that

$$\int_V \nabla.\mathbf{B} dV = \int_S \mathbf{B}.d\mathbf{S} \tag{4.19}$$

such that the divergence of the magnetic field **B** is the sum of the fluxes into (or out of) the volume V through the surface S. This can be shown to be equivalent to

$$\nabla.\mathbf{B} \triangle R_a.(R_b \times R_c) = \sum \triangle \mathbf{B}_a.(\triangle R_b \times \triangle R_c) \tag{4.20}$$

under the conditions for a tetrahedron as given above. Hence, for any estimate of curl of the magnetic field, the divergence of the field can be estimated under the assumption that the field varies linearly between spacecraft.

For further details on this analysis technique, see Dunlop *et al.* (1988); Robert *et al.* (1998).

In this thesis, the results of the curlometer are calculated using 3×3 matrices of the spacecraft positions and magnetic field data relative to some reference spacecraft to determine the curl of the field. If

$$\triangle \mathbf{B} = \begin{pmatrix} \triangle \mathbf{B}_2 \\ \triangle \mathbf{B}_3 \\ \triangle \mathbf{B}_4 \end{pmatrix}, \triangle \mathbf{R} = \begin{pmatrix} \triangle \mathbf{R}_2 \\ \triangle \mathbf{R}_3 \\ \triangle \mathbf{R}_4 \end{pmatrix}, \tag{4.21}$$

where $\triangle \mathbf{B}_a = \mathbf{B}_a - \mathbf{B}_1$ then the gradient of the field along the separation vectors is given by

$$\nabla \mathbf{B} = \triangle \mathbf{R}^{-1} \triangle \mathbf{B} \tag{4.22}$$

The curl of the field is then given by

$$\nabla \times \mathbf{B}_a = \nabla \mathbf{B}_{cb} - \nabla \mathbf{B}_{bc} \tag{4.23}$$

where $a \neq b, c$ and b,c=1,2,3 where b and c are cyclic. Similarly, the divergence of the field is given by

$$\nabla . \mathbf{B} = \sum_{a=1}^{3} \nabla \mathbf{B}_{aa} \tag{4.24}$$

The uncertainty in the curl estimate, based on the uncertainty in the positions of the spacecraft and the measurement uncertainty in the magnetic field data, is given by

$$\left(\frac{\delta \nabla \times \mathbf{B}}{\nabla \times \mathbf{B}} \right)^2 = 6 \left(\frac{\delta \mathbf{B}^2}{\mathbf{B}} + \left(4\sqrt{2} + 1 \right) \frac{\delta \mathbf{R}}{\mathbf{R}^2} \right) \tag{4.25}$$

where δ represents the quantity's uncertainty. Using $\delta \mathbf{R}$ =2 km and $\mathbf{R}$=100 or 1000 km along with $\delta \mathbf{B}$ =0.1 nT and $\mathbf{B}$=5 nT gives an uncertainty in the curl of between 13 and 5%.

4.4   Modelling the curlometer

The curlometer approximates the variation of the magnetic field between two points in a tetrahedron to be linear. For a line current extending infinitely in the Z direction (which will be referred to as an infinite line current), the magnetic field components in the X and Y directions vary as

$$\mathbf{B}_x \propto \frac{1}{X^2 + Y^2} \sin \left(\frac{x}{y} \right) \tag{4.26}$$

$$\mathbf{B}_y \propto \frac{-1}{X^2 + Y^2} \cos \left(\frac{x}{y} \right) \tag{4.27}$$

Given that the variation in this is a fairly simple current system is non-linear, it is unlikely that more complex current systems show a linear variation. However, without a priori knowledge of the current systems being detected, the variation of the magnetic field cannot be predicted. As such, a linear variation is taken as it is the simplest and easiest to compute.

Throughout this thesis, I make extensive use of results from the curlometer. Given that this is an approximation technique, it is appropriate to investigate the limits of this approximation. In order to do this, I test the results of the curlometer against a current system with an explicitly known magnetic field variation (an infinite line current) and for a more complex current system (line currents with a 2D Gaussian distribution), for which the magnetic field has to be calculated numerically from the Biot-Savart law. Robert *et al.* (1998) previously investigated the effect of the tetrahedron quality on the results of

the curlometer. In this study, I investigate the effect of the currents themselves. As such, I shall use a perfect tetrahedron throughout.

4.4.1 Model set-up
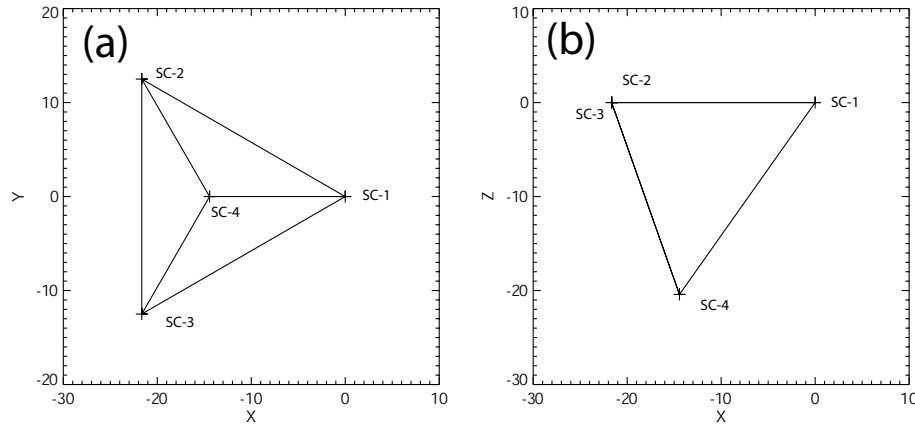
Figure 4.2: Diagram showing the positions of the spacecraft used in the curlometer modelling in (a) the XY plane and (b) the XZ plane.

The spacecraft (SC) positions (the points where the magnetic field is calculated) were defined to be a perfect tetrahedron. SC-1 was placed at the origin, SC-2 in the -X, +Y quadrant, SC-3 in the -X, -Y quadrant and SC-4 below the XY plane. Figure 4.2 shows the spacecraft positions in the XY and XZ planes. The spacecraft separation was set to 25 in arbitrary units.

4.4.2 Line currents

The simplest current system to model is an infinite line current, as the magnetic field can be explicitly calculated from Biot-Savart's law. However, such a current system is a physical impossibility. As such, the infinite line current is used to demonstrate that the position of the current relative to the spacecraft causes variations in the results from the curlometer. It should be noted that, since the current is infinitely thin, the real current density within the tetrahedron is not dependant on the current's location within the tetrahedron and the real current density is zero when the current is outside the tetrahedron.

For a line current $\mathbf{J}$ in the Z direction, Biot-Savart's law, which determines the magnetic field associated with a given current system, is solved explicitly to give

$$B_\phi = \frac{\mu_0 J}{2\pi r} \tag{4.28}$$

$$B_R = 0 \tag{4.29}$$

$$B_Z = 0 \tag{4.30}$$

where $R = X^2 + Y^2$ and $\phi = \tan^{-1}(Y/X)$.

Figure 4.3 shows the results from the curlometer for an infinite line current in the Z direction. The input current density is calculated to be the input current divided by the magnitude of the vector sum of the areas of the three tetrahedron faces with SC-1 at a vertex. This was equal to the area of one tetrahedron face. This enables the ratio of the current density from the curlometer to the "true" current density (j_{curl}/j) to be calculated. The coloured contour plots show the various parameters returned by the curlometer technique when the current is passing through that point.

The first point of note is that the patterns in panels (a)-(c) are rotationally symmetric, as one would expect for the model set-up. Apart from when the current location is close to one of the spacecraft, the determined current density for currents passing through the tetrahedron is between 40 and 80% of the true value (panels (a) and (d)). The divergence of the magnetic field detected by the curlometer ($div\mathbf{B}$) is generally low inside the tetrahedron, increasing outside the tetrahedron near the tetrahedron vertices (panel (b)). Unlike the current, however, the divergence is low when the current passes through the location of one of the spacecraft. $|div\mathbf{B}|/|curl\mathbf{B}|$ is low inside the tetrahedron, dominated by the low divergence, and increases outside the tetrahedron. Well inside the tetrahedron, $|div\mathbf{B}|/|curl\mathbf{B}|$ is very low, only increasing along the edges of the tetrahedron. Panel (e) shows that $|div\mathbf{B}|/|curl\mathbf{B}|$ is generally less than 0.1 inside the tetrahedron.

It is interesting to note that the curlometer is able to detect currents external to the tetrahedron. Close to the limits of the tetrahedron these approach the lower levels of the currents detected within the tetrahedron ($\sim$40% of the true current density), but this very rapidly drops of with distance.

In the above, the line current was perpendicular to one of the faces of the tetrahedron at all times. However, in reality, currents can have any orientation with respect to the tetrahedron. Figure 4.4 shows the ratio of the current from the curlometer to the true current density for various angles of rotation about the X, Y and Z axes for various offsets in the Z, Z and Y directions respectively. The line current was at -7.5 in the X direction and the initial spacecraft positions were as described above.

For the majority of orientations of the current for which the current is still within the tetrahedron, the curlometer returns a current that is between 40 and 60% of the true current density. This is similar to the 40 to 80% shown in Fig. 4.4. The maxima at 0, 180 and 360° in panels (a) and (b) are due to the vicinity of the current to the spacecraft that is initially out of the XY plane (SC-4). As the Z offset approaches the initial value of the spacecraft's Z-location, the current is outside the tetrahedron for most of the rotation angles, hence the detected currents are low. Notice that for rotation about the Z-axis, the only variation comes from varying the position at which the current passes through the tetrahedron.
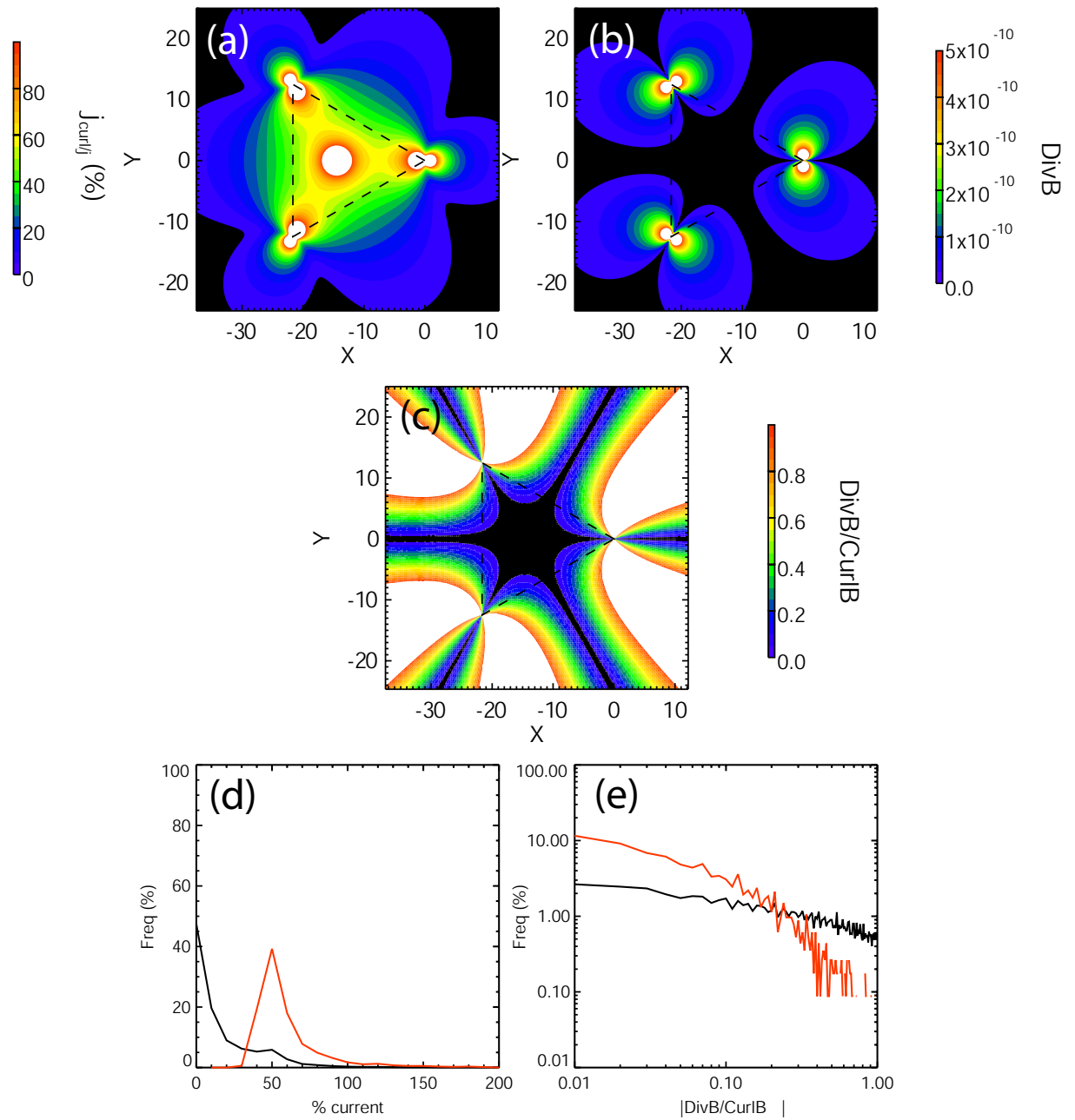
Figure 4.3: Results from the curlometer for an infinite line current in the Z direction at varying XY coordinates. Panels (a)-(c) show, respectively, the percentage of the true current density detected, the divergence of the magnetic field detected and $|div\mathbf{B}|/|curl\mathbf{B}|$ with respect to the X and Y coordinates of the line current. Panels (d) and (e) show, respectively, histograms of the percentage of true current density detected and $|div\mathbf{B}|/|curl\mathbf{B}|$ for the whole area (black line) and for the tetrahedron (red line).
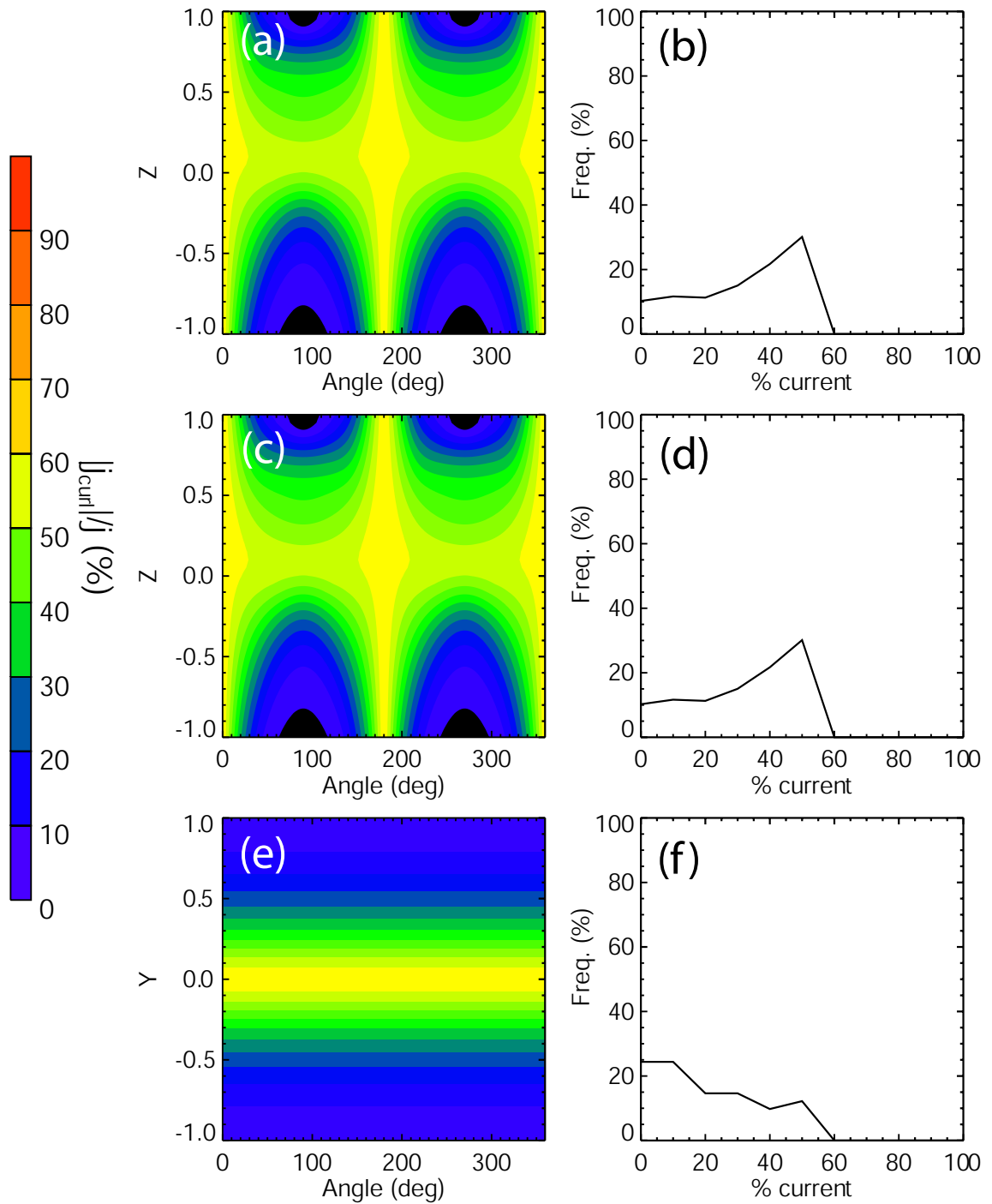
Figure 4.4: Percentage of the true current density detected by the curlometer for rotations of the spacecraft tetrahedron about (a) the X axis for various displacements of the tetrahedron in the Z direction, (c) the Y axis for various displacements of the tetrahedron in the Z direction, and (e) the Z axis for various displacements in the Y direction. Panels (b), (d) and (f) show histograms of j_{curl}/j for panels (a), (c) and (e) respectively.

The infinite line current is the limiting case of a current system in which the gradients in the magnetic field are maximised. As noted above, the variation in the field is clearly non-linear. However, real current systems are spatially extended. As such, the variations in the field may approach the linear approximation. In the following, spatially extended current systems are examined using the curlometer.

4.4.3   2D Gaussian current distributions

Given that the motion of any charged particles around a magnetic field-line is helical, currents in the magnetosphere will be distributed over a volume of space. If the space-craft tetrahedron is sufficiently widely spaced, it would be expected that some localised current systems may be approximated as line currents, but it is more likely that a current distribution will have a significant volume compared to the tetrahedron. For example, the 1D Harris current sheet (Harris, 1962) has been shown to have a half-thickness of 27,000 km (McComas *et al.*, 1986), whereas the Cluster separation has been maximised at $\sim$10,000 R_E. As such, I now expand on the above by considering a current distribution with infinite extent in the Z-direction, but with a 2D Gaussian distribution in the XY plane (distribution with a Gaussian function in the X and Y directions).

For a 2D Gaussian distribution of current in the XY plane centred on [X,Y], the magnetic field at $\mathbf{r}' = [x', y', z]$ given by the Biot-Savart law gives

$$B(\mathbf{r}')_X = -\frac{j_0\mu_0}{2\pi\sigma_X\sigma_Y}\int_{-\infty}^{\infty}\int_{-\infty}^{\infty}\frac{e^{-(x^2+y^2)/2}(y'-y)}{(x'-x)^2+(y'-y)^2}dxdy \qquad (4.31)$$

$$B(\mathbf{r}')_Y = \frac{j_0\mu_0}{2\pi\sigma_X\sigma_Y}\int_{-\infty}^{\infty}\int_{-\infty}^{\infty}\frac{e^{-(x^2+y^2)/2}(x'-x)}{(x'-x)^2+(y'-y)^2}dxdy \qquad (4.32)$$

where σ is the width of the Gaussian and j_0 is a constant. These equations cannot be solved explicitly. In order to determine the magnetic fields, the solutions to these equations were estimated by summing the current distribution over 3σ in the positive and negative X and Y directions.

Figure 4.5 shows the results from the curlometer for a 2D Gaussian current distribution with σ of 5 (20% of the spacecraft separation) in both X and Y directions. As before, the coloured contour plots show the results of the various parameters returned by the curlometer technique, but now for when the centre of the current system (i.e. the location of the mean current) is at that point. The true current density is calculated for each point by summing the current elements that pass within the limits of the tetrahedron and dividing by the area as before.

Comparing j_{curl}/j between Fig. 4.4a and Fig. 4.5c, it is apparent that the variations in the currents determined when the centre is located within the tetrahedron are smoothed out for the 2D Gaussian current distribution. This is emphasised in Fig. 4.5g, where

Figure 4.5: The inputs to and outputs from the curlometer for a 2D Gaussian current distribution with a σ of 5 in the X and Y directions. Panel (a) shows the input current distribution, centred on SC-1. Panel (b) shows current density within the tetrahedron for various locations of the mean current. Panels(c)-(e) show the current density determined by the curlometer, $|div\mathbf{B}|/|curl\mathbf{B}|$, and j_{curl}/j for various locations of the mean current. Panel (f) shows histograms of j_{curl}/j for all locations (black) and points inside the tetrahedron (red). Panel (g) shows the true current density (black) and curlometer current density (red) along the X-axis and panel (h) j_{curl}/j along the X-axis. Panels (b) and (c) have been scaled to the maximum true current density. The colour scale for panels (d) and (e) is shown.

the current density determined by the curlometer (red trace) is almost constant within the limits of the tetrahedron. There are true current densities for points outside the tetrahedron (panel (b)), although this is expected for a distributed current system. It should be noted that calculating the true current density is subject to errors due to the summing of a square grid over a triangular area. As the limits of the tetrahedron converge, and the limits don't lie along the axes of the model cells, the true current density is under-valued. This is most apparent as the lack of rotational symmetry in panel (e). The under-valued true current density leads to the over-valued j_{curl}/j near SC-1 in panel (e) and the greater number of points in the 100-120% range of the red trace in panel (f). Panel (f) shows that the majority of points within the tetrahedron estimate the current to be 40-120% of the true current value and the distribution is fairly constant between 50 and 130%. Panel (g) suggests that the current detected by the curlometer plateaus when the centre of the current system is within the tetrahedron, whereas the true current density rises to a peak. $|div\mathbf{B}|/|curl\mathbf{B}|$ has a similar form to before, although the ratio is higher within the tetrahedron, but the results are still small (< 0.3).

Similar to Fig. 4.5, Fig. 4.6 shows the results from the curlometer for a current distribution with a σ of 30 (120% of the spacecraft separation). It is apparent that, compared to the smaller current system, the majority ($\sim$100%) of the current density is now being detected by the curlometer at all locations of the current centre (panels (e) and (f)). Panels (g) and (h) show that the curlometer is slightly over-estimating the currents by up to 10%. Panel (d) shows that $|div\mathbf{B}|/|curl\mathbf{B}|$ inside the tetrahedron is very low. This is in keeping with the almost 100% detection of the true current density.

Figure 4.7 shows the percentage of the true current detected by the curlometer at X=-10 on the X-axis for current distributions with varying σ. For low σ, when the current distribution is wholly contained within the tetrahedron, the curlometer tends to under estimate the current density, detecting about 60% of the true current density. As the current system size increase, the curlometer tends to detect more of the true current density. Once σ is greater than 15 (60% of the spacecraft separation), the curlometer tends to over-estimate the true current by approximately 10%. The sawtooth-like feature superimposed on the trace is due to the size of the integrating steps and does not affect the general trend.

Figure 4.8 shows the percentage of the maximum curlometer current for varying scale sizes of the tetrahedron against a fixed current system. In this model, I have fixed the current system to have a σ of 1, such that the scale size of the tetrahedron (the separation between spacecraft) is relative to the current system scale size. At scale sizes of less than half the current sheet σ, the current detected is maximised. As the scale size increases, the current detected decreases, reaching 90% when the tetrahedron covers one σ and dropping to 50% when the tetrahedron covers 3σ.
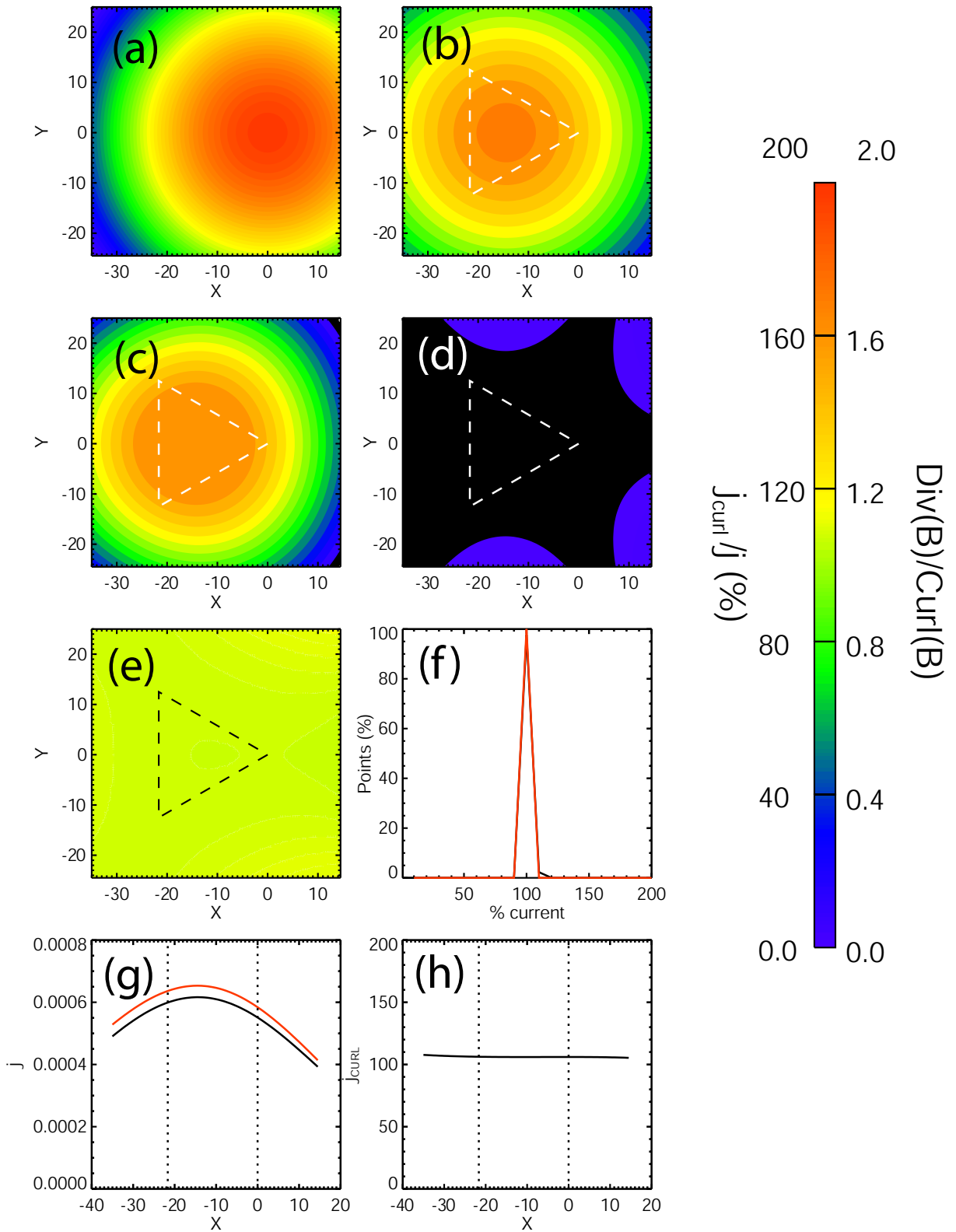
Figure 4.6: The inputs to and outputs from the curlometer for a 2D Gaussian current distribution with a σ of 30 in the X and Y directions. Panel (a) shows the input current distribution, centred on SC-1. Panel (b) shows current density within the tetrahedron for various locations of the mean current. Panels(c)-(e) show the current density determined by the curlometer, $|div\mathbf{B}|/|curl\mathbf{B}|$, and j_{curl}/j for various locations of the mean current. Panel (f) shows histograms of j_{curl}/j for all locations (black) and points inside the tetrahedron (red). Panel (g) shows the true current density (black) and curlometer current density (red) along the X-axis and panel (h) j_{curl}/j along the X-axis. Panels (b) and (c) have been scaled to the maximum true current density. The colour scale for panels (d) and (e) is shown.

Figure 4.7: Percentage of the true current detected by the curlometer for various 2D Gaussian current distributions centred at X=-10 with σ varying between 0.25 and 25.
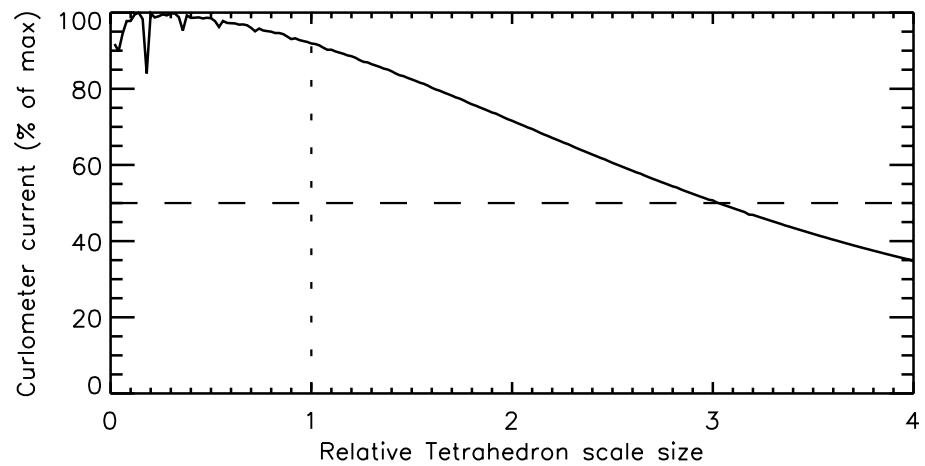
Figure 4.8: Percentage of the maximum curlometer current at X=0 against the relative scale size of the tetrahedron to the current system.

4.4.4 2D Gaussian current sheets

As regions of differently orientated magnetic flux are separated by current sheets, such as the magnetotail current sheet, it is useful to test the response of the curlometer to such distributions. Again, due to the helical nature of the particle motions in the magnetosphere, infinitely thin current sheets cannot exist and, as such the current sheet is taken to be an extension of the 2D Gaussian current distribution, described above, with σ in the Y direction that is larger than the spacecraft separation.

Figure 4.9 shows the results from the curlometer, in the same format as Fig. 4.5, for a current distribution with σ of 60 in the X direction and 5 in the Y direction. Panels (c), (e) and (f) show that, inside the majority of the tetrahedron, the curlometer underestimates the current by about 80%, with the under-estimation increasing as the current sheet approaches Y=0. $|div\mathbf{B}|/|curl\mathbf{B}|$ was high, especially compared to Figs. 4.5 and 4.6.

Figure 4.10 shows the ratio of current density from the curlometer to true current density against σ of the current system in the Y direction in the middle of the tetrahedron. The σ in the X direction was 50. Much like Fig. 4.7, when σ in the Y direction is smaller than the scale size of the tetrahedron, the current density is under estimated. For σ above 12, the current density tends to be over estimated by approximately 10%.

Figure 4.11 shows the results from the curlometer for 7.5° rotations of the tetrahedron about the Z-axis. Although, like the effect of rotating the tetrahedron about a line current, there is little variation in the currents between the different rotation angles, there is a noticeable change in the div-curl ratio for different angles. In particular, when the separation of two of the spacecraft becomes comparable to the scale size of the current system and these two spacecraft straddle the current system, $|div\mathbf{B}|/|curl\mathbf{B}|$ becomes relatively large ($\sim$1, see column (iv)). Yet, when two of the spacecraft are aligned in the X direction i.e. along the length of the current system, $|div\mathbf{B}|/|curl\mathbf{B}|$ becomes low, such as for circular 2D Gaussian current systems. As the tetrahedron approaches this orientation, the variation in the curlometer current density to true current density decreases, such that the percentage of points at the peak ratio is higher. Comparing the peak ratio for the tetrahedron orientated with two spacecraft in the plane of the current sheet with Fig. 4.10 shows that the current is closer to the true current density for a given σ.
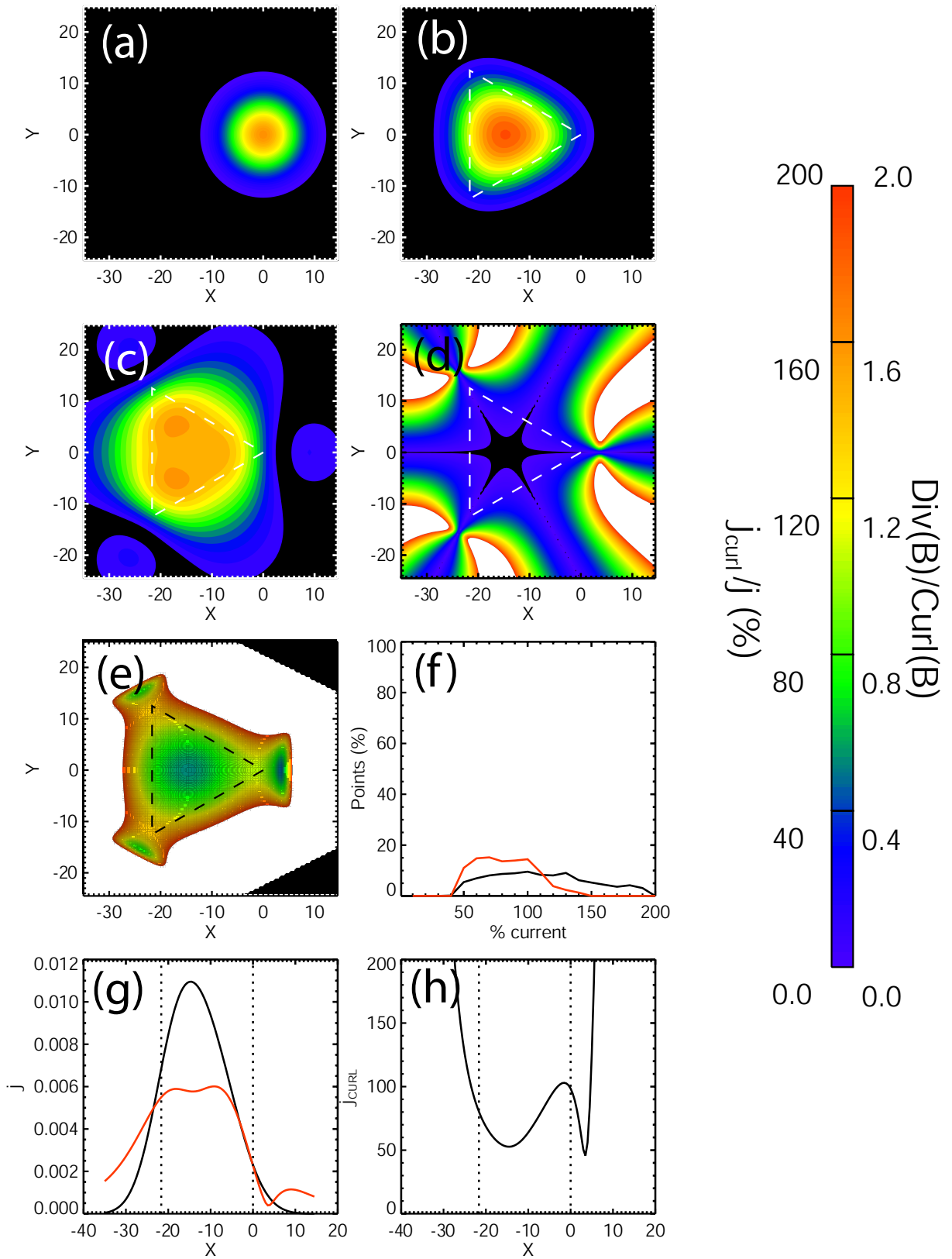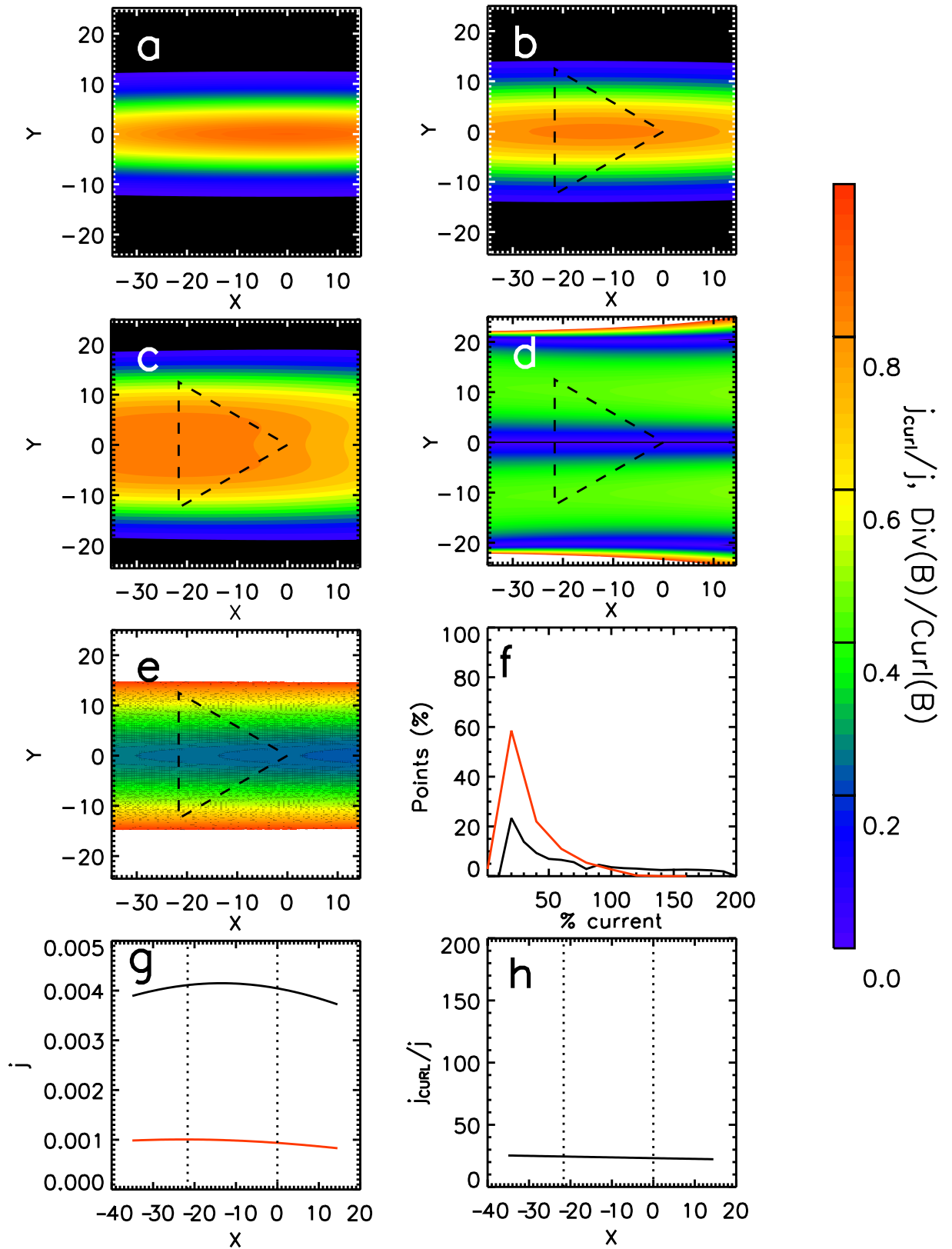
Figure 4.9: The inputs to and outputs from the curlometer for a 2d Gaussian current distribution with σ of 60 in the X direction and 5 in the Y direction. Panel (a) shows the input current distribution, centred on SC-1. Panel (b) shows current density within the tetrahedron for various locations of the mean current. Panels(c)-(e) show the current density determined by the curlometer, $|div\mathbf{B}|/|curl\mathbf{B}|$, and j_{curl}/j for various locations of the mean current. Panel (f) shows histograms of j_{curl}/j for all locations (black) and points inside the tetrahedron (red). Panel (g) shows the true current density (black) and curlometer current density (red) along the X-axis and panel (h) j_{curl}/j along the X-axis. Panels (b) and (c) have been scaled to the maximum true current density. The colour scale for panels (d) and (e) is shown.

Figure 4.10: Percentage of the true current detected by the curlometer for various 2D Gaussian current sheets distributions centred at X=-10 with σ varying between 0.25 and 25 in the Y direction.
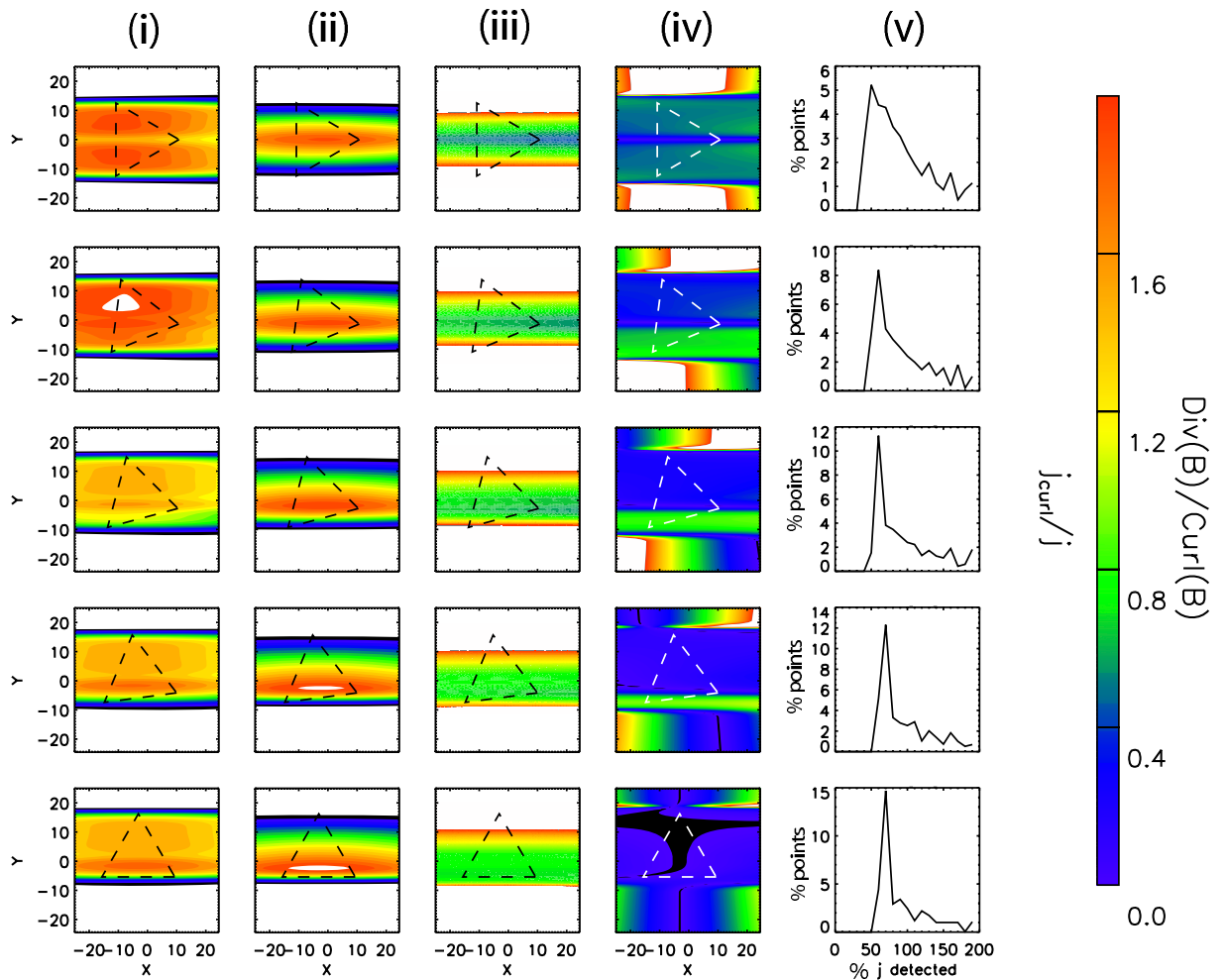
Figure 4.11: Results from the curlometer for a 2D Gaussian current sheet with a σ of 50 in the X direction and 15 in the Y direction for various rotations of the tetrahedron about the Z axis. Column (i) shows the current density from the curlometer, (ii) shows the true current density, (iii) shows the percentage of the true current detected by the curlometer, (iv) shows $|div\mathbf{B}|/|curl\mathbf{B}|$ and (v) shows histograms of the percentage of the true current detected by the curlometer.

4.4.5   Discussion of modelling results

The curlometer is a technique for estimating the current density within a tetrahedron by assuming a linear variation of the field between any two vertices. The results from this technique have been examined for a set of known current distributions and compared this with the true current values. Using a simple line current, the effect of the spatial location of the current with respect to the tetrahedron and the effect of rotating the tetrahedron against a fixed current were examined. Expanding upon this, a 2D Gaussian current distribution was used to investigate the response of the curlometer to current systems of different scale sizes. The results show that the curlometer under-estimates the current passing through the tetrahedron for current systems with a σ of half the spacecraft separation, and over-estimates the currents for current systems with a σ greater than half the spacecraft separation.

The results from Figs. 4.3 and 4.4 show that the position of a line current relative to the spacecraft has a greater effect on the current determined by the curlometer than the angle at which it passes through the tetrahedron. The current is under-estimated throughout the majority of the tetrahedron by, on average, 45% , although near when the current is close to the spacecraft, the current is over-estimated.

For 2D Gaussian current distributions, both with equal σ in the X and Y directions and those approximating current sheets, the current detected by the curlometer tends towards a constant value across the tetrahedron. For smaller current distributions, this value can be 50% of the true current density within the tetrahedron, although if the current distribution is centred close to one of the spacecraft in the plane of the distribution, the current value tends towards the true current density. When the σ of the current system is approximately half of the spacecraft separation, the current determined by the curlometer is 100% of the true current density. As the current scale size increases, the curlometer tends to over estimate the current by about 10%.

For the majority of current distributions, $|div\mathbf{B}|/|curl\mathbf{B}|$ within the limits of the tetrahedron was small. In fact, many of the values were below 0.02, the limits of our scale. Using $|div\mathbf{B}|/|curl\mathbf{B}|$ as a quality indicator would suggest that the current was well defined. For those current distributions where the current density from the curlometer approached the true current density, this is reassuring. However, for those results where the current is over- or under-estimated, $|div\mathbf{B}|/|curl\mathbf{B}|$ appears to be forced to be low, such as in Fig. 4.9. Also, for the current sheet like distributions, the $|div\mathbf{B}|/|curl\mathbf{B}|$ ratio increased when two spacecraft were both close to the current sheet, despite the current being well defined (Fig. 4.11). It is therefore unclear how useful $|div\mathbf{B}|/|curl\mathbf{B}|$ is as an indicator of the quality of the currents detected.

Results from the Cluster mission show that $|div\mathbf{B}|/|curl\mathbf{B}|$ can be highly variable, reaching values of 1 or more. In this experiment, those values were achieved when the

small current systems were outside the tetrahedron, but close to the spacecraft in the XY plane. When the current system is centred on these locations, the curlometer is still able to detect the current, although grossly over-estimated. A line current, for example, will have no current density inside the tetrahedron when it is located outside the tetrahedron, but the curlometer is still able to detect it (Fig. 4.3). As such, high values of $|div\mathbf{B}|/|curl\mathbf{B}|$ may indicate that the dominant current being detected by the curlometer is centred outside of the tetrahedron.

The results from the curlometer have previously been modelled by Dunlop *et al.* (2002) and Runov *et al.* (2005). Dunlop *et al.* (2002) compared low temporal resolution data from the Cluster spacecraft with the Tsyganenko (1989) magnetic field model for various plasma regimes that Cluster encounter during an orbit. Their results showed that the observed currents (subject to measurement errors) and the currents from the model (limited by the model) were generally in good agreement and that the shape of the tetrahedron could significantly affect the results of the curlometer. They also suggested that temporal variations in the field might be the cause of large values of $|div\mathbf{B}|/|curl\mathbf{B}|$. Runov *et al.* (2005) briefly examined the response of the curlometer to Harris current sheets of various thickness (500-2000 km). Their results show that $|div\mathbf{B}|/|curl\mathbf{B}|$ decreases with increasing current sheet thickness, and then plateaus. Furthermore, by comparing the true current with the observed current to determine the error in the current, they showed that $|div\mathbf{B}|/|curl\mathbf{B}|$ is not a good indicator of the error in the curlometer technique for large current systems. I have not compared $|div\mathbf{B}|/|curl\mathbf{B}|$ and the error in the current, although the results presented are in keeping with the observations the $|div\mathbf{B}|/|curl\mathbf{B}|$ decreases with current sheet thickness.

This investigation has not considered either localised temporal variations in the magnetic field or the limitations of the curlometer with respect to the accuracy of the magnetic field and the spacecraft positions. The first of these would require either some random variation to be applied to each of the magnetic fields observed by each spacecraft or a more in depth model that could deal with multiple species and energies of particles rather than the simplified current systems presented here. The second of these have often been considered to be incorporated within the determination of $div\mathbf{B}$, although Robert *et al.* (1998) showed there was no one-to-one correlation between the errors in $\mathbf{J}$ and $|div\mathbf{B}|/|curl\mathbf{B}|$. However, given that our magnetic values and spacecraft positions were determined exactly, this may explain the low $|div\mathbf{B}|/|curl\mathbf{B}|$ values obtained.

Chapter 5

Current systems of bursty bulk flows and auroral streamers during a period of multiple substorms

As discussed in Chapter 2, BBFs have been shown to be associated with localised current systems (Sergeev *et al.*, 1996) which take the form of a current wedge (Earthward field-aligned currents on the dawnward side, tailward field-aligned currents on the dawnward side). These currents excite auroral activity, commonly seen as auroral streamers (Lyons *et al.*, 1999; Nakamura *et al.*, 2001a,b). Although previous studies have predicted and shown the sense of this current system in the magnetosphere (Sergeev *et al.*, 1996) and the currents on one side of a BBF (Snekvik *et al.*, 2007), they have not shown the magnitude of these currents across the whole of the flow. However, the ionospheric currents associated with auroral streamers and at the footpoints of BBFs have been inferred (Amm *et al.*, 1999; Grocott *et al.*, 2004; Sergeev *et al.*, 2004a; Nakamura *et al.*, 2005a). In order to further understand BBFs and their contribution to the magnetosphere-ionosphere current systems, it is necessary to determine their currents in the magnetosphere.

This chapter presents a case study of the magnetospheric current system of a substorm-time BBF. The currents are determined using the curlometer technique (see Chapter 4) on data from the Cluster spacecraft. I show that the current systems are consistent with previously published results. Further, I use particle data to show that the BBF observed was the result of reconnection further down the tail and discuss a creation mechanism for BBFs based on the reconnection model of Cowley (1984).

5.1 Instrumentation

Figure 5.1 presents the locations of the Cluster and IMAGE spacecraft in XY, XZ and YZ planes in GSM coordinates (spacecraft data will be given in GSM coordinates unless otherwise stated) at 00:00, 01:00 and 02:00 UT on 25 August 2003. The Cluster spacecraft separation has been magnified by a factor of 200 and Cluster 1 (Rumba, black) is plotted at the correct location. The dashed lines represent the magnetic field-lines of the model of Tsyganenko and Stern (1996) (hereafter referred to as the T96 model) which pass through the location of Cluster 1 at these times. All the Cluster spacecraft were south of, and moving away from, the centre of the plasma sheet in the post-midnight sector, with Cluster 4 (Tango, blue) furthest south and Cluster 1-3 (Rumba, black, Salsa, red and Samba, green) at approximately the same Z location. Cluster 1 was closest to dawn and Cluster 2 was closest to dusk. Cluster 3 was furthest down tail. At 01:00 UT Cluster 1 was located at [-18.62,-3.58,-0.96] R_E and the average separation of the spacecraft was 120 km. Cluster data are presented here from the FluxGate Magnetometer (FGM; Balogh *et al.*, 2001), the Cluster Ion Spectrometer CODIF sensor (CIS; Rème *et al.*, 2001), and the Plasma Electron And Current Experiment High Energy Electron Analyser (PEACE HEEA; Johnstone *et al.*, 1997). The FGM data presented is based on the full resolution (22 Hz) data from the Cluster Active Archive. Plots of the data from the PEACE HEEA sensor also include a trace of the spacecraft potential, as measured by the Electric Fields and Waves instrument (EFW; Gustafsson *et al.*, 2001).

The IMAGE spacecraft passed through perigee at approximately 23:30 UT on 24th August 2003 and was travelling sunward and duskward during the interval, passing over the southern magnetic pole shortly after midnight. Data is presented from the Far-UltraViolet Wideband Imaging Camera (FUV-WIC; Mende *et al.*, 2000a,c) on board IMAGE.

Interplanetary magnetic field and solar wind data were obtained by the Advanced Composition Explorer spacecraft (ACE; Stone *et al.*, 1998) located in the solar wind upstream of the Earth at [227,-26,15] R_E GSM. Data are employed from the magnetometer (MAG; Smith *et al.*, 1998) and Solar Wind Electron Proton Alpha Monitor (SWEPAM; McComas *et al.*, 1998) instruments. The data have been lagged by 45 min to the magnetopause using the method of Khan and Cowley (1999), with an uncertainty of $\pm$ 3 min.

Ground-based magnetometer data are presented from the west coast magnetometer stations of the Greenland magnetometer chain operated by the Danish Meteorological Institute (DMI) (e.g. Popov *et al.*, 2001) and from the Antarctic low power magnetometer (LPM) chains operated by the British Antarctic Survey (BAS) and the Japanese National Institute for Polar Research (NIPR). Figure 5.2 indicates the locations of these magnetometer stations in magnetic coordinates at 01:16 UT on 25 August 2003. The magnetic footpoint of the Cluster spacecraft, calculated using the T96 model, is shown as a red star
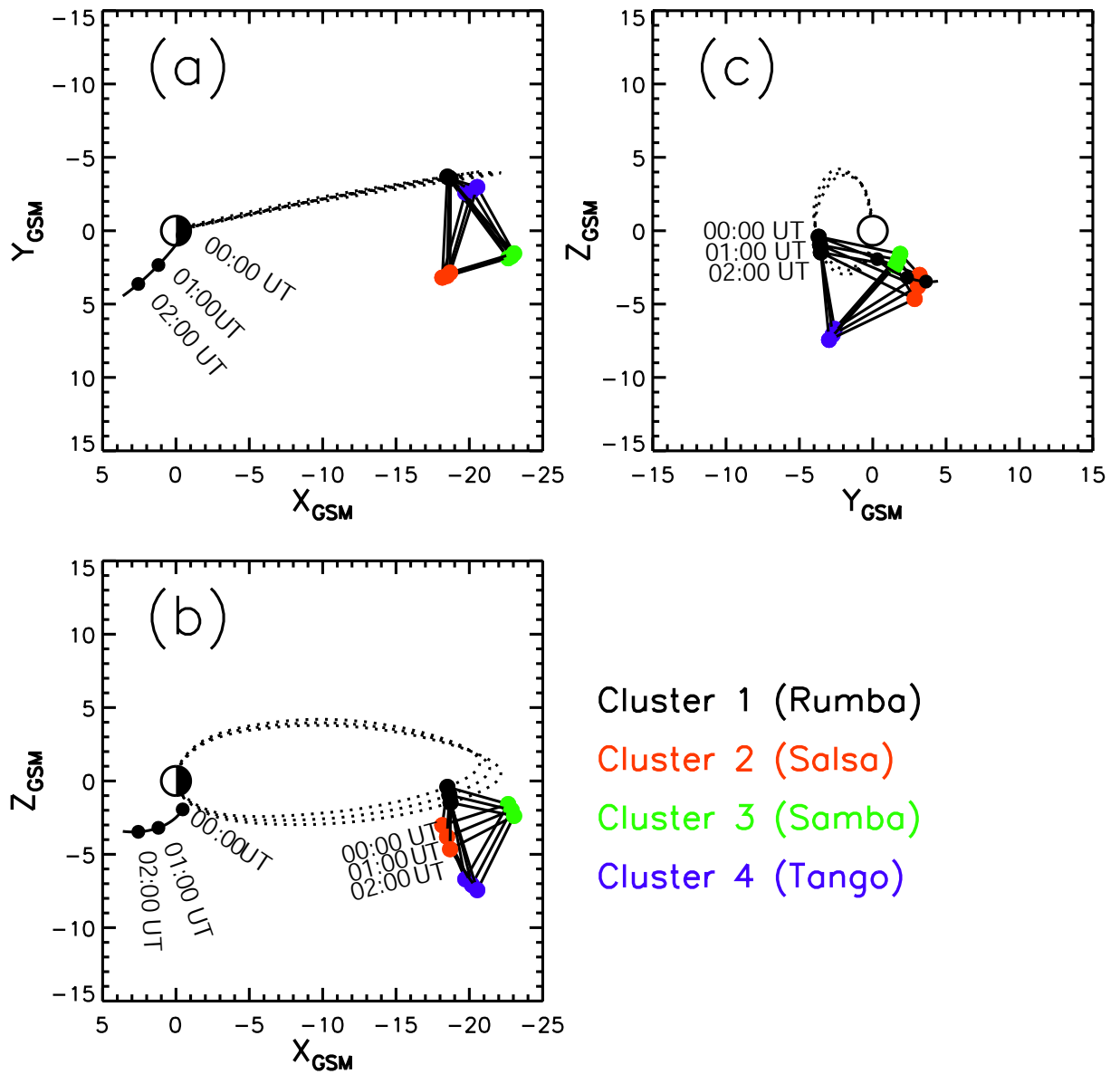
Figure 5.1: Plots of the Cluster and IMAGE orbital positions at 00:00, 01:00 and 02:00 UT in the (a) XY, (b) YZ and (c) XZ in GSM coordinates. The Cluster tetrahedron is magnified by a factor of 200. Cluster 1 (Rumba, black) is plotted at the correct location. The dotted lines represent the magnetic field-lines passing through Cluster 1 as determined by the Tsyganenko T96 model (Tsyganenko and Stern, 1996).

in each panel.

Ionospheric flow data from the SuperDARN radars are presented. The line of sight velocities from beams 2 and 5 of the Stokkseyri radar are shown, as well as the outputs from the Map Potential Model (Ruohoniemi and Baker, 1998) using inputs from the northern hemisphere radars. The field of view of the Stokkseryi radar is shown in Fig. 5.2a, along with beams 2 (equatorward-most beam) and 5 (poleward-most beam).

5.2   Observations

5.2.1   Interval Overview

Presented in Fig. 5.3 are the IMF B_X, B_Y, B_Z, magnetic field magnitude and clock angle (a-e respectively) and (f) the solar wind dynamic pressure from data the ACE spacecraft along with (g) the AE and (h) the AU (red) and AL (blue) indices from 12:00 UT 24th August 2003 to 12:00 UT 25th August 2003. The vertical black line represents 00:00 UT on the 25th August. The red vertical dashed lines represent substorm expansion phase onsets detected by Cluster.

During the 12 hours leading up to the interval there had been 5 hours of high activity (AE > 200 nT), but the two hours directly preceding the interval in question had been fairly quiet in terms of electrojet activity. The interval of interest occurs at the start of an 8 hour period during which the AE index is consistently above 400 nT, indicating an extensive active period. Comparing the AU and AL indices during the active periods, both pre- and post-midnight, indicates that the auroral electrojets were dominated by westward electrojet currents (Baumjohann and Treumann, 1996).

Data from the ACE spacecraft shows that the IMF was predominantly northward during the 12 hour period leading up to the event apart from a 5 hour period of increased electrojet activity when the IMF was southward with a clock angle close to 150°. During the period of enhanced electrojet activity after midnight, the IMF was again predominantly southward, although there were a number of sustained northward turnings of the magnetic field.

During the 24 hour period shown in Fig. 5.3, the Cluster detected six expansion phase onsets, indicated as the red vertical dashed lines. Comparing these onset times with the auroral electrojet indices shows that all bar one of the onsets is associated with a clear enhancement in the AE index, as expected. The number of substorm expansion phase onsets detected and the long periods of high electrojet activity indicate that the magnetosphere was in a generally disturbed state during this time.
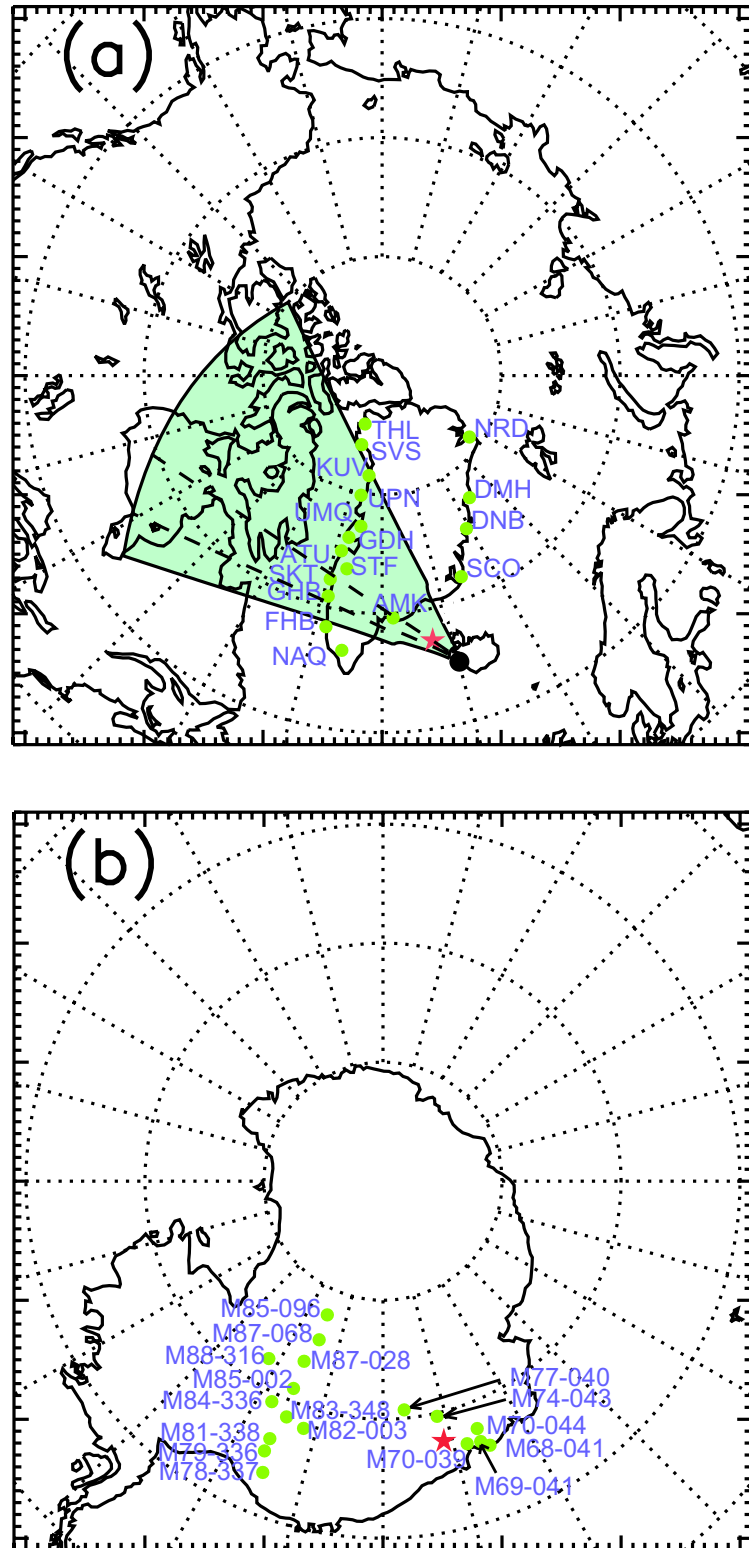
Figure 5.2: Maps indicating (a) the locations of the Greenland magnetometer chain and (b) the Antarctic low power magnetometer chains in AACGM coordinates at 01:16 UT on 25 August 2003 (12:00 MLT is at the top and 18:00 MLT to the left). The Cluster footpoint is indicated by the red star. The radial dotted lines indicate hours of MLT, while the dotted concentric circles are shown for every 10° of magnetic latitude. The field of view of the Stokksyeri radar is shown in green, with beams 2 (equatorward-most) and 5 (poleward-most) shown as the dashed lines.
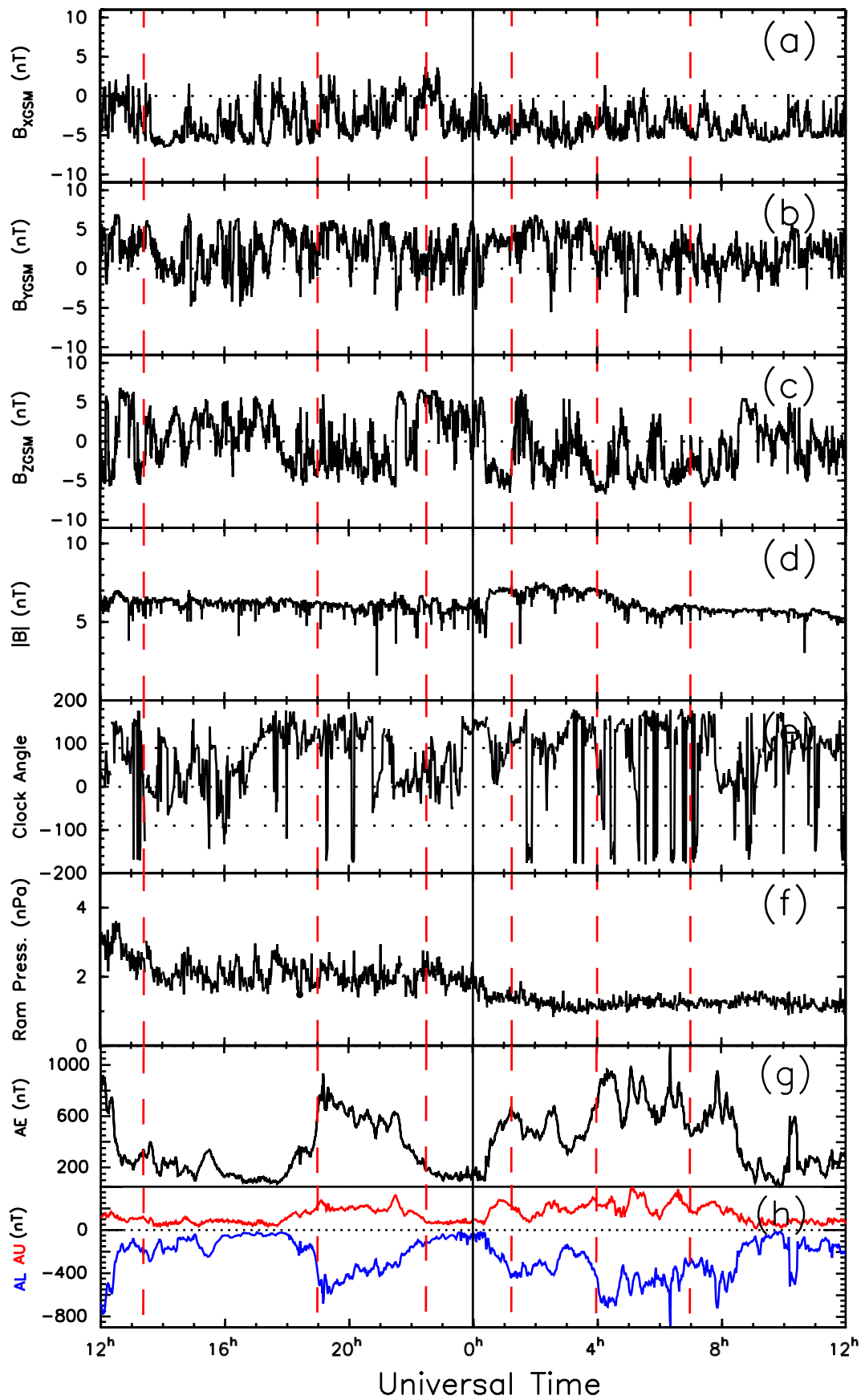
Figure 5.3: Plots of solar wind data from the ACE spacecraft and the auroral electrojet indices. Panels (a)-(e) show the IMF B_X, B_Y, and B_Z, magnetic field magnitude and clock angle respectively. Panel (f) shows the solar wind dynamic (ram) pressure. Panel (g) shows the AE index and panel (h) shows the AU (red) and AL (blue) indices. The dotted lines in panels (a)-(c) and (h) indicate 0 nT. The black vertical line indicates midnight. The dashed vertical red lines indicate substorm onsets.
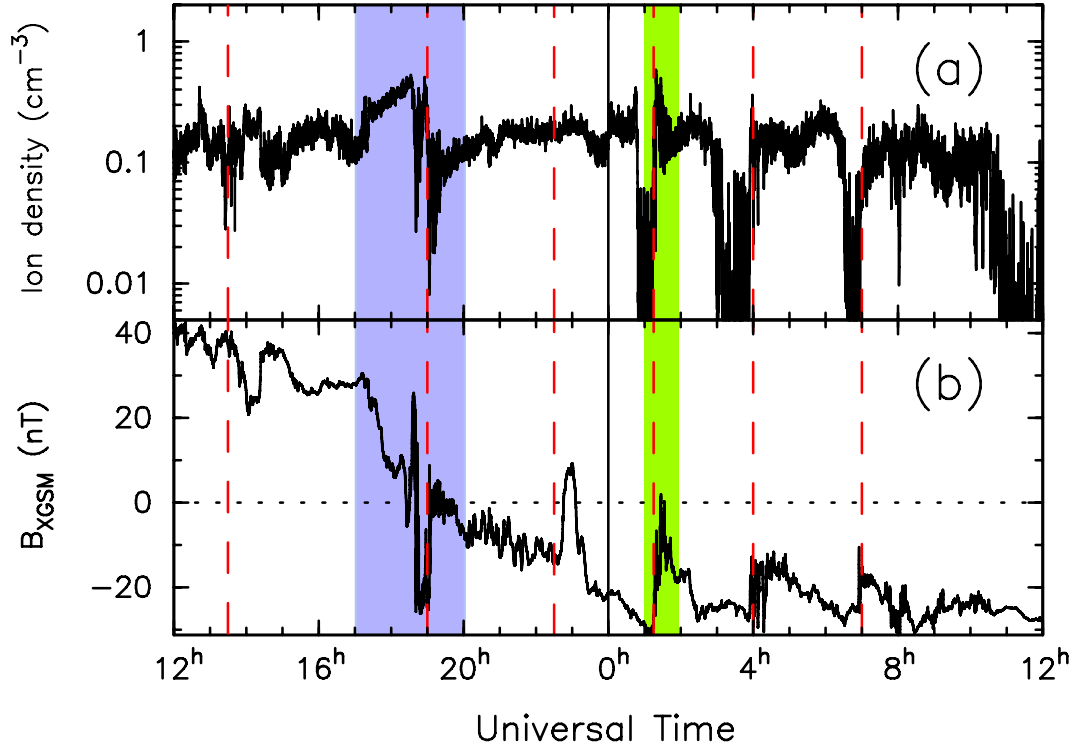
Figure 5.4: Plots of (a) the plasma ion density and (b) the B_X GSM component of the magnetic field from the CIS CODIF and FGM instruments on board Cluster 4. The dotted line in panel (a) indicates 0 nT. The black vertical line indicates midnight. The red dashed vertical lines indicate substorm onsets. Cluster's encounter with the inner central plasma sheet is highlighted in blue. The hour investigated here is highlighted in green.

Figure 5.4 shows (a) the plasma ion density and (b) the B_X component of the magnetic field from the CIS CODIF and FGM instruments on board Cluster 4 from 12:00 UT 24th August 2003 to 12:00 UT 25th August 2003. The dashed and solid vertical lines are as above. The hour investigated here is highlighted in green. Initially Cluster was above the neutral sheet, as indicated by the positive B_X component, and in the plasma sheet. Between 17:00 and 20:00 UT on the 24th August, highlighted in blue in Fig. 5.4, Cluster passed into the inner central plasma sheet and across the neutral sheet, as indicated by the plasma density increasing and the B_X component turning negative. It is interesting to note that after midnight, the three substorms detected by Cluster were preceded by Cluster passing out of the plasma sheet and into the lobes, as indicated by decreases in the plasma density to $\sim$0.1 cm^{-3}.

5.2.2 Cluster Observations

Data from the Cluster FGM and CIS instruments from Cluster 4 between 01:00 and 02:00 UT, encompassing the substorm, are presented in Fig. 5.5. CIS data were unavailable from Cluster 1 and 2 and data from Cluster 3 were noisy and will not be discussed here. Discussion of ion moments from the CIS instrument on board Cluster 4 will refer to the proton moments derived from the CODIF sensor, since the proton densities detected
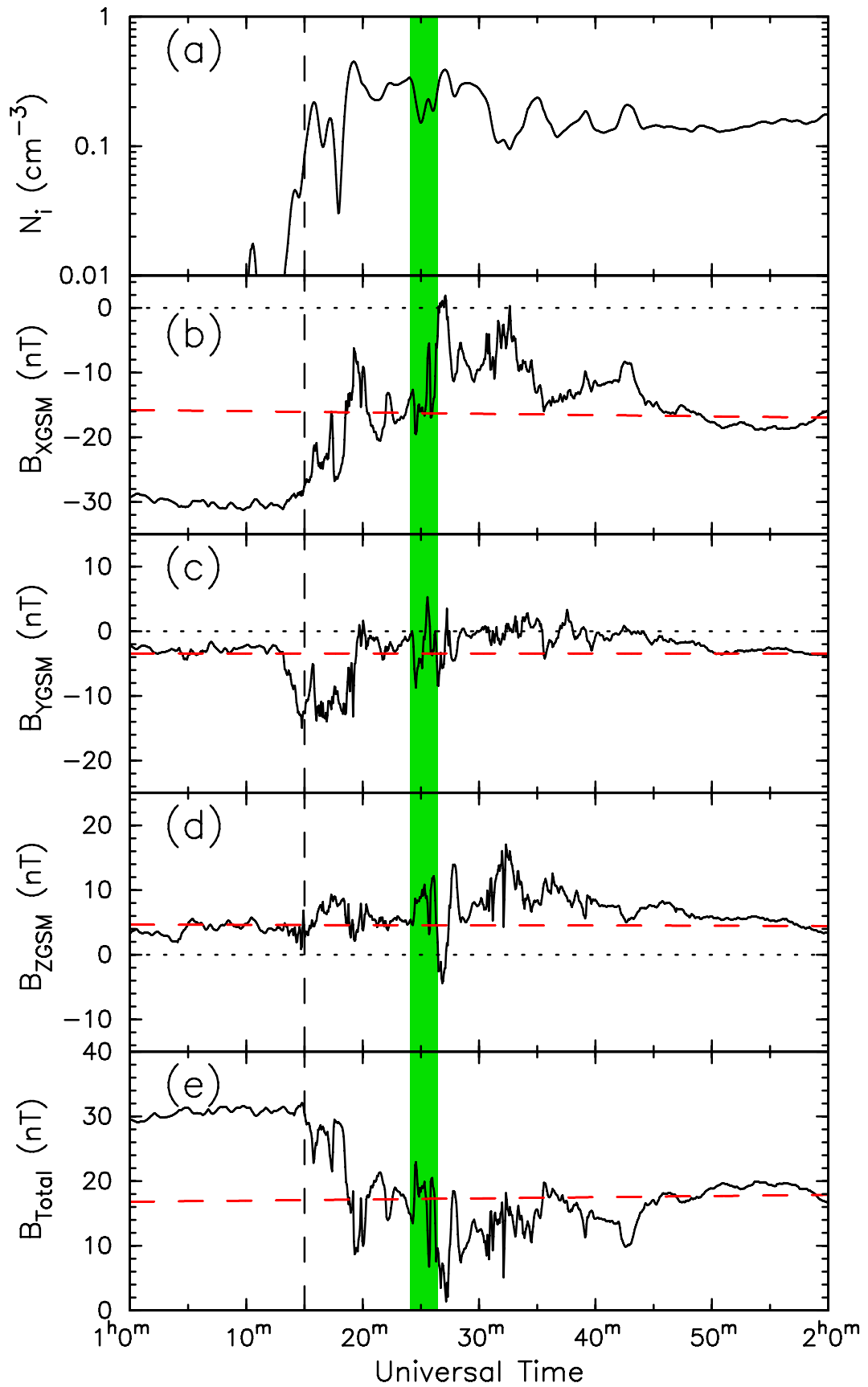
Figure 5.5: Plots of the ion and magnetic field data from Cluster 4, showing (a) the ion density, (b)-(e) the B_X, B_Y, and B_Z components of the magnetic field in GSM coordinates, and the magnetic field magnitude. The dotted lines represent the zero value in panels (b)-(e), while the red dashed line represents the T96 model field value. The vertical dashed line indicates the time at which Cluster 4 detected the substorm expansion phase. The shaded area indicates Cluster's encounter with the BBF.

by the CIS instrument were much larger than the densities of other ions. Differences in the FGM data from the four spacecraft are unnoticeable on the timescales presented here and as such, overall magnetic field conditions are taken to be those at Cluster 4. The FGM data have been smoothed using a 4 s Box Car filter. Figure 5.5a shows the ion density moments from the CIS instrument. Figure 5.5b-e shows the B_X, B_Y and B_Z magnetic field components in GSM coordinates and the magnetic field magnitude respectively from the FGM instrument. The red dashed line in Figs. 5.5b-e represents the T96 model magnetic field values at the location of the spacecraft. The vertical dashed line at 01:15 UT indicates the time at which Cluster first detected evidence of the substorm expansion phase, evidenced as a decrease in the magnetic field magnitude of $\sim$30 nT over the following 12 min, dominated by a decrease in the B_X component indicating a dipolarisation of the magnetic field. The shaded area indicates the time at which Cluster encountered the BBF.

At 01:13 UT, the ion density (Fig. 5.5a) began to increase from 0.01 cm^{-3} to 0.3 cm^{-3}, indicating that the plasma sheet boundary layer (PSBL) encompassed the spacecraft. Between 01:15 and 01:27 UT, the magnetic field magnitude (Fig. 5.5e) dropped by $\sim$30 nT, dominated by a decline in the B_X component (Fig. 5.5b). The B_Z component (Fig. 5.5d) was elevated above that of the model field throughout most of the interval, which, coupled with the decrease in the B_X component, indicates that the field became more dipole-like at this time. This is taken to be an indication that the Cluster spacecraft detected a substorm expansion phase onset at 01:15 UT. Since Cluster was initially in the southern lobe and moving away from the central plasma sheet, the plasma sheet configuration changed so as to engulf the spacecraft.

Previous studies have used various criteria to define BBFs. Cao *et al.* (2006) summarised several of these in their statistical investigation of BBFs detected by the Cluster spacecraft. Angelopoulos *et al.* (1994) defined a BBF as segments of continuous total ion flow velocity faster than 100 km s^{-1}, with a peak in the velocity of more than 400 km s^{-1} whilst the observing spacecraft was in the inner plasma sheet ($\beta > 0.5$). Raj *et al.* (2002) replaced the peak velocity and β conditions with the conditions that the peak flow velocity perpendicular to the magnetic field, v_{perp}, greater than 250 km s^{-1} and that $\beta_{XY} > 2$ (based on the X and Y components of the magnetic field). I adapt the above to emphasise the convective element of the model such that $v_{perp} > 300$ km s^{-1} for the flow enhancement to be considered a BBF, noting that previously used limits were arbitrary and not based on any physical model. Based on the prediction of the model of Chen and Wolf (1993) that the under-populated flux tubes that make up a BBF are convecting magnetic structures in which the magnetic field magnitude is enhanced, I distinguish between flow bursts within the BBF based on the magnetic field magnitude. I also compare the magnetic field data and ion density to distinguish between separate flow bursts. This differs from the definition given by Angelopoulos *et al.* (1992), who used the plasma flow data to define flow bursts.

At 01:24 UT, approximately 9 min after Cluster detected the substorm expansion phase, the spacecraft encountered a bursty bulk flow consisting of two flow bursts (indicated by the shaded region in Fig. 5.5) followed by a low magnetic field event in which the magnetic field magnitude at Cluster dropped to ~1nT . I now consider data from the Cluster spacecraft which illustrate the passage of the BBF and the subsequent low field event.

Presented in Fig. 5.6 are data from the FGM and CIS instruments between 01:18 and 01:30 UT. Figure 5.6a shows the ion density. Figure 5.6b shows the ion velocity perpendicular to the magnetic field (black), defined as $\mathbf{b} \times (\mathbf{V} \times \mathbf{b})$ where $\mathbf{b}$ is the unit magnetic field vector, the ion velocity parallel to the magnetic field (blue), and the total ion velocity (red). Figure 5.6c shows plasma beta (β, black) and the plasma beta calculated using only the B_X and B_Y GSM components (β_{XY}, blue). Figure 5.6d-g shows the B_X, B_Y and B_Z GSM components of the magnetic field and the magnetic field magnitude respectively. The green shaded area indicates the time at which the BBF engulfed Cluster. The horizontal dotted line in Figs. 5.6b-f indicates the zero value. The red dashed lines in Fig. 5.6d-g represent the T96 model field value. The dotted vertical lines represent the start of each of the two flow bursts. The dashed vertical lines enclose the low field event.

Between 01:24:15 and 01:26:15 UT, the ion velocity perpendicular to the magnetic field at Cluster (Fig. 5.6b) increased to >300 km s^{-1} with a peak value of 720 km s^{-1} and a mean value of 500 km s^{-1}. Simultaneously, the magnetic field strength increased in all components by 5 nT indicating that Cluster encountered a BBF. The ion density detected by Cluster at this time halved (Fig. 5.6a). There was a brief drop in the magnetic field magnitude between 01:25:30 and 01:25:50 UT coincident with a recovery in the ion density, indicating that the BBF consisted of two flow bursts or plasma "bubbles" as described by Chen and Wolf (1993). Following the encounter with the BBF, the magnetic field strength dropped to ~5 nT at 01:26:20 UT and continued to drop until 1:27:20 UT, with the B_X (Fig. 5.6c) and B_Z (Fig. 5.6e) components reversing just before the field strength reached its minimum value. During the recovery of the B_X and B_Z components, the B_Y (Fig. 5.6d) component also briefly reversed. It is noted that the plasma β and β_{XY} were similar throughout. At the time of the BBF, both were approximately 2, whereas during the PSBL crossings both were less than.

Previous studies have shown the scale size of BBFs in the Y direction to be between 1 and 5 R$_E$ and in the X direction to be >10 R$_E$ (Sergeev *et al.*, 1996; Angelopoulos *et al.*, 1997; Kauristie *et al.*, 2000; Nakamura *et al.*, 2001b; Amm and Kauristie, 2002; Nakamura *et al.*, 2004). It is therefore assumed that the separation of the Cluster spacecraft during the interval in question (~120 km) was significantly less than the scale size of the BBF. Considering the two flow bursts as localised magnetic field structures, the orientation of the boundaries of these structures, and the directions of the normals to the boundaries, can be determined by considering the local boundary as a planar surface and applying minimum variance analysis (MVAB) (Sonnerup and Cahill, 1967; Sonnerup and Scheible,
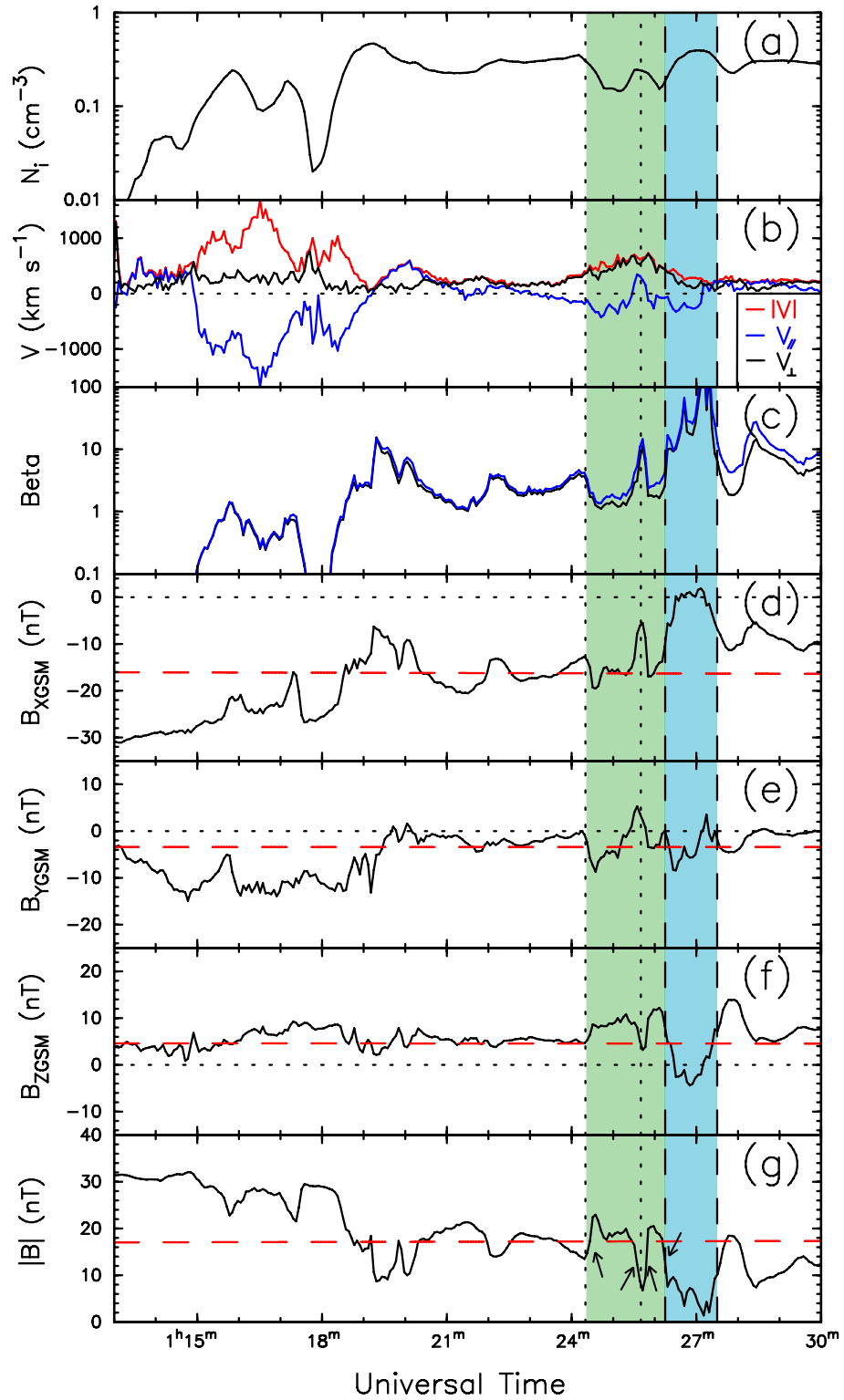
Figure 5.6: Plots of the ion and magnetic field data from Cluster 4, showing (a) the ion density, (b) the ion velocity (red: total, blue: field parallel, black: field perpendicular), (c) the plasma beta, (d)-(g) the B_X, B_Y, and B_Z components of the magnetic field in GSM coordinates, and the magnetic field magnitude. The black dotted lines represent the zero values. The red dashed lines in panels (d)-(g) represents the T96 model field value. The green shaded area indicates the time at which Cluster 4 encountered the BBF and the blue shaded area indicates the low field event. The arrows indicate the magnetic features used in the MVAB and four-spacecraft timing analysis. The dotted vertical lines represent the start of each of the two flow bursts. The dashed vertical lines enclose the low field event.

UT	MVAB	λ_2/λ_3	4SC	Vel. $\mathrm{km\,s^{-1}}$
01:24:25	(0.406, 0.147, 0.897)	31.6	(0.297, 0.239, 0.924)	160
01:25:32	(0.286, -0.911, 0.289)	16.6	(0.691, -0.223, 0.688)	165
01:25:47	(0.214, 0.573, 0.780)	7.6	(0.446, 0.073, 0.892)	190
01:26:15	(0.605, 0.332, 0.722)	36.6	(0.444, 0.333, 0.871)	170

Table 5.1: The means of the outputs of the minimum variance analysis (MVAB) across the Cluster spacecraft and the outputs of the four-spacecraft timing analysis (4SC) at various universal times. The universal times indicate the start of a 5 s period of data analysed by each method. The vectors are the normals to the boundaries of the flow bursts.

1998) and four-spacecraft timing analysis (Russell *et al.*, 1983; Harvey, 1998) techniques to the magnetic field data. The arrows in Fig. 5.6g indicate the variations in the total magnetic field used in the four-spacecraft timing analysis. The results of these two analysis techniques are given in Table 5.1. The universal times indicate the start of a 5 s period of data analysed by each method. The ratios of the intermediate to minimum eigenvalues (λ_2 and λ_3 respectively) are given as an indicator of the quality of the MVAB results, with larger ratios indicating a more reliable result. The velocity is the velocity of the boundary along the vector as determined by the four-spacecraft timing analysis. The mean results from MVAB from all four Cluster spacecraft are given for 01:24:25 and 01:26:15 UT. The mean results from MVAB from Cluster 2, 3 and 4 are given for 01:25:32 UT and from Cluster 1, 2 and 3 for 01:25:47 UT. At these times, the vectors from the remaining spacecraft were significantly different from those presented. Also, the ratios of the intermediate to minimum eigenvalues, were low (of the order of 1), indicating that the MVAB results were poor compared with the results from the other spacecraft. The ratios of the intermediate to minimum eigenvalues given are, in most cases, greater than those obtained by Nakamura *et al.* (2001b), who used this method to find the normal to the discontinuity in the magnetic field at the surface of a number of BBFs. Comparison of the full resolution FGM data from each spacecraft (not shown) for the field reversals shows that the field reversals were "nested" such that the last spacecraft to detect the negative change in B_Z was the first to detect the positive change in B_Z. This signature is consistent with the low field strength event moving across the Cluster tetrahedron and then moving back. However, the time lags between the spacecraft were small and the variability in the magnetic field components across the four Cluster spacecraft increased during the low field event, such that further analysis of the structure and the determination of the motion and orientation of the structure using either four-spacecraft timing or MVAB is badly defined, although a visual inspection of the data suggests motion predominantly in the Z_{GSM} direction.

Figure 5.7 shows the MVAB (blue) and four-spacecraft timing analysis (black) vectors normal to the flow boundaries as arrows, and the flow boundaries themselves as lines in the XY, XZ and YZ planes at 01:24:25, 01:25:32, 01:25:47, and 01:26:15 UT (rows a-d respectively). The green arrows represent the unit vectors of ion velocity perpendicular to the field at those times. The sense of the MVAB and four-spacecraft timing vectors are
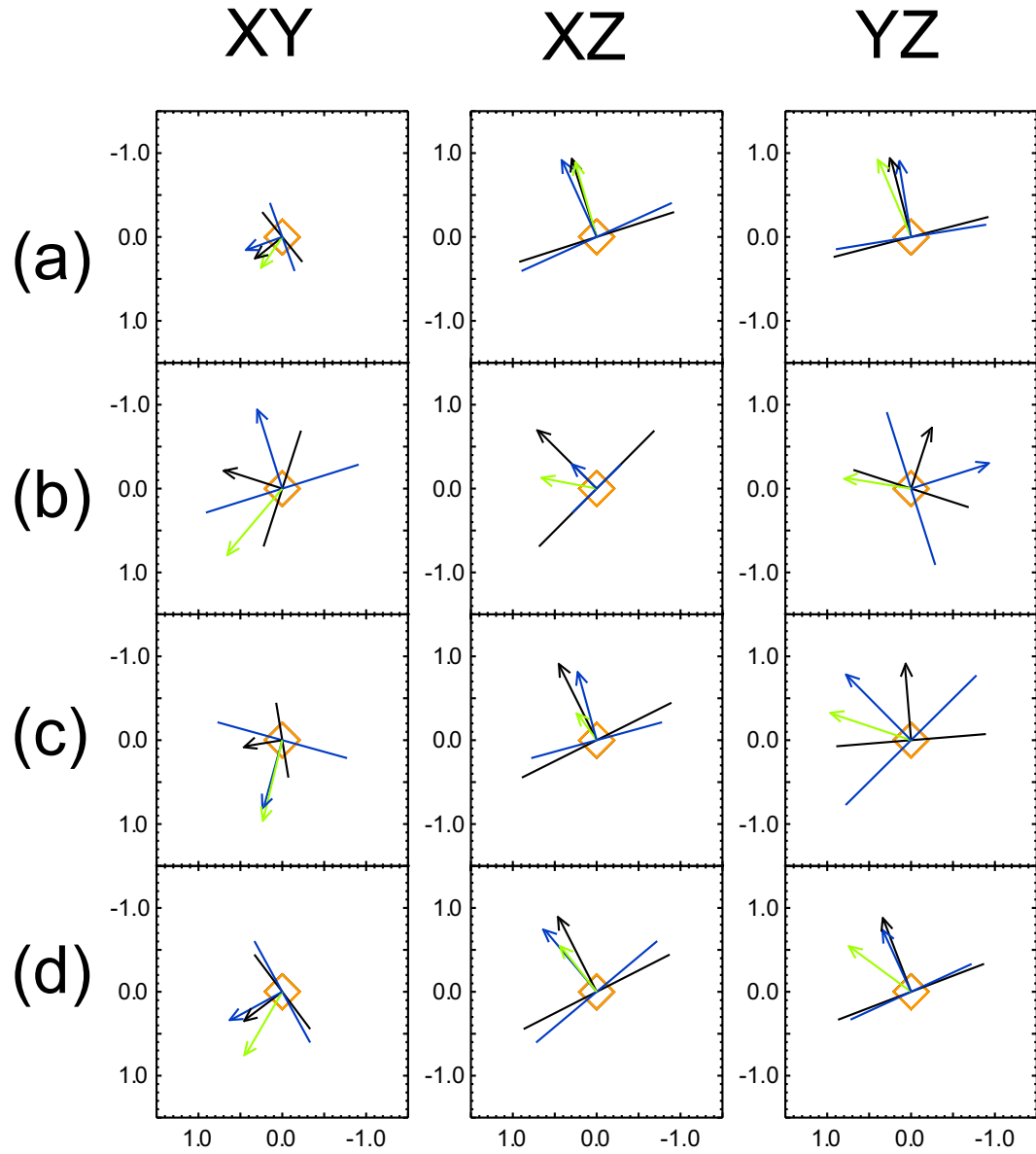
Figure 5.7: Plots of the boundaries of the BBF flow bursts as determined by MVAB (blue) and four-spacecraft timing analysis (black) at the four times given in table 5.1 (lines (a)-(d) respectively) in the XY, XZ and YZ GSM planes. The horizontal axes are in the X_{GSM}, X_{GSM} and Y_{GSM} directions respectively. The lines represent the boundary of the BBF flow bursts and the arrows represent the normals to the boundary. The green arrows indicate the ion velocity perpendicular to the magnetic field at the given times.

similar, such that, in each case, the vectors are pointing through the same quadrant. Rows (a) and (d) show a particularly good correspondence between the two analysis techniques, whereas in rows (b) and (c), in which the MVAB vectors had a lower eigenvalue ratio, the correspondence is less good between the two techniques. The vectors in the XZ plane show that the normals to the boundaries and the motion of the field-lines were predominantly in the Z direction, although this is expected, given that the plasma sheet field-lines are highly distended and contracting. The orientation of the boundary changes in the dusk-dawn direction between rows (a) and (b), representing the boundaries of the first flow burst. This change is not seen between rows (c) and (d), representing the boundaries of the second flow burst, such that both boundaries are orientated towards dusk. It is noted that at each boundary the ion velocity perpendicular to the field, i.e. the field-line motion, was directed more towards dusk than the boundaries in each case.

Comparison of the instantaneous magnetic field vector between the four Cluster space-craft enables the curl and divergence of the magnetic field within the tetrahedron to be estimated by the curlometer technique and the net current through the spacecraft tetra-hedron to be calculated (Dunlop *et al.*, 1988; Robert *et al.*, 1998, and Chapter 4). Figure 5.8 shows the results of the curlometer analysis. Figure 5.8a-d shows the j_X, j_Y, j_Z and field parallel (i.e. field-aligned currents) currents. Positive field-aligned currents indicate a tailward directed current. DivB/CurlB (Fig. 5.8e) acts as an indication of the quality of the result from the curlometer, with lower ratios indicating more reliable results. The analysis output has been smoothed using a 10 s Box Car filter in order to reduce the variability in the data and highlight the large scale structure. The blue line in Fig. 5.8e is DivB/CurlB smoothed with a 60 s Box Car filter to further highlight the lower ratio at the time of the BBF. The unsmoothed currents (not shown) are highly variable, with the polarity of the current changing rapidly. However such small scale current systems are beyond the scope of this thesis, in which I consider the variations in the current on the scale of the flow bursts themselves.

Between 01:24 and 01:28 UT the field-aligned currents are enhanced (Fig. 5.8d). During the passage of each flow burst (between 01:24 and 01:27 UT) the field-aligned currents are initially tailwards and then turn Earthwards. The currents in both Earthward and tailward directions have peak magnitudes of $\sim$5 mA km^{-2}. These values of the field-aligned currents in the plasma sheet can be scaled up, although somewhat crudely, using the T96 model magnetic field to give an estimate of the ionospheric field-aligned currents associated with the detected flow of $\sim$18 A km^{-2}. During the low field event that follows the BBF (indicated by the blue shading), the field-aligned currents become larger, with peaks > 10 mA km^{-2}. The means of the magnitudes of the components of the magnetic field and current data show that the B_Z component of the magnetic field and j_Y com-ponent of the current were largest during this period, suggesting that Cluster detected the cross-tail current sheet. DivB/CurlB (Fig. 5.8e) drops during the passage of the BBF and the low field event, indicating that the results of the curlometer are due to currents
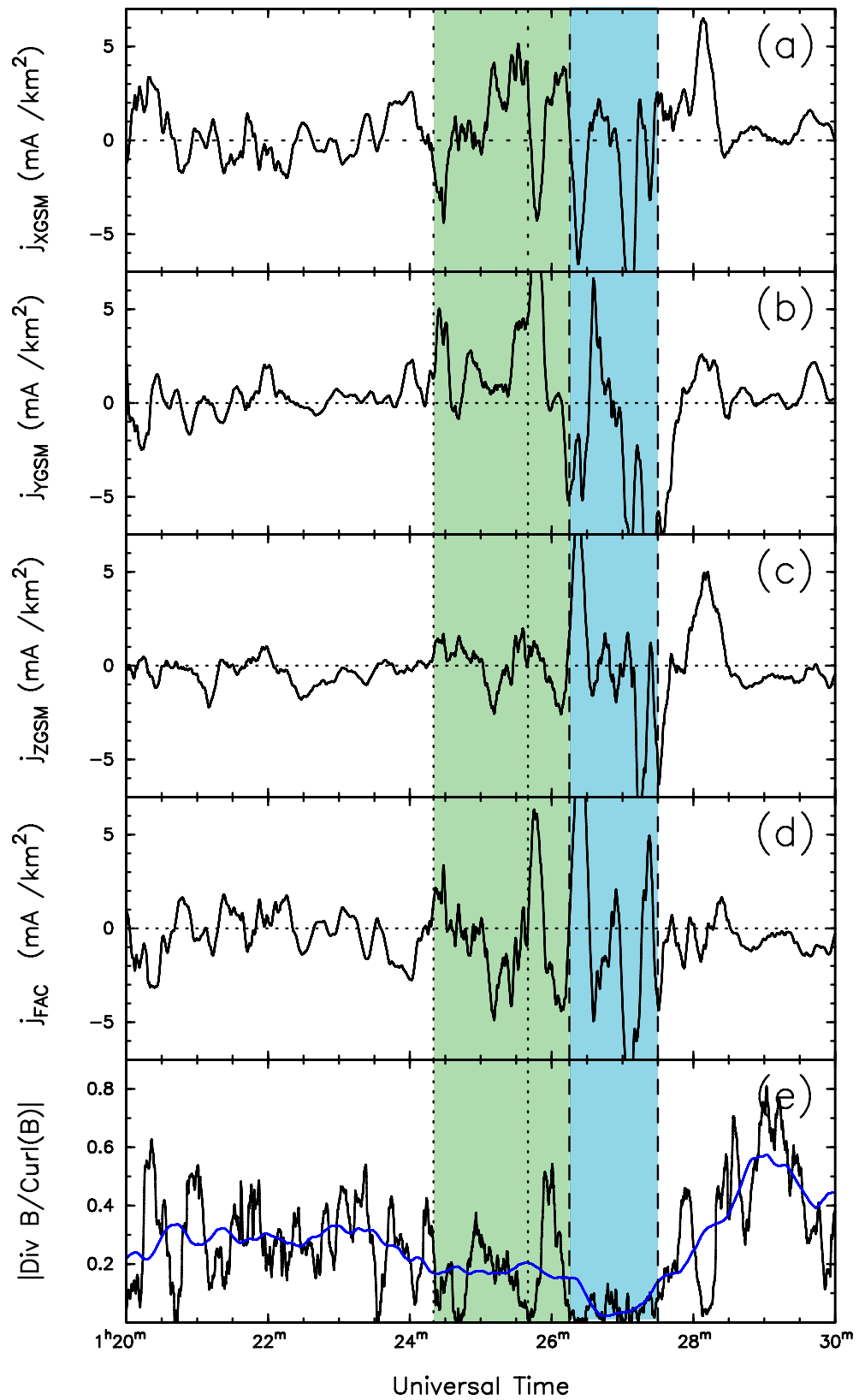
Figure 5.8: Plots of the results of the curlometer analysis, showing (a)-(d) the j_X, j_Y, j_Z and field-aligned components of current density and (e) DivB/CurlB. The data have been smoothed with a 10 s Box Car filter. The horizontal dotted lines represent the zero values in panels (a)-(d). The blue line (panel (e)) shows the ratio of the moduli of the divergence and curl of the magnetic field smoothed with a 60 s Box Car filter. The green shaded area indicates the time at which Cluster encountered the BBF and the blue shaded area indicates the low field event. Positive field-aligned currents represent tailward flow. The dotted vertical lines represent the start of each of the two flow bursts. The dashed vertical lines enclose the low field event.

flowing through the spacecraft tetrahedron.

Figure 5.9 shows (a) a spectrogram of the pitch angle distribution of ions with energies greater than 1 keV from the CIS instrument on board Cluster 4 and line plots of the same data at (b) 01:15:13, (c) 01:17:04, (d) 01:21:10, (e) 01:24:57, (f) 01:28:55 UT. These times are indicative of Cluster first entering the PSBL, Cluster approaching the inner edge of the PSBL, Cluster located in the plasma sheet before the BBF, Cluster's encounter with the BBF and Cluster re-entering the plasma sheet, respectively. A pitch angle of 180° represents Earthward flowing ions. Presented in Fig. 5.10 is the omnidirectional ion differential number flux in the energy range 10 eV to 30 keV between 01:10 and 01:30 UT from the CIS CODIF instrument on board Cluster 4. Panel (a) presents the data as a spectrogram whereas panel (b) shows the differential number flux against ion energy at 01:17:04 UT (black) and 01:24:57 UT (yellow). The letters at the bottom of Fig. 5.9a and Fig. 5.10a indicate the times of the pitch angle distributions presented in Fig. 5.9b-f. From Fig. 5.10, it can be seen that throughout the interval of interest, the majority of the ion population had energy range taken in Fig. 5.9.

Between 01:15 and 01:18 UT Fig. 5.10a shows short-lived dispersed energy signatures, with Cluster 4 first encountering ions with energies of 10-20 keV, then encountering ions with energies of 1-10 keV. The ion pitch angle distributions at this time (Fig. 5.9b and c) show that the ions consisted mainly of bidirectional field-aligned beams. Figure 5.9a shows that, in fact, these beams were first Earthward, then bidirectional, indicating that Cluster first encountered newly reconnected field-lines at the edge of the PSBL before passing into the bidirectional streaming region. After 01:20 UT, the pitch angle distribution became fairly isotropic (Fig. 5.9d) indicating that Cluster was within the plasma sheet. Figure 5.9e indicates that when Cluster encountered the BBF the ions again consisted of bidirectional beams, although the differential number flux in the Earthward beam was higher than in the tailward beam. At this time, the non-field aligned component of the pitch angle distribution dropped below the plasma sheet level (Fig. 5.9c), indicating that the beam was not superimposed on the plasma sheet but was a separate plasma population. Comparing the differential ion fluxes between the inner edge of the PSBL and the BBF (Fig. 5.10b, black and yellow lines respectively) indicates that the ion population at the inner edge of the PSBL was similar to the ion population detected during the BBF encounter. After Cluster encountered the BBF, the spacecraft re-entered the plasma sheet, as seen by the isotropic pitch angle distribution (Fig. 5.9e) and the similarity between the ion differential number fluxes (Fig. 5.10a).
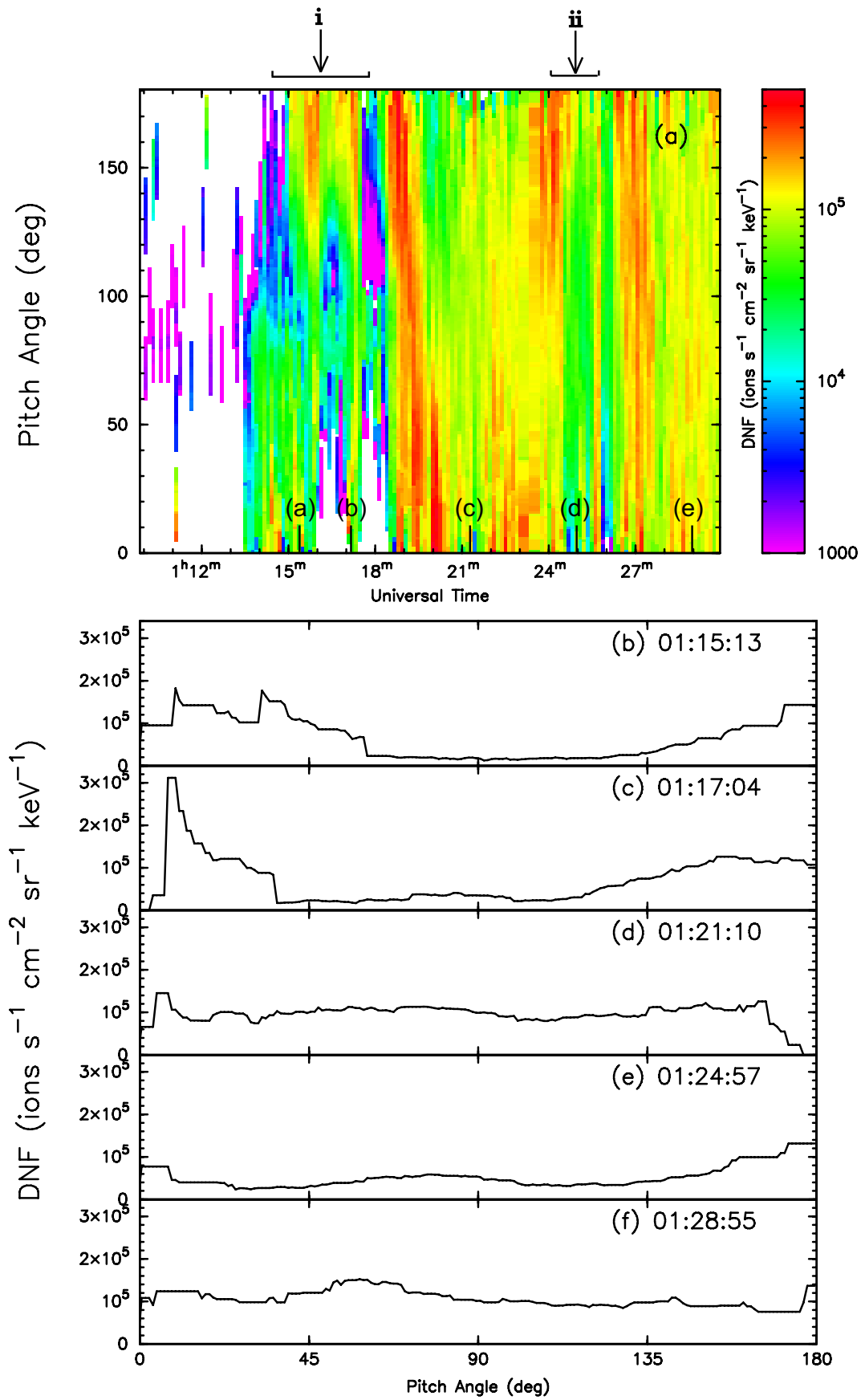
Figure 5.9: The pitch angle distribution of the ion differential number flux for ions with energy greater than 1 keV from CIS CODIF on board Cluster 4 presented as (a) a spectrogram and at (b) 01:15:13, (c) 01:17:04, (d) 01:21:10, (e) 01:24:57, (f) 01:28:55 UT. A pitch angle of 180° represents Earthward flowing ions. Interval (i) in panel (a) indicates the PSBL crossing and (ii) indicates the BBF encounter.
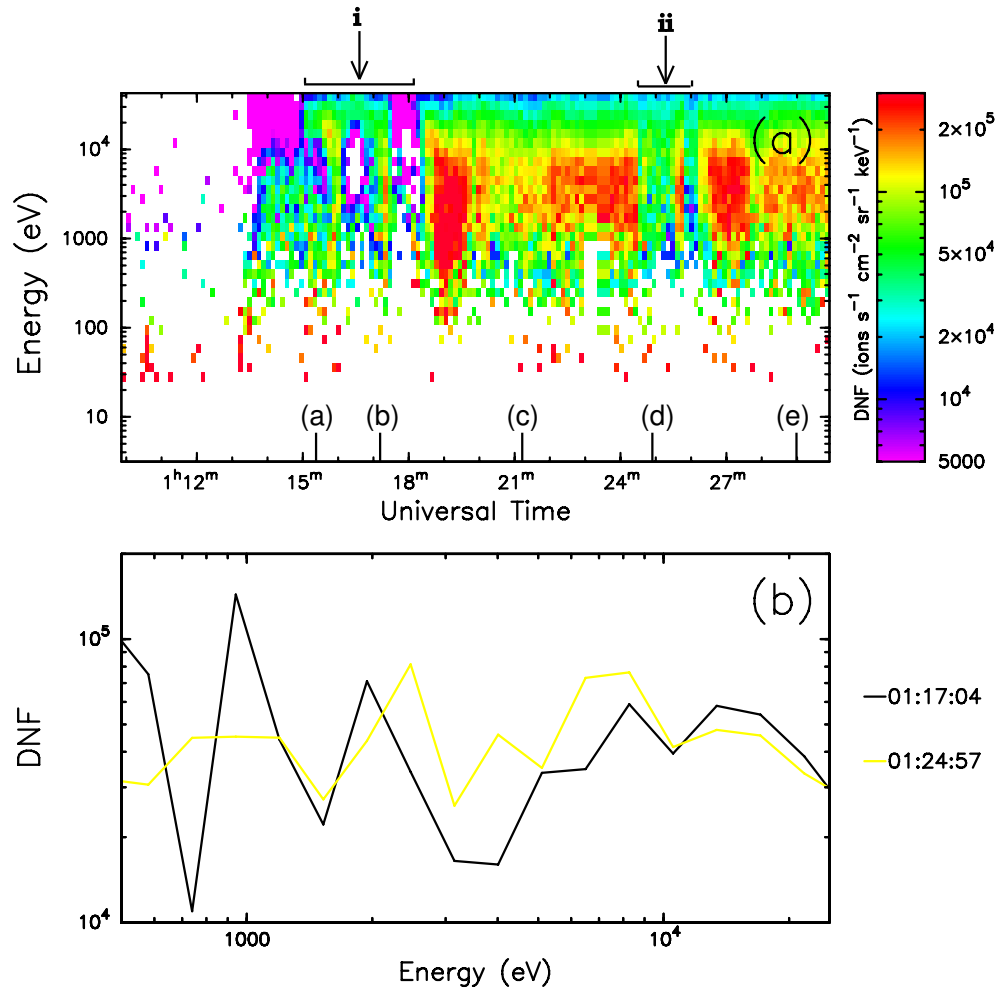
Figure 5.10: (a) Spectrogram of the ion differential number flux for energies in the range 10 eV-30 keV across all pitch angles from the CIS CODIF sensor (b) the ion differential number flux against energy at 01:17:04 (black) and 01:24:57 UT (yellow). The labels on the bottom axis of panel (a) represent the times of the traces in Fig. 5.9. Intervals i and ii indicate the times at which Cluster encountered the PSBL and BBF respectively.

Presented in Fig. 5.11 are the differential energy fluxes of electrons moving parallel, perpendicular and antiparallel to the magnetic field (a-c respectively) from the PEACE HEEA sensor on board Cluster 4 for the interval 01:10-01:30 UT. The spacecraft potential from the EFW instrument is shown in volts as a black trace at the bottom of each panel. Between 01:10 and 01:18 UT, there is a high flux of low energy ($<$60 eV) electrons, although comparison with the spacecraft potential shows that these are photo-electrons and not part of the natural plasma population. Between 01:24 and 01:26 UT (Fig. 5.11 arrow ii) the perpendicular electron flux decreased and the electron flux increased in the parallel and antiparallel directions, indicating that Cluster encountered field-aligned beams of electrons, which we interpret as the signature of newly reconnected field-lines (e.g. Keiling *et al.*, 2006), complementing the ion data. However, the differential energy flux and energy of the electrons was lower during the PSBL crossing compared with the BBF encounter.
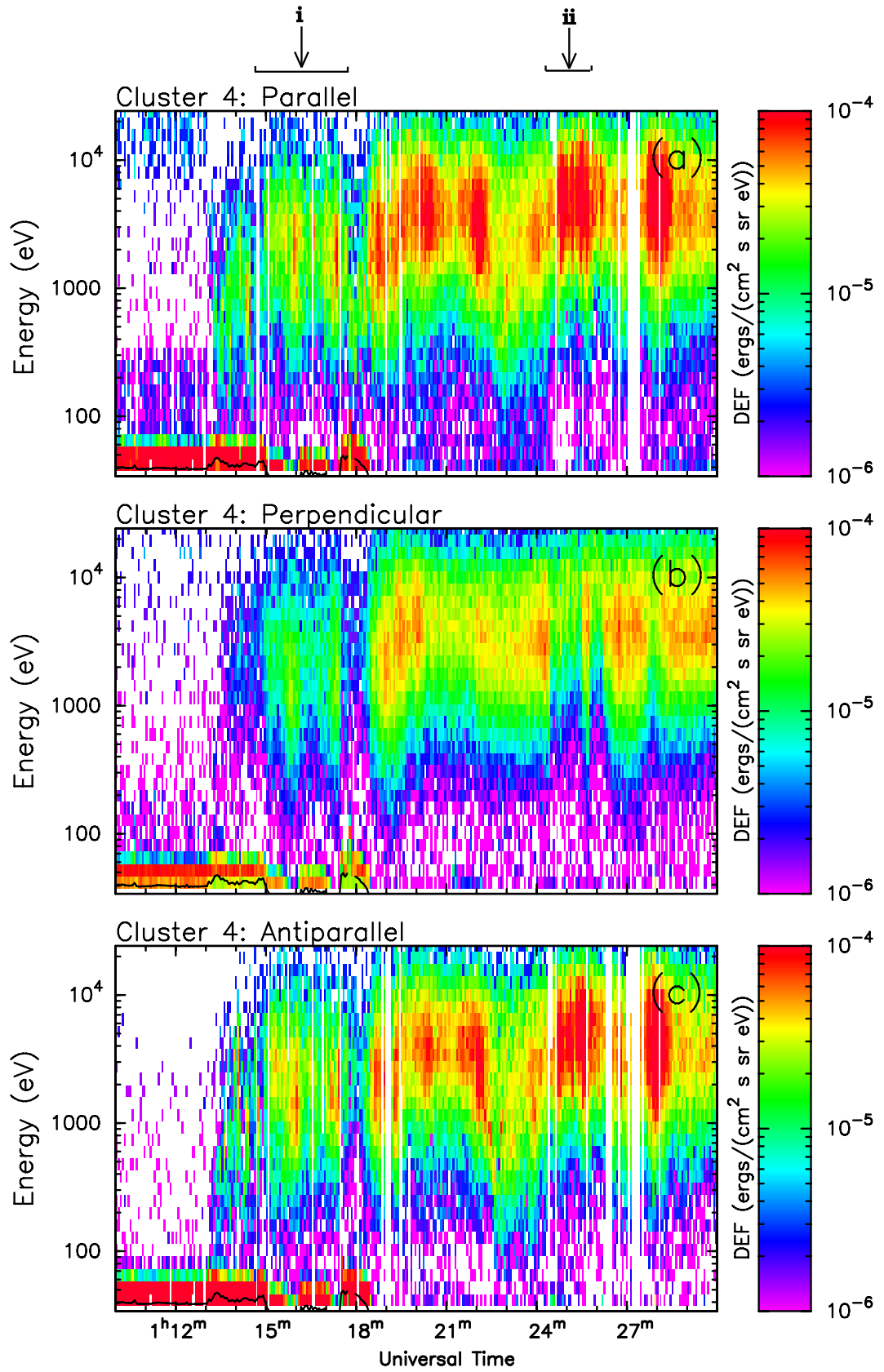
Figure 5.11: Spectrograms of the differential energy flux of electrons in the energy range $37\text{-}2.2\times10^4$ eV (a) parallel, (b) perpendicular and (c) antiparallel to the magnetic field from the PEACE HEEA sensor on board Cluster 4. The black trace in each panel represents the spacecraft potential in volts. Arrows i and ii indicate the times at which Cluster encountered the PSBL and BBF respectively.

5.2.3   IMAGE FUV-WIC observations

Figure 5.12 shows a series of consecutive images of the southern hemisphere auroral region taken by the FUV-WIC instrument on board the IMAGE spacecraft between 01:15 and 01:37 UT. The images have been mapped into AACGM coordinates and plotted in MLT - invariant latitude coordinates based on spacecraft pointing data. The dotted rings represent -80° -70° and -60° of invariant latitude from the top of the image outwards. The radial dotted lines represent hours of MLT. The top of each panel represents the 06:00-18:00 MLT meridian and the vertical dotted lines represent the 00:00 MLT meridian. The T96 model, applied using data from the ACE spacecraft lagged by 44 min, with an error of ±3 min, using the technique of Khan and Cowley (1999), puts the mapped footpoint of Cluster 4 at ∼01 MLT throughout the interval. Figure 5.12L shows the location of the BAS and NIPR LPM magnetometer chains in the southern hemisphere (green dots) and the DMI magnetometers in the northern hemisphere (blue dots) at 01:15:45 UT are shown in the same coordinate system. The Cluster footpoint in the southern hemisphere is shown as a red star. The FUV-WIC data have been calibrated such that the flat-field and dayglow have been removed. Comparing Fig. 5.12a and Fig. 5.12b shows that there was a brightening of the auroral bulge between the images at 01:15:45 and 01:17:48 UT centred at ∼01:00 MLT which extended over 2 hours of MLT towards dusk and dawn. This indicates the start of an auroral substorm expansion phase, which occurred ∼1-3 min after Cluster detected the substorm expansion phase in the tail. Figures 5.12c-k show that the auroral bulge expanded polewards, as expected for an auroral substorm, covering ∼15° of magnetic latitude at its widest point at 01:36 UT. Figure 5.12 panels c-k also show that the auroral breakup was predominantly in the post-midnight sector. Although the breakup was over the NIPR LPM magnetometers (around 01 MLT, Fig. 5.12a), the breakup did not expand duskwards to encompass the BAS LPM magnetometers until 01:26:03 UT (Fig. 5.12f). An auroral streamer was evident dawnward of the Cluster 4 footpoint in the images between 01:21-01:27 UT (Figs. 5.12d-f), highlighted by white circle), giving it a lifetime of 6-10 min, based on the cadence of the FUV-WIC instrument.

Presented in Fig. 5.13 is a time series of auroral luminosity above 3 kR from FUV-WIC taken between magnetic latitudes of -67° and -68° and between 23 and 02MLT from 01:19 to 01:27 UT. The luminosity in each image has been normalised to the maximum luminosity along the trace, such that the maximum data value is 1. The auroral streamer that was detected at 01:21 UT is evident as a peak in the 00-01 MLT range between 01:21 and 01:26 UT, indicated by the arrows on Fig. 5.13. Successive traces show that this peak moves westwards with a velocity of ∼3 km s^{-1}. Amm *et al.* (1999) and Sergeev *et al.* (2004a) showed that the bright, duskward edge of an auroral streamer is associated with large, upward currents whereas the trailing diffuse aurora is associated with smaller downward currents. Although the peak of the streamer is evident in Fig. 5.13, the edge of the diffuse aurora is not well defined. As such, the width of the streamer, and therefore the width of the BBF, cannot be estimated solely from the auroral data.
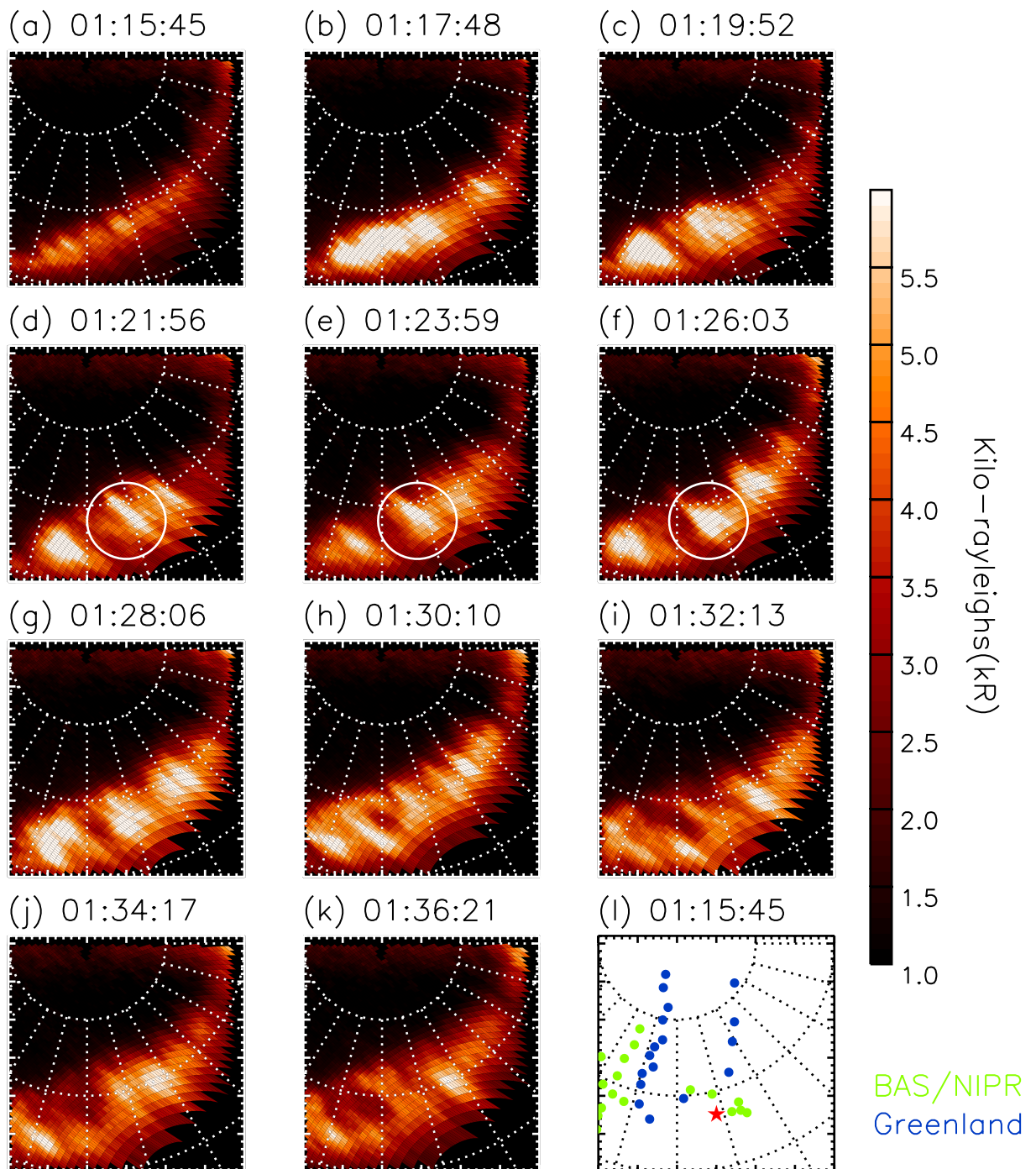
Figure 5.12: Eleven consecutive auroral images from the FUV-WIC instrument on board the IMAGE spacecraft, taken between 01:15 and 01:37 UT mapped into AACGM coordinate system. The top of each panel represents the 06:00-18:00 MLT meridian. The vertical dotted line in each panel represents the 00:00 MLT meridian. The colour scale of the images is shown on the right hand side. Panel (l) shows the locations of the BAS and NIPR LPM magnetometer chain in the southern hemisphere (green dots) and the DMI magnetometer chain in the northern hemisphere (blue dots) in AACGM coordinates at 01:15:45 UT and plotted as above. The footprint of the Cluster spacecraft in the southern hemisphere at that time is shown as a red star in panel (l).
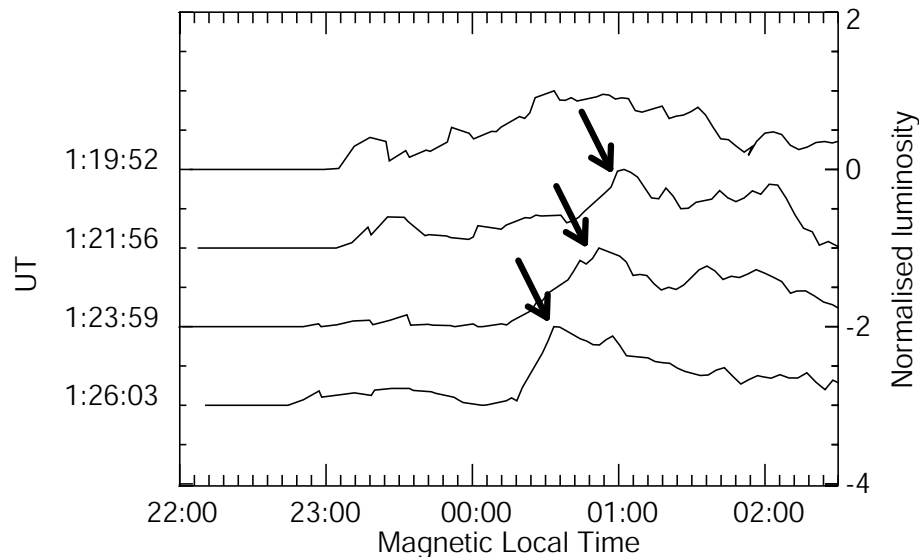
Figure 5.13: Time series of normalised auroral luminosity above 3 kR between 01:19 and 01:27 UT. Each trace has been normalised to the maximum luminosity along the trace. The traces plot these values between magnetic latitudes of -67° and -68° in the range 22:00-02:00 MLT. Each successive trace is offset by -1. The arrows indicate the signature of the auroral streamer.

5.2.4   Ground-based observations

Figure 5.14 shows stacked plots of the northward magnetic field component, averaged over 20s, detected by the DMI west coast magnetometer chain between 00:00 and 03:00 UT. A substorm expansion phase onset, indicated by a sharp negative bay, was seen at 01:15 UT at Narsarsuaq (NAQ), propagating 14° northwards to (UPN) by 01:30 UT. This substorm expansion phase onset was preceded by an earlier onset at 00:40 UT that was seen at NAQ and FHB. Filtering the NAQ data using a 4 min high pass filter (Fig. 5.14 bottom trace) shows that the negative bay indicating the substorm expansion phase onset was accompanied by a significant increase in Pi2 band noise. Similarly, Fig. 5.15 shows stacked plots of the northward magnetic field component detected by the BAS LPM chain, which is approximately magnetically conjugate to the Greenland magnetometer chain, between 00:00 and 03:00 UT. The substorm expansion phase onset was indicated by the negative bay at 01:25 UT, 10 min after the onset detected in the Greenland magnetometers but in conjunction with the movement of the auroral breakup over the magnetometers (Fig. 5.12f). This negative bay was first observed, although comparatively weakly, at M81-388, and propagated up to 7° polewards, reaching M87-028 at 01:35 UT. It should be noted that the BAS LPM data is subject to timing uncertainties of between 58 (at M81-338) and 2170 s (at M79-336), with an average uncertainty (discounting M79-336) of ~180 s, caused by instrumental effects.

Figure 5.16 shows stacked plots of the (a) eastward, and (b) vertically downward magnetic field components detected by the NIPR LPM chain between 01:15 and 01:35 UT. The vertical dashed line represents the time at which FUV-WIC observed the auroral streamer over the NIPR LPM chain. The eastward component (Fig. 5.16a) shows a sawtooth-like
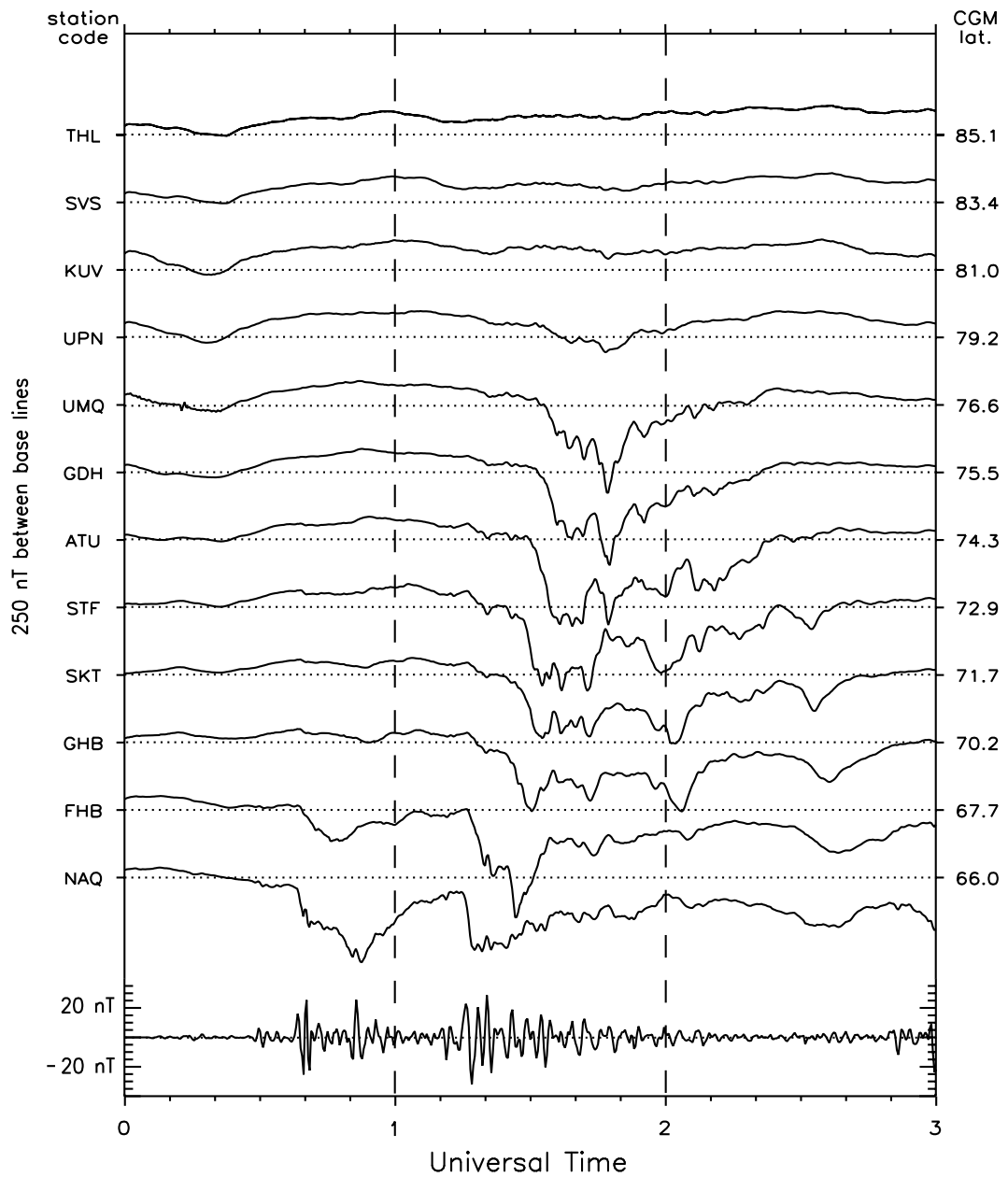
Figure 5.14: Plots of the northward (H) component of the magnetic field from the west coast magnetometer chain of the DMI Greenland magnetometer network. The dotted horizontal lines represent the baseline (0 nT) for each station. The stations are plotted in descending latitudinal order and the stations corrected geomagnetic latitudes are shown on the right hand side of the plot. Each plot baseline is separated by 250 nT. The vertical dashed lines indicate hours. The lower trace shows the northward (H) component of the magnetic field from NAQ filtered using a 4 min high pass filter.
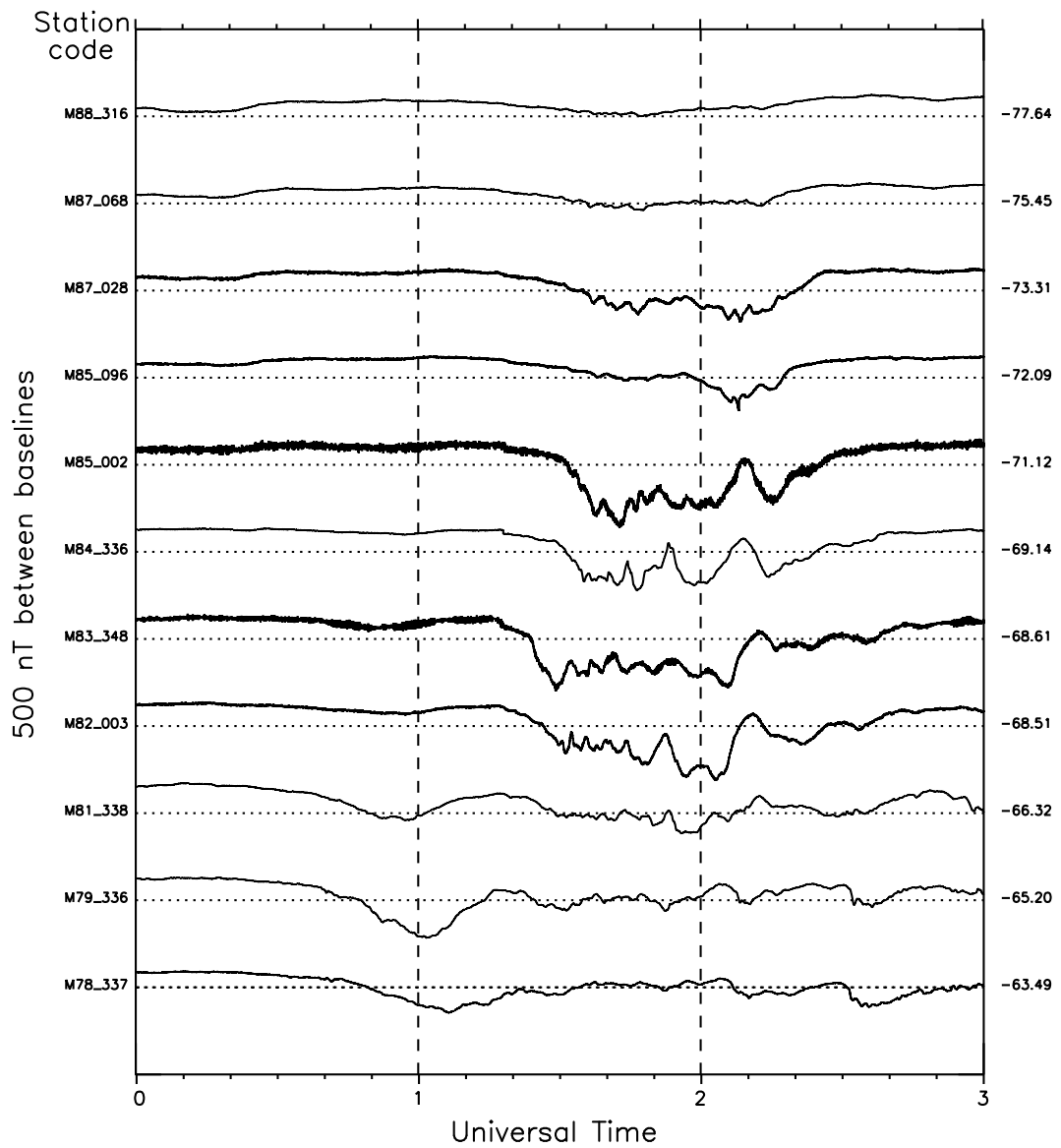
Figure 5.15: Stacked plots of the northward (H) component of the magnetic field detected by the BAS LPM chain. The dotted horizontal lines represent the baseline (0 nT) for each station. The stations are plotted in ascending latitudinal order and the stations corrected geomagnetic latitudes are shown on the right hand side of the plot. Each plot baseline is separated by 500 nT. The vertical dashed lines indicate hours.
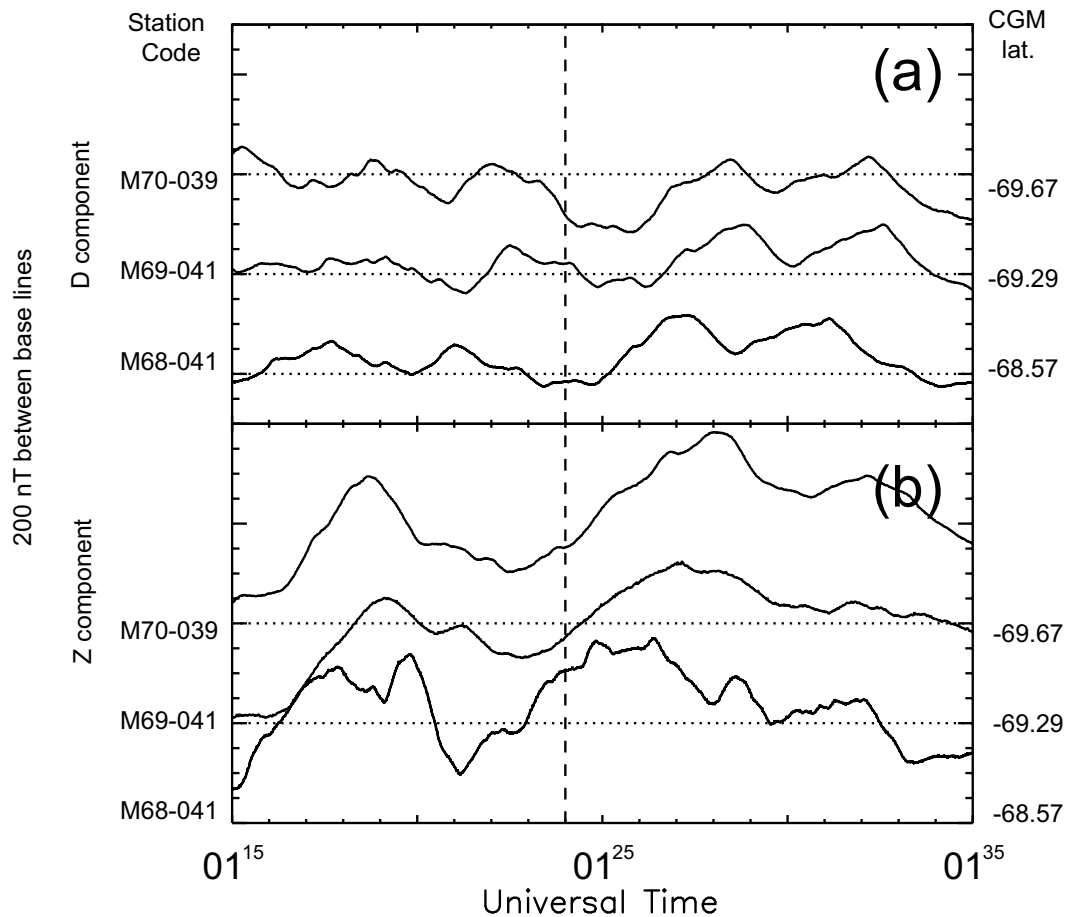
Figure 5.16: Plots of the (a) eastward (D) and (b) vertically downward (Z) components of the magnetic field detected by the NIPR LPM chain. The dotted horizontal lines represent the baseline (0 nT) for each station. The stations are plotted in ascending latitudinal order and the stations corrected geomagnetic latitudes are shown on the right hand side of the plot. Each plot baseline is separated by 200 nT. The vertical dashed line indicates when the auroral streamer was above the magnetometer stations, as determined by the FUV-WIC data.

signature accompanied by a minimum in the vertically downward (Fig. 5.16b) component at the time of the passage of the streamer. This indicates the passage of a weaker east-west current system, in which the current direction changed in the vertical direction during the passage of the structure. However, it should be noted that although the signature is observed at the three stations, timing uncertainties in the data of the order of 100 s for both M70-039 and M68-041 mean that the data cannot be used to determine the motion, if any, of the magnetic structure. The timing uncertainties in the data from M69-041 were <1 s.

Figure 5.17 shows the Map Potential Model (Ruohoniemi and Baker, 1998) output between 01:16 and 01:40 UT using data from the northern hemisphere SuperDARN radars to constrain the model. The model was calculated using an eighth order fit and a velocity threshold on the Hepner-Maynard boundary of 150 km s^{-1}. The vectors show the ionospheric plasma velocities determined by the model, with the colours indicating the speed of the flow, and the black lines show the electric potential. The vector in the top right-hand corner of each plot shows the IMF in the YZ plane lagged from the ACE
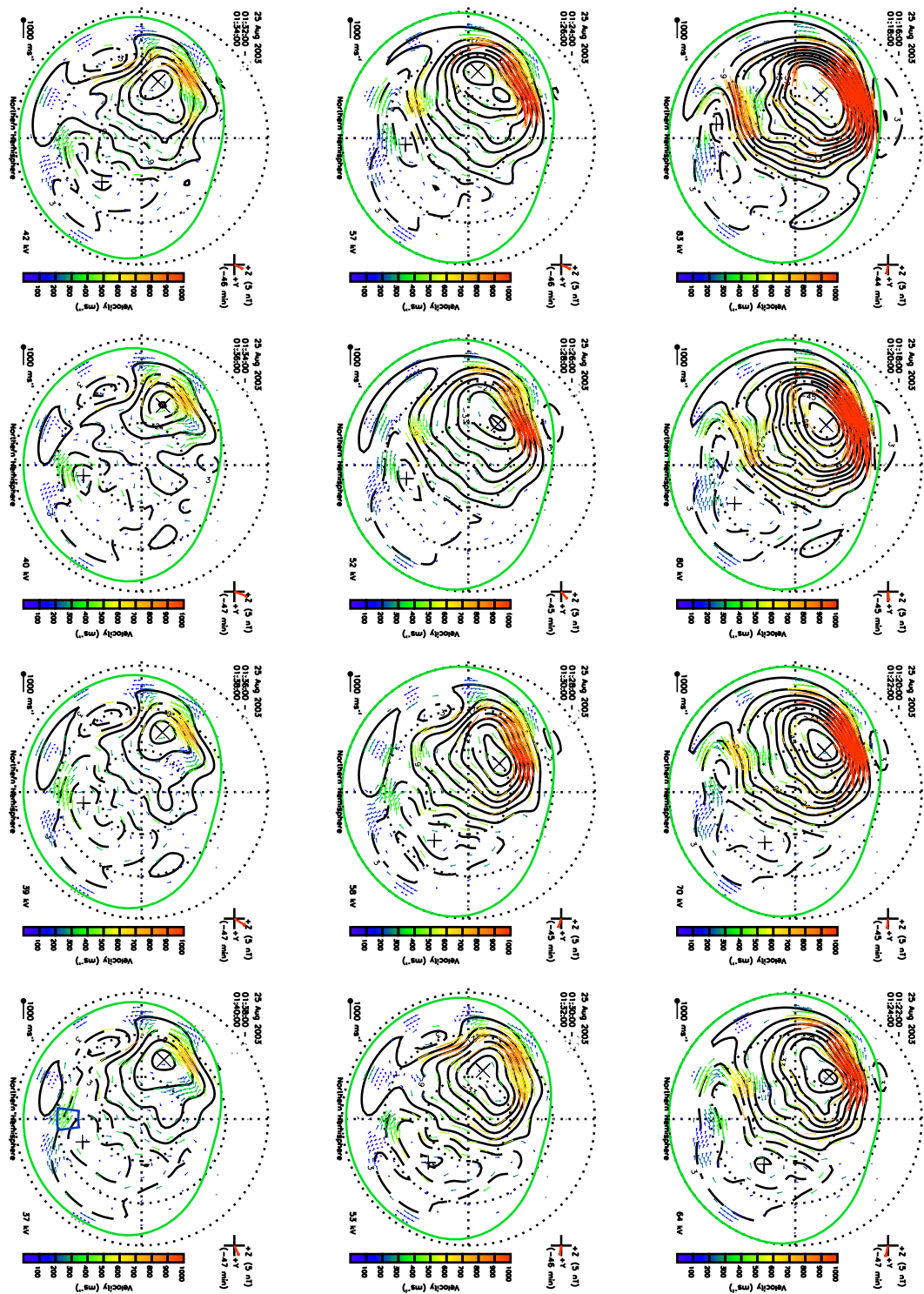
Figure 5.17: Outputs from the Map Potential Model between 01:16 and 01:40 UT. The coloured vectors show the modelled ionospheric velocities based on input from the SuperDARN radars, with the colours indicating speed (colour bar shown on the right-hand side). The black lines are contours of electric potential. The time of each plot is given in the left hand corner and the IMF in the YZ plane is shown in the right hand corner.
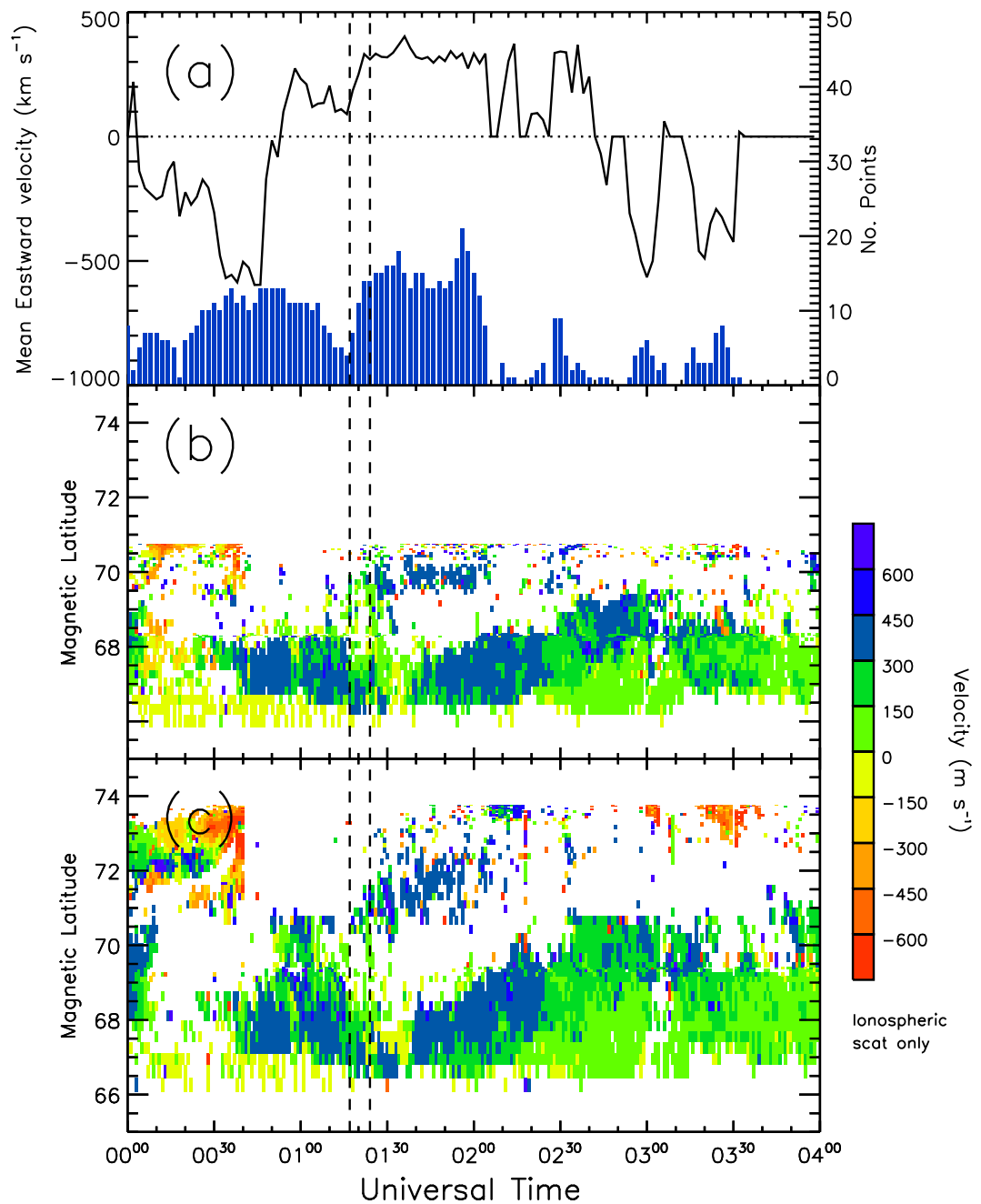
Figure 5.18: Plots of (a) the mean eastward velocity of the velocities vectors from the Map Potential Model constrained by radar data in the blue sector indicated in Fig. 5.17 and the line of sight velocity from beams (b) 2 and (c) 5 of the Stokkseyri coherent scatter radar. The dashed lines indicate the substorm expansion phase onset and the time at which Cluster detected the BBF.

spacecraft.

On the dayside, there is a clear region of fast flow in the post-noon sector, which slows and shrinks as the IMF turns northward, indicating that dayside reconnection was taking place for approximately 10 min following the substorm onset. At the time of the onset (01:17 UT), the dawn-side convection cell extended into the pre-midnight sector, with clear evidence of slow (>200 $\mathrm{km\,s^{-1}}$) return flows. In the post-midnight sector these are persistent throughout the interval shown. From 01:22 UT, there is a localised region of fast flow polewards of the slow return flows centred on the midnight meridian. These flows persist throughout the interval.

Figure 5.18a shows the mean eastwards velocity of the velocities vectors from the Map Potential Model constrained by radar data in a 1 hr MLT by 5° magnetic latitude sector centred on the midnight meridian and 72.5° magnetic latitude and shown as a blue box in the bottom right panel of Fig. 5.17. This box encompasses the majority of the fast flow vectors mentioned above. The blue bars in panels (a) show the number of points within the sector which have been constrained by radar data. The lower two panels in Fig. 5.18 shows the line-of-sight velocity along beams (b) 2 and (c) 5 of the Stokkseyri radar, whose field of view was over the midnight meridian during the interval in question. The dashed lines indicate the substorm onset and the detection of the BBF at Cluster.

Prior to 02:00 UT there were a fairly steady number of points within the sector that were constrained by data from the radars. At 00:50 UT, the velocity within the sector changed from westwards to eastwards, indicating that the dawnside convection cell extended into the pre-midnight sector, as seen in Fig. 5.17. At the substorm onset, the speed of the flows increases, reaching a maximum just before the detection of the BBF at Cluster, and remains elevated until 02:00 UT, at which time the number of points constrained by the radar decreases such as to make the mean velocity unreliable. The data from the Stokkseyri radar shows that at the time of the BBF detection at Cluster, fast flows began to develop polewards of 70° magnetic latitude, and lasting until 02:00 UT, when the scatter detected by the radar reduced in those magnetic latitudes.

5.3   Discussion

Previous studies of the ionospheric current systems associated with the passage of auroral streamers or BBFs have investigated the currents during various phases of substorm activity. Amm *et al.* (1999) investigated the current systems associated with an auroral streamer detected 14 min after an auroral breakup and found currents of $\sim$25 $\mathrm{A\,km^{-2}}$. Grocott *et al.* (2004), Sergeev *et al.* (2004a), and Nakamura *et al.* (2005a) investigated the current systems associated with BBFs during fairly quiet periods (potentially substorm growth phases) and found currents ranging from 0.2 to 7 $\mathrm{A\,km^{-2}}$. The range of these

current values (two orders of magnitude) suggests that substorm phase is important to the currents associated with a BBF.

5.3.1 Aurora and ground-based observations

In this study, the substorm expansion phase onset preceded the BBF observations. Southern hemisphere auroral data (Fig. 5.12), northern hemisphere magnetometer data (Fig. 5.14), and Cluster FGM data (Fig. 5.5) show that the substorm expansion phase onset occurred around 01:15 UT, indicated by an auroral breakup, the formation of an east-west current system accompanied by Pi2 band noise, and a large drop in the tail magnetic field. However, southern hemisphere magnetometer data from the BAS LPM chain indicates that an electrojet didn't form in the southern hemisphere until 01:25 UT. The timing discrepancy between the Greenland and BAS magnetometers is explained by estimating the position of the auroral breakup region in the northern hemisphere. Østgaard *et al.* (2004) empirically showed that the offset in location of auroral activity between hemispheres is related to the solar wind conditions. Using their results, the Greenland magnetometers were estimated to have been near the centre of the breakup region, whereas Fig. 5.12f shows the auroral breakup region was not over the BAS chain until 01:26 UT. The timing discrepancy between the formation of the electrojets in the northern and southern hemispheres ($\sim$600 s) is much larger than the timing error in the BAS LPM data ($\sim$180 s).

Data from the NIPR LPM chain showed magnetic signatures of auroral streamers, similar to, but weaker than, those reported by Amm *et al.* (1999). The observations of these signatures were centred at 01:24 UT and with a duration of $\sim$6-8 min. The magnetic field detected by these magnetometers before and during the substorm was highly variable, although by comparing the magnetometer and auroral data the magnetic signatures seen around 01:24 UT can be attributed to the BBF. Using the Tsyganenko T96 model and the velocity of the streamer determined from the auroral data this gives the BBF a width of $\sim$3-4 R_E. This agrees with the expected dawn-dusk spatial size of a BBF of 3-5 R_E (Angelopoulos *et al.*, 1997; Kauristie *et al.*, 2000; Nakamura *et al.*, 2001b). Integrating the ion velocity perpendicular to the field from Cluster 4 during the BBF encounter, and considering that Cluster is essentially stationary during that period (velocity of the order of 1 $\mathrm{km\,s^{-1}}$ since the spacecraft were near apogee), gives the size of the BBF as 2.3 R_E.

Data from the SuperDARN radars, in particular the radar at Stokksyeri, show that following the onset of the substorm a region of fast ionospheric flow developed across the midnight meridian in the northern hemisphere (Figs. 5.17 and 5.18). This region is somewhat similar to the regions of fast ionospheric flow associated with quiet time BBFs observed by Grocott *et al.* (2004, 2007). This was approximately 1-1.5 hr MLT eastwards of the footpoint of the Cluster spacecraft and the equivalent MLT of the auroral

streamer in the southern hemisphere. Using the correction of Østgaard *et al.* (2004), the displacement of the auroral streamer, and hence the associated ionospheric signatures, would have been ∼1.7 hr MLT westwards in the northern hemisphere and thus within the region of fast flow detected by the Stokkseryi radar. However, without supporting auroral images, it is impossible to discern whether or not these flows were truly associated with the BBF or were flows indicating tail reconnection directly associated with the substorm.

5.3.2 BBF observations

As discussed previously, the magnetic field magnitude data from Cluster indicates that the BBF encountered consisted of two flow bursts or "bubbles", as described in the model of Chen and Wolf (1993). During the BBF encounter, the B_X component of the magnetic field remained negative, although the gradient of the B_Y component of the field varied from negative to positive twice during the encounter. From Sergeev *et al.* (1996), this indicates that the spacecraft twice encountered the duskward then dawnward edge of an under-populated flux tube bundle. This is confirmed by both the MVAB analysis and four-spacecraft timing for the first flux tube bundle, showing that the orientation of the boundaries of the flux tube bundle was towards dusk and then dawn (Fig. 5.7). MVAB and four-spacecraft timing analysis indicates that as the Cluster spacecraft exited from the second flux tube through a boundary that was orientated towards dusk as opposed to dawn, although the boundary motion was still Earthwards. In this case, the spacecraft exited the flow tailwards of the widest point, such that the boundary of the flow was tapering back towards the flow centre (see Chen and Wolf, 1993, Fig. 5). The motion of the field-lines, as indicated by the ion velocity perpendicular to the field, was duskwards of the orientation of the boundary. Since the currents and magnetic field shear both suggest that Cluster passed through the flow bursts from the dusk side to the dawn side, this would indicate that the direction of travel of the BBF was not along its length. Figure 5.19 illustrates the relative motion of the Cluster spacecraft across the BBF in the XY plane south of the centre of the plasma sheet. The yellow arrow represents Earthward field-aligned currents whereas the grey arrow represents tailward field-aligned currents. Beneath the illustration is the expected form of the field-aligned currents detected by Cluster during its passage through the BBF, with positive field-aligned currents indicating tailward currents. This is consistent with the lateral current variation in the field aligned currents expected from the model of Chen and Wolf (1993) as shown by Sergeev *et al.* (1996). The various analysis methods used show that the flow bursts had significant velocity in the Z direction and that the orientation of the normals to flow boundaries were consistently towards the middle of the plasma sheet. This is consistent with highly stretched magnetic flux tubes convecting and contracting through the plasma sheet.

The event studied by Amm *et al.* (1999) had background conditions most similar to the event presented here (multiple substorms and streamer detected after an auro-
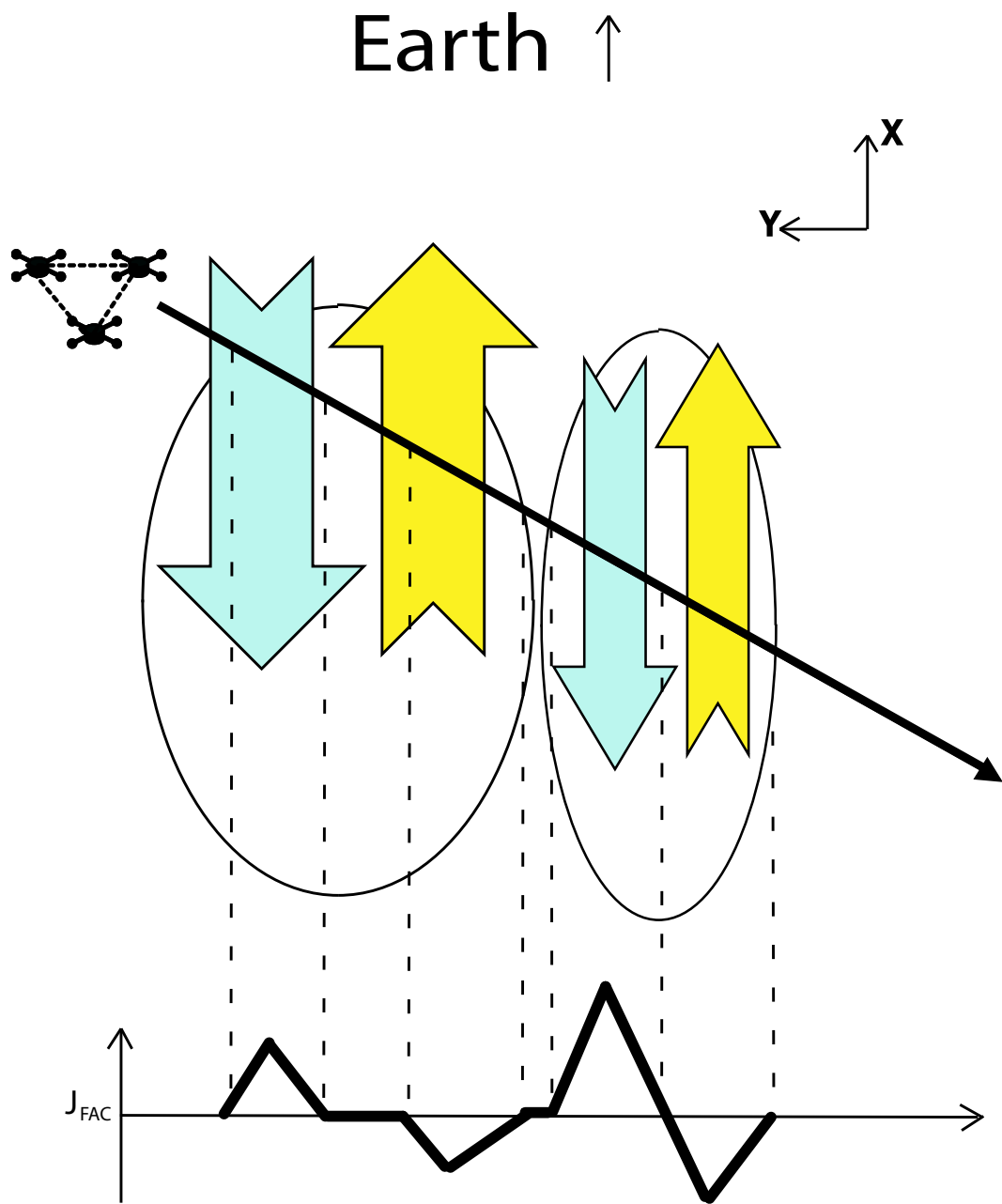
Figure 5.19: Diagram illustrating the relative motion of the Cluster spacecraft across the BBF, looking down on the BBF in the XY plane from the current sheet (i.e. into the southern magnetosphere). The BBF consists of two flow bursts. Field-aligned currents associated with the BBF are shown as yellow (Earthward) and blue (tailward) arrows. In both flow burst encounters, the Cluster spacecraft entered the flow burst on the duskward side, close to the nose of the flow, then traversed through to the dawnwards side of the flow burst. The graph indicates the field-aligned currents detected by the spacecraft during their encounter with the each flow burst.

ral breakup) and, correspondingly, showed very similar field-aligned ionospheric currents (25 A km^{-2} compared with 18 A km^{-2} detected in our event). The ground magnetic field data presented by Amm *et al.* (1999) shows a far stronger eastward component signature associated with the passage of the auroral streamer for a comparatively small change in current.

The event studied by Grocott *et al.* (2004) occurred during a relatively quiet time, with no apparent substorm activity and was associated with ionospheric currents of ~ 0.2 A km^{-2}. The authors compared their ionospheric data with data from FUV-WIC and found that their current system coincided with an auroral enhancement which had a brightness approximately an order of magnitude lower than the brightness of the streamer presented here. Cowley and Bunce (2001) showed that the energy flux into the ionosphere due to field-aligned currents driven by a field-parallel voltage, such as those that cause the aurora, is related to the square of the field-aligned current, based on the theory of Knight (1973) and Lundin and Sandahl (1978). Assuming that, at the energies involved in the currents under discussion, the auroral luminosity is directly related to the energy flux of the electrons then the results of Grocott *et al.* (2004) are quantitatively consistent with the results presented here.

The field reversals in the B_X and B_Z directions suggests that, after the passage of the BBF, Cluster crossed a current sheet. This is in agreement with the currents determined by the curlometer method (Fig. 5.8), which shows strong currents detected in the YZ plane. Comparison of the magnetic fields across the four Cluster spacecraft shows that the magnetic signature was "nested" such that the current sheet moved across the spacecraft then returned, or that the spacecraft encountered a convecting feature into which they penetrated to differing depths. The magnetic field components during the encounter with this current sheet were not sufficiently ordered to allow for meaningful determination of the direction of the motion of the current sheet. Sergeev *et al.* (1996) showed that the model of Chen and Wolf (1993) predicted that flux tubes in front of a plasma bubble would be displaced by its passage. Sergeev *et al.* (1996) considered the case of a bubble where the normal to the edge of the bubble was in the XY plane to demonstrate that there would be a front-side shear. It is, therefore, conceivable that if the bubble was tilted about the X-axis, such that the normal to its edge on the duskward and dawnward flanks had some Z component, that plasma would be displaced in the Z direction also. After the bubble's passage, the displaced plasma would recoil back towards its original position since the bubble causes no persistent dipolarisation of the field, as shown by Lyons *et al.* (1999). If the current sheet is displaced by this travelling feature and recoils after its passage, the current sheet may overshoot its former position. This could explain why Cluster briefly detects the current sheet and may also be an indication of neutral sheet wave generation.

5.3.3 Reconnection as BBF generation mechanism

The origins of BBFs are not yet understood, although they have often been associated with reconnection processes (e.g. Chen and Wolf, 1993; Birn *et al.*, 1999; Sitnov *et al.*, 2005). Based on the simple model of plasma sheet acceleration, as discussed in Cowley (1984), BBF creation by reconnection is considered. In this model it is initially assumed that the magnetosphere is under-going Dungey Cycle convection (Dungey, 1961) such that there is a reconnection X-line in the far tail. Furthermore, it is assumed that substorm expansion phase conditions are created by the reconnection of open magnetic flux in the tail by a near-Earth neutral line (NENL) reconnection X-line (Baker *et al.*, 1996, and references therein). In this simple model, the rate of reconnection (E_Y), the B_Z component of the magnetic field across the current sheet and the velocity of the reconnected field-lines (de Hoffmann-Teller velocity, V_{HT}, de Hoffmann and Teller (1950)) are related by

$$E_Y = B_Z.V_{HT} \tag{5.1}$$

where, for stress balance, V_{HT} is equal to the Alfvén speed of the lobe plasma at the reconnection site less the speed of the lobe plasma at the reconnection site (see Chapter 1). Plasma flows into the reconnection site at the $\mathbf{E} \times \mathbf{B}$ velocity from both the northern and southern lobes and flows out at the velocity of the Earthward (V_{BE}) and tailward (V_{BT}) beams, found by coordinate transformation to be

$$V_{BE} = 2V_A - V_L \equiv V_{HT} + V_A \tag{5.2}$$

where V_A is the Alfvén speed of the lobe plasma and V_L is the lobe plasma speed. Considering that BBFs show increased ion velocity and B_Z component then it is apparent, from Equations 5.1 and 5.2, that the creation of BBFs requires an increased rate of reconnection (assuming V_A is fixed for a given location in the lobe under the timescales being considered). BBFs can show a decreased plasma density (e.g. Lyons *et al.*, 1999; Nakamura *et al.*, 2005a), as in the case presented here. From the model of Cowley (1984), it can be shown that plasma density on the newly reconnected field-lines is equal to the density in the lobe source region. As such, in order to create a low density fast flow, the density of the lobe plasma at the source of the flow must be lower than that of the surrounding compressed central plasma sheet. One possibility is that density perturbations within the lobe plasma are coupled with an increased rate of reconnection at the tail X-line, although the mechanisms for creating the density perturbations in the lobes that would necessarily also cause an increase in the reconnection rate upon the field-line reaching the plasma sheet are unclear. Another possibility is that a burst of reconnection occurs closer to the Earth than the global X-line or alternatively, a part of the X-line, localised in the Y direction, moves Earthward. Since lobe plasma density increases with increasing tailward distance, the site of the bursty reconnection would create a low density injection into the plasma sheet if the X-line reconnects through to the open field-lines of

the lobe. The reconnected field-lines associated with the low density injection, i.e. the BBF, will necessarily have a higher de Hoffmann-Teller velocity than those reconnected at the substorm X-line since the de Hoffmann-Teller velocity is equal to the Alfvén speed of the lobe plasma being reconnected and Alfvén velocity is inversely proportional to the plasma density. As such, the BBF will convect through the plasma sheet. What is unclear, from the data presented, is the evolution of the BBF X-line. CIS instrument data shows that the ion density and velocity returns to pre-BBF values over ~ 1.5 min after the velocity in the X direction reaches its maximum. However, analysis of the flow boundaries indicates that Cluster does not pass along the whole length of the flow, rather it exits through the side, such that Cluster does not observe the full evolution of the flow.

Figure 5.20 shows a series of diagrams depicting the proposed evolution of the plasma sheet during this event. For reference, Fig. 5.20a shows a model of the variation of the lobe density with distance downtail based on Cowley (1984). Initially, the plasma sheet is thin and being populated by the Dungey cycle X-line (Fig. 5.20b) and Cluster is in southern tail lobe. At some (undetermined) time, a new X-line formed Earthwards of the Dungey cycle X-line. This X-line reconnects the closed field-lines of the plasma sheet and then begins to reconnect the open field-lines of the lobe. This is the substorm expansion phase onset, leading to the expansion phase signatures noted above. After this onset, the plasma sheet expands so as to engulf Cluster (Fig. 5.20c). At some later time (also undetermined), a third X-line forms in the central plasma sheet, Earthward of the substorm X-line. The rate of reconnection at this new X-line is higher than that of the substorm X-line, such that the X-line reconnects through the closed field-lines and eventually reconnects the open field-lines of the lobes. This X-line injects plasma from the lobes Earthwards of the substorm line (Fig. 5.20e), such that the ion density on these field-lines is lower than the surrounding field-lines. Since the Alfvén speed of the plasma is inversely related to the plasma density, the speed of the field-lines away from the reconnection site is higher, hence the field-lines convect through the plasma sheet as a BBF. As noted above, the data presented are insufficient to determine the full evolution of the new X-line. For illustrative purposes, the BBF is shown as a convecting bundle of flux that is no longer being fed by the X-line that created it (Fig. 5.20f and g), with the X-line retreating downtail in a manner similar to the substorm recovery phase (e.g. Hones (1984)).

The above model considers the origins of a BBF to be reconnection of open field-lines. This agrees with the work of Lyons *et al.* (1999),Nakamura *et al.* (2001b) and Grocott *et al.* (2004) who associated BBFs with pseudo-breakups, which are often considered to be the localised closure of open flux. If substorm reconnection is considered to take place at a single X-line, as in the NENL and current disruption models, and the creation of a BBF to occur Earthwards of that line then such a burst of reconnection would create a flux rope Earthwards of the substorm reconnection site as shown in Fig. 5.20e. The substorm X-line creates a flux rope between itself and the downtail (Dungey cycle) X-line, hence there would be two flux ropes in the tail. It has been suggested that the
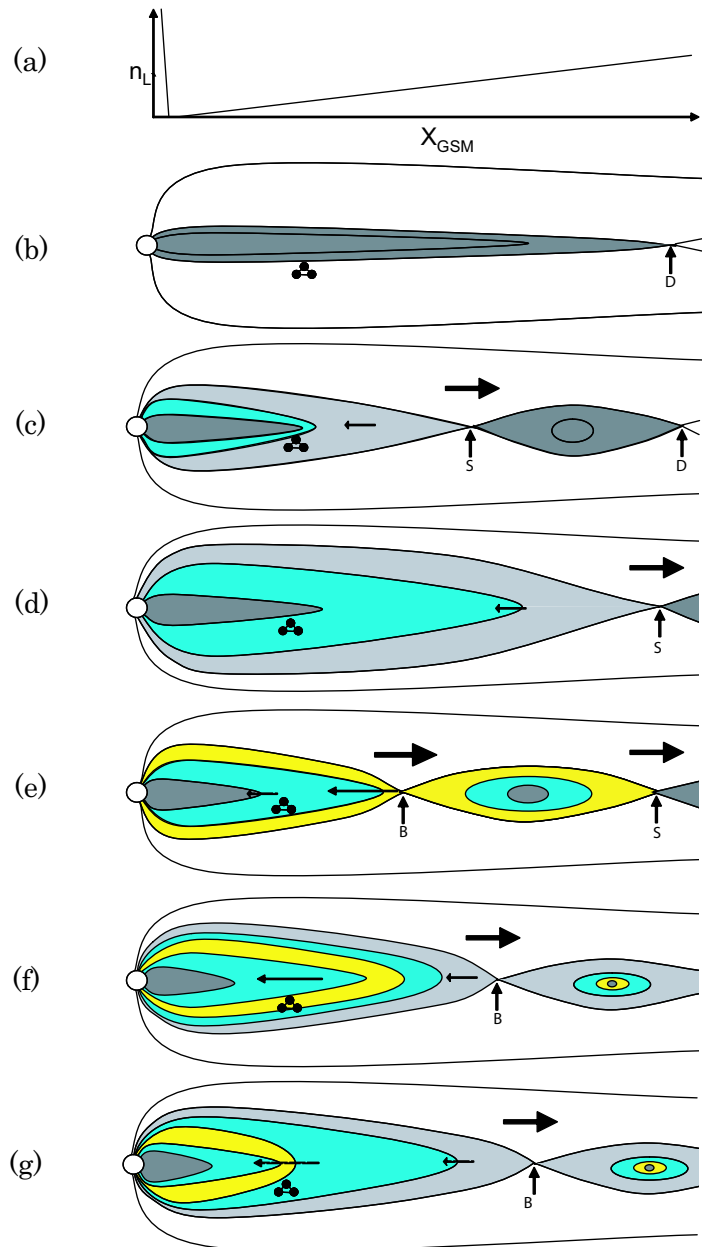
Figure 5.20: A series of diagrams depicting the generation of a BBF by open field-line reconnection. The colours represent field-lines with different ion densities. Tailward pointing arrows indicate the motion of the X-lines and Earthward pointing arrows indicate the motion of the reconnected field-lines. Panel (a) shows the variation of the plasma density in the lobes based on Cowley (1984). Initially the plasma sheet is thin and being populated by the Dungey cycle reconnection X-line (panel (b)), with Cluster (represented by the triangle) in the lobe. A substorm X-line forms Earthwards of the Dungey cycle X-line and reconnects through the closed field-lines, forming a plasmoid between itself and the Dungey cycle X-line. When the substorm X-line begins to reconnect lobe field-lines, the plasmoid is disconnected from the Earth and the plasmoid and substorm X-line retreat tailward. The plasma sheet then expands and the Cluster spacecraft are engulfed by the PSBL populated by the substorm X-line (panel (c)). As the substorm X-line retreats further downtail and the plasma sheet continues to expand, the Cluster spacecraft are engulfed by the central plasma sheet (panel (d)). A new X-line, localised in the Y direction) forms Earthward of the substorm X-line. This reconnects through the closed field-lines, creating a plasmoid between itself and the substorm X-line, and begins to reconnect lobe field-lines. This injects lower density lobe plasma into the plasma sheet and creates a BBF (yellow) (panel (e)). The injected plasma then convects through the plasma sheet as a BBF (panels (f) and (g))

passage of multiple flux ropes is a signature of multiple X-line reconnection (e.g. Slavin *et al.*, 2005), hence the detection of BBFs during substorms could also be considered to be a signature of multiple X-lines. Alternatively, the generation of a BBF could be considered to show that substorm reconnection does not occur on one "global" X-line, but on a series of X-lines separated in the Y direction, such as has been suggested for flux transfer events at the dayside magnetopause. A BBF could be generated by an X-line markedly Earthwards of the average position of the substorm X-lines. The model is also applicable to "quiet" time observations of BBFs. It is generally accepted that Dungey Cycle reconnection in the tail is ongoing. As such, any reconnection Earthwards of the Dungey Cycle X-line would inject low density plasma into the plasma sheet. A recent study by Grocott *et al.* (2007) has provided evidence of localised tail reconnection during quiet times, termed tail reconnection during IMF northward non-substorm intervals, or TRINNI, and the detection of an associated BBF, hence reconnection is a viable method by which to inject BBFs into the plasma sheet during both quiet and disturbed times. It should be noted that this model does not consider the evolution of the motion of the BBF through the substorm populated plasma sheet and is complementary to the model of Chen and Wolf (1993), who only considered the time evolution of a plasma bubble after its generation and not the generation mechanism itself.

Particle data from the CIS and PEACE instruments during the BBF are consistent with the above reconnection model. During reconnection, both ions and electrons are energised in the field-aligned direction. The velocity of the electrons away from the reconnection site is greater than that of the ions, hence electrons will mirror in the inner magnetosphere and return along the field-lines before the ions such that bidirectional electron beams form before bidirectional ion beams. During this event, bidirectional ion and electron beams are observed by Cluster when it passes into the PSBL at 01:15 UT (Fig. 5.9a and b and Fig. 5.11). During the encounter with the BBF at 01:24 UT, Cluster observed bidirectional electron and ion beams, although the Earthward ion beam had a greater differential number flux than the tailward beam (Fig. 5.9c and Fig. 5.11), suggesting that the spacecraft were sufficiently close to the reconnection site that the majority of the ion population had insufficient time to mirror in the inner magnetosphere and return to the spacecraft position, such that the BBF consisted of recently reconnected field-lines. Cluster detected a dispersed ion energy signature when the spacecraft crossed the PSBL (Fig. 5.10a), confirming that the PSBL was the result of reconnection. During the BBF encounter, the ions were energised to a level similar to that in the PSBL, although there was no apparent energy dispersion. Given that estimates of the width of the BBF from ground-based data and from integrating the ion velocity perpendicular to the magnetic field during the BBF encounter are ~ 3 R_E and BBFs are considered to be long and narrow (Sergeev *et al.*, 2000; Amm and Kauristie, 2002), and that the spacecraft crossed the width of the BBF, it is conceivable that the spacecraft did not travel far enough along the BBF to detect any energy dispersion. The similarity between the ion density during the passage of the BBF and the earlier PSBL crossing (Fig. 5.5a) suggests that the BBF

reconnection site was close to the location of the substorm X-line location when Cluster was engulfed by the PSBL.

5.4   Summary

On the 25 August 2003, the Cluster spacecraft detected a substorm expansion phase at 01:15 UT, indicated by a drop in the total magnetic field. At 01:24 UT, during the substorm expansion phase, the Cluster spacecraft encountered a bursty bulk flow consisting of two under-populated flux tube bundles travelling Earthward and duskward at $\sim$500 km s^{-1}. At the same time, an auroral streamer was seen in FUV-WIC data of the southern hemisphere close to the footpoint of the Cluster spacecraft. Field-aligned currents of $\sim$5$\times$ 10^{-3} A km^{-2} flowing in the BBF were measured using the curlometer technique. These currents were initially tailward and then became Earthward for each flux tube bundle. Four-spacecraft timing analysis and MVAB, combined with the magnetic field shears, at the flux tube bundle boundaries showed that Cluster entered the flux tube bundles on the duskward and exited on the dawnward side.

The observations show that the curlometer technique can be used to obtain the currents within BBFs and that these currents are consistent with previous investigations. The current system observed exhibited a bipolar field-aligned current system as had previously been predicted by Sergeev *et al.* (1996). Furthermore, the currents and auroral signatures observed were consistent with Grocott *et al.* (2004) (after the application of the theory of Knight (1973)) and, as such, the observations show that there is a quantitative link between BBFs and auroral streamers.

The observations are consistent with a model of the reconnection of open field-lines Earthward of the substorm reconnection region for BBF generation based upon the plasma sheet acceleration model of Cowley (1984). The pitch angle distribution of the ions from the CIS instrument on Cluster 4 showed that during the passage of the BBF the ions were approximately field-aligned in an Earthwards direction, whereas the electrons showed bidirectional beams, indicating that Cluster encountered recently reconnected field-lines. The elevated B_Z component indicates that the reconnection event that generated the BBF had a greater rate of reconnection than the source of the plasma sheet detected around the flow. Since the lobe plasma density increases with distance from the Earth, reconnection of open (lobe) field-lines closer to the Earth than the substorm X-line would inject lower density plasma into the plasma sheet. This is also consistent with the notion that pseudo-breakups are BBFs outside of substorm times.

Chapter 6

Statistical study of bursty bulk flow current systems

In this study, data is employed from the first four Cluster tail seasons to quantitatively investigate the current systems associated with BBFs. Using the curlometer technique I determine the BBF currents encountered by Cluster. The spatial distribution of these currents and their relationship with substorm phase, determined from auroral indices is then considered.

Data are employed from the Cluster FluxGate Magnetometer (FGM; Balogh *et al.*, 2001) and the Cluster Ion Spectrometer (CIS; Rème *et al.*, 2001). Data from CIS refers to proton moments from the CIS CODIF sensor. Due to a degradation of the CIS instrument on Cluster 3 that has lead to an inaccuracy of the determination of V_Z, and the failure of the CIS instrument on Cluster 2, CIS moments are restricted to those from Cluster 1 and Cluster 4. FGM data from all four spacecraft are used. Spin resolution data from these instruments are used to identify BBFs. FGM data sampled at 5 Hz are then used to determine the current systems of the BBFs by the curlometer technique (Dunlop *et al.*, 1988; Robert *et al.*, 1998).

A number of previous studies have correlated BBF occurrence rates with the AE index (Angelopoulos *et al.*, 1994; Cao *et al.*, 2006). I continue in this vein, so as to compare the results with these studies. However, rather than pre-defining a lower limit on active times, similar to Cao *et al.* (2006), I determine substorm phases from the data.

The following describes the identification and surveying methods used in this study, including a case study to demonstrate the results. I then describe the basic statistics of the dataset, before investigating the statistics of the BBF current systems.

6.1 Identification

Previous investigations have used various methods to identify BBFs. Some of these have previously been summarised by Cao *et al.* (2006). Angelopoulos *et al.* (1994) defined the inner plasmA sheet (IPS) as the region in which the plasmA beta due to the ions, β_i, is greater than 0.5 and the outer plasmA sheet as the region where β_i <0.5. BBFs were then defined as any continuous ion flow when the ion velocity V_i >100 km s^{-1} with V_i >400 km s^{-1} and β_i >0.5 for at least one sample. Raj *et al.* (2002) emphasised the convective nature of BBFs, choosing that the ion flow speed perpendicular to the magnetic field, V_{perp}, >250 km s^{-1} and β_{XY} >2, where β_{XY} is the plasmA beta calculated using B_X and B_Y. In their case study, Forsyth *et al.* (2008a) used a lower limit of V_{perp} to 300 km s^{-1} instead of 100 km s^{-1} along with the variability of the plasmA density and the magnetic field to define a BBF encounter and separate two flow bursts.

In this investigation, I adapt the limits of Forsyth *et al.* (2008a). Firstly, high speed flows are identified as events during which $V_{perp} > 400$ km s^{-1} and $\beta > 0.5$ for at least 2 data points in 1 min. The limits of the flow burst are then defined as the times at which V_{perp} drops below 200 km s^{-1}, 100 km s^{-1} below the limit of Forsyth *et al.* (2008a). Also, in order to avoid surveying the magnetosheath, the survey is restricted to days-of-year 200-300 and to X_{GSM} <-10 R$_E$, $|Y_{GSM}|$ <10 R$_E$ and $|Z_{GSM}|$ <5 R$_E$. In order to avoid detecting the tail current sheet, a subset of events is defined during which the B_X was positive or negative at all Cluster spacecraft throughout the BBF, hereafter referred to as the current sheet criterion. Lastly, any events during which $B_Z < 0$ nT on any of the spacecraft were rejected to avoid complications associated with flux ropes and plasmoids.

Previous studies of BBFs have shown an increasing relative occurrence of BBFs with increasing AE index (Angelopoulos *et al.*, 1994). Although AE can give an indication of the strength of the ionospheric currents at any time, individual values cannot determine substorm phase. In this study, time series of AU and AL are used to identify substorm phase, splitting the substorm into four categories; growth phase (phase 1), expansion phase (phase 2), recovery phase (phase 3) and miscellaneous or indeterminate phase (phase 0). The growth phase is identified by an increase in AU and a steady or slowly decreasing AL caused by driven-ionospheric convection due to dayside reconnection prior to an expansion phase. The expansion phase is identified by a rapid decrease in AL caused by the formation of auroral electrojets. The recovery phase is identified as the period following the minimum in AL in which AL returns to a fairly steady value or a subsequent expansion phase is detected. Phase 0 is any time when the phase of the substorm is indeterminate or there is no apparent substorm activity. It should be noted that Phase 0 events may in fact be growth phase events with little or no ground signature.

A further "phase" (phase 4) is defined as any periods during which AL is depressed to values under -100 nT over a period of more than 1 hr and then remains low for an
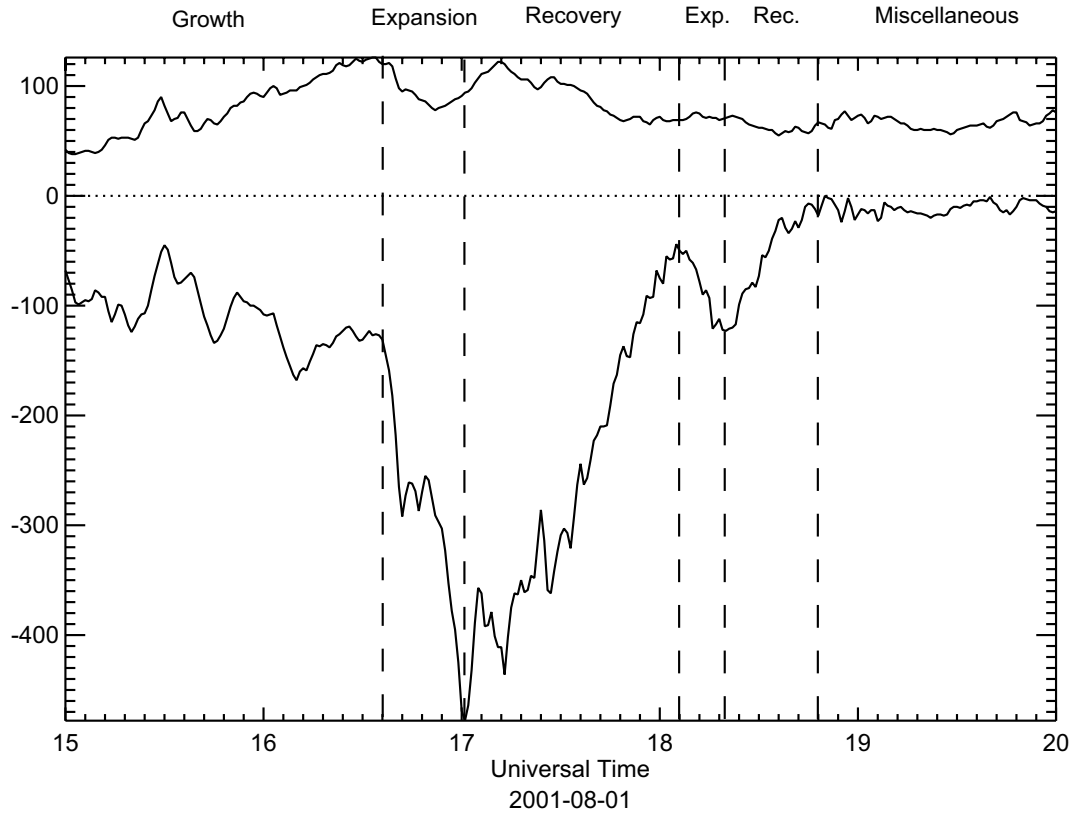
Figure 6.1: Diagram indicating the identification of various substorm phases using the AL and AU auroral indices.

extended period, indicating prolonged strong ionospheric currents. A comparison with the Dst index shows that these times coincide with storm activity. It should be noted that storm-time substorms which exhibit the signatures as above are classed using Phases 1-3.

6.1.1 An example event

In order to demonstrate the identification techniques and the data employed in this study, a brief case study of a BBF detected on 17th September 2001 is presented. Figure 6.2 shows data from the Cluster spacecraft between 12:48 and 13:11 UT and the AU and AL indices for the whole day. Panel (a) shows the B_X component of the magnetic field detected by the four Cluster spacecraft (Cluster 1: black, Cluster 2: red, Cluster 3: green, Cluster 4: blue) and Panel (b) shows the latitude angle of the magnetic field (the angle between the field in the Z direction and the field in the XY plane). Panel (c) shows the ion velocity perpendicular to the magnetic field from Cluster 1 (calculated as $\mathbf{b} \times \mathbf{V} \times \mathbf{b}$ where $\mathbf{b}$ is the direction of the magnetic field) in the X (black), Y (red) and Z (blue) directions, Panel (d) shows the ion density and Panel (e) shows the plasmA beta from Cluster 1. Panels (f)-(h) show the results of the curlometer. Panel (f) shows the j_X (black), j_Y (red) and j_Z (blue) components of the current. Panel (g) shows the field aligned current and Panel (h) shows $|div\mathbf{B}|/|curl\mathbf{B}|$. The dashed vertical lines indicate the start and end of
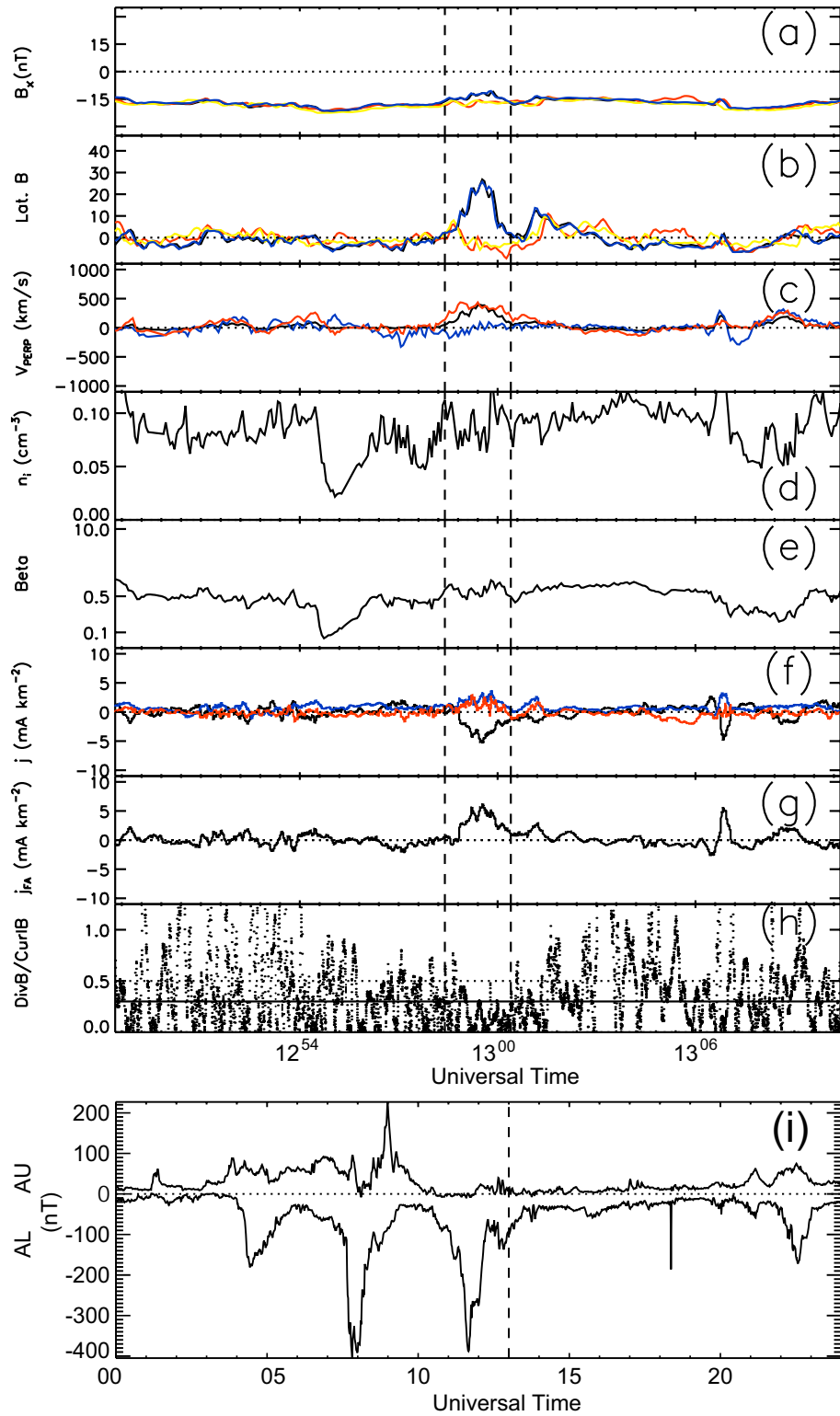
Figure 6.2: Plot of data from the Cluster spacecraft between 1248 and 1311 UT and auroral indices from 17th September 2001. Panels (a) and (b) show B_X and the magnetic field latitude angle from Cluster (Cluster 1: black, Cluster 2: red, Cluster 3: green, Cluster 4: blue). Panel (c) shows the ion velocity perpendicular to the magnetic field from Cluster 1 in the X (black), Y (red) and Z (blue) directions. Panels (d) and (e) show the ion density and plasmA β respectively. Panels (f)-(h) show results of the curlometer with the currents in X (black), Y (red) and Z(blue) directions in panel (f), the field-aligned current in panel (g) and $|div\mathbf{B}|/|curl\mathbf{B}|$ in panel (h). The dotted lines represent zero values. The dashed lines in panels (e) and (h) indicate a value of 0.5. The solid horizontal line in panel (h) indicates a value of 0.3. The dashed vertical lines indicate the start and end of the BBF. Panel (i) shows the AU and AL indices between 0000 and 2400 UT.

the BBF.

The BBF signature can be clearly seen as an increase in the perpendicular ion velocity at Cluster 1 between 1258 and 1301 UT (panel (c)), accompanied by a decrease in B_X and an increase the latitude angle (panels (a) and (b)). This magnetic signature is also seen in the Cluster 4 data, although it is not apparent in the data from Cluster 2 and 3, indicating that Cluster 1 and 4 passed into the BBF whereas Cluster 2 and 3 did not. During the interval, the plasmA density and plasmA β remained fairly constant, apart from small decreases between 1254 and 1256 UT. Taking $\beta > 0.5$ to indicate that Cluster was in the plasmA sheet, after Angelopoulos *et al.* (1992), it can be seen that Cluster 1 was in the plasmA sheet during the BBF encounter and for the following 5 minutes, although the spacecraft was evidently close to the edge of the plasmA sheet given the plasmA β varies about 0.5 throughout.

Throughout the interval the current magnitudes were low (~ 1 mA/km^2, panel (f)). During the BBF encounter, currents in all directions were enhanced, with j_X becoming dominant. This is reflected in the increase in field-aligned current, which reaches 5 mA/km^2 during the BBF encounter. During this time, $|div\mathbf{B}|/|curl\mathbf{B}|$ was low (< 0.1), indicating that the currents determined were reliable. Although only two of the Cluster spacecraft passed through the BBF, the determination of the field aligned current was good since the field aligned current is required to support the shear in the magnetic field between the more dipolar BBF field lines and the surrounding field lines.

Two further high-speed flows were observed between 1305 and 1310 UT, also accompanied by an increase in the latitude angle and field-aligned current. However, these are excluded from the survey as the plasmA β during these flows was below the 0.5 threshold.

Figure 6.2i shows the AU and AL indices for 17th September 2001. These indices show that the day was very disturbed, with four large events ($AL > 200$ nT) and five smaller events. The BBF occurred during the recovery phase of one of the smaller events, indicated by the dashed line, which was an enhancement following a much larger event between 1100 and 1200 UT.

6.2   Statistics of the dataset

Using the plasmA beta and velocity conditions described, 1804 flow burst events were identified between days 200 and 300 in the years 2001 to 2004. Table 6.1 shows the number of BBFs detected by each Cluster spacecraft during each year (noting that CIS on Cluster 2 is inoperative). It is apparent that in 2002 and 2004 Cluster 3 observed many more flow bursts than either Cluster 1 or 4, whose numbers of observed flow bursts were comparable for all years. Due to a degradation of the CIS-CODIF detector on

Cluster	2001	2002	2003	2004
Separation (km)	2000	3700	200	1000
C1	55(10)	58(9)	102(39)	92(40)
C3	53	556	226	341
C4	51(11)	78(20)	95(41)	97(41)

Table 6.1: Table of flow bursts detected by each of the Cluster spacecraft in the years 2001 to 2004 using the plasmA beta and plasmA velocity conditions given. The numbers in the brackets show the number of flow bursts detected when the current sheet criterion was applied.

Phase	Time (hours)	Percentage of total
Phase 0	100.8	21
Growth	82.6	17
Expansion	62.4	13
Recovery	129.6	27
Storm	110.4	23

Table 6.2: Cumulative lengths of the various substorm phases from the days in 2001 in which Cluster detected BBFs.

Cluster 3, the calculated plasmA moments have reduced accuracy in V_Z. This increased uncertainty in the plasmA velocity, which is key to the selection criteria, means that the BBF identifications from Cluster 3 cannot be relied upon. As such, I concentrate on the 628 flow bursts detected by Cluster 1 and 4. The bracketed numbers in Table 6.1 shows the number of BBFs detected by Cluster 1 and 4 during each year using the conditions described, including the current sheet crossing criterion. Cluster 1 and Cluster 4 observed similar numbers of flow bursts each year, with 2002 showing the largest difference between the two spacecraft. The numbers of flow bursts detected away from the current sheet were significantly higher during 2003 and 2004 compared with 2001 and 2002. Brown *et al.* (2008) noted that during 2001 and 2002, data coverage from the Cluster spacecraft was not over the entire orbit. Data was returned from approximately 50% of each orbit. This accounts for the lower detection rates during these years.

The occurrence frequencies of all the flow bursts and for those flow bursts meeting the current sheet criterion in different substorm phases are shown in Fig. 6.3. The total occurrence rate for both spacecraft is shown as the blue bars and the occurrence rates for the individual years are shown as coloured lines. Panels (a) and (b) show occurrence rates for Cluster 1 and panels (c) and (d) show the same for Cluster 4. Panels (a) and (c) show the results for all of the detected BBFs and panels (b) and (d) show the results for those BBFs that met the current sheet criterion.

The majority of BBFS detected by Cluster were detected during the recovery phase, followed by the expansion phase, phase 0 and the growth phases. However, growth phase events may be included in the phase 0 events (periods when there was no obvious substorm activity) since weak growth phases with no discernible AU/AL signature would have classed as phase 0. From the days in 2001 when Cluster encountered BBFs, the total
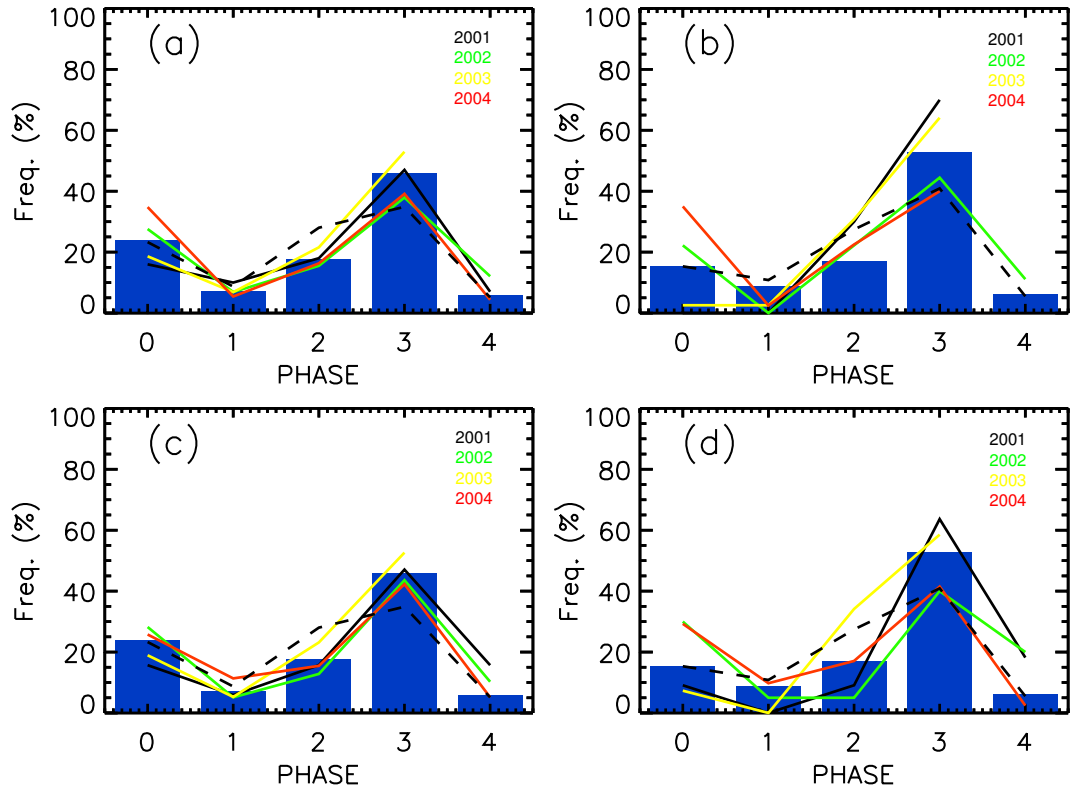
Figure 6.3: Histograms of flow burst occurrence rate against substorm phase for Cluster 1 (panels (a) and (b)) and Cluster 4 (panels (c) and (d)). Panels (a) and (c) show the results from all the flow bursts detected in the survey, whereas panels (b) and (d) show the results from those flow bursts in which the Cluster spacecraft did not cross the central current sheet. The blue bars show the total occurrence rates from both spacecraft, whereas the coloured lines show the occurrence rate for the labelled spacecraft. Black represents 2001, green represents 2002, yellow represents 2003, red represents 2004. The dashed line represents the total occurrence rate multiplied by ratio of expansion phase length to phase length.

time the magnetosphere spent in each phase was determined. These times are shown in Table 6.2, along with the percentage of the total time that the magnetosphere was in each phase. Using these times, the occurrence rate is normalised with respect to the length of the recovery phase(e.g. for a phase that is half as long as the recovery phase, the relative occurrence rate is twice the actual occurrence rate). The dashed lines in Fig. 6.3 shows the relative occurrences. The relative flow burst occurrence was highest in the recovery phase, although it is more comparable with the expansion phase than if the duration of the phases is not taken into account. Combining the phase 0 and growth phase events makes the relative occurrence rate of events in the growth phase larger than in the expansion phase.

Comparison of the occurrence frequencies of the various phases between the two Cluster spacecraft and between the whole dataset and the subset defined by the current sheet criterion shows that the occurrence rates were similar between spacecraft and between the full dataset and the subset. As such, the current sheet criterion does not appear to bias the results in favour of any particular phase.

The spatial distributions of the BBFs detected by Cluster 1 and 4 are shown in Fig. 6.4. Panels (a), (c) and (e) show the distribution in the YX, YZ and XZ planes, whereas panels
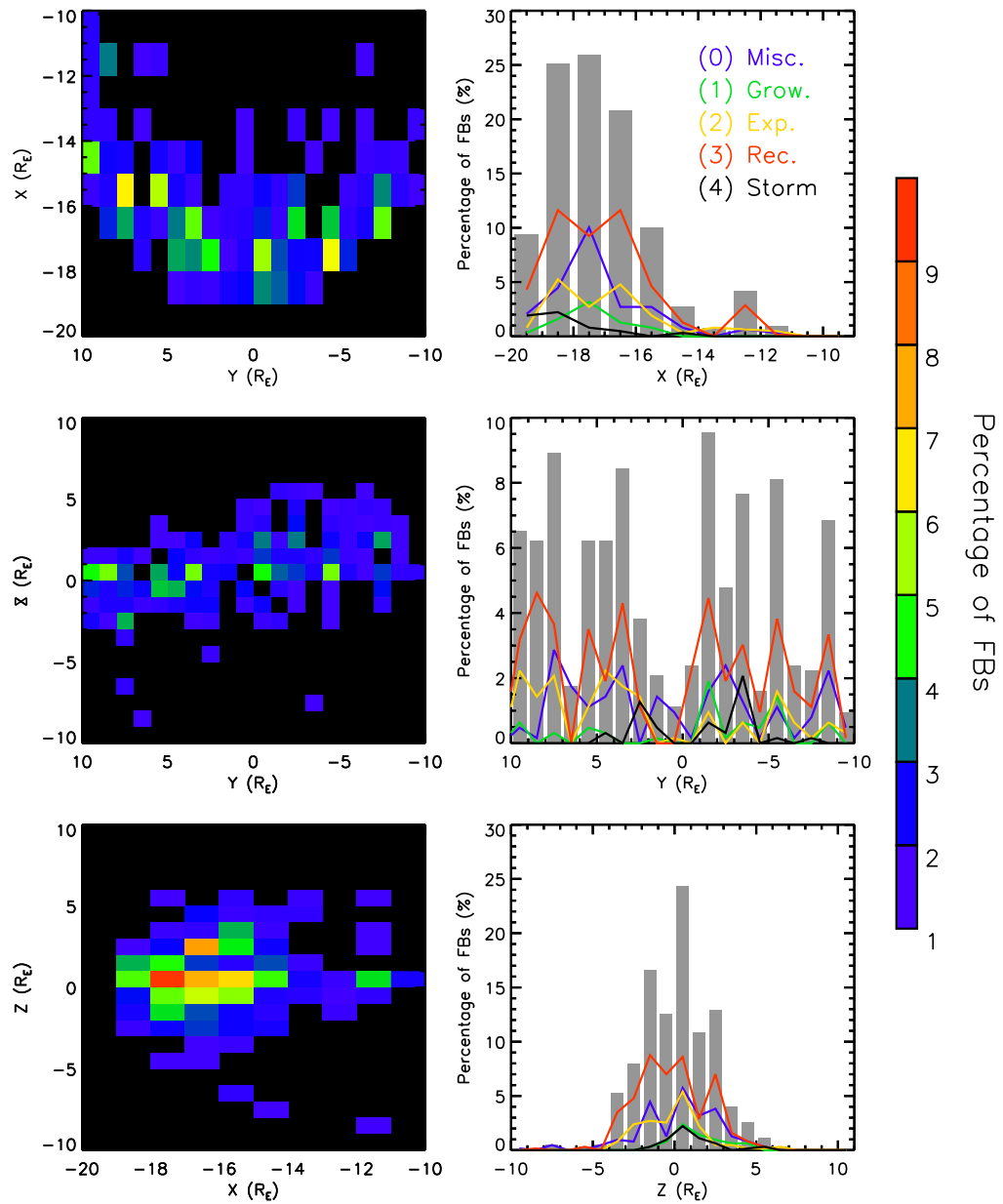
Figure 6.4: Plots of the spatial distribution of all of the BBF events detected by Cluster 1 and 4. Panels (a), (c) and (e) show the distributions in the YX, YZ and XZ planes respectively. Panels (b), (d) and (f) show histograms of the distribution in the X, Y and Z directions respectively. The bars show the distribution of all of the BBFs, whereas the lines show the distributions of the BBFs in the five defined phases.

(b), (d) and (f) show distribution histograms in the X, Y and Z directions respectively. From panels (a) and (e), the effect of the Cluster orbit on our dataset can be seen. Cluster detected BBFs at decreasing Z values with increasing radial distance. Panels (b) and (f) show that the spatial distribution peaks at -17 R_E in the X direction and +2 R_E in the Z direction. In the Y direction, the distribution is fairly uniform (panel (d)), apart from a drop-out between -2 and +1 R_E. Comparing the spatial distributions for the various phases (coloured traces), there is a spatial dependance based on the substorm phase in the Y and Z directions. In the azimuthal (Y) direction, the majority of the expansion phase BBFs were detected in the pre-midnight sector, whereas in the Z direction, the recovery phase BBFs made up almost the entirety of the BBFs detected at Z < -1 R_E.

Figure 6.5 shows (a) the mean total ion velocity against X position, components of mean ion velocity perpendicular to the magnetic field, defined as $\mathbf{b} \times \mathbf{V} \times \mathbf{b}$ against their respective positions (i.e. $V_{\perp X}$ versus X, panels b to d) and (e) $V_{\perp Z}$ against B_X for all the flow bursts detected. Panels (a) and (b) suggest that the correlation between ion velocity or perpendicular ion velocity in the X direction and BBF location in the X direction is poor. However, it should be noted that, as seen in Fig. 6.4 (and later in Fig. 6.9 and Fig. 6.10), the sampling of the magnetotail in the X direction is dominated by orbital effects. In the Y direction, there is a clear relationship between the perpendicular Y velocity and position in the Y direction, such that flows appear to flow away from the centre of the tail, i.e. towards dawn on the dawnward side and towards dusk on the duskward side, although there is a fair amount of scatter. In the Z direction, again there is little or no correspondence between the position and velocity. However, when consideration is made for the side of the current sheet the spacecraft are on (B_X positive or negative), it appears that the velocity is normally directed towards the current sheet, although as with the perpendicular Y velocity, there is a fair amount of scatter. Upon closer inspection, it would appear that a linear fit is not appropriate but rather the relationship is a function similar to an arctangent.

6.2.1 Statistics of the curlometer

The curlometer technique, which is used throughout this study to determine the currents associated with the flow bursts, estimates the curl of the magnetic field across faces of the Cluster tetrahedron by assuming that the magnetic field varies linearly between spacecraft. This linear approximation is often not the true variation of the field and, as a result, we can also determine a divergence of the magnetic field from the curlometer. As Gauss's Law states that $\nabla.\mathbf{B} = 0$, any measured divergence indicates a failing in the technique, combining errors due to the non-linearity of the magnetic field variations and measurement errors. Robert *et al.* (1998) showed that, statistically, $|div\mathbf{B}|/|curl\mathbf{B}|$ and $\Delta J/J$ were similar, although there was no one to one correlation. However, since we cannot know $\Delta J/J$ without a priori knowledge of the current system, $|div\mathbf{B}|/|curl\mathbf{B}|$ is
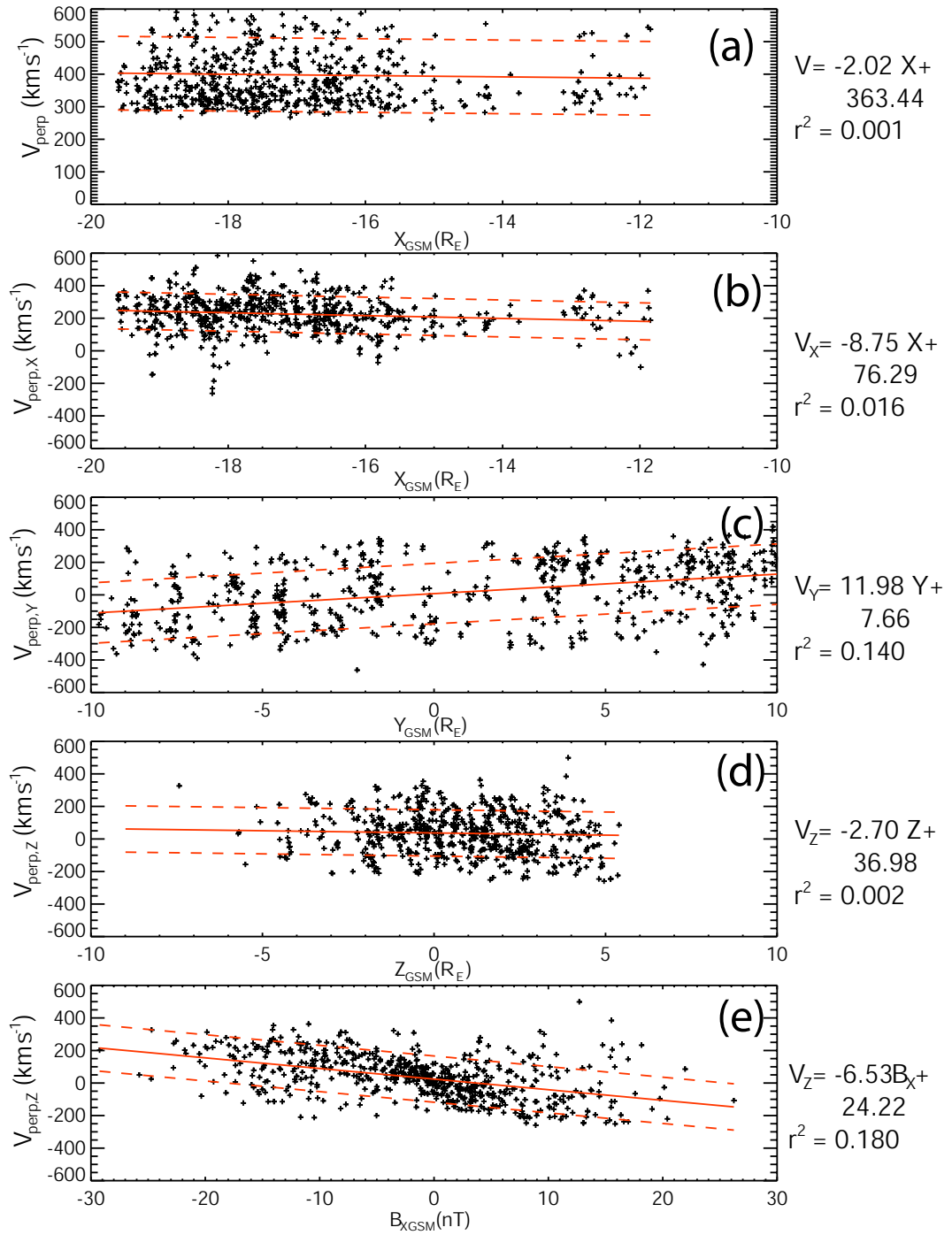
Figure 6.5: Plots of ion velocity and ion velocity perpendicular to the magnetic field against position and B_X. Panels (a) and (b) shows the mean total ion velocity and mean perpendicular ion velocity in the X direction against X. Panels (c) and (d) show the perpendicular ion velocity in the Y and Z directions against Y and Z respectively. Panel (e) shows the perpendicular ion velocity in the Z direction against B_X. The red lines in each panel represent the line of best fit to the data (solid lines) and the standard error (dashed lines).

used as an indicator of the quality of **j**.

In Chapter 4, I showed that the comparative size of the spacecraft tetrahedron to the current system enables the curlometer to detect more (or less) of the true current. Given that the spacecraft separation was approximately an order of magnitude smaller in 2003 than in the other years, it is prudent at this stage to separate the data into two subsets; the large separation dataset (LSD), consisting of data from 2001, 2002 and 2004, and the small separation dataset (SSD), consisting of data from 2003.

Figure 6.6 shows histograms of the number of flow bursts with a given percentage range of their Div/CurlB data points below a given threshold of $div\mathbf{B}/curl\mathbf{B}$. For both the LSD and SSD, increasing the $div\mathbf{B}/curl\mathbf{B}$ threshold increases the number of flow bursts with larger percentages of their data below the $div\mathbf{B}/curl\mathbf{B}$ threshold, as one might expect. Comparing the LSD and SSD panels indicates that, in general, events in the SSD have a higher percentage of their data points associated with $div\mathbf{B}/curl\mathbf{B}$ below the given threshold than those in the LSD. For a threshold $div\mathbf{B}/curl\mathbf{B}$ <0.1, there are almost no BBFs with more than 50% of their data points below the threshold, whereas for a threshold of $div\mathbf{B}/curl\mathbf{B}$ <0.5, most of the BBFs have more than 70% of their data points below the threshold. In order to investigate the flow burst current systems, those events where more than half the flow burst has $div\mathbf{B}/curl\mathbf{B}$ <0.3 are selected. This reduces the data-set to approximately half the events in the LSD and the majority of events in the SSD.

Figure 6.7 shows (a and b) histograms of the distribution of $|div\mathbf{B}|/|curl\mathbf{B}|$ for the maximum BBF field-aligned current ($|div\mathbf{B}|/|curl\mathbf{B}|_{max}$) and (c and d) $|div\mathbf{B}|/|curl\mathbf{B}|_{max}$ against the percentage of data points within the event with $|div\mathbf{B}|/|curl\mathbf{B}|<0.3$ for the large and small separation datasets. Panels (a) and (b) show that for both datasets, the largest number of events have a $|div\mathbf{B}|/|curl\mathbf{B}|_{max} < 0.1$, approximately 50% of the events in each dataset. In 2002 and 2004, there was a peak at $|div\mathbf{B}|/|curl\mathbf{B}|_{max} = 0.3$, although in general the number of events decreases with increasing $|div\mathbf{B}|/|curl\mathbf{B}|_{max}$. Panels (c) and (d) show that for $|div\mathbf{B}|/|curl\mathbf{B}|_{max} < 0.1$, the percentage of data points below $|div\mathbf{B}|/|curl\mathbf{B}|= 0.3$ is generally greater than 50%, especially for the small separation dataset. However, there are still a significant number of points for which the percentage of data points is under $|div\mathbf{B}|/|curl\mathbf{B}|= 0.3$, but $|div\mathbf{B}|/|curl\mathbf{B}|_{max} > 0.1$, approaching $|div\mathbf{B}|/|curl\mathbf{B}|_{max} = 1$ in some cases. This suggests that simply using the percentage of points under $|div\mathbf{B}|/|curl\mathbf{B}|=0.3$ as a quality indicator may not be sufficient. As such, I apply a further condition that $|div\mathbf{B}|/|curl\mathbf{B}|_{max} < 0.1$, hence the maximum current is well defined.

Figure 6.8 presents histograms of the $|div\mathbf{B}|/|curl\mathbf{B}|$ ratio,the field aligned current and the total current for BBFs detected by the Cluster 1 and 4 in the years 2001-2004. The different colours represent those data points from events with 40% (blue), 50% (brown), 60% (yellow), 70% (green) and 80% (red) of their points below $|div\mathbf{B}|/|curl\mathbf{B}|=0.3$. The
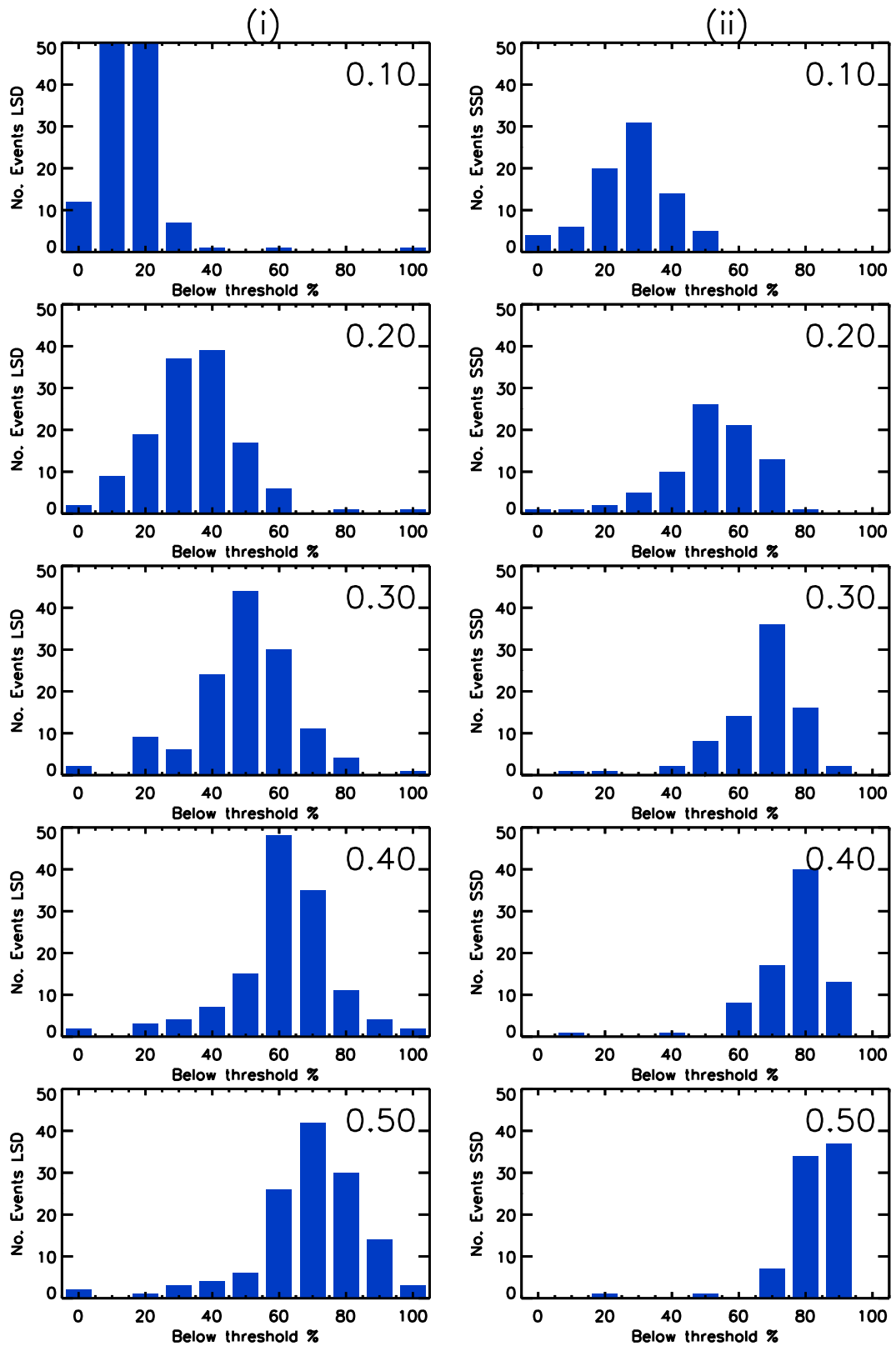
Figure 6.6: Histograms of percentage of a BBF event below a specified $|div\mathbf{B}|/|curl\mathbf{B}|$ threshold for the (i) the LSD and (ii) the SSD. The limits used are 0.1 to 0.5 in increments of 0.1.
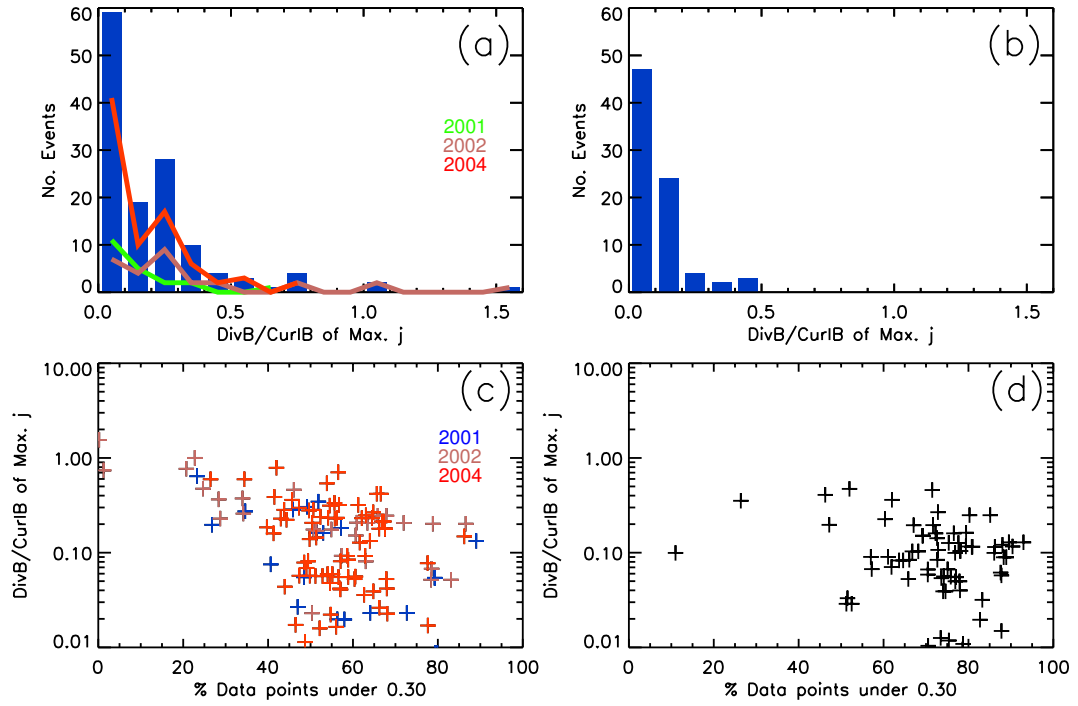
Figure 6.7: Histograms of $|div\mathbf{B}|/|curl\mathbf{B}|_{max}$ for (a) the LSD and (b) the SSD. Panels (c) and (d) show $|div\mathbf{B}|/|curl\mathbf{B}|_{max}$ against the percentage of data points with $|div\mathbf{B}|/|curl\mathbf{B}|<0.3$ for the LSD and SSD respectively.

black bars show the distributions for all the events that meet the current sheet criterion.

Clearly, the number of data points increased from 2001 to 2004, as described earlier. Taking this into account, 2001, 2002 and 2004 show similar trends. The current density peaks at ~ 2 mA km^{-2} and has very few values above 6 mA km^{-2} and the majority of the field-aligned currents are <5 mA/km^{-2}. In contrast, the results from 2003 have a different profile. The current density peaks at 4 mA km^{-2} and extends to much higher values whilst the field-aligned current also extends to higher values.

Comparing the different percentage thresholds, it is clear that the number of data points available decreases more rapidly with increasing threshold for 2001, 2002 and 2004, as is expected from Fig. 6.6. The higher values of $|div\mathbf{B}|/|curl\mathbf{B}|$ drop off more rapidly than the lower values, again, as expected for applying a stricter limit on the number of points below a $|div\mathbf{B}|/|curl\mathbf{B}|=0.3$. The number of points in the lower values of field-aligned current and current density decrease more rapidly with increasing percentage threshold indicating that smaller currents are less well defined. This, again, is expected. For example, if the divergences detected at two times were similar, but the currents varied by a factor of two, $|div\mathbf{B}|/|curl\mathbf{B}|$ for the smaller current would be twice as large as that for the larger current.

Comparing the 2001, 2002 and 2004 data (LSD data), when the Cluster separation was of the order of 1000 km with the 2003 data (SSD data), when the Cluster separation was of the order of 100 km, suggests that the current systems are structured on different
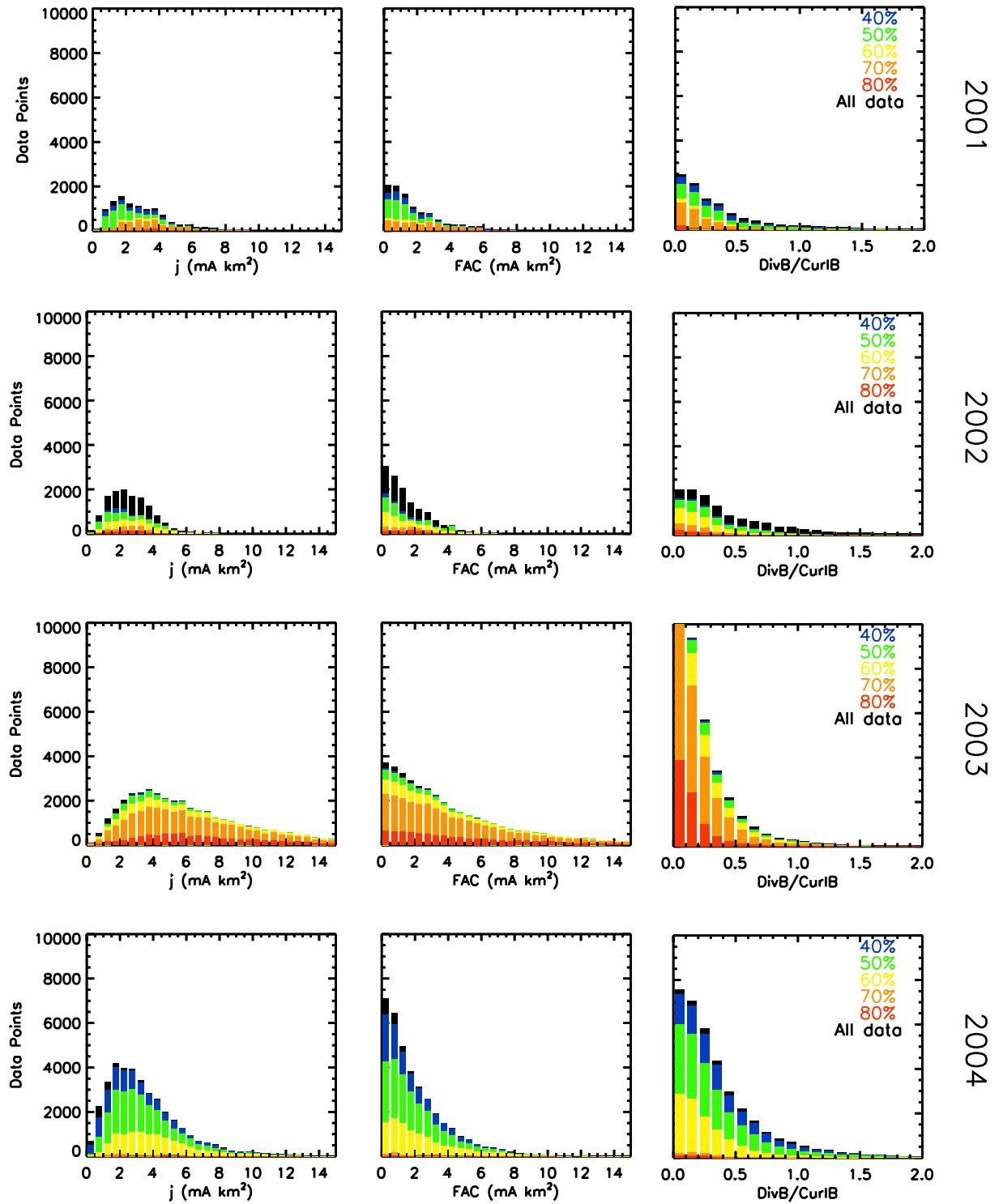
Figure 6.8: Histograms of Div B/Curl B, field-aligned current and current magnitude for BBFs detected by Cluster 1 and 4 in the years 2001 to 2004. The colours show datasets with various percentage thresholds for the number of points within the BBF with $|div\mathbf{B}|/|curl\mathbf{B}|<0.3$.

scale sizes. If this were not the case, then it would be expected that j would not vary with the tetrahedron scale size.

6.3 Statistics of BBF currents

Figures 6.9 and 6.10 show the location, substorm phase and maximum field-aligned current of the LSD and SSD respectively. The circle positions represent the location of Cluster when the spacecraft encountered BBFs, the circle sizes represent the maximum field-aligned current and the colours represent the substorm phase (miscellaneous (blue), growth (green), expansion (yellow), recovery (red) and storm (black)). Also presented are the occurrence rate of BBFs with respect to substorm phase in the pre- and post-midnight sectors.

The results from both datasets are similar. The figures show that the spatial distribution of BBF occurrence is dominated by the Cluster orbit in the X and Z directions, although in the Y direction, the distribution is fairly uniform, as indicated by Fig. 6.4b. Figures 6.9(a) and (b) show that larger field-aligned currents were more common in the pre-midnight sector for the LSD, whereas Figs. 6.10(a) and (b) show that higher currents occur in the post-midnight sector for the SSD. Panels (d) and (e) in both figures show that there were more expansion phase events in the pre-midnight sector by more than a factor of three for both the LSD and SSD.

MVA (see 4) is used to determine the orientation of edge of the BBF at the start of the Cluster spacecraft's encounter. The variance matrices were calculated for the spacecraft that encountered the BBF between 20 s to 25% of the BBF duration centred on the start of the BBF encounter. To aid the removal of any temporal variations, the magnetic field data was filtered using a 20 s Boxcar filter. The variance matrix with the largest λ_2/λ_3 ratio was selected. Any results with $\lambda_2/\lambda_3 < 10$ were discarded (Eastwood *et al.*, 2005). This leaves 26 BBFs in the LSD and 7 in the SSD.

Figure. 6.11 shows the field-aligned current against the MVA angle in the XY plane. The figure shows that the orientation of the edge of the flows at the time of substorm entry are grouped into two ranges centred on -30° (towards dawn) or 90° (towards dusk), with a spread of about ±50°for each group. Also, there is no apparent dependency in the field-aligned current on the angle at which the spacecraft enter the flow. However, given the small number of events available, and that most of the bins contain single events, it is difficult to judge whether or not this is a true effect, or merely due to the small sample of events used.
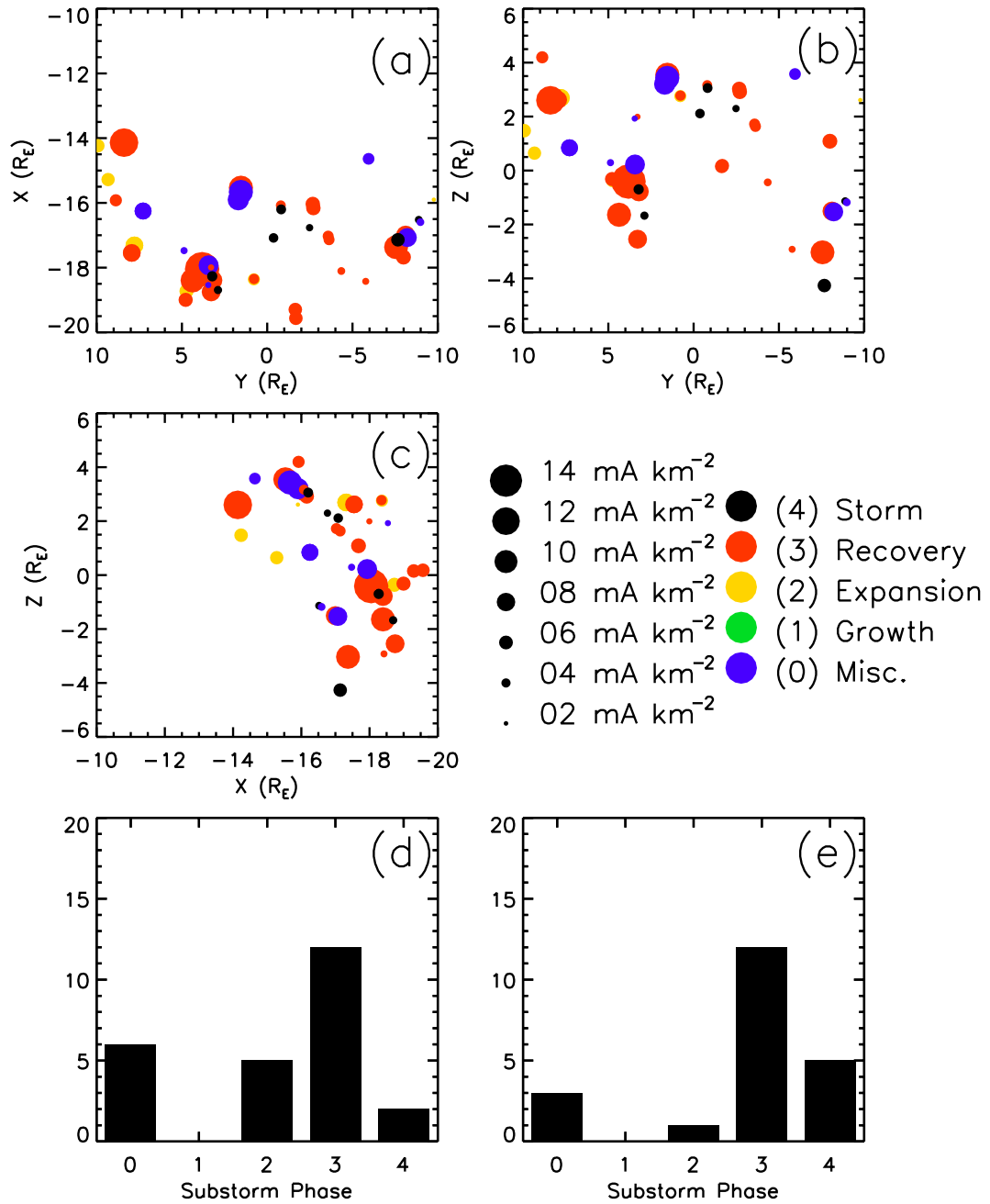
Figure 6.9: Plot of BBF location in (a) YX, (b) YZ and (c) XZ coordinates for the LSD. The size of the circles indicates the maximum field-aligned current and the colour represents the substorm phase ((miscellaneous (blue), growth (green), expansion (yellow), recovery (red) and storm (black)). Panels (d) and (e) show the occurrence substorm phase in the pre- and post-midnight sectors respectively.
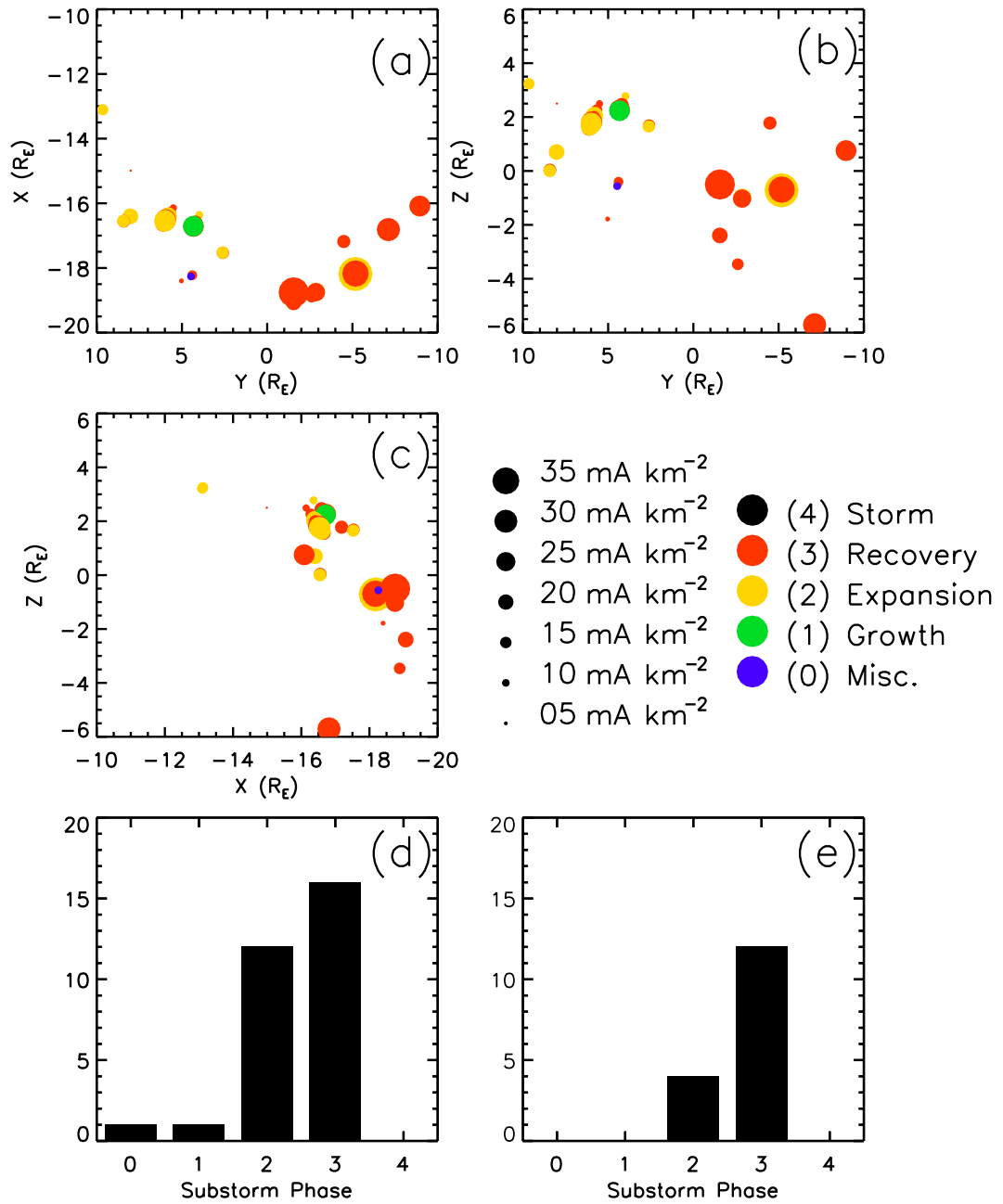
Figure 6.10: Plot of BBF location in (a) YX, (b) YZ and (c) XZ coordinates for the SSD. The size of the circles indicates the maximum field-aligned current and the colour represents the substorm phase ((miscellaneous (blue), growth (green), expansion (yellow), recovery (red) and storm (black)). Panels (d) and (e) show the occurrence substorm phase in the pre- and post-midnight sectors respectively.
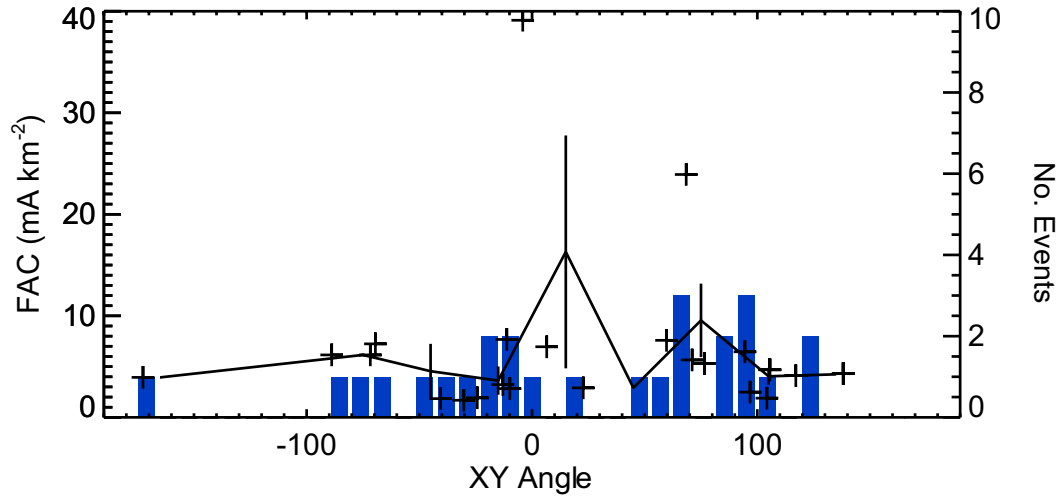
Figure 6.11: Plot of the MVA angle in the XY plane. The blue bars show the number of events in 10° bins. The black lines show the field-aligned current means in 30° bins with the standard error.

Presented in Fig. 6.12 are means of the mean and maximum field-aligned currents binned in the X, Y and Z directions for the LSD (i) and the SSD (ii) in bins of 1 R_E in the X and Z directions and 2 R_E in the Y direction. The mean currents appear to increase with distance downtail for both the LSD and SSD, although the increase is minimal ($\sim$10%) and may be accounted for by the standard errors. The maximum currents, on the other hand, appear to be fairly constant, again to within the errors shown. Azimuthally across the tail, there is a clear difference between the current values in the pre- and post-midnight sectors in both the LSD and SSD, although the variation is not the same in the two datasets. Given that the two datasets relate to different scale sizes of the tetrahedron, it is not clear whether or not these are statistical flukes or some variation due to the change in scale size. The pre-midnight currents are approximately double the post-midnight currents in both the maximum currents and mean currents for the LSD, whereas the opposite is true for the SSD. In the Z direction, the currents appear to peak at Z=1 R_E in both the SSD and LSD datasets. For the LSD, there appear to be two further peaks at $\pm$4 R_E, although the standard errors suggests that the currents could be constant, apart from near Z=1 R_E.

In their study, Forsyth *et al.* (2008a) suggested that the magnitude of the field-aligned current associated with BBFs was dependant on the substorm phase during which they were observed, based on a collation of earlier case studies. This is now investigated a statistical manner.

Figure 6.13 shows comparisons of the BBF field-aligned currents against substorm phase and the AE index. Panels (a) and (b) show the mean mean and mean maximum field-aligned currents (red and black traces respectively) against substorm phase for the LSD and SSD (panels (a) and (b) respectively). The blue bars show the number of BBFs in each phase. Panels (c) and (d) show the mean and maximum field-aligned currents against AE for the different phases (blue, green, yellow, red, black for phases 0 to 4 respectively)
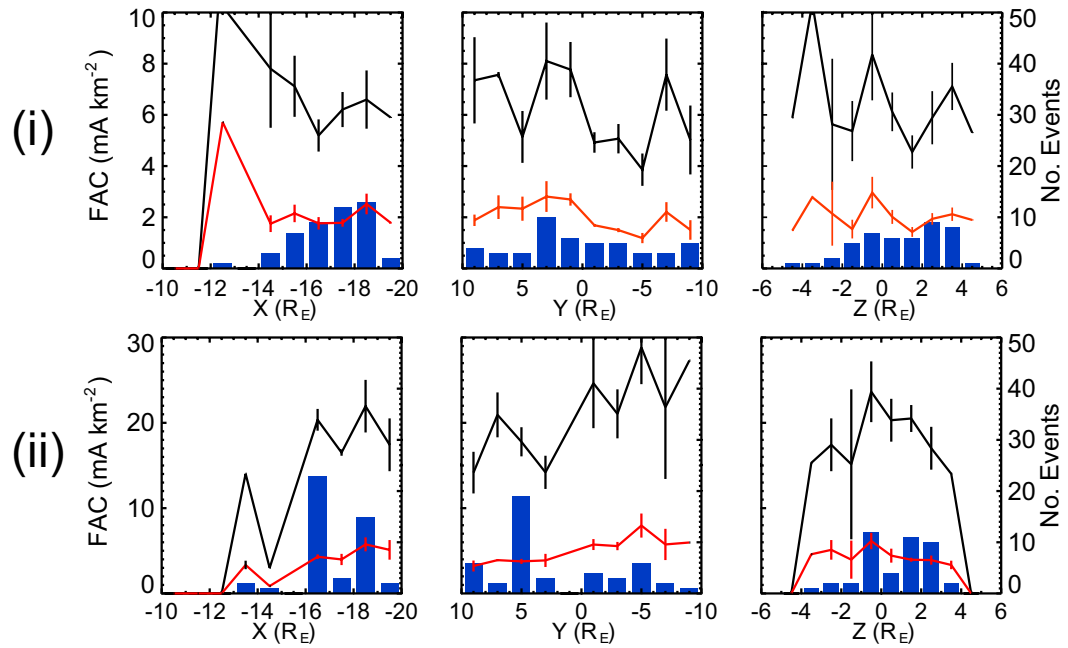
Figure 6.12: Histograms of the mean binned mean (red) and mean binned maximum (black) field-aligned currents against the X, Y and Z GSM positions of the BBfs for the (i) LSD and (ii) SSD. X and Z are binned in 1 R_E bins and Y is binned in 2 R_E bins. The vertical lines show the standard error in the mean in each bin.
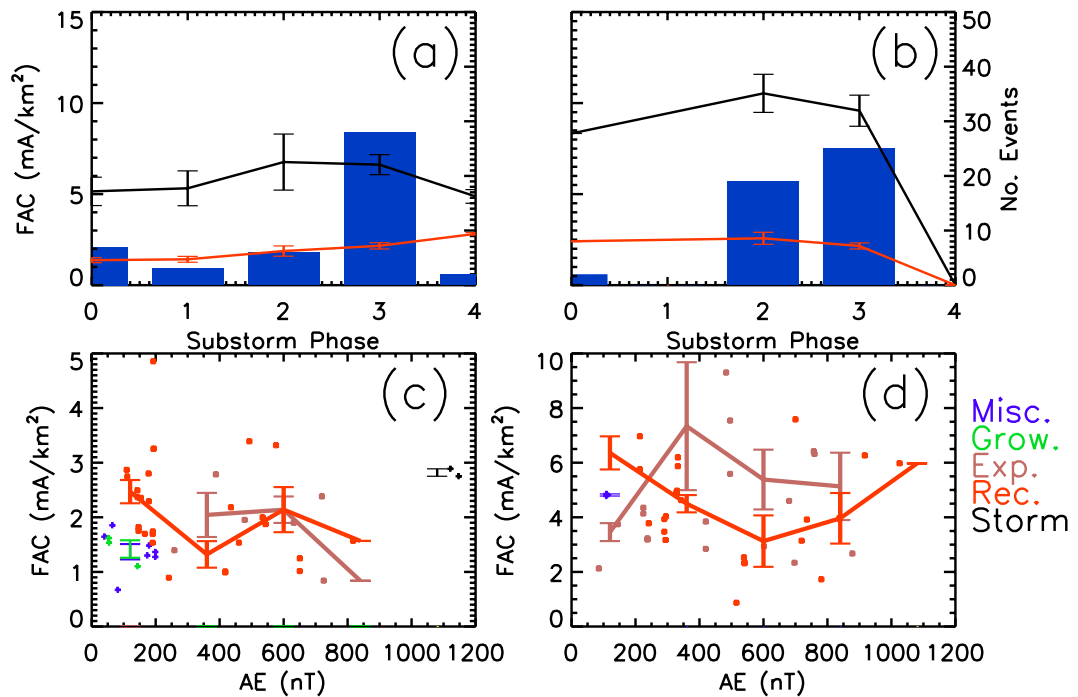
Figure 6.13: Histograms of the means of the mean (red) and maximum (black) field-aligned currents against substorm phase and AE for (a) the LSD and (b) the SSD. The mean field-aligned current against AE is shown in panels (c) and (d) for the LSD and SSD respectively. In panels (a) and (b), phase 0 is miscellaneous, 1 is growth, 2 is expansion, 3 is recovery and 4 is storm. In panels (c) and (d), blue represents miscellaneous phase events; green represents growth phase events; dark green represents expansion phase events; red represents expansion phase events; black represents storm time events. The traces in panels (c) to (d) represent the binned mean. AE are binned in 5 bins from 0 to 1200 nT.

for the LSD and SSD respectively. The traces show the mean binned mean field-aligned currents in bins of 240 nT of AE. For the SSD, in which we only have a significant number of events during phases 2 and 3, there is an decrease in the field-aligned currents observed from the expansion to recovery phases. The LSD shows a similar current distribution for the maximum currents, although extending from the miscellaneous through to the expansion phase currents. However, the standard errors in the LSD data would equally allow for no current variations between phases. Although comparing field-aligned currents and substorm phases suggests that there may be a relationship between the two, there is no apparent relationship between the AE index at the time of the BBF and the mean field-aligned currents.

6.4   Discussion

The CIS and FGM CAA Cluster datasets have been surveyed for the occurrence of BBF flow bursts between days 100 to 200 in the years 2001 to 2004. The results from Cluster 3 show a clear discrepancy in the number of flow bursts detected due to a known instrumental error in the particle velocities from the CIS instrument due to a degradation of the detector anodes. As such, the initial survey (using Cluster 1 and 4) returned 628 flow burst events. A subset of these BBFs was defined in which B_X had the same sense on all spacecraft throughout the event, removing any tail current sheet crossings so as to enable the determination of the field-aligned currents associated with the flow bursts. This subset consisted of 211 events.

6.4.1   BBF statistics

The importance of BBFs to the substorm cycle has been discussed within the literature. Angelopoulos *et al.* (1994) showed that the occurrence rate of BBFs increases with AE, suggesting that BBFs are associated with geomagnetic disturbances. The braking of these flows bursts has been implicated in the formation of the substorm current wedge (Shiokawa *et al.*, 1997, 1998a), whereas auroral activations on the nightside polar cap boundary (poleward boundary intensifcations or PBI) and auroral streamers observed during later substorm phases and outside of substorm times have been related to BBF activity (e.g. Henderson *et al.*, 1998; Amm *et al.*, 1999; Lyons *et al.*, 1999; Grocott *et al.*, 2004; Nakamura *et al.*, 2001b; Forsyth *et al.*, 2008a). However, a quantitative analysis of flow burst occurrence with substorm phase has, up to this point, not been carried out. I have used the AU and AL indices as an indicator of substorm phase. The results show quite clearly that the number of flow bursts detected is far higher during the recovery phase than any other substorm phase (Fig. 6.3). However, an analysis of the duration of the phases for the days on which flow bursts were detected in 2001 indicates that phase

0, recovery and growth phases are ∼2 times as long as the expansion phase. The relative occurrence of flow bursts is similar for the growth (including phase 0), expansion and recovery phases, although still increasing from the growth to recovery phase.

The results presented have implications on the role of BBFs in the substorm cycle. The substorm current wedge forms at, or shortly after, the onset of the substorm expansion phase. If BBFs are the mechanism that drives the inner tail to become more dipolar and diverts the tail current into the magnetosphere (Shiokawa *et al.*, 1998b; Birn *et al.*, 1999), then one might expect to see a larger number of BBFs during the growth or expansion phases. However, the survey results show that more BBFs were detected during the recovery phase of substorms. As such, the results imply that BBFs are not important in setting up the substorm current wedge and thus supporting the current disruption model of substorm onset.

During the recovery phase, the substorm current wedge weakens. This is apparent from the definition of the recovery phase used in this study (after the minimum in the AL index). An increase in the AL index indicates a reduction in the substorm electrojet, which is fed by the substorm current wedge. However, one might expect the injection of further BBFs into the inner magnetosphere to bolster the waining current wedge. A more pertinent study should consider the times relative to the onsets of the various substorm stages at which the BBFs were detected in order to gauge the effect of the recovery phase BBFs in slowing the reduction in the SCW.

A further consideration of the number of BBFs detected is the question of continuing reconnection following the start of the recovery phase. Current understanding implies that the recovery phase begins when the substorm reconnection X-line begins to retreat down the tail (Hones, 1984; Baker *et al.*, 1996). One might consider that the higher occurrence rate of BBFs in the recovery phase suggests that as the substorm X-line retreats tailwards there are an increasing number of localised bursts of reconnection Earthwards of it. However, as BBFs are convective features, it is difficult to determine the time and location of their generation. BBFs detected in the early recovery phase may in fact have been generated in the expansion phase, but taken sufficient time to convect through the tail that they were detected in the recovery phase. Again, analysis of the relative timings of BBFs with respect to the onsets of the substorm phases may provide a valuable insight into when BBFs are created.

The results presented show that the ion velocity perpendicular to the magnetic field does decrease with radial direction, although not dramatically (Fig. 6.5b). However, Fig. 6.4 shows that the majority of BBFs detected at smaller radial distances were detected at larger distances from the equatorial plane, such that the associated field lines would cross the current sheet far downtail. As such, our results neither confirm or refute the suggestion that the braking of flow bursts is important in the formation of the substorm current wedge (Shiokawa *et al.*, 1997, 1998a). The ion velocity perpendicular to the

magnetic field in the azimuthal direction (Fig. 6.5c) shows a dependance on azimuthal location, reminiscent of the Dungey Cycle (Dungey, 1961) convection pattern. Grocott *et al.* (2007) showed that the sense of the IMF B_Y component can have a bearing on the direction of the convection of BBFs both in the magnetosphere and ionosphere (see their Fig. 6 or Fig. 2.8), such that easterly (westerly) convection occurred in the pre-midnight (post-midnight) sector. This could potentially explain the scatter in Fig. 6.5c. In the vertical direction, there was no apparent dependance in the vertical velocity and position (Fig. 6.5d), although there was a clear relationship between B_X and vertical velocity (Fig. 6.5e). Taking B_X as a proxy for distance from the cross-tail current sheet, then the vertical velocities were towards the current sheet and increased with increasing distance from it, appearing to reach a maximum of ~ 200 km s^{-1}.

6.4.2 Results from the curlometer

In order to investigate the current systems associated with the BBFs using the curlometer technique, it is necessary to consider $|div\mathbf{B}|/|curl\mathbf{B}|$ within the dataset. Since the curlometer is an approximation technique, it is possible to calculate a divergence of the magnetic field which is thus an indicator of the limitations of the technique. Figure 6.6 shows only a small portion of each event is associated with $|div\mathbf{B}|/|curl\mathbf{B}| < 0.1$, whereas the majority of the events have more than 70% of the event associated with $|div\mathbf{B}|/|curl\mathbf{B}| < 0.5$. Figure 6.7 further shows that a high proportion of an event below a threshold $|div\mathbf{B}|/|curl\mathbf{B}| = 0.3$ does not necessarily indicate that the maximum current will be well defined (i.e. $|div\mathbf{B}|/|curl\mathbf{B}|_{max}$ is low). From these figures I have specified limiting criteria on $|div\mathbf{B}|/|curl\mathbf{B}|$ within the dataset. Firstly, more than 50% of each BBF must have $|div\mathbf{B}|/|curl\mathbf{B}| < 0.3$. Figure 6.6 shows that this removes approximately half of the events in the LSD but only a small number of events from the SSD. As this allows for a fairly large error in the current ($\sim 30\%$), the study was further restricted to those events in which $|div\mathbf{B}|/|curl\mathbf{B}|$ of the maximum current was less than 0.1, such that in the event that the mean current is poorly defined, there can be confidence in the maximum current.

Clearly, as the percentage of the event below the $|div\mathbf{B}|/|curl\mathbf{B}|$ limit increases, higher $|div\mathbf{B}|/|curl\mathbf{B}|$ values are omitted from the data. However, the opposite is true for the currents, such that the lower currents are omitted (Fig. 6.8ii and iii). This indicates that the strength of the current has more of an effect on $|div\mathbf{B}|/|curl\mathbf{B}|$ and that larger currents will tend to be associated with lower $|div\mathbf{B}|/|curl\mathbf{B}|$. Figures 6.6 and 6.8 show that, for the large separation dataset, the data available during the large separation tail seasons is highly dependant on the choice of $|div\mathbf{B}|/|curl\mathbf{B}|$ and the percentage of the event below a certain limit. Although there is an effect on the small separation data, it is not as great. One might expect that this is the case and that the linear approximations made by the curlometer become more valid over smaller separations.

That $|div\mathbf{B}|/|curl\mathbf{B}|$ was generally lower for the SSD is consistent with the results from Chapter 4, which showed that for smaller current distributions relative to the tetrahedron, $|div\mathbf{B}|/|curl\mathbf{B}|$ was larger (Fig. 4.5 and Fig. 4.6). Furthermore, we can see from Fig. 4.8 that when the scale size of the tetrahedron is smaller than the width of the current system, the current detected is fairly constant for all scale sizes, whereas as the scale size of the tetrahedron increases, the current detected drops. Approximating the current system to be larger than the SSD separations and the difference in currents detected to be ~ 50 % (Fig. 6.8) then the approximate scale size (1 standard deviation) of the BBF current systems is 300-400 km. For a normal distribution, 99% of the current is within ± 3 standard deviations, giving the whole current system a width of 1800 to 2400 km, comparable with the current system width found by Snekvik *et al.* (2007) (0.3 R_E). Given that BBFs commonly have widths of 1-3 R_E (Nakamura *et al.*, 2004), this implies a thin current layer running along the edge of the BBF, such as those shown in the simulations of Birn *et al.* (2004). In their Fig. 6, Forsyth *et al.* (2008a) show the field-aligned currents from two flow bursts. The first of these shows two opposing field-aligned current systems separated by a brief interval of very low field-aligned current, consistent with the simulations of Birn *et al.* (2004) and the suggestion of a thin current layer. The case study presented here (Fig. 6.2) shows a current system that peaks in the centre of the detected flow and not near the edges. However, Fig. 6.2 also shows that two of the spacecraft remained outside the BBF. As such, it is likely that the spacecraft passed along one side of the BBF. The direction of the field-aligned current (parallel to the magnetic field) and the B_X component (negative, i.e. away from the Earth) suggest that the spacecraft skimmed through the duskward edge of the flow.

6.4.3   BBF currents

The mean field-aligned current distributions in Fig. 6.12 suggest that the currents increase with increasing distance from Earth. Despite the poor coverage in the SSD the standard errors on the mean currents are similar in each bin. However, the standard errors are sufficiently large to suggest that there is no variation in currents with radial distance down the tail. In contrast, the maximum currents from the LSD suggest a drop in the currents away from Earth, although again, the standard errors are sufficient to suggest that there is no variation. The distribution in the Z direction for both the LSD and SSD show a peak in both mean and maximum currents between -1 and 0 R_E. The standard errors in the maximum currents suggest that a linear fit may be appropriate, although this is not the case for the mean currents. In the Y direction, however, there is a clear variation in both the mean and maximum currents outside of the standard errors. For the LSD, there is a peak in the currents between -5 and 0 R_E and a minimum in the currents between 0 and 5 R_E. The standard errors suggest that the minimum is particularly well defined. In the SSD, the variation is in opposition to the LSD.

Due to the fact that the LSD and SSD refer to datasets from different scale sizes of the Cluster tetrahedron, it is not clear whether or not the change in the variation in the currents across the tail is due to a statistical fluke or the change in the tetrahedron scale size. One possibility is that there is a change in the current densities detected based on the scale size of the tetrahedron due to the way the curlometer estimates the current. The results suggest that in the pre-midnight sector the currents in the individual events have a wide distribution but a lower peak, whereas in the post-midnight sector the current systems have a higher peak, but a much narrower distribution. Given that field-aligned currents are related to the shear in the magnetic field through Ampére's Law, this would suggest that the shear between the flow magnetic field lines and surrounding magnetic field lines is greater in the post-midnight sector and that the flow channel is narrower. One possible explanation for the greater shear in the magnetic field is the distance downtail that reconnection occurs to generate the flow burst. If, in the simplest scenario, the ionospheric footprint of the flow burst field lines is restricted to move at the same velocity as the surrounding field lines, yet the magnetospheric loop of the field lines move faster than the surrounding field lines, then the further downtail the flow burst is generated, the greater the shear between the surrounding field lines and the flow by the time it reaches the orbit of Cluster and the greater the field-aligned currents. The implication of this would be that reconnection does not occur at the same point across the whole tail, rather it occurs at a greater downtail distance in the post-midnight sector. However, Grocott *et al.* (2007) showed that BBFs were associated with fast azimuthal flows in the ionosphere so assuming that the ionospheric end of the field line is stationary with respect to the surrounding field lines is clearly not applicable, although as long as the relative speed of the flow burst to the surrounding field lines is greater than the relative speed of their ionospheric footpoints, our suggestion is still valid.

Based on a literature survey, Forsyth *et al.* (2008a) suggested that there is a relationship between substorm phase and the field-aligned currents associated with BBF flow bursts. The results from the LSD and SSD support this (Fig. 6.13). For both the LSD and SSD, the mean currents decrease from the expansion to the recovery phase. For the LSD, the current increased from the phase 0 and growth phases to the expansion phase. Unfortunately we have no growth phase events from the SSD, so cannot confirm whether this is true for the SSD. The standard errors in the maximum currents are large, such that the variation is within these uncertainties. For the LSD, the standard errors on the mean currents are much smaller, but only slightly larger than the variation in the means. In tandem with this, the results from the LSD showed that flow burst currents peaked in the pre-midnight sector between -5 and 0 R_E. Frey *et al.* (2004) showed that the median substorm expansion phase onset location was at 23 MLT, in the same region in which we saw the larger currents. This would further suggest a link between the field-aligned current magnitude associated with BBFs and substorm phase.

It is notable that the range of the mean currents presented is not of the order suggested

by Forsyth *et al.* (2008a), although this may be due to the limitations of the curlometer technique. Smaller currents tend to be associated with larger $|div\mathbf{B}|/|curl\mathbf{B}|$, by nature of the ratio. As such, the smaller currents detected by Grocott *et al.* (2004) and Nakamura *et al.* (2005a) may not have met the selection criteria, causing the currents detected to be larger in general.

The comparison between the field-aligned currents and AE index for the flow bursts shows no particular correlation for either the LSD or SSD, which is consistent with Angelopoulos *et al.* (1994), who showed that there was no apparent difference between BBFs in active and quiet times. This is not necessarily inconsistent with the results presented that indicate that later substorm phases are associated with larger currents since the magnitude of AE is not a specific indicator of substorm phase.

6.5   Summary

Based on data from the Cluster spacecraft during their tail seasons in the years 2001 to 2004, BBF flow burst occurrences with respect to substorm activity and their associated current systems have been investigated. The survey consisted of 628 events, of which 211 were detected sufficiently far from the tail current sheet to use the curlometer to determine the field-aligned currents associated with the flows.

Comparing flow burst occurrence with substorm phase, determined from auroral indices, has shown that flow bursts are most common during substorm recovery phases and in the pre-midnight sector and least common in the growth phase. From this, it is implied that the flow bursts may bolster the waning substorm current wedge. Also, the lower occurrence rate of BBFs in the growth phase brings into question the idea that BBFs are critical in forming the substorm current wedge and, as such, would suggest that the current disruption model of substorm onset is more likely.

The currents detected by the curlometer show variations across the tail, although the variations differ depending on the scale size at which the current system is examined. At small scale sizes (100 km), the currents observed were larger in the post-midnight sector, whereas at large scale sizes (1000 km), the currents observed were large in the pre-midnight sector. The current does not vary significantly on either scale size in the X or Z directions.

Comparing the currents observed during the different substorm phases shows that the currents are highest during the expansion phase and lowest during the growth phase. However, the variation in the currents is not as large as can be found by comparing previous studies of the ionospheric current associated with BBFs. This inconsistency is most likely due using $|div\mathbf{B}|/|curl\mathbf{B}|$ in the selection of events which, by its nature,

excludes events with low currents.

Chapter 7

Solar wind and substorm excitation of the wavy current sheet

This study investigates the tail and auroral dynamics following a solar wind pressure pulse and two substorms. I expand upon the study by Zhang *et al.* (2002), including data from Polar, GOES 8 and 10 and Cluster, enabling a determination of the global picture of the magnetotail dynamics at this time. Comparing magnetotail data and auroral observations, I confirm that the substorm dipolarization front is related to auroral activity across 12 R_E of the magnetotail. Using four-spacecraft timing analysis, I show that the motion of these dipolarization fronts is comparable to the motion of the current sheet waves following them, suggesting that these two features propagate via the same mechanism. Furthermore, the results enable the determination of which of two models of current sheet waves is more likely for this event.

7.1   Instrumentation

In this study, data are employed from the Cluster FGM (Balogh *et al.*, 2001), CIS-CODIF sensors (Rème *et al.*, 2001), PEACE-HEEA sensors (Johnstone *et al.*, 1997), Polar MFE (Russell *et al.*, 1995) and GOES 8 and 10 Magnetometers. The data from GOES 8 are subject to an offset in the B_Z component and, hence, a correction of -7 nT is applied (Tsyganenko *et al.*, 2003). Prior to 08:08 UT, Cluster FGM was running in EXT mode. This mode stores spin resolution FGM data in memory usually reserved for storing burst mode data whilst the spacecraft are not telemetering data . The data are telemetered to the ground at the first opportunity. These data are calibrated using the on-board calibrations and have an increased uncertainty in the timestamps due to the collection method (see Balogh *et al.*, 2001; Brown *et al.*, 2008, for details). After 08:08 UT, FGM data based on the 5 Hz resolution data from the Cluster Active Archive (CAA) are employed. This data has been calibrated to facilitate the multi-spacecraft analysis techniques used

in this study. Polar MFE data has a temporal resolution of 6 s, whereas GOES MAG data has a temporal resolution of 60 s. The moments from the PEACE-HEEA sensors have been calculated on the ground from a reduced angular resolution 3D particle distribution (3DX - see Johnstone *et al.* (1997)). Ground moments use improved calibrations and improved corrections for the effects of the spacecraft potential. The 3D distributions are not telemetered on every spin, so the moments have a lower temporal resolution which varies between spacecraft. Spacecraft data are presented in GSM coordinates unless otherwise stated.

Figure 7.1 shows the location of the Cluster and Polar spacecraft and Fig. 7.2 shows that of Polar, GOES 8 and GOES 10 in GSM coordinates between 06:00 and 12:00 UT. The Cluster tetrahedron at 06:00UT is magnified by a factor of 20, with Cluster 1 plotted at the correct location. The locations of Cluster 1, Polar, GOES 8 and GOES 10 at 06:00, 09:00 and 12:00 UT are shown as asterisks, open circles and triangles respectively. Cluster was in the northern magnetosphere, with Cluster 1 at [-16.6,-9.1,4.2] R_E at 06:00 UT, moving to [-16.6,-8.5,1.5] R_E by 12:00 UT. Cluster 1 was the most Earthward spacecraft, whereas Cluster 2, 3 and 4 were at approximately the same downtail distance. Cluster 2 (red) was the most duskward and northernmost spacecraft. Cluster 3 (green) was the southernmost spacecraft and Cluster 4 (blue) was closest to dawn. The spacecraft were separated by 1700-2000 km. Polar was initially in the southern magnetosphere at [-3.0,-2.3,-1.9] R_E at 06:00 UT moving to [-5.2,-6.4,4.5] R_E by 12:00 UT. The GOES spacecraft were in the northern magnetosphere throughout the interval. GOES 8 was the most dawnward spacecraft, initially at [-6.1,-1.4,2] R_E and moved to [1.5,-6.4,0.7] R_E by 12:00 UT, passing through the magnetic local time sector of Cluster and Polar. The closest separation of Polar and GOES 8 occurred at 08:29 UT, with the spacecraft passing within 9600 km of each other. GOES 10 was initially located in the pre-midnight sector at [-4.3,4.9,1.1] R_E, moving to [-4.6,-4.1,2.3] R_E by 12:00 UT.

Figure 7.3 shows the magnetic footprints of Cluster 1, Polar, GOES 8 and GOES 10 between 06:00 and 12:00 UT, calculated using the Tsyganenko (1989) model (hereafter referred to as the T89 model) with an input of $K_P = 4$, in (a) MLT - invariant latitude coordinates from the Altitude Adjusted Corrected GeoMagnetic coordinate system (Baker and Wing, 1989) and (b) geographic longitude - latitude coordinates. Cluster remained close to 02 MLT throughout, whereas Polar was located at 3 ± 0.5 MLT throughout. From 07:30 to 08:30 UT GOES 8, Cluster and Polar were within one hour of MLT of each other.

Solar wind data are provided by the magnetometer (Smith *et al.*, 1998) and Solar Wind Electron Proton Alpha Monitor (SWEPAM; McComas *et al.*, 1998) instruments on board the ACE spacecraft (Stone *et al.*, 1998). During the interval ACE was situated at approximately [245,-15,30] R_E, sunward of the Earth. Solar wind data from ACE are lagged by comparing the IMF with magnetometer data from the IMAGE magnetometer array (Luhr, 1994; Viljanen and Häkkinen, 1997), which was on the dayside between 7 and 13 MLT, following the technique demonstrated by Volwerk *et al.* (2004).
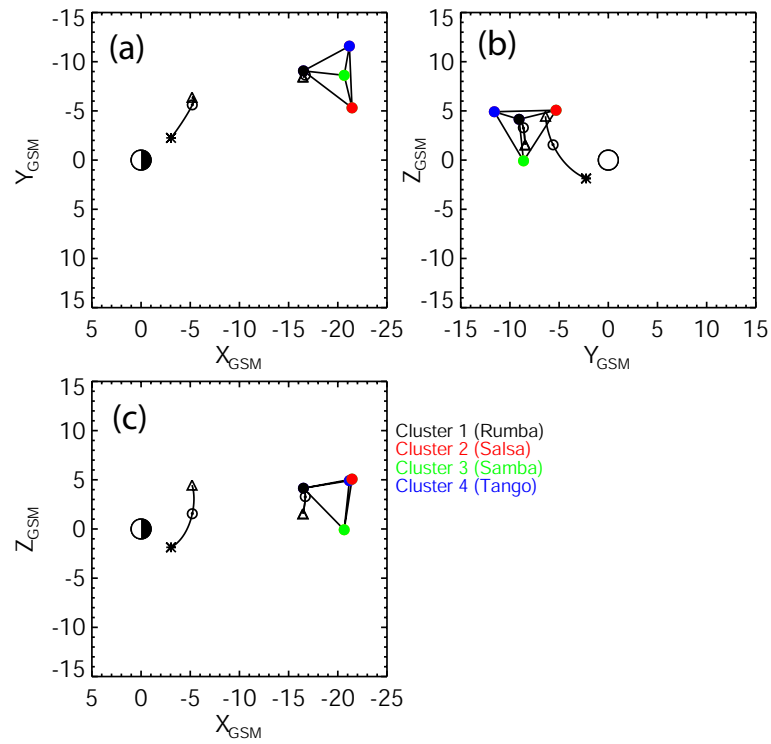
Figure 7.1: Plots of the Cluster and Polar orbital positions between 06:00 and 12:00 UT in the (a) X-Y, (b) Y-Z and (c) X-Z in GSM coordinates. The Cluster tetrahedron at 06:00 UT is magnified by a factor of 20. Cluster 1 (Rumba, black circle) is plotted at the correct location. The locations of Cluster 1 and Polar at 09:00 and 12:00 UT are shown by dotted circles and triangles respectively.
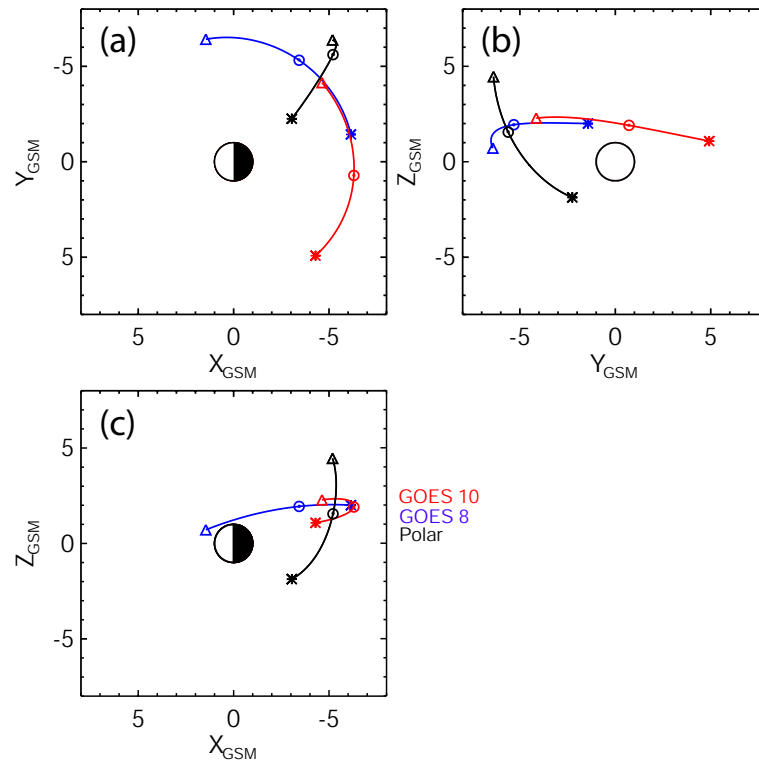
Figure 7.2: Plots of the GOES 8, GOES 10 and Polar orbital positions between 06:00 and 12:00 UT in the (a) X-Y, (b) Y-Z and (c) X-Z in GSM coordinates. The locations of the spacecraft at 06:00, 09:00 and 12:00 UT are represented by asterisks, dotted circles and triangles respectively.
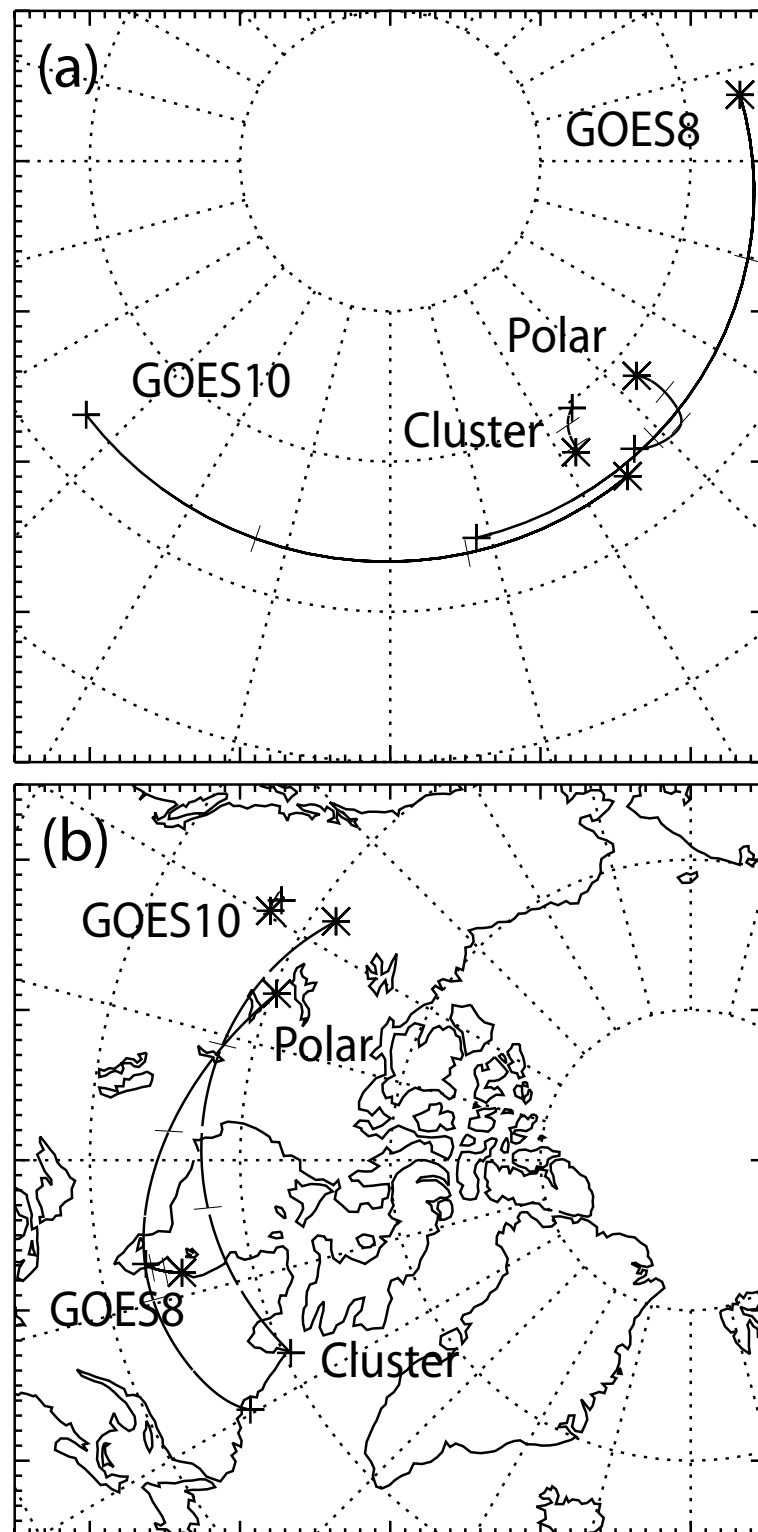
Figure 7.3: (a) MLT - invariant latitude (AACGM) and (b) geographic longitude and latitude locations of the magnetic footprints of Cluster 1, Polar, GOES 8 and GOES 10 between 06:00 and 12:00 UT calculated using the T89 model. The initial and final positions of the spacecraft are shown as crosses and asterisks respectively. The spacecraft positions are marked by dashes at 2-hourly intervals.

Northern hemisphere auroral data are also employed from the Far UltraViolet imager (FUV; Mende *et al.*, 2000a,b,c) on board the IMAGE spacecraft. During the interval, IMAGE was passing over the northern polar region, passing through apogee at 08:10 UT.

7.2 Observations

7.2.1 Solar wind observations

Solar wind ram pressure, density and velocity data from ACE are shown in Fig. 7.4 in panels (a)-(c) respectively. The IMF B_X, B_Y and B_Z are shown in panel (d)-(f) in GSM coordinates respectively. The IMF clock angle is shown in panel (g). The interval covered is 06:00-12:00 UT. In order to determine the solar wind conditions at Earth, it is necessary to lag the data from ACE. It has previously been shown that the high-latitude ionosphere and the IMF are strongly coupled, especially following solar wind pressure pulses (e.g. Volwerk *et al.*, 2004). The northward (H) component of the magnetic field from a number of the IMAGE magnetometer chain magnetometers, which cover 58-76° of magnetic latitude and were on the dayside during the interval, are shown in Fig. 7.5. At 07:15 UT there was a distinct change in the magnetic field. Stations north of Bear Island (BJN) showed large, long period variations, whereas stations south of Masi (MAS) showed a lower amplitude variability on a much smaller timescale. Comparing the magnetometer positions with images from FUV-WIC on the IMAGE spacecraft indicate that this difference in the dayside magnetic field response to the pressure pulse was dependant on whether stations were on open or closed fieldlines. The increased variability of the dayside magnetic field suggests that the lag between ACE and the Earth was 50 minutes. Data from ACE are presented with this lag applied. This is less than, but comparable with, the 60 min lag used by Zhang *et al.* (2002), and the 64 min lag predicted by the model of Khan and Cowley (1999). This discrepancy is probably due to the propagation of the shock wave in the frame of the solar wind.

At 07:15 UT, a solar wind pressure pulse, in which the solar wind ram pressure increased by a factor of five and dominated by a change in the solar wind density, impacted the magnetosphere (Fig.7.4(a)-(c)). The ram pressure then slowly decreased, reaching 6 nPa by the end of the interval, with increases of ∼2 nPa at 08:55 and 10:20 UT. Prior to the initial pressure pulse, the ram pressure was 2 nPa and the IMF was consistently southward. Data from 00:00 UT (not shown) indicates that the IMF was southward for almost 5 hours prior to the interval shown in Fig. 7.4. Just before the pressure pulse, the IMF B_Z dropped to 0 nT. Coincident with the pressure pulse, the IMF B_Z increased briefly before decreasing to vary about 0 nT. The IMF turned northward at 07:48 UT and varied about northward and southward from that time. Also following the pressure pulse, B_Y varied pseudo-periodically about 0 nT with a periodicity of 20-30 min until
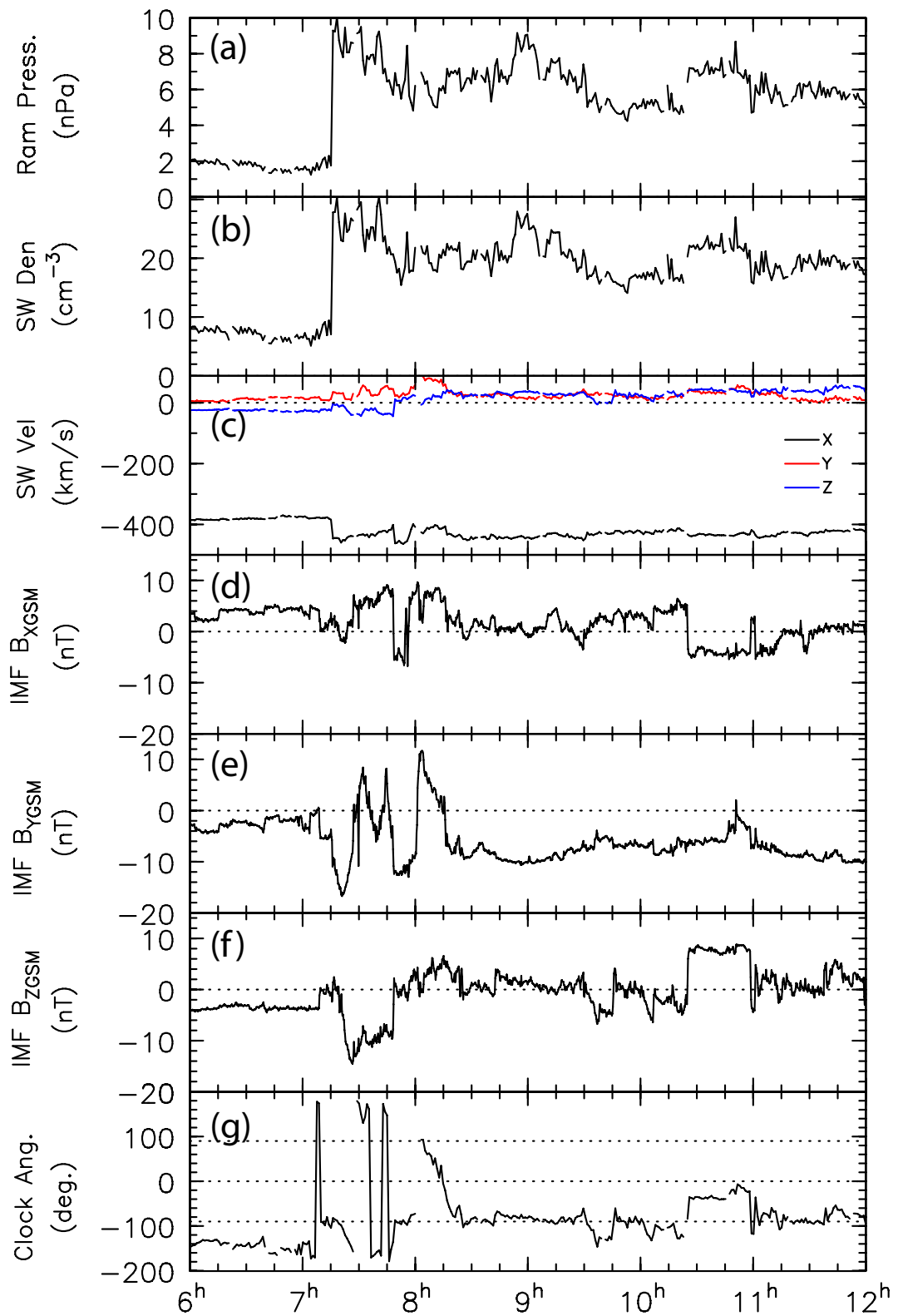
Figure 7.4: Plot of solar wind data from ACE. The data have been lagged by 50 minutes. Panel (a) shows the solar wind ram pressure. Panel (b) shows the ion density. Panel (c) shows the V_X (black), V_Y (red) and V_Z (blue) ion velocity components in GSM coordinates. Panel (d)-(f) shows the IMF in X, Y, and Z GSM coordinates respectively. Panel (g) shows the IMF clock angle in degrees.
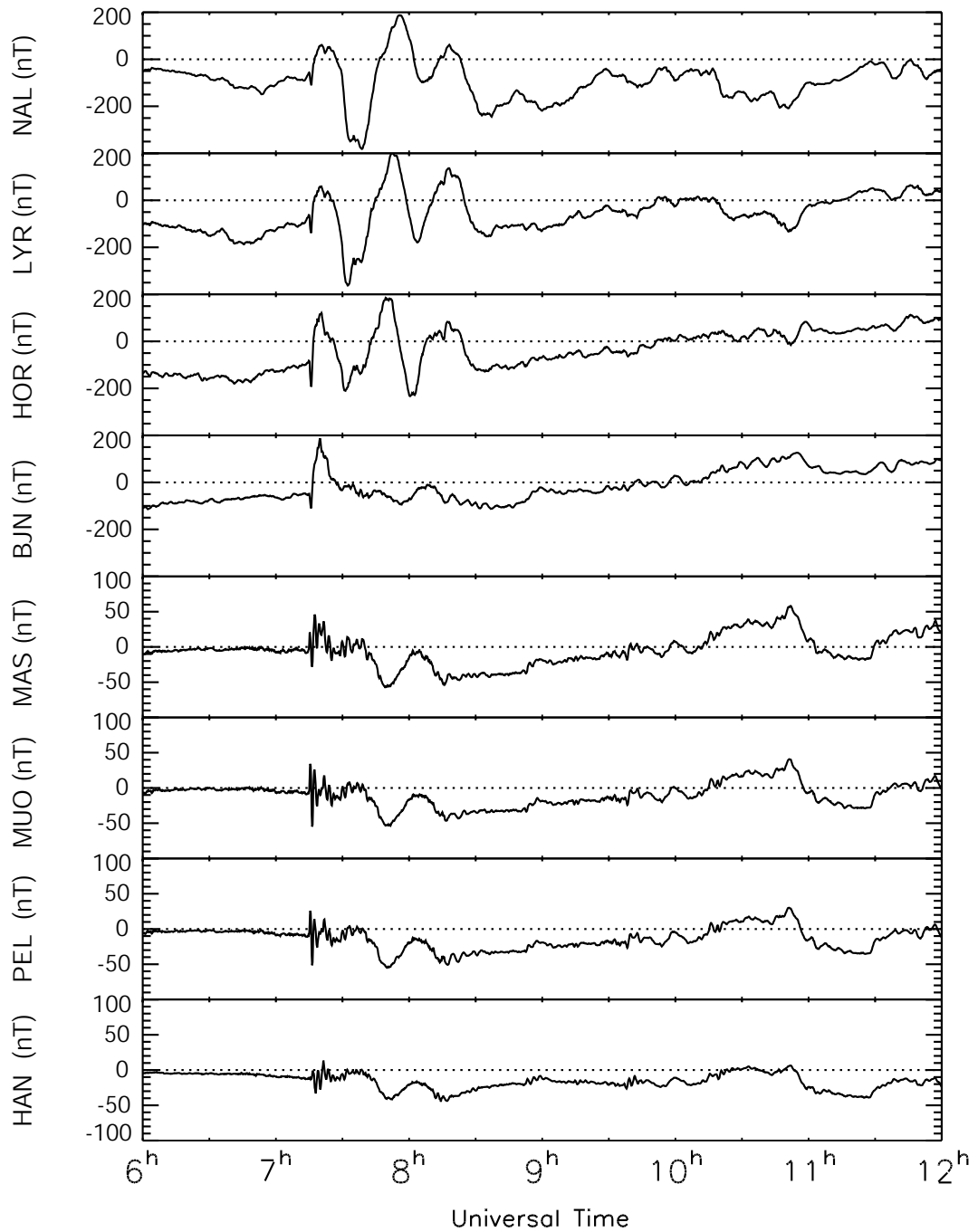
Figure 7.5: Plot of northward (H) component ground magnetometer data from selected stations in the IMAGE network. The dotted horizontal lines represent 0 nT.

08:20 UT, at which time it became persistently negative at -8 nT.

7.2.2 Magnetospheric compression and substorm dipolarizations

Figure 7.6 is a stack plot of magnetic field data from Cluster 1. Panels (a)-(c) show the GSM B_X, B_Y and B_Z components of the field. Panel (d) shows the magnetic field magnitude. Panel (e) shows the latitude angle of the field, taken to be the angle between the B_Z component and the B component in the XY plane. The blue traces represent EXT mode data, whereas the black traces represent data from the CAA. The red traces represent the model magnetic field values from the T89 model. The horizontal dashed lines represent zero in each panel.

From 06:00 to 07:15 UT the magnetic field detected by Cluster 1 was well matched by the model magnetic field, although B_Z was almost double the model value, hence the magnetotail was slightly more dipolar than the model would indicate. From 06:45 UT, the B_Z component dropped reaching half the model value by 07:15 UT, indicating that the magnetotail was stretching. At 07:18 UT, B_X and the magnetic field magnitude rapidly doubled, accompanied by a drop in the latitude angle, indicating that Cluster detected the compression of the magnetotail by the solar wind pressure pulse. Following the pressure pulse, there were two large dipolarizations at 07:50 and 08:37 UT, seen as a more than doubling of B_Z (panel c) and indicated by the vertical dashed lines in the plot. Between 10:30 and 11:15 UT, the magnetic field at Cluster became highly variable, as seen most prominently in the variation of the latitude angle, and the magnetic field magnitude dropped. This indicates that Cluster detected a substorm expansion phase. It should be noted that the three intervals when the largest (>50°) latitude angle enhancements were recorded are indicative of Cluster crossing the current sheet ($B_X = 0$ nT) and are not dipolarizations of the magnetotail.

Figure 7.7 shows (a) the electron density moments from the four Cluster spacecraft and (b) the ion moments from Cluster 1 and 4 from the PEACE and CIS instruments respectively. Between 08:30 and 10:00 UT, both the electron and proton densities were steady at 0.4 cm^{-3}. There was no apparent variation associated with the magnetic field variations in the FGM data. At 10:30 UT there was an increase followed by a brief decrease in the densities, coincident with the magnetic field variations seen in the FGM data associated with a substorm expansion phase.

Figure 7.8 shows a plot of magnetometer data from GOES 8 (black), 10 (blue) and Polar (red). The T89 magnetic field model is shown as the dashed lines in the respective colour of the spacecraft. Panels (a)-(c) show the B_X, B_Y and B_Z components of the magnetic field in GSM coordinates. Panel (d) shows the magnetic field magnitude. Panel
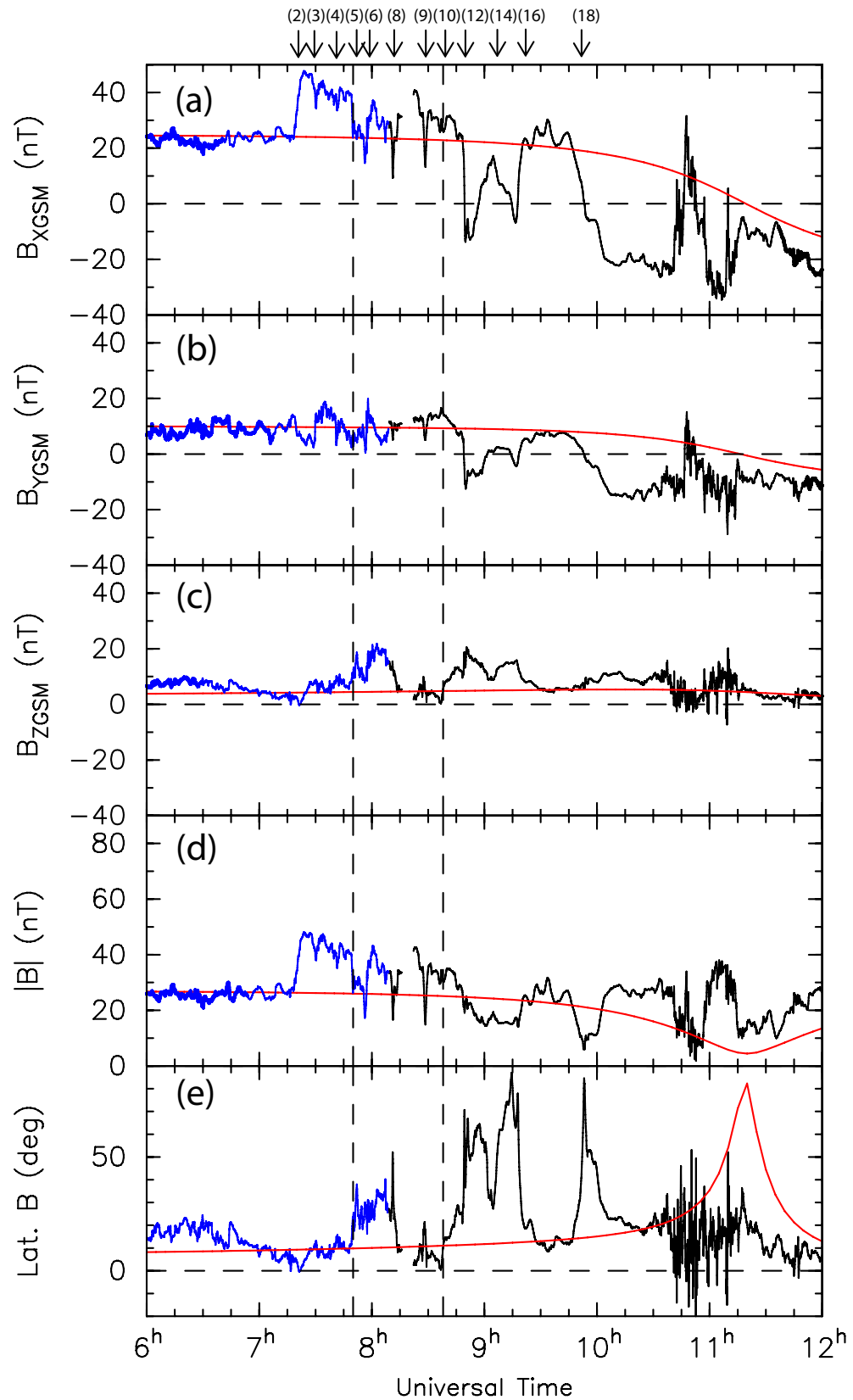
Figure 7.6: Plot of FGM data from Cluster 1. Panels (a)-(c) show the B_X, B_Y and B_Z magnetic field components in GSM coordinates. Panel (d) shows the magnetic field magnitude. Panel (e) shows the angle between the B_Z component and the component of the magnetic field in the XY plane (the latitude angle). The blue traces represent EXT mode data, whereas the black traces represent CAA data. The red trace is the output from the T89 magnetic field model. The horizontal dashed lines indicate zero in each panel. The dashed vertical lines indicate the start of the two substorm dipolarizations. The markers above panel (a) indicate events indicated in Tab. 7.3
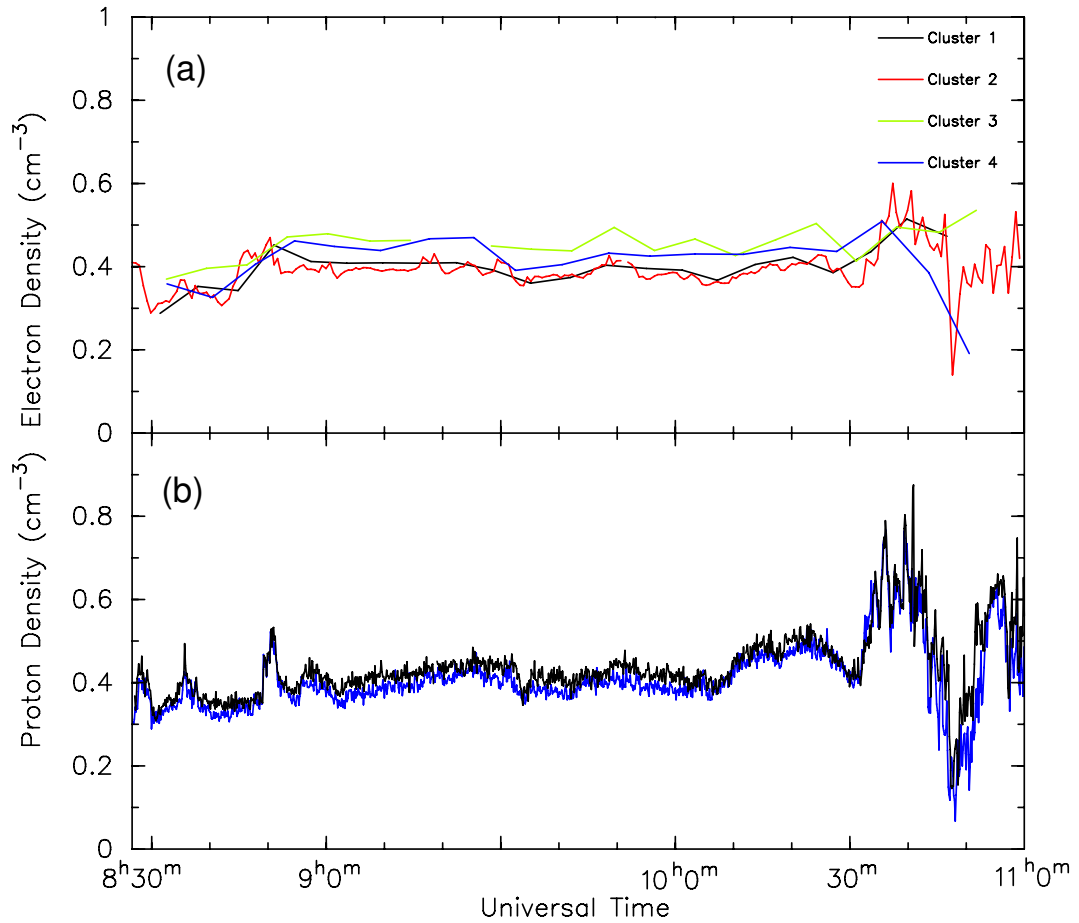
Figure 7.7: Plot of electron and ion density moments from the PEACE-HEEA and CIS-CODIF instruments on-board the Cluster spacecraft. Data is shown from Cluster 1 (black), Cluster 2 (red), Cluster 3 (green), Cluster 4 (blue).

(e) shows the magnetic field latitude angle as described before.

Prior to 07:00 UT, the magnetic fields at the GOES spacecraft were reasonably well matched by the T89 model, although, compared to the model, the magnetic field was slightly stretched, indicated by the slightly depressed B_Z components (Fig. 7.8c), particularly at GOES 10. Data from the Polar spacecraft show that it also detected a stretched field at this time in the post-midnight sector (Fig. 7.8c). At 07:15 UT, B_X and B_Y increased in magnitude at GOES 8 and Polar followed shortly by a larger increase in B_X and B_Z at GOES 10. That these increases are not associated with a dipolarization of the field indicates that the spacecraft detected an increase in the Region 1 currents caused by the pressure pulse. Polar also detected a circularly polarised wave at this time with a period of ∼150 s. GOES 8 and GOES 10 each detected two dipolarizations of the magnetic field at 07:47 UT and 08:45 UT and 07:35 and 08:25 UT respectively, indicated by the arrows in Fig. 7.8c. A final dipolarization of the magnetic field at GOES 8 at 09:00 UT brought the magnetic field level back towards the model field level, suggesting that the spacecraft moved out of the disturbed tail region and round onto the flanks of the magnetosphere. Polar detected two dipolarizations of the magnetic field at 08:08 and 08:40 UT respectively. The second of these dipolarizations was associated with a large
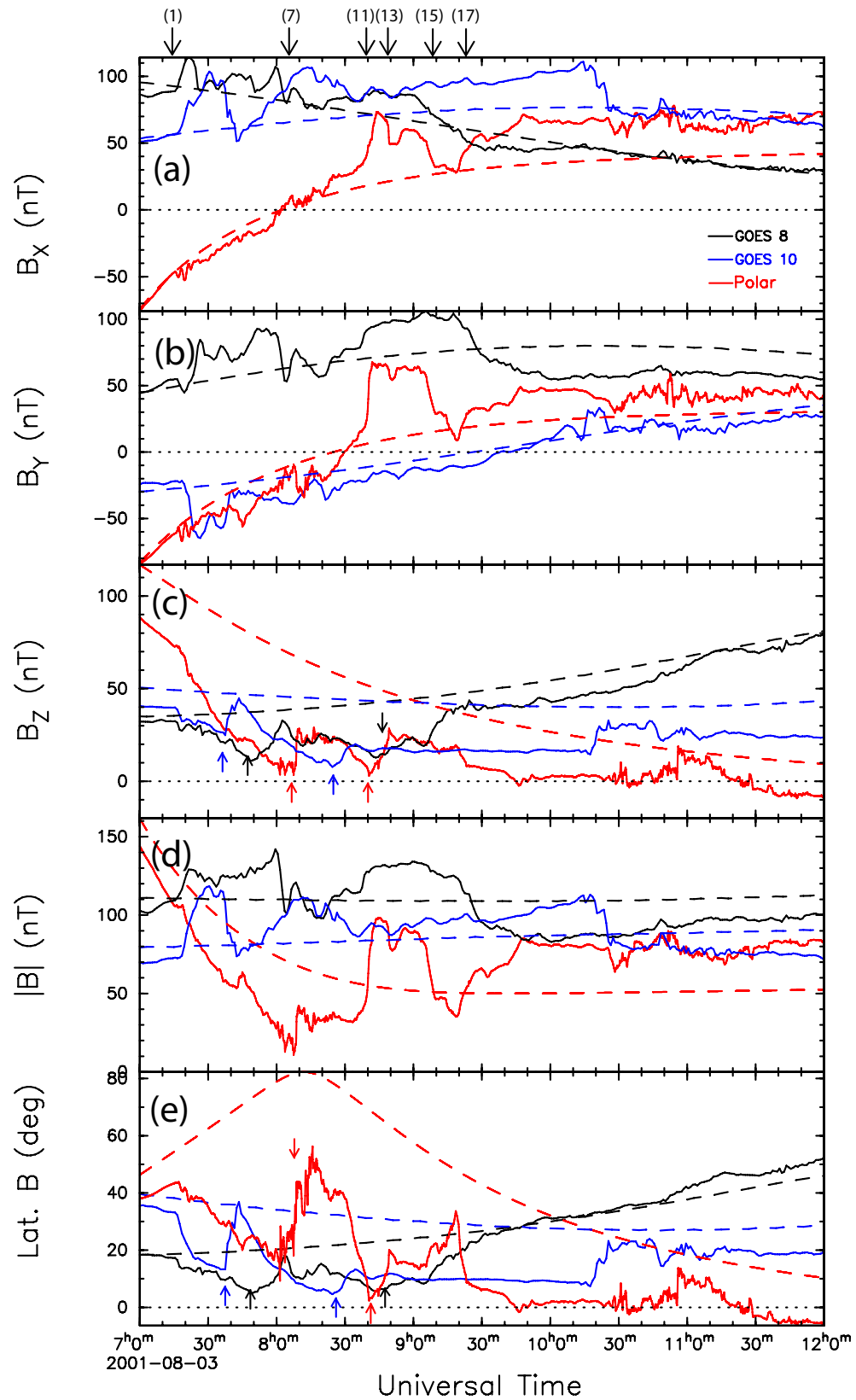
Figure 7.8: Plot of magnetometer data from GOES 8 (black) and GOES (blue) 10 and Polar (red). Panels (a)-(c) show the B_X, B_Y and B_Z magnetic field components in GSM coordinates. Panel (d) shows the magnetic field magnitude. Panel (e) shows the latitude angle as described above. The dashed traces show the output from the T89 magnetic field model in the respective colours of the spacecraft. The horizontal dotted lines indicate zero in each panel. The arrows in panels (c) and (e) indicate the dipolarizations examined, with the colour relating to the various spacecraft.

increase in B_X and B_Y, with similar but more extended increases observed by GOES 8. This would indicate that GOES 8 and Polar detected the Earthward directed current that makes up part of the substorm current wedge. It is interesting to note that GOES 10 did not see a signature of the return current, although this is likely due to the location of the spacecraft at that time. The dipolarization at GOES 10 at 10:15 UT was due to the substorm expansion phase at that time. The substorm detected at Cluster appears as increased field variability and increased latitude angle from 10:25 UT.

In the following, it is assumed that the field variations are locally planar, in particular on the scale size of the Cluster tetrahedron. As such, MVA and four-spacecraft timing analysis (see Chapter 4) are used to determine the propagation direction of the compression front and dipolarizations in the tail.

Tables 7.1 and 7.2 show the results of MVA and four-spacecraft timing analysis of the magnetic field data from Cluster and Polar for events 2, 5 and 10 (Table 7.1) and events 1, 7 and 11 (Table 7.2). These represent the pressure pulse (events 1 and 2), and four dipolarisations (events 5, 7, 10 and 11). Also listed are the angular differences between the MVA and four-spacecraft timing vectors from Cluster (Table 7.1) and between the Polar MVA and Cluster MVA and Polar MVA and four-spacecraft timing vectors (Table 7.2). The MVA results are obtained from a 2 min window centred on the time listed, whereas the results from the four-spacecraft timing analysis are from a 10 min window centred on the time given. This larger window for the four-spacecraft timing analysis aids the comparison of the field between multiple spacecraft and visual checking of the results. The lags between the spacecraft were determined from local minima and maxima in the B_X component for the pressure pulse event and the B_Z component for the dipolarizations. The data were also smoothed using a 40 s Boxcar filter in order to remove any small scale fluctuations in the magnetic field. Results shown in italics were determined using EXT mode data from Cluster.

The results from the four-spacecraft timing analysis indicate that the normal to the compression front at Cluster was orientated predominantly in the Z direction, whereas the dipolarization fronts were travelling in the dawnward and Earthward. The MVA vectors for the pressure pulse and the second dipolarization, when $\lambda_2/\lambda_3 > 10$, are consistent with this. The MVA vector for the first dipolarization agrees that the dipolarization front was orientated towards dawn, but suggests a stronger orientation in the Z direction and an opposite sense in the X direction. However, the low λ_2/λ_3 ratio suggests that the minimum variance direction was not well defined for this event.

The MVA results from Polar suggest that the orientation of the compression front was either Earthward or tailward, given that the X component of the normal was the largest (0.82), although the occurrence of the wave in the Polar data at that time and the spacecraft's rapid transit through the inner magnetosphere distorts the results of the MVA. The results also show that the first dipolarization front was orientated strongly in

No.	Event	UT	MVA (X, Y, Z)	λ_2/λ_3	4SCT (X, Y, Z)	Speed	Clock (km s^{-1})	Ang. Diff
2	Press. Pulse	07:19	(-0.26, 0.16, -0.98)	12.2	(0.06, 0.33, -0.94)	67	161	17
5	Dipolarization	07:50	(-0.27, -0.61, -0.74)	2.03	(0.64, -0.77, 0.04)	80	-87	75
10	Dipolarizarion	08:37	(0.47, -0.88, -0.07)	18.1	(0.44, -0.76, -0.49)	42	-57	29

Table 7.1: The means of the outputs of the minimum variance analysis (MVA) and four spacecraft timing (4SCT) across the Cluster (Cl) spacecraft at various universal times. The clock angle is the angle in the YZ plane between the Z-axis and the normal direction in degrees. The angular difference is the angle between the MVA and four-spacecraft timing vectors.

No.	Event	UT	MVA (X, Y, Z)	λ_2/λ_3	Ang. Diff. MVA	Ang. Diff. 4SCT
1	Press. Pulse	07:17	(0.82, 0.57, 0.05)	9.79	100	79
7	Dipolarization	08:07	(-0.33, -0.79, -0.51)	4.44	18	68
11	Dipolarization	08:40	(-0.027, -0.13, -0.99)	10.2	80	55

Table 7.2: The results of minimum variance analysis (MVA) of Polar (P) MFE data at various universal times. The angular differences are the angles between the Polar MVA vectors and the MVA and four-spacecraft timing vectors from the corresponding event at Cluster.

the Y direction, in keeping with the propagation of a dipolarization front from GOES 10 towards dawn. This vector was also similar to the MVA vector from Cluster (within 18°), but with a similarly low λ_2/λ_3. Conversely, the second dipolarization front was directed almost entirely in the Z direction, quite different from the implied propagation from the GOES spacecraft and the results from Cluster. However, given that GOES 8 and Polar detected the substorm current wedge (SCW) at this time, this would suggest that the variations in the magnetic field at Polar were dominated by the Earthward contraction of the innermost fieldlines carrying the SCW. However, it is not clear why the SCW did not appear to have the same motion as the dipolarization at Cluster.

Figure 7.9 shows the average auroral luminosity between 55 and 80° magnetic latitude in bins of 1 hour of MLT from the FUV-WIC on-board the IMAGE spacecraft. The MLT marked indicates the westward edge of the bin, such that the 00 MLT covers 00-01 MLT. The traces have been normalised by subtracting the minimum value from all the values for each trace. The traces are separated by 1500 R.

At 07:15 UT, the auroral luminosity across the night side began to increase, reaching a peak at 07:27 UT. The largest increase occurred between 23 and 02 MLT, where the average luminosity increased by 750-1000 R, whereas outside this range the increase was $\sim$500 R. At 07:40 UT there was an increase of over 1000 R in the 22 MLT sector, indicated by a black, vertical dashed line in Fig. 7.9 accompanied by a 500 R increase in the 23 MLT sector. This propagated eastward, with the peak of the brightening reaching the 04 MLT sector by 08:18 UT, indicated by a dashed line in Fig. 7.9, before decaying to reach a local minimum at 08:48 UT. A further, smaller enhancement appeared at 08:18 UT in the 22 MLT sector and again propagated eastward, with the peak of the brightening reaching the 03 MLT sector by 09:12 UT, again indicated by dashed lines in Fig. 7.9, before decaying to a minimum at 10:00 UT. The eastward velocities of these auroral disturbances were 2.4 and 1.5 $\mathrm{km\,s^{-1}}$ respectively. The motion of these two enhancements across the auroral region is shown by the two red lines in Fig. 7.9. Following the second enhancement, the auroral luminosity decreases towards its minimum value across all MLT sectors bar 20 and 04 MLT. There was then a final enhancement, initiated in the 23 MLT sector at 10:12 UT, which propagated both eastward and westward.

Comparing the auroral data (Fig. 7.9) with the Cluster (Fig. 7.6) and Polar and GOES (Fig. 7.8) magnetometer data, it becomes apparent that the eastward moving brightenings are associated with localised dipolarizations of the magnetotail. At 07:35 UT, GOES 10 observed a dipolarization, at which time the spacecraft was located close to 22 MLT. Between 07:45 and 08:00 UT, the magnetic field at GOES 8 and Cluster dipolarised, followed by a sharp dipolarization at Polar at 08:08 UT. At this time, these spacecraft were in the 02 MLT sector. In concert with each of these events was the large, rapid increase in auroral luminosity in the 22 and 01 MLT sectors respectively. A second dipolarization was observed by Cluster and GOES 8 starting at $\sim$08:40 UT, associated with the second auroral brightening arriving in the 02 MLT sector. This indicates that
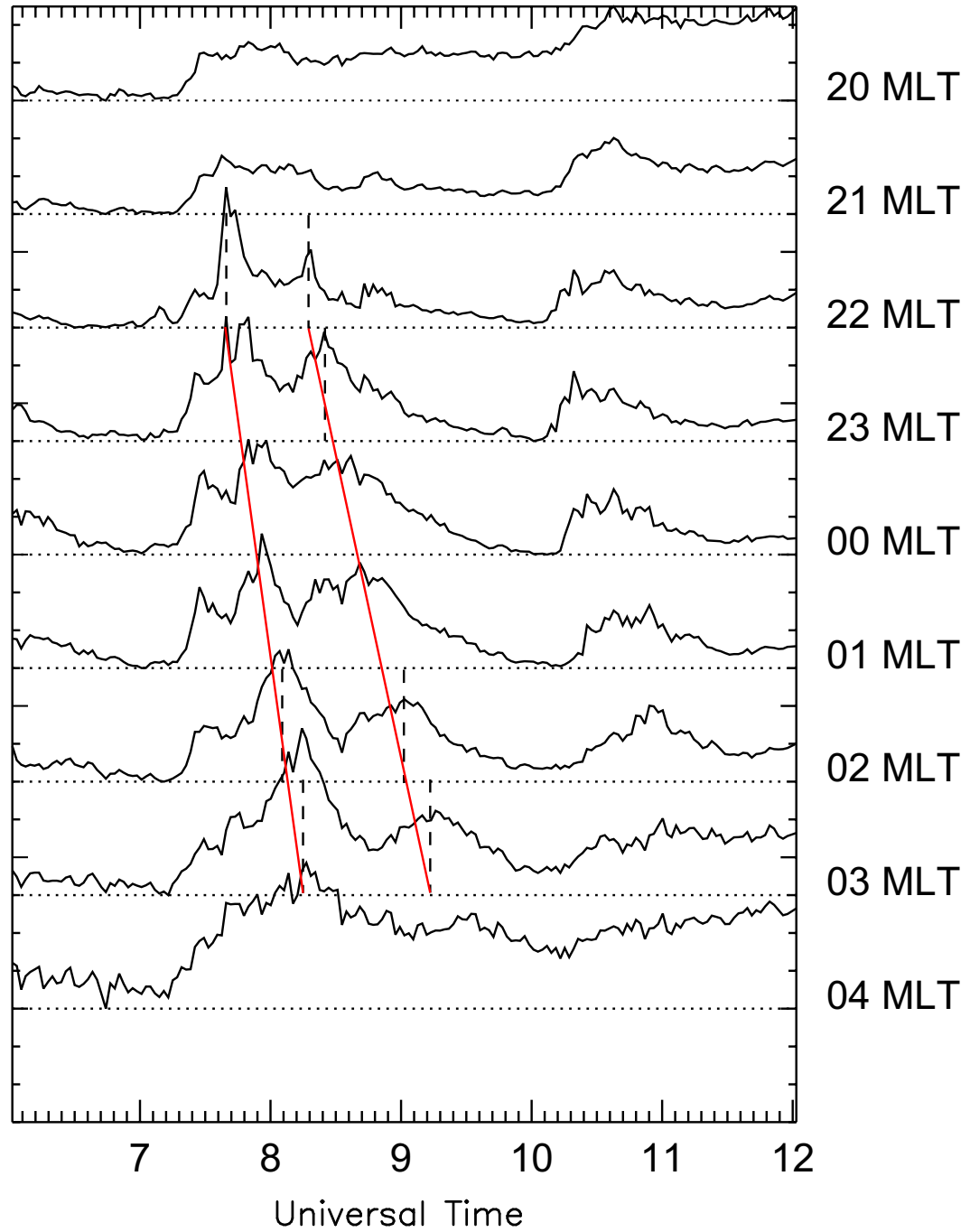
Figure 7.9: Plot of auroral luminosity measured by FUV WIC on board the IMAGE spacecraft averaged over 1 hour of MLT and 55 to 80°magnetic latitude. Each trace has had its minimum value subtracted, such that the dotted lines indicate the minimum value which has been set to 0 R. The traces are separated by 1500 R.

the dipolarizations were associated with the auroral substorm activity. Using the T89 model to map the velocity of the dipolarization fronts into the ionosphere gives eastward velocities of 5.6 and 2.5 $km\,s^{-1}$, approximately twice the speed of the aurora.

In summary, data from the magnetometers on-board Cluster, Polar and GOES 8 and 10 have shown that prior to the solar wind pressure pulse the magnetotail was stretched due to an extended period of southward IMF. Following the arrival of the pressure pulse, the magnetosphere was compressed outside 6 R_E and the Region 1 currents were enhanced. The effects of the pressure pulse travelled downtail from GOES to Cluster, as one would expect for a travelling solar wind pressure front. Following the pressure pulse, dipolarizations were observed at GOES 10, GOES 8, Cluster and Polar at 07:35, 07:47, 07:50 and 08:08 UT, respectively, and again at 08:25, 08:45, 08:37 and 08:40 UT, respectively. The dawnward motion of these dipolarizations was consistent with observations of dawnward moving aurora in the IMAGE FUV data, indicating that the dipolarizations were due to the occurrence of substorms and that the substorm dipolarizations could be observed across a distance of 12 R_E downtail.

7.2.3   Current sheet wave observations

Following the solar wind pressure pulse, Cluster observed multiple, pseudo-periodic reductions and recoveries in the B_X component of the magnetic field, accompanied by local peaks in the magnetic field latitude angle starting at 07:30 UT (Fig. 7.6). After 08:48 UT, Cluster crossed the current sheet several times. These current sheet crossings have previously been studied by Zhang *et al.* (2002), who determined that they were due to current sheet waves. Given that B_X reduces on approach to the current sheet, it is apparent the periodic reductions in B_X prior to the current sheet crossings were also due to a wavy current sheet.

Tables 7.3 and 7.4 list 12 current sheet oscillations from the Cluster and Polar datasets. These are indicated by the arrows in Figs. 7.6 and 7.8. Table 7.3 lists the results from MVA and four-spacecraft timing analysis from Cluster and Table 7.4 lists the MVA results from Polar as described above.

The angles between the MVA and four-spacecraft timing vectors from the Cluster data indicate that the two techniques give similar results for the direction of the current sheet wave, with the vectors being within $\sim 10°$ -20° of each other even though the λ_2/λ_3 ratio indicates that some of the MVA results are fairly poor ($\lambda_2/\lambda_3 < 10$). Comparing the MVA results from Polar with the MVA and four-spacecraft timing analysis results from Cluster shows that these vectors were not so well aligned, with the angle between the vectors varying between 45° and 70° . However, upon closer inspection, it is obvious that all the vectors after 07:57 UT were directed dawnwards and Earthwards at both Cluster and Polar, apart from the MVA vector from event 14 (Cluster). The largest variations between

No.	UT	MVA (X, Y, Z)	λ_2/λ_3	4SCT (X, Y, Z)	Speed (km s^{-1})	Clock	Ang. Diff
3	07:30	(0.23, 0.11, 0.97)	5.61	(0.122, 0.31, 0.94)	66	18	13
4	07:41	(0.19, 0.31, 0.93)	4.74	(-0.14, 0.09, 0.99)	82	5	23
6	07:57	(0.47, -0.86, 0.17)	1.81	(0.16, -0.98, 0.08)	70	-85	21
8	08:10	(0.19, -0.97, 0.13)	19.7	(0.13, -0.94, 0.32)	61	-71	13
9	08:27	(0.38, -0.92, 0.11)	12.0	(0.25, -0.93, -0.26)	40	-74	22
12	08:48	(0.41, -0.88, -0.24)	4.47	(0.35, -0.89, -0.29)	7	-108	15
14	09:05	(-0.21, -0.98, 0.05)	3.4	(0.20, -0.94, -0.28)	29	-106	15
16	09:20	(0.22, -0.83, -0.51)	12.8	(0.2, -0.94, -0.28)	29	-106	15
18	09:50	(0.30, -0.95, 0.06)	5.58	(0.64, -0.76, 0.14)	25	-80	21

Table 7.3: The means of the outputs of the minimum variance analysis (MVA) and four spacecraft timing (4SCT) across the Cluster (C1) spacecraft at various universal times. The clock angle is the angle in the YZ plane between the Z-axis and the normal direction in degrees. The angular difference is the angle between the MVA and four-spacecraft timing vectors.

No.	UT	MVA (X, Y, Z)	λ_2/λ_3	Ang. Diff. MVA	Ang. Diff. 4SCT
13	08:49	(0.53, -0.57, 0.631)	4.55	56	52
15	09:08	(0.84, -0.54, -0.06)	38.8	70	46
17	09:25	(0.38, -0.55, 0.74)	2.72	54	67

Table 7.4: The results of minimum variance analysis (MVA) of Polar (P) MFE data at various universal times. The angular differences are the angles between the Polar MVA vectors and the MVA and four-spacecraft timing vectors from the corresponding event at Cluster.

the Cluster and Polar vectors appears to be in the Z component; the Z components from the four-spacecraft timing analysis at Cluster were all less than 0.33 and predominantly negative, whereas the components from the MVA at Polar were generally larger than this but positive. Also, the X component of the Polar MVA vectors was a factor of two or more larger.

To summarise; Cluster and Polar observed large, rapid changes in the magnetic field B_X component following the solar wind pressure pulse, signalling the presence of current sheet waves. MVA and four-spacecraft timing analysis show that the current sheet waves were travelling predominantly in the -Y direction at Polar and Cluster. However, the Z component of the normal to the current sheet had opposite senses at Cluster and Polar, such that the angle between the current sheet orientation at Cluster and Polar was large.

7.2.4   Ground Magnetometer Observations

Shown in Fig. 7.10 are the northward (H) magnetic field component data from the CANOPUS magnetometer chain stations that run across 4 hr of MLT at constant magnetic latitude. The red lines show the data filtered between 1000 and 2000 s. Following the pressure pulse at 07:15 UT, a magnetic bay formed in the Gillam (GILL) and Rabbit Lake (RABB) magnetometer traces. At the more easterly stations, a long lived magnetic bay is not apparent, although there are periodic ($\sim$20 min) variations. The filtered data (red traces) show these more clearly and show that these variations even appear at Gillam, although weaker than at the other stations.

Figure 7.11 shows the spectral power from FFTs of the CANOPUS data shown in Fig. 7.10 between 07:30 and 10:00 UT. This window was taken so as to avoid the complications associated with analysing the near-step function at 07:15 UT due to the solar wind pressure pulse. Also shown is the FFT of the B_X component of the magnetic field detected by Cluster during the same time. Evident at each of the stations, including Cluster, is a peak in the spectral power at 0.77 mHz (21 min), marked with the dotted line. Figure 7.12 shows the longitudinal profile of the FFT power and phase for the 0.78 mHz signal. The power maximises at -68° latitude (Fort Simpson, FSIM) and drops off rapidly to the west, but less rapidly to the east. The power maximum is also associated with a minimum in the phase difference, with the phases approaching the same values at the extremities of the chain. This indicates that there was a wave source in the vicinity of Fort Simpson.
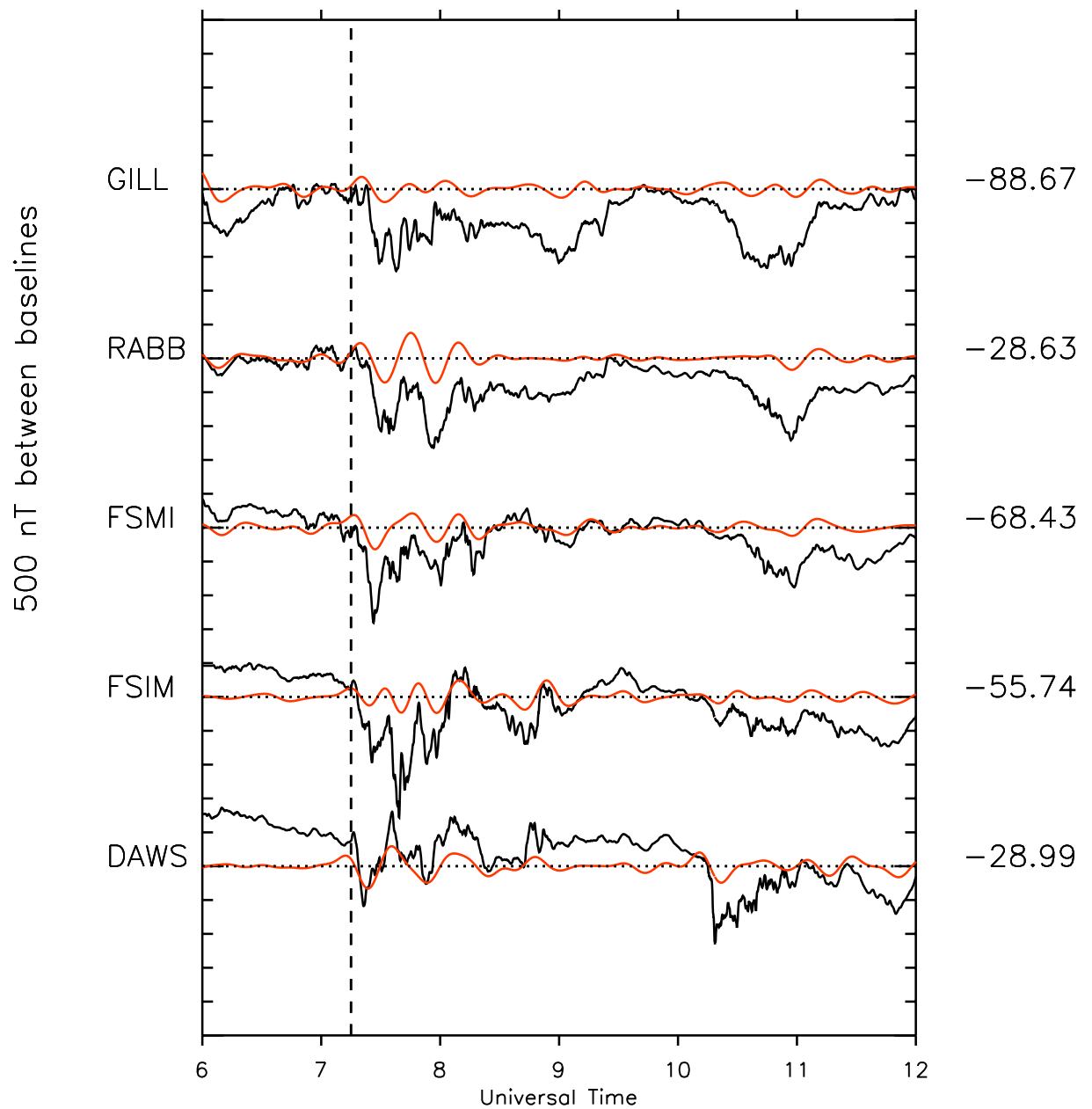
Figure 7.10: Plot of magnetometer data from stations in the CANOPUS magnetometer chain running across 4 hr of MLT showing the northward (H) component of the magnetic field. The red lines show the data filtered between 1000 and 2500 s.
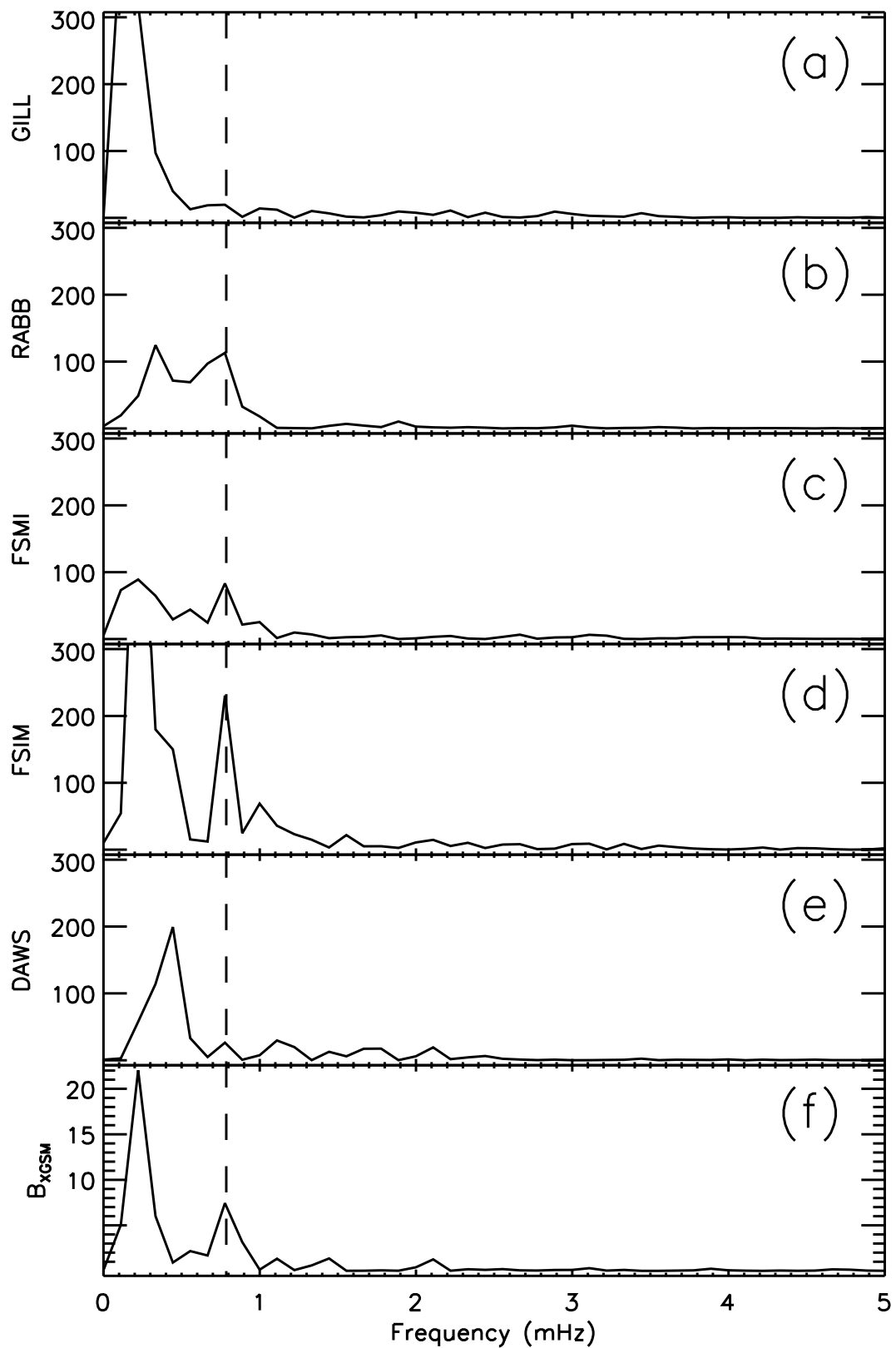
Figure 7.11: Plot of the FFTs of the northward (H) component of the magnetic field from stations in the CANOPUS magnetometer chain running across 4 hr of MLT and Cluster 1. The FFT was performed on data between 07:30 and 10:00 UT.
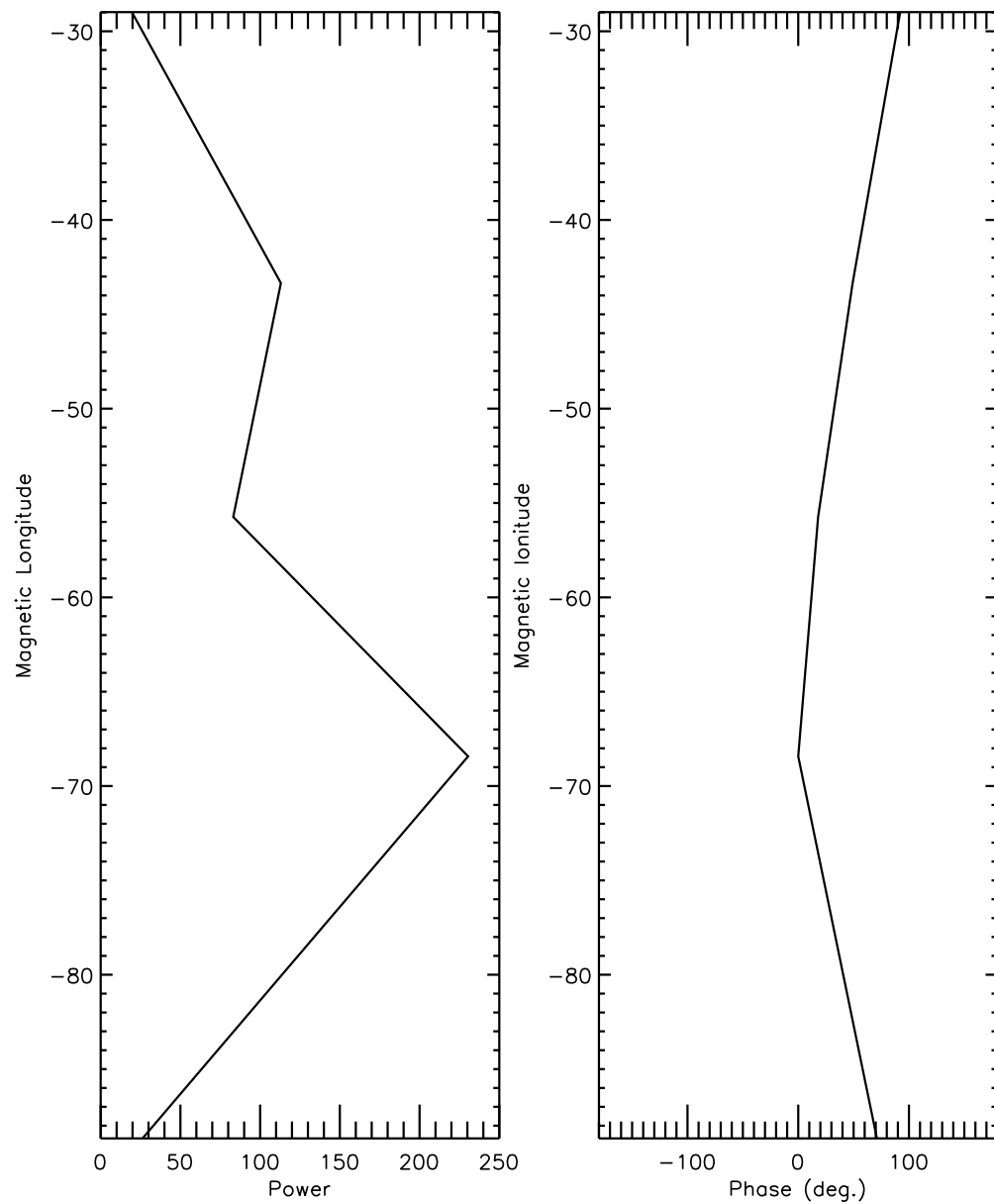
Figure 7.12: Plots of the FFT spectral power and phase difference from FSIM for stations in the CANOPUS magnetometer chain running across 4 hr of MLT against their magnetic longitude for a frequency of 0.77 mHz.

7.2.5   Current sheet wave models

Various models have been proposed to explain how the current sheet supports waves propagating perpendicular to the magnetic field. Early models based on MHD were unable to explain the relatively low speed of the cross-tail waves ($\sim$100 km s^{-1}) compared with the local sound speed ($\sim$1000 km s^{-1}) whereas models based on ion drift fail to explain wave motion in the dawnward direction (Sergeev *et al.*, 2004b, and references therein). Golovchanskaya and Maltsev (2005) proposed a model based on the application of the ballooning instability waves (Safargaleev and Mal'Tsev, 1986) in a curved magnetic field. From Liu (1997), they find that the frequency of the current sheet wave is given by

$$\omega^2 = V_A^2 k_c \left(k_b + k_c + \sqrt{(k_b + k_c)^2 + O\left(k_\parallel^2\right)} \right) \tag{7.1}$$

where V_A is the Alfvén velocity of the particles in the current sheet, k_c is the inverse of the radius of curvature of the field line, k_b is the inverse of the scale length of the magnetic field variation perpendicular to the field and $k_\parallel$ is the inverse of the scale length of the magnetic field variation along the magnetic field. In the approximation that $k_b, k_\parallel \ll k_c$, and estimating taking $k_c = B_x^{lobe}/(aB_Z)$, where a is the current sheet half-thickness, this becomes

$$\omega = \frac{\sqrt{2}V_A B_X^{lobe}}{aB_Z} \tag{7.2}$$

Assuming that the magnetic pressure of the lobes is balanced by the thermal pressure in the current sheet it can be shown that the thermal velocity of the current sheet particles is $v_T = B_X^{lobe}/(\mu_0\rho)^{1/2}$. Taking the further assumption that the magnetic field in the lobes is dominated by B_X^{lobe} and the magnetic field in the sheet tends towards B_Z, the angular frequency of the current sheet wave becomes

$$\omega = \sqrt{2}\frac{v_T}{a} \tag{7.3}$$

From the dispersion relation for ballooning instability waves, Golovchanskaya and Maltsev showed that the group velocity of the wave is

$$v_y^{group} = \frac{\omega k_c^2}{a\left(k_c^2 + k_y^2\right)^{3/2}} \tag{7.4}$$

where k_y is the wave vector of the current sheet wave. Assuming that $k_y \approx k_c$, this can be re-arranged such that the current sheet half-thickness can be calculated from other observable variables,

$$a = \frac{v_T t}{4\pi} \equiv \frac{B_X^{lobe} t}{4\pi(\mu_0\rho)^{1/2}} \tag{7.5}$$

where t is the period of the wave in the Y direction.

Erkaev *et al.* (2008) considered that the WKB approximation was inappropriate for

the current sheet. Instead, they proposed a model based on linearised MHD solved in a piecewise manner from the centre to the edge of the current sheet then from the edge of the current sheet to the ionosphere. From this, they determined that the flapping frequency was given by

$$\omega_f = \sqrt{\frac{1}{\mu_0 \rho} \left\langle \frac{\partial B_x}{\partial z} \right\rangle \frac{\partial B_z}{\partial x}} \tag{7.6}$$

where ρ is the current sheet density and the group velocity was

$$v_g = \frac{\omega_f \triangle}{\sqrt{k^2 \triangle^2 + \lambda_k^2}} \tag{7.7}$$

where $\triangle$ is the current sheet half-thickness, k is the wave number and λ_k is the dimensionless numerical solution to $\tan \lambda_k = k\triangle/\lambda_k$. Note that the equations have been converted from the given form in Erkaev *et al.* (2008), in Gaussian units, to a form in SI units.

As both the above models can either determine the current sheet half-thickness or require it as an input, we use the data from the Cluster spacecraft to determine the current sheet thickness for each of the current sheet crossings.

$$Z * (t) = \int_{t_1}^{t_2} \frac{\partial B_L}{\partial t} [\nabla_n . B_L]^- 1 \tag{7.8}$$

where B_L is the magnetic field in the maximum variance direction (approximately the X direction) and $\nabla_n.B_L$ is the gradient of the B_L component in the direction perpendicular to the current sheet. The current sheet half-thickness can then be determined from the profile of the current density, $|\mathbf{j}|$, determined from the curlometer technique against Z*. Figure 7.13 shows (a) B_L, (b) the current density profile in the Z* direction. The vertical lines in (b) show the current sheet half-thickness. The current sheet profile for the final event (0950 UT) shows that the current sheet was bifurcated at this time. As such, the current sheet half-thickness is taken as the distance from the minimum between the two peaks to the position of half maximum current.

Runov *et al.* (2006) showed that the distance of the barycentre of the Cluster spacecraft from the centre of the current sheet (Z*) could be calculated as

Data from the PEACE and CIS-CODIF sensors (Fig. 7.7) show that the particle density during this interval was $\sim$0.4 cm^{-3}. Using an ion population of 95% H+ and 5% O+, as detected by the CIS-CODIF sensor, the lobe magnetic field in the X direction to
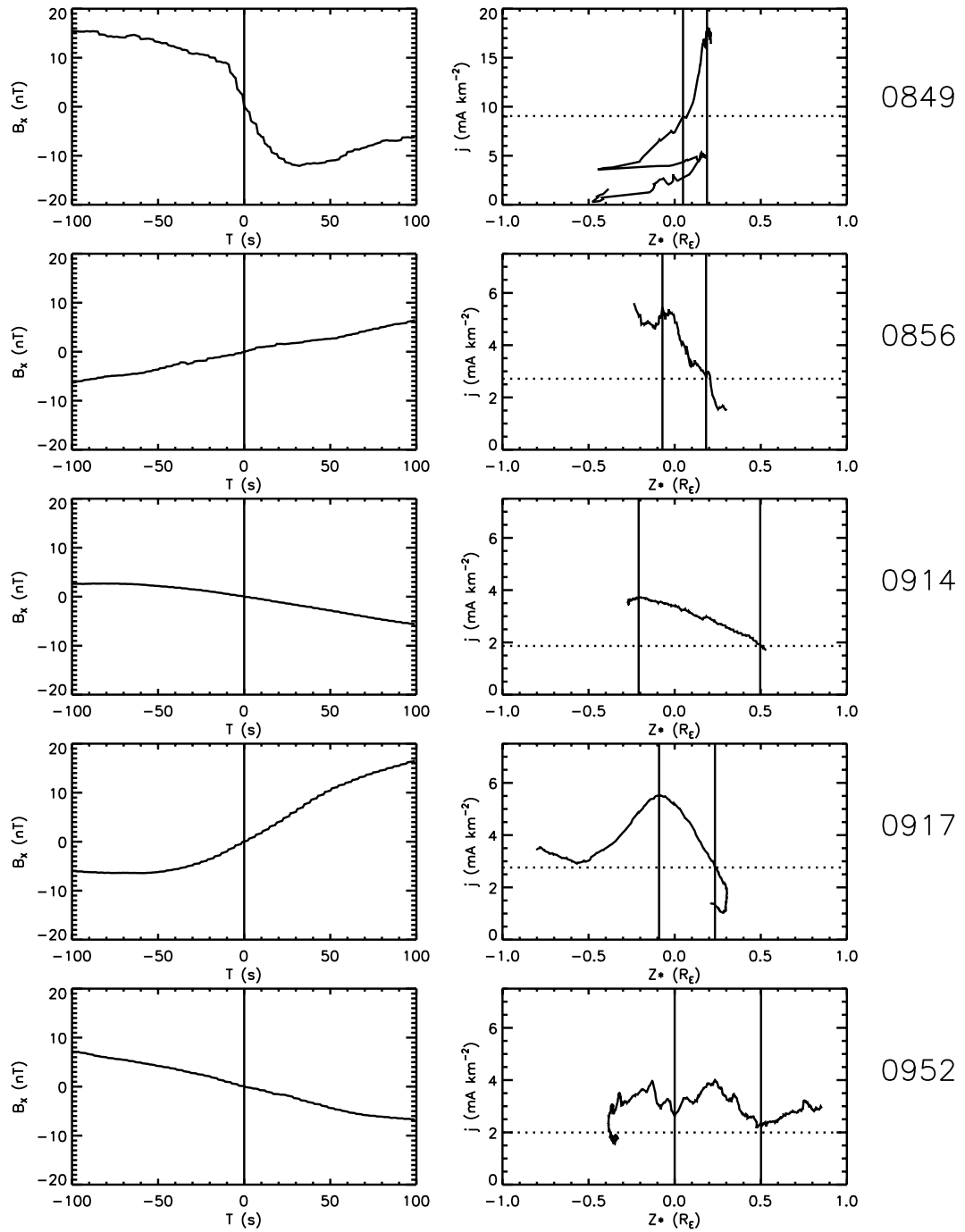
Figure 7.13: Plots of (a) the average B_X across the Cluster spacecraft and (b) the total current density against Z* for each of the current sheet crossings by Cluster.
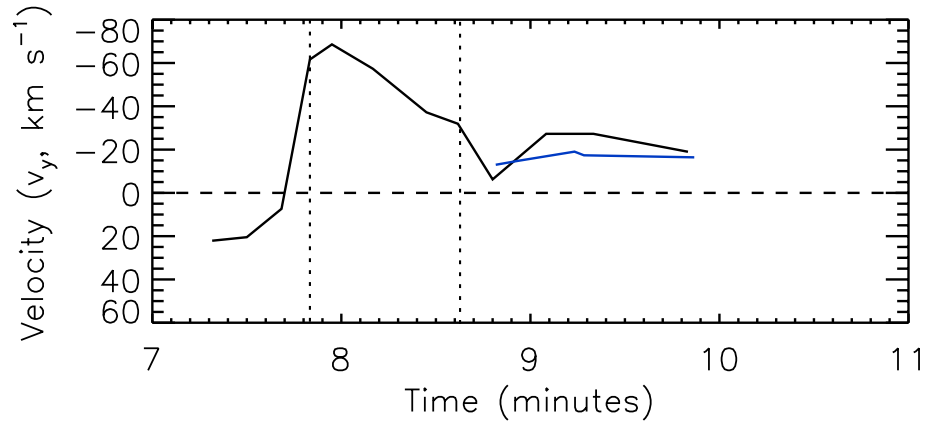
Figure 7.14: Plot of the velocity in the Y direction (black), determined from four-spacecraft analysis, for the dipolarization and wave fronts against time from the observation of the magnetospheric compression at Cluster and the velocity calculated from the Erkaev *et al.* (2008) model using the observed current sheet half-thicknesses and a wave period of 20 min. The dashed lines indicate the times of the dipolarizations.

be 30 nT then, from Equation 7.4, the current sheet thickness required to support the wave is 0.6 R_E per minute of wave period. Using the 20 min wave period that was used by Zhang *et al.* (2002), the current sheet thickness required to support the wave for the Golovchanskaya and Maltsev (2005) model is approximately 12 R_E which is an order of magnitude larger than the observed thicknesses and comparable with the tail radius (see Chapter 1.

Using the mean magnetic field gradients determined by Cluster during each 200 s surrounding each of the current sheet crossings and the same ion density as above, the wave periods in the Erkaev *et al.* model are determined to be between 2 to 8.5 min. Using the average magnetic field gradients during the interval gives a wave period of 6 min. These periods are somewhat smaller than the observed period of approximately 20 min, although within an order of magnitude of the observed period. Using the calculated wave frequencies, the wave speeds from the Erkaev *et al.* model were 44 to 130 $km\,s^{-1}$, although using a 20 min period gives velocities from 13 to 20 $km\,s^{-1}$, approximately two-thirds of the observed velocities.

Figure 7.14 shows the temporal variation of the velocity in the Y GSM direction, determined from the four-spacecraft timing analysis of the Cluster data, along with the velocities calculated from the Erkaev *et al.* model for a wave period of 20 min (blue trace). The observed and model velocities follow similar trends, although the model velocities are approximately two-thirds of the observed velocities, as noted above.

7.3 Discussion

7.3.1 Magnetospheric compression and substorm dipolarizations

In this study, a solar wind pressure pulse was seen to compress the magnetosphere prior to the onset of two substorms following an extended period of southward IMF. Data from Cluster indicates that 4 minutes following the arrival of a solar wind pressure pulse at the dayside, the magnetic field magnitude in the tail increased by a factor of $\sim$1.5, dominated by an increase in the B_X component (Fig. 7.6a and d). Data from GOES 8, GOES 10 and Polar also showed increases in the magnetic field magnitude at this time (Fig. 7.8) associated with an enhancement in the Region 1 currents. Polar observed a circularly polarised wave at this time, with a period of $\sim$2.5 min. The solar wind pressure pulse excited global auroral activity. Data from FUV-WIC on board the IMAGE spacecraft showed that, following the solar wind pressure pulse, the average luminosity in the nightside MLT sectors increased by up to 1000 R, with the largest increase occurring from 23 to 03 MLT.

Comparing the vectors from the MVA and four-spacecraft timing at Cluster for the pressure pulse and two dipolarizations suggests that when the minimum variance direction is well defined ($\lambda_2/\lambda_3 > 10$) the two techniques give similar results, in keeping with Eastwood *et al.* (2005). Under these conditions, the dipolarization was observed to move dawnward. Even when $\lambda_2/\lambda_3 < 10$, the MVA vectors had a Y component comparable to the four-spacecraft timing vector, both at Cluster and Polar. Comparing these results with the auroral data suggests that the substorm dipolarization front was extended over 12 R_E and that the movement of the dipolarization front and the auroral substorm are related. This is consistent with (Liou *et al.*, 2002) and Nakamura *et al.* (2005b) who showed the correlation between the motion of an auroral substorm and dipolarizations at geostationary orbit and the detection of a substorm dipolarization front across 5 R_E respectively. The eastward motion of the aurora is also consistent with the IMF B_Y control of the motion of the auroral bulge (Liou *et al.*, 2006; Liou and Ruohoniemi, 2006a,b).

That the auroral features move at half the projected speed of the dipolarization fronts in the ionosphere could be due to several factors. Firstly, the T89 model does not account for the occurrence of the substorms. Figures 7.6 and 7.8 show that the T89 model does not match the dynamics of the magnetosphere at this time. As such, there will be an error in the field-line mapping. Furthermore, the auroral velocities are based on intensity changes in 1 h bins of MLT, introducing an uncertainty in the auroral velocities. It is therefore suggested that the auroral velocities and projected velocities of the dipolarizations are in good agreement with one another.

7.3.2   Current sheet wave

Following the solar wind pressure pulse, Cluster and Polar observed large, rapid decreases and recoveries in the magnetic field magnitude, dominated by drops in the B_X component and accompanied by increases in the latitude angle, although the variations in the field at Polar were not observed until after the second substorm. In a previous study of this time, Zhang *et al.* (2002) showed that, after 08:48 UT, the variations in the magnetic field at Cluster were due to the spacecraft crossing the current sheet several times. They related these current sheet crossings to current sheet waves and used four-spacecraft timing analysis on the B_X=0 nT crossings to determine that the waves travelled in the dawnward direction. I have expanded upon this study, incorporating data from a larger dataset and including data from the Polar spacecraft. Although prior to 08:48 UT Cluster does not cross the current sheet, the periodic reductions in the B_X component indicate that the current sheet wave was present at this time.

Sergeev *et al.* (2006) compared MVA and the determination of the current vector and maximum variance direction as methods for determining the direction of a current sheet wave with four-spacecraft timing analysis. They found that MVA provided the poorest comparison with the four-spacecraft timing analysis. However, the curlometer technique cannot be applied to Polar data. Consequently, we use MVA to determine the orientation of the current sheet wave at Polar and Cluster and provide a comparison between these results and the four-spacecraft timing analysis.

Only three out of the nine Cluster observations of the current sheet wave had values of $\lambda_2/\lambda_3 > 10$. Despite this, the angles between the vectors from the MVA and four-spacecraft timing analysis were fairly low. Interestingly, comparing the angle between the MVA vectors at Polar and the MVA and four-spacecraft timing analysis vectors at Cluster shows that the vectors are consistently out by $> 40°$ despite one of the events having a particularly high λ_2/λ_3. This suggests there was some offset between the Polar and Cluster vectors, most likely due to their large separation. Comparing the vectors directly shows that the Y components are fairly consistent but the angle in the XZ plane was oppositely directed between Cluster and Polar. The results of the MVA and four-spacecraft timing analysis at Cluster (Table 7.3) and MVA at Polar (Table 7.4) has shown that for all the waves observed following the substorms, the waves were travelling in the dawnward direction, although it is not possible to determine whether or not the waves at Polar were travelling in this direction or the opposite direction unambiguously. However, given that the dipolarization fronts and auroral enhancements were travelling dawnwards, it seems reasonable to suggest that the same is true for the current sheet wave in the vicinity of Polar.

Despite FGM EXT mode being designed to provide contextual information and not usually being suited to multi-spacecraft analysis (Brown *et al.*, 2008), comparison between

the MVA and four-spacecraft timing analysis of the data and comparison of the results of these techniques between the EXT mode data and 5 Hz CAA data would suggest that the results are reliable in this case, given the similarity between the vectors obtained at different times and the relatively small angle between the vectors from the two different techniques.

Prior to the first substorm, Cluster observed periodic variations in the magnetic field with phase fronts orientated predominantly in the Z direction. The orientation of these variations was more in keeping with the orientation of the compression front observed at 07:19 UT. It is unclear whether this oscillation of the magnetosphere prior to the first substorm is the generation mechanism for the current sheet wave and that the substorms acted to modify the wave's propagation, or whether the substorms introduced new waves into the system.

That the spacecraft does not cross the current sheet following the first substorm may be due to several factors. Using the change in B_X as a proxy for the amplitude of the oscillation, it appears that the wave amplitude increases following each substorm. As such, the amplitude of the oscillation may have only become sufficient following the second substorm to cause the spacecraft to cross the current sheet. Alternatively, as Cluster was moving towards the current sheet from the northern part of the magnetotail, Cluster would have approached closer to the average position of the current sheet between the two substorms, such that it was close enough to cross the current sheet following the second substorm. Petrukovich *et al.* (2006) noted that the wave amplitude increased with increasing tilt of the current sheet for a fortuitous event on 3rd August, 2004. This does not appear to be the case for the oscillations studied here.

7.3.3　Ground-based observations

Observations of the magnetic field at the ground several hours of magnetic local time suggest that some effect of the wavy current sheet can be observed by ground magnetometers. Figure 7.11 indicates that a 21 min signal was detected at both Cluster and across the CANOPUS magnetometer chain during the interval in which the wavy current sheet was detected by Cluster. This signal can be seen quite clearly in Fig. 7.10. Furthermore, the wave appears to propagate from the vicinity of Fort Simpson, which was in an earlier MLT sector than Cluster, such that the wave propagation was in the same sense as the wave observed by Cluster. However, there are a number of issues which remain unresolved. Over the 2.5 hr over which the FFT was determined, the Cluster spacecraft was stationary compared with the CANOPUS magnetometers (see Fig. 7.3), which moved through 2.5 hr MLT. As such, one might expect the signal on the ground to have been Doppler shifted, which does not appear to be the case. However, this might be accounted for by the resolution of the FFT, as the change in the frequency would have

been less than 10%. However, it should be noted that separating the wave activity from substorm electrojet activity is non-trivial, and further studies are needed to confirm that these waves can regularly be observed.

7.3.4   Wavy current sheet models

The observations of the current sheet waves were used to compare the current sheet wave models of Golovchanskaya and Maltsev (2005) and Erkaev *et al.* (2008). As both models either define or use the current sheet thickness in their calculation of further parameters, it was necessary to determine the current sheet thickness. This was determined from the current profile across the current sheet Runov *et al.* (2006). The observations show that the current sheet was thickening between 0849 and 0917 UT before thinning slightly.

Using the model of Golovchanskaya and Maltsev (2005) to determine the thickness of the sheet necessary to support the observed wave returned a sheet thickness of approximately 12 R_E, which is an order of magnitude larger than observed. This is most likely due to the invalidity of one or more of the assumptions used to obtain the wave properties from the ballooning instability equations. In contrast, using the observed current sheet thicknesses to determine the expected wave velocities from the model of Erkaev *et al.* (2008) returned values that were close to those observed and that followed the same trend (Fig. 7.14). As such, the Erkaev *et al.* model appears to be more applicable in this situation. It is worth noting, however, that using the Erkaev *et al.* model to calculate the expected wave frequencies using the observed magnetic field gradients returned values that an order of magnitude smaller than observed. This may represent an over simplification of the tail magnetic field topology used by Erkaev *et al.* (2008) or may indicate that the observed magnetic field gradients are not indicative of the global properties of the magnetosphere. The most likely explanation is that it is some combination of both effects.

These models do not consider the generation mechanism for the flapping motion of the current sheet, only the mechanism that supports the wave propagation. Erkaev *et al.* (2008) suggest that BBFs created by reconnection events may excite the wave activity "like a ship moving on a water surface". This is consistent with a near-Earth neutral line injecting Earthward-moving flux into the plasma sheet (Cowley, 1984), such as is expected during substorms, and exciting the wave. The results presented suggest that there is a strong link between the substorm expansion phase and the wavy current sheet, clearly showing that the current sheet wave and substorm dipolarizations move with comparable speeds, that the cross tail current sheet wave occurred after the substorm onsets and that the lifetime of the auroral enhancements was comparable with the lifetime of the current sheet waves. However, the results also show the presence of a periodic variation orientated in the Z direction in the magnetotail prior to the substorm onset.

It is not clear what effect this earlier wave had on the generation of the current sheet wave. One possibility is that the excitation of the wavy current sheet occurs in two parts. Firstly, the solar wind pressure pulse compresses the magnetosphere, and hence the current sheet. This causes the current sheet to oscillate in the Z_{GSM} direction. Following this, two substorms dipolarize the mid-tail. This disruption in the mid-tail changes the magnetic field oscillation from an oscillation in the Z_{GSM} direction to a wave propagating in the $-Y_{GSM}$ direction with approximately the same period, with the amplitude of the oscillation increasing following each substorm. The similarity between the propagation of the current sheet waves and the two dipolarization fronts suggests that the propagation mechanism is the same for both.

7.4   Summary

This study has examined an interval of current sheet wave activity following a solar wind pressure pulse and incorporating two substorms. Substorm dipolarizations were observed by GOES 8 and 10, Polar and Cluster. The auroral expansion was observed by IMAGE FUV-WIC. The motions of the aurora, dipolarization fronts and current sheet waves were compared. Furthermore, the data from Cluster was used to evaluate two models of current sheet waves.

The results show that the dipolarization fronts, which were observed across 12 R_E, and the current sheet waves propagated from the centre of the tail towards the dawn flank at approximately the same velocities, with the velocities decreasing systematically with time. When mapped into the ionosphere, these velocities were comparable to the expansion velocity of the aurora. That the cross-tail waves occur following the substorm onsets indicates that the substorms, rather than the solar wind pressure pulse, was the source of the waves. The similarity between the velocities observed implies that there is a connection between them and may indicate that the expansion velocity is determined by the same mechanism that determines the wave velocities.

The two most recent models of current sheet waves, which both incorporate a curved magnetic field through the current sheet, were tested against the observations. The model of Golovchanskaya and Maltsev (2005) over-estimated the current sheet thickness compared with the observations, which were comparable with the expected value of the current sheet thickness during a disturbed period. In contrast, the model of Erkaev *et al.* (2008) reproduced the wave velocity and frequency to within a factor of four. Using a 20 min wave period, the velocities from the Erkaev *et al.* model matched the trends of the observed velocities. As such, it is concluded that, in this case, the current sheet waves can be explained using MHD applied to curved field-lines and not by the ballooning instability.

Chapter 8

Conclusions and further work

> *'Begin at the beginning,' the King said, very gravely,*
> *'and go on till you come to the end: then stop.'*
> "Alice's Adventures in Wonderland", Caroll (1865)

In this thesis I have investigated dynamical features in the magnetotail including bursty bulk flows, substorms and current sheet waves through both case studies (Chapter 5 and 7) and statistical surveys (Chapter 6). These investigations have been carried out using a wide range of data sources, both ground- and space-based, which were detailed in Chapter 3. In the following, I summarise the conclusions drawn from the three studies presented and discuss possible extensions to the work that would further our understanding of the dynamical processes in the magnetosphere.

8.1   BBF current systems

Previous studies of BBFs have determined a number of their properties, both statistically and through individual case studies. BBFs are flux tubes of depleted plasma that are more dipolar than the surrounding flux tubes and that propagate through the magnetotail, transporting energy and magnetic flux (Angelopoulos *et al.*, 1992; Chen and Wolf, 1993; Angelopoulos *et al.*, 1994; Sergeev *et al.*, 1996; Nakamura *et al.*, 2004). Their nature dictates that they are associated with field-aligned currents to support their dipolarized state (Chen and Wolf, 1993; Sergeev *et al.*, 1996). This field-aligned current system has lead to their association with auroral streamers (Henderson *et al.*, 1998) and has previously been observed during various substorm phases in the ionosphere and magnetosphere (Amm *et al.*, 1999; Grocott *et al.*, 2004; Nakamura *et al.*, 2005a; Snekvik *et al.*, 2007). In Chapter 5, I showed that, using the curlometer technique, data from the Cluster spacecraft could be used to examine the magnetospheric currents associated with BBFs and

determined the magnetospheric currents associated with a BBF consisting of two separate flow bursts (Fig. 5.8). The data showed that the current pattern across the individual flow bursts was bipolar, as expected from Sergeev *et al.* (1996), and the current magnitude, mapped into the ionosphere, was comparable with the currents observed by Amm *et al.* (1999). Furthermore, I showed that the auroral luminosity of the auroral streamer and mapped ionospheric currents were consistent with the results of Grocott *et al.* (2004) under the assumption that the auroral luminosity varies directly with the energy input and that the current is related to the square of the energy input (Knight, 1973; Cowley and Bunce, 2001). This provides a direct, quantitative link between BBFs and auroral streamers.

Previously observed currents associated with BBFs varied by two orders of magnitude (Amm *et al.*, 1999; Grocott *et al.*, 2004; Nakamura *et al.*, 2005a) and appear to be related to substorm phase. The results from Chapter 5 agreed with this assertion. In Chapter 6 I presented a statistical survey of BBFs observed by the Cluster spacecraft between 2001 and 2004. The selection criteria used identified 628 events, of which 211 were observed during intervals in which all the Cluster spacecraft remained on the same side of the cross-tail current sheet. Using the AL and AU auroral indices to determine substorm phase, I showed that BBFs observed during quiet times or substorm growth phases had smaller field-aligned currents than during the expansion and recovery phases (Fig. 6.13). However, there was no apparent relationship between the mean and maximum BBF currents and AE index at the time of the BBF encounter. Also, the variation in the current magnitudes was not as large as previously reported (Forsyth *et al.*, 2008a, and Chapter 5). This is possibly due to the limitations of the curlometer technique and the limits set on $|div\mathbf{B}|/|curl\mathbf{B}|$ for the BBF events.

Comparing current magnitudes with BBF position showed that the currents did not tend to vary with radial distance or Z. There were, however, variations in the currents across the tail, although the variations were opposite on the two scale sizes investigated. When the Cluster spacecraft were separated by $\sim$1000 km, the BBF currents detected were larger in the pre-midnight sector in which the majority of substorm breakups occur (Frey *et al.*, 2004). At smaller scale sizes the opposite is true. It is unclear from the results whether or not this variation is due to the change in scale size or merely a statistical anomaly.

8.2 BBFs as magnetotail phenomena

Early studies of BBFs suggested that they were generated by bursts of reconnection in the tail (Angelopoulos *et al.*, 1992; Chen and Wolf, 1993). In fact, MHD models of the magnetosphere have been reported to generate fast flows similar to BBFs (Birn and Hesse, 1996; Birn *et al.*, 1999). In Chapter 5, I presented observations of ions and electrons from

Cluster as the spacecraft passed through the PSBL and during the spacecraft's encounter with a BBF. The particle data showed that the particle distribution functions were similar for the PSBL crossing, a feature known to be the product of reconnection (Cowley, 1984), and the BBF. Pitch angle distributions of ions and electrons (Figs. 5.10 and 5.11) show that during the BBF, the ion and electron motion was predominantly field-aligned. In particular, the ion pitch angle distribution was more strongly Earthwards, indicating that the BBF field lines were recently reconnected such that the ions had not had sufficient time to mirror in the polar regions and return to the magnetotail.

The importance of BBFs to the substorm cycle has been discussed in many previous works. In particular, BBFs have been implicated in setting up the substorm current wedge (Birn and Hesse, 1996; Shiokawa *et al.*, 1997, 1998a,b; Birn *et al.*, 1999) at the start of the substorm expansion phase. In Chapter 6, I showed that BBFs occur more frequently during the substorm recovery phase as opposed to the substorm growth phase, raising questions about the role of BBFs in the substorm cycle. In the NENL model, BBFs occur after the onset of reconnection in the tail and set up the substorm current wedge in the inner magnetosphere. The lower occurrence rates of BBFs in the growth and expansion phases would suggest that BBFs are not critical in setting up the SCW, thus supporting the current disruption model of substorm onset. Also, the occurrence of BBFs during the recovery phase may maintain the pressure gradient that supports the substorm current wedge and thus slow the decay of the SCW and the recovery of the magnetosphere to its pre-substorm state. Given that the end of the expansion phase occurs when the substorm X-line begins to retreat down tail, this also implies that bursts of reconnection occur Earthward of the X-line as it retreats.

8.3   The wavy current sheet

Large scale oscillations of the magnetotail current sheet have been related to both substorm and BBF activity (Nakagawa and Nishida, 1989; Sergeev *et al.*, 2006). In Chapter 7, I showed that the propagation of substorm dipolarization fronts and current sheet waves were consistent with the motion of auroral activations and that the two features propagated across the tail with similar velocities. These features were observed following a solar wind pressure pulse and two substorms. Comparing my results with the models of Golovchanskaya and Maltsev (2005) and Erkaev *et al.* (2008) shows that the model of Erkaev *et al.* gives a better fit to the observations. The period of the current sheet wave increased with time. This increase was consistent with a linear increase in the plasma sheet thickness of the Erkaev *et al.* model.

Although the results presented were unable to determine the source of the waves, it is plausible that the two substorms drove the current sheet into oscillation. However, it is not clear what feature of the substorm would cause this. Erkaev *et al.* (2008) suggested

that BBFs could provide a generation mechanism, with the more dipolar flux tube acting "like a ship moving on a water surface". Taking this "wake" model and given that the wave speed in the case study presented was approximately 40 km s^{-1} and the peak velocity in BBFs is greater than 400 km s^{-1}, then the resultant waves would be orientated strongly towards dawn and dusk, as reported. However, further studies would be required to provide observational or modelling evidence of the simultaneous observations of both features.

8.4 Further work

The BBF survey presented in this thesis suggested that the currents associated with BBFs vary on scale size as well as with substorm phase and location. The Cluster mission, currently the only space mission with multiple spacecraft flying in a close formation, is restricted to observe the current system at one scale size, although this scale size can be altered for successive orbits. The proposed Cross-Scale mission, which would consist of a larger number of spacecraft ($\sim$10) flying in close formation in a near equatorial orbit, with spacecraft separated on different scale sizes, could address the issue of current scale sizes by observing the current system on multiple scale sizes simultaneously. Furthermore, the extended period of time spent in the plasma sheet compared with the Cluster mission, due to its near equatorial orbit, should provide a greater number of BBF encounters. These factors would enable a more accurate determination of the current profile across BBFs.

The BBF survey presented offers the opportunity to compare properties of BBFs detected by Cluster with other instruments and observatories. In particular, comparing the BBF velocity in the magnetosphere with observations of the convection of the ionosphere would be of particular interest. Grocott *et al.* (2004) and Grocott *et al.* (2007) have investigated the convection associated with BBFs on a case-by-case basis. These authors have suggested that there is a solar wind control mechanism for the motion of BBFs based on the distortion of the tail and ionospheric convection by the IMF B_Y component. Utilising the BBF survey in conjunction with the SuperDARN radars could further our understanding of magnetotail reconnection and how the magnetosphere reacts to the solar wind. Furthermore, the current survey only covers 2001-2004. As new, validated data is made available for the latter years of the Cluster mission, the survey could be expanded, increasing the number of events available for study.

BBFs are thought to be a key component of the substorm cycle, important for flux and energy transport and the diversion of the cross tail current. The results presented indicated that BBFs are more common during the expansion and recovery phases of BBFs, although spacecraft observations are spatially limited (the Cluster spacecraft covered approximately 2% of the width of the tail at any given time during 2001 to 2004). Auroral observations of the whole of the nightside auroral zone with high-time, high-spatial res-

olution imagers might enable the effects of BBFs to be more readily identified such that their true importance to the dynamics of the magnetotail might be discovered.

The mechanism for exciting current sheet waves is still unknown. The results presented here suggest that our understanding of the propagation of these waves, and other features in the magnetosphere has improved. However, limited coverage of the magnetosphere makes it difficult to determine if local variations can cause large scale dynamic activity. Observations using NASA's THEMIS spacecraft might provide further insight, since these five spacecraft systematically cover large regions of the magnetotail in an equatorial orbit. Using data from the spacecraft when they are separated in azimuth could allow for the detection of current sheet waves travelling in opposite directions, or in fact BBFs in the centre of the tail coupled with wave activity towards the flanks.

In this thesis, I presented results from auroral zone ground magnetometer stations during a period in which a current sheet wave was observed. The results suggested that the effect of the wave was detected at the ground (Fig. 7.10 to 7.12), although the results also suggested that the wave was travelling in the opposite direction on the ground to that in the magnetotail. Given the large number of magnetometer chains in the auroral zones and their extensive coverage, they are potentially a useful monitor of wavy current sheet activity. Further studies into the effect of current sheet waves on the magnetic field detected by ground magnetometers need to be undertaken such that the signature of the wavy current sheet can be determined unambiguously.

Appendix A

Magnetometer Stations

A.1   CARISMA magnetometer chain

Station	Code	Geog. Lat.	Geog. Lon.	Mag. Lat.	Mag. Lon.
Contwoyto	CONT	65.75	248.75	73.46	301.25
Dawson	DAWS	64.05	220.89	66.28	271.40
Eskimo Point	ESKI	61.11	265.95	71.59	330.75
Fort Churchill	FCHU	58.76	265.91	69.39	331.33
Fort Simpson	FSIM	61.76	238.77	67.79	291.69
Fort Smith	FSMI	60.03	248.07	67.99	304.36
Gillam	GILL	56.38	265.36	67.1	330.99
Island Lake	ISLL	53.86	265.34	64.69	331.43
Fort McMurray	MCMU	56.66	248.79	64.87	306.94
Pinawa	PINA	50.20	263.96	61.00	329.93
Rabbit Lake	RABB	58.22	256.32	67.710	316.70
Rankin Inlet	RANK	62.82	267.89	73.32	333.51
Taloyoak	TALO	69.54	266.45	79.26	327.19

Table A.1: Locations of the CARISMA magnetometers in geographic coordinates and geomagnetic (AACGM) coordinates.

A.2   Greenland magnetometer chain

West Station	Code	Geog. Lat.	Geog. Lon.	Mag. Lat.	Mag. Lon.
Thule	THL	77.47	290.77	84.97	29.68
Savissivik	SVS	76.02	294.90	83.24	33.04
Kullorsuaq	KUV	74.57	302.82	80.87	42.03
Upernavik	UPN	72.78	303.85	79.12	40.01
Umanaq	UMQ	70.68	307.87	76.53	42.26
Godhavn	GDH	69.25	306.47	75.40	38.93
Attu	ATU	67.93	306.43	74.13	37.71
Sondre Stromfjord	STF	67.02	309.28	72.74	40.51
Sukkertoppen	SKT	65.42	307.10	71.55	36.87
Godthab	GHB	64.17	308.27	70.11	37.50
Frederikshab	FHB	62.00	310.32	67.56	38.72
Narsarsuaq	NAQ	61.16	314.56	65.85	42.97

Table A.2: Locations of the Greenland chain magnetometers in geographic coordinates and geomagnetic (AACGM) coordinates.

East Station	Code	Geog. Lat.	Geog. Lon.	Mag. Lat.	Mag. Lon.
Nord	NRD	81.60	343.33	81.11	103.14
Danmarkshavn	DMH	76.77	341.37	77.27	85.00
Daneborg	DNB	74.30	339.78	75.13	78.64
Scoresbysund	SCO	70.48	338.03	71.50	71.73
Ammassalik	AMK	65.60	322.37	68.99	53.39

Table A.3: Locations of the Greenland chain magnetometers in geographic coordinates and geomagnetic (AACGM) coordinates.

A.3   LPM magnetometer chains

BAS Station	Geog. Lat.	Geog. Lon.	Mag. Lat.	Mag. Lon.
M78-337	-77.52	23.42	-68.51	49.77
M79-336	-79.68	24.12	-69.80	46.10
M81-338	-80.89	22.25	-70.24	43.11
M82-003	-81.50	3.00	-68.69	36.18
M83-348	-82.90	12.25	-70.39	36.42
M84-336	-84.36	23.85	-72.15	35.50
M85-002	-85.36	2.06	-71.25	29.49
M85-096	-85.39	95.97	-77.83	29.50
M87-028	-87.00	28.41	-73.49	28.44
M87-069	-86.51	68.18	-75.64	30.17
M88-316	-88.03	43.87	74.29	25.42

Table A.4: Locations of the British Antarctic Survey Low Power Magnetometers in geographic coordinates and geomagnetic (AACGM) coordinates.

NIPR Station	Geog. Lat.	Geog. Lon.	Mag. Lat.	Mag. Lon.
H100 (M69-041)	-69.30	41.32	-66.87	72.42
Skallen (M70-039)	-69.67	39.40	-66.73	70.64
Cape Omega (M69-041)	-68.58	41.08	-66.42	73.37

Table A.5: Locations of the Japanese National Institute of Polar Research Low Power Magnetometers in geographic coordinates and geomagnetic (AACGM) coordinates.

A.4   IMAGE magnetometer chain

Station	Geog. Lat.	Geog. Lon.	Mag. Lat.	Mag. Lon.
Ny Ålesund (NAL)	78.92	11.95	76.01	112.27
Longyearbyen (LYR)	78.20	15.82	75.05	113.01
Horsund (HOR)	77.	15.6	73.94	110.48
Bear Island (BJN)	74.50	19.20	71.27	108.94
Masi (MAS)	69.46	23.70	65.96	106.93
Muonio (MUO)	68.02	23.53	64.51	105.70
Pello (PEL)	66.90	24.08	63.34	105.36
Hankasalmi (HAN)	62.30	26.65	58.51	105.16

Table A.6: Locations of a selection of magnetometer stations in the IMAGE chain in geographic coordinates and geomagnetic (AACGM) coordinates.

Appendix B

Basic instrumentation

B.1 Fluxgate Magnetometers

Fluxgate magnetometers (FGM) are probably the simplest and most common magnetometers used for the investigation of the near-Earth plasma environment. Figure B.1 shows the basic construction of (a) a ring core FGM and (b) a linear core FGM. The detector consists of two high-permeability cores with primary coils wound round each. A secondary coil is wound around both cores. The cores are then aligned such that the currents in the two primary coils are in opposing directions. If no external magnetic field is present then, when equal currents are passed through the primary coils, the induced magnetic fields vary at the same rate and, being equal and opposite, cancel out. By selecting appropriate core material and current amplitudes, the magnetic fields induced by the currents in the primary coils can be made to saturate, i.e. no longer increase with increasing current. When a high frequency alternating current is passed through the primary coils, the magnetic field induced in the cores is saturated during each half cycle. If an external magnetic field is present and the field has a component along the axis of the cores, then the field induced in one of the coils will reach saturation before that of the other, leading to a temporal variation in the magnetic field which, by Faraday's Law, induces a voltage in the secondary coil proportional to the rate of change of the magnetic field. Measuring this voltage gives a measure of the magnetic field along the core of the detector. The vector field can be wholly detected using three cores aligned such that there axes are non-coplanar, usually mutually perpendicular.

B.2 Quadrispherical or "top hat" plasma detectors

Quadrispherical, or "top hat", detectors (Carlson *et al.*, 1982) enable a plasma instrument to have a 360° field of view, although this is often restricted to 180°. When attached

to the side of a spinning spacecraft, these then give a 4π sr particle distribution once every spin. The "top hat" detector consists of a position sensitive detector, such as a charge-couple device (CCD) and three hemispherical sections of increasing radius; a complete inner hemisphere, an outer hemisphere with a circular aperture at the top, and a partial hemisphere covering the aperture on the outer hemisphere. Figure B.2 shows the basic construction of a quadrispherical detector (a) side-on and (b) top-down. The three hemispherical plates are shown (labelled (1)-(3)) along with the position sensitive detector (label (4)). Particles are deflected into the instrument through the circular aperture and are accelerated around the inner hemisphere by an electric field across the gap between the inner and outer hemispheres (red lines in Fig. B.2a). Particles with an energy/charge ratio within a selected range are allowed to pass between the inner and outer plates by selecting the voltage applied to the inner hemisphere. Particles with energies outside the selected energy range will collide with either the inner or outer hemispheres. Once a particle has passed through the hemispherical section, it can be detected by a position sensitive detector, such as a charge-couple device (CCD). The hemispherical shape of the instrument focuses the particle trajectories such that particles travelling in the same direction but that enter at different points are focussed onto the position sensitive detector at the same point (Fig. B.2b).
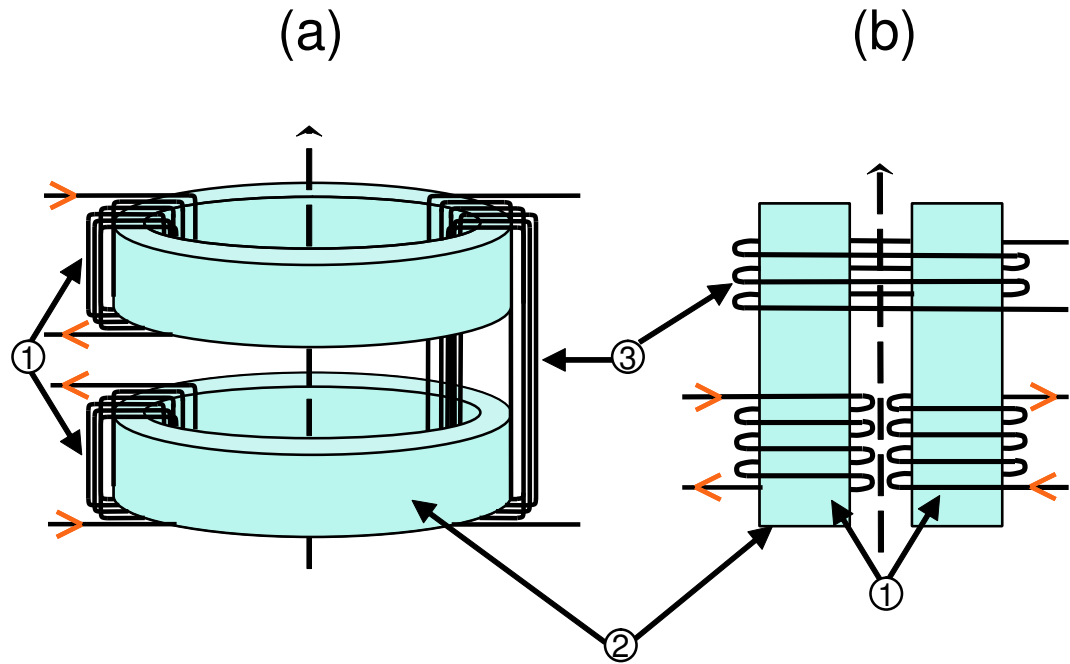
Figure B.1: Diagram of (a) ring core and (b) linear fluxgate magnetometer detectors. Shown are the primary coils (1) with opposing currents flowing shown as red arrows, the high permeability ferromagnetic cores (2), and the secondary (output) coil (3). The dashed line represents the axis of the detector.
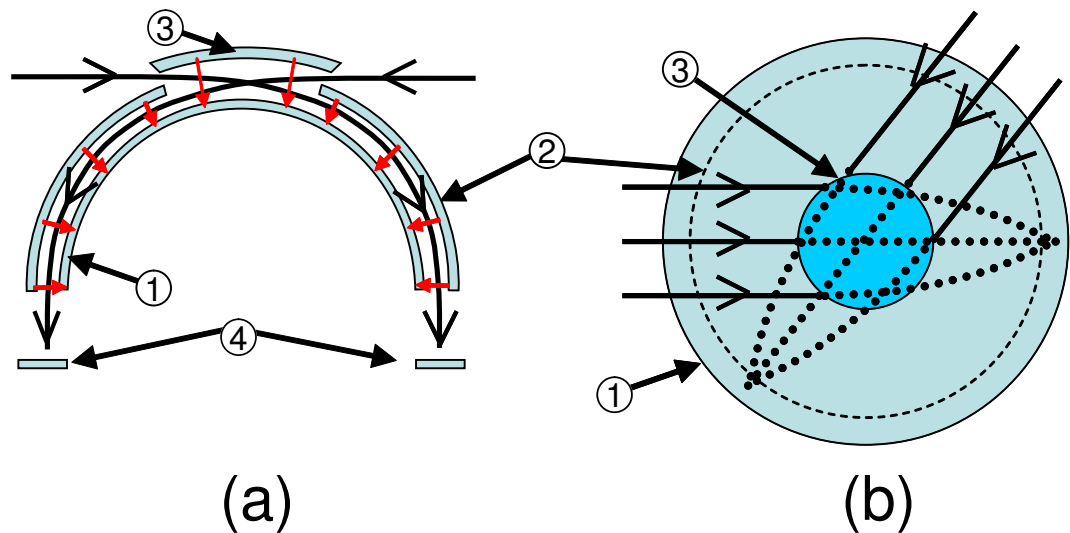
Figure B.2: (a) Cut-through and (b) top down diagram of a quadrispherical plasma detector. Shown are the (1) inner, (2) outer and (3) "top hat" plates and (4) the circular position sensitive detector. The red arrows indicate the electric field direction for a positive charge detector (the field is reversed for negative charges). The black line represents the path of a positively charged particle through the detector. Based on Carlson *et al.* (1982, Fig. 1)

Appendix C

List of Abbreviations

Abbreviation	Details
ACE	Advanced Composition Explorer
AU	Astronomical Unit (1.5×10^{11} m)
BBF	Bursty Bulk Flow
CIS	Cluster Ion Spectrometry experiment
CODIF	Composition and Distribution Function analyser
EFW	Electric Fields and Waves experiment
FB	Flow Burst
FGM	Fluxgate Magnetometer
FUV-WIC	Far UltraViolet Wideband Imaging Camera
G	The gravitational constant (6.672×10^{-11} N m^2 kg^{-2})
GOES	Geostationary Operational Environmental Satellite
HIA	Hot Ion Analyser
k	Boltzmann constant (1.3807×10^{-23} J k^{-1})
LSD	Large Separation Dataset
MHD	Magnetohydrodynamic(s)
MVA	Minimum Variance Analysis
PEACE	Plasma Electron and Current Experiment
R_E	Earth radius/radii (6378 km)
SSD	Small Separation Dataset

References

GOES I-M Databook, Space Systems Loral, 1997.

Acuña, M. H., Ogilvie, K. W., Baker, D. N., Curtis, S. A., Fairfield, D. H., and Mish, W. H.: The Global Geospace Science Program and Its Investigations, *Sp. Sci. Rev.*, **71**, 5–21, doi: doi:10.1007/BF00751323, 1995.

Akasofu, S.-I.: The development of the auroral substorm, *Planet. Sp. Sci.*, **12**, 273–282, 1964.

Amm, O. and Kauristie, K.: Ionospheric signatures of bursty bulk flows, *Surv. Geophy.*, **23**, 1–32, 2002.

Amm, O., Pajunpää, A., and Brandström, U.: Spatial distribution of conductances and currents associated with a north-south auroral form during a multiple-substorm period, *Ann. Geophys.*, **17**, 1385–1396, 1999.

Angelopoulos, V., Baumjohann, W., Kennel, C. F., Coronti, F. V., Kivelson, M. G., Pellat, R., Walker, R. J., Luehr, H., and Paschmann, G.: Bursty bulk flows in the inner central plasma sheet, *J. Geophys. Res.*, **97**, 4027–4039, 1992.

Angelopoulos, V., Kennel, C. F., Coroniti, F. V., Pellat, R., Kivelson, M. G., Walker, R. J., Russell, C. T., Baumjohann, W., Feldman, W. C., and Gosling, J. T.: Statistical characteristics of bursty bulk flow events, *J. Geophys. Res.*, **99**, 21 257–21 280, 1994.

Angelopoulos, V., Phan, T. D., Larson, D. E., Mozer, F. S., Lin, R. P., Tsuruda, K., Hayakawa, H., Mukai, T., Kokubun, S., Yamamoto, T., Williams, D. J., McEntire, R. W., Lepping, R. P., Parks, G. K., Brittnacher, M., Germany, G., Spann, J., Singer, H. J., and Yumoto, K.: Magnetotail flow bursts: association to global magnetospheric circulation, relationship to ionospheric activity and direct evidence for localization, *Geophys. Res. Lett.*, **24**, 2271–2274, doi: doi:10.1029/97GL02355, 1997.

Baker, D. N. and Pulkkinen, T. I.: Large-Scale Structure of the Magnetosphere, in New Perspectives on the Earth's Magnetotail, edited by A. Nishida, D. N. Baker, and S. W. H. Cowley, pp. 21–32, 1998.

Baker, D. N., Pulkkinen, T. I., McPherron, R. L., and Clauer, C. R.: Multi-spacecraft study of a substorm growth and expansion phase features using a time-evolving field model., in Solar System Plasmas in Space and Time, pp. 101–110, 1994.

Baker, D. N., Pulkkinen, T. I., Angelopoulos, V., Baumjohann, W., and McPherron, R. L.: Neutral line model of substorms: Past results and present view, *J. Geophys. Res.*, **101**, 12 975–13 010, doi: doi:10.1029/95JA03753, 1996.

Baker, K. B. and Wing, S.: A new magnetic coordinate system for conjugate studies at high latitudes, *J. Geophys. Res.*, **94**, 9139–9143, 1989.

Balogh, A., Carr, C. M., Acuña, M. H., Dunlop, M. W., Beek, T. J., Brown, P., Fornaçon, K.-H., Georgescu, E., Glassmeier, K.-H., Harris, J., Musmann, G., Oddy, T., and Schwingenschuh, K.: The Cluster Magnetic Field Investigation: Overview of in-flight performance and initial results, *Ann. Geophys.*, **19**, 1207–1217, 2001.

Bauer, T. M., Baumjohann, W., and Treumann, R. A.: Neutral sheet oscillations at substorm onset, *J. Geophys. Res.*, **100**, 23 737–23 742, doi: doi:10.1029/95JA02448, 1995.

Baumjohann, W. and Treumann, R. A.: London: Imperial College Press, 1996.

Baumjohann, W., Paschmann, G., Sckopke, N., Cattell, C. A., and Carlson, C. W.: Average ion moments in the plasma sheet boundary layer, *J. Geophys. Res.*, **93**, 11 507–11 520, 1988.

Baumjohann, W., Paschmann, G., and Cattell, C. A.: Average plasma properties in the central plasma sheet, *J. Geophys. Res.*, **94**, 6597–6606, 1989.

Baumjohann, W., Paschmann, G., and Luehr, H.: Characteristics of high-speed ion flows in the plasma sheet, *J. Geophys. Res.*, **95**, 3801–3809, 1990.

Biermann, L.: Kometenschweife und solare Korpuskularstrahlung, *Zeitschrift fur Astrophysik*, **29**, 274–286, 1951.

Biermann, L.: Über den Schweif des Kometen Halley im Jahre 1910, *Zeitschrift Naturforschung Teil A*, **7**, 127–136, 1952.

Biermann, L.: Solar corpuscular radiation and the interplanetary gas, *The Observatory*, **77**, 109–110, 1957.

Birn, J. and Hesse, M.: Details of current disruption and diversion in simulations of magnetotail dynamics, *J. Geophys. Res.*, **101**, 15 345–15 358, doi: doi:10.1029/96JA00887, 1996.

Birn, J., Hesse, M., and Schindler, K.: MHD simulations of magnetotail dynamics, *J. Geophys. Res.*, **101**, 12 939–12 954, doi: doi:10.1029/96JA00611, 1996.

Birn, J., Hesse, M., Haerendel, G., Baumjohann, W., and Shiokawa, K.: Flow braking and the substorm current wedge, *J. Geophys. Res.*, **104**, 19 895–19 904, doi: doi: 10.1029/1999JA900173, 1999.

Birn, J., Raeder, J., Wang, Y., Wolf, R., and Hesse, M.: On the propagation of bubbles in the geomagnetic tail, *Ann. Geophys.*, **22**, 1773–1786, 2004.

Brown, P., Dunlop, M. W., Balogh, A., Carr, C., Gloag, J., Lucek, E., and Oddy, T.: Calibration techniques for magnetometers implementing on-board de-spinning algorithms, *Adv. Space Res.*, **41**, 1571–1578, doi: doi:10.1016/j.asr.2007.09.028, 2008.

Burch, C. R.: Reflecting microscopes , *Proceedings of the Physical Society*, **59**, 41–46, 1947.

Burch, J. L.: IMAGE mission overview, *Sp. Science Reviews*, **91**, 1–14, 2000.

Cao, J. B., Ma, Y. D., Parks, G., Reme, H., Dandouras, I., Nakamura, R., Zhang, T. L., Zong, Q., Lucek, E., Carr, C. M., Liu, Z. X., and Zhou, G. C.: Joint observations by Cluster satellites of bursty bulk flows in the magnetotail, *J. Geophys. Res.*, **111**, A04 206, doi: doi:10.1029/2005JA011322, 2006.

Carlson, C. W., Curtis, D. W., Paschmann, G., and Michel, W.: An instrument for rapidly measuring plasma distribution functions with high resolution, *Adv. Sp. Res.*, **2**, 67–70, doi: doi:10.1016/0273-1177(82)90151-X, 1982.

Caroll, L.: Alice's Adventures in Wonderland, London: Macmillan, 1865.

Chapman, S. V. and Ferraro, V. C. A.: A New Theory of Magnetic Storms, *Nature*, **126**, 129–130, 1930.

Chen, C. X. and Wolf, R. A.: Interpretation of high-speed flows in the plasma sheet, *J. Geophys. Res.*, **98**, 21 409–21 419, 1993.

Chen, C. X. and Wolf, R. A.: Theory of thin-filament motion in Earth's magnetotail and its application to bursty bulk flows, *J. Geophys. Res*, **104**, 14 613–14 626, doi: doi:10.1029/1999JA900005, 1999.

Chisham, G., Lester, M., Milan, S. E., Freeman, M. P., Bristow, W. A., Grocott, A., McWilliams, K. A., Ruohoniemi, J. M., Yeoman, T. K., Dyson, P. L., Greenwald, R. A., Kikuchi, T., Pinnock, M., Rash, J. P. S., Sato, N., Sofko, G. J., Villain, J.-P., and Walker, A. D. M.: A decade of the Super Dual Auroral Radar Network (SuperDARN): scientific achievements, new techniques and future directions, *Surveys in Geophysics*, **28**, 33–109, doi: doi:10.1007/s10712-007-9017-8, 2007.

Cowley, S. W. H.: The Distant Geomagnetic Tail in Theory and Observation, in Magnetic Reconnection in Space and Laboratory Plasmas, edited by E. W. Hones, Jr., pp. 228–239, 1984.

Cowley, S. W. H. and Bunce, E. J.: Origin of the main auroral oval in Jupiter's coupled magnetosphere-ionosphere system, *Planet. Sp. Sci.*, **49**, 1067–1088, 2001.

Cudworth, R.: The true intellectual system of the universe , 1678.

de Hoffmann, F. and Teller, E.: Magneto-Hydrodynamic Shocks, *Physical Review*, **80**, 692–703, doi: doi:10.1103/PhysRev.80.692, 1950.

Dungey, J. W.: Interplanetary magnetic field and the auroral zones, *Phys. Rev. Lett.*, **6**, 47–48, doi: doi:10.1103/PhysRevLett.6.47, 1961.

Dunlop, M. W., Southwood, D. J., Glassmeier, K.-H., and Neubauer, F. M.: Analysis of multipoint magnetometer data, *Adv. Space Res.*, **8**, 273–277, doi: doi:10.1016/0273-1177(88)90141-X, 1988.

Dunlop, M. W., Balogh, A., Glassmeier, K.-H., and Robert, P.: Four-point Cluster application of magnetic field analysis tools: The Curlometer, *J. Geophys. Res.*, **107**, A01 384, doi: doi:10.1029/2001JA005088, 2002.

Eastwood, J. P., Balogh, A., Lucek, E. A., Mazelle, C., and Dandouras, I.: Quasi-monochromatic ULF foreshock waves as observed by the four-spacecraft Cluster mission: 1. Statistical properties, *J. Geophys. Res.*, **110**, A11 219, doi: doi:10.1029/2004JA010617, 2005.

Erkaev, N. V., Semenov, V. S., and Biernat, H. K.: Magnetic double gradient mechanism for flapping oscillations of a current sheet, *Geophys. Res. Lett.*, **35**, L02 111, doi: doi:10.1029/2007GL032277, 2008.

Escoubet, C. P., Fehringer, M., and Goldstein, M.: The Cluster mission, *Ann. Geophys.*, **19**, 1197–1200, 2001.

Fairfield, D. H. and Ness, N. F.: Configuration of the geomagnetic tail during substorms., *J. Geophys. Res.*, **75**, 7032–7047, 1970.

Fear, R. C.: Cluster Multi-Spacecraft Observations of Flux Transfer Events (Thesis), University College London (University of London), 2006.

Forsyth, C., Lester, M., Milan, S. E., Grocott, A., Frey, H. U., Lucek, E., Reme, H., and Watermann, J.: Observations of tail dynamics using ground and space based instruments during a period of multiple substorm events, in Proceedings of the Eighth International Conference on Substorms (ICS-8), edited by Syrjäsuo and Donovan, pp. 65–70, University of Calgary, Alberta, Canada, 2007.

Forsyth, C., Lester, M., Cowley, S. W. H., Dandouras, I., Fazakerley, A. N., Fear, R. C., Frey, H. U., Grocott, A., Kadokura, A., Lucek, E., Rème, H., Milan, S. E., and Watermann, J.: Observed tail current systems associated with bursty bulk flows and auroral streamers during a period of multiple substorms, *Ann. Geophys.*, **26**, 167–184, 2008a.

Forsyth, C., Lester, M., Lucek, E., Dandouras, I., Fazakerley, A. N., Fear, R. C., Singer, H., and Yeoman, T. K.: Solar wind and substorm excitation of the wavy neutral sheet, *Ann. Geophys.*, **submitted**, 2008b.

Freeman, M. P. and Morley, S. K.: A minimal substorm model that explains the observed statistical distribution of times between substorms, *Geophys. Res. Lett.*, **31**, 12 807–12 900, doi: doi:10.1029/2004GL019989, 2004.

Frey, H. U., Mende, S. B., Angelopoulos, V., and Donovan, E. F.: Substorm onset observations by IMAGE-FUV, *J. Geophys. Res.*, **109**, A10 304, doi: doi:10.1029/2004JA010607, 2004.

Gibson, W. C., Burch, J. L., Scherrer, J. R., Tapley, M. B., Killough, R. L., Volpe, F. A., Davis, W. D., Vaccarello, D. C., Grismore, G., Sakkas, D., and Housten, S. J.: The IMAGE Observatory, *Sp. Sci. Rev.*, **91**, 15–50, 2000.

Golovchanskaya, I. V. and Maltsev, Y. P.: On the identification of plasma sheet flapping waves observed by Cluster, *Geophys. Res. Lett.*, **32**, L02 102, doi: doi:10.1029/2004GL021552, 2005.

Greenwald, R. A., Baker, K. B., Dudeney, J. R., Pinnock, M., Jones, T. B., Thomas, E. C., Villain, J.-P., Cerisier, J.-C., Senior, C., Hanuise, C., Hunsucker, R. D., Sofko, G., Koehler, J., Nielsen, E., Pellinen, R., Walker, A. D. M., Sato, N., and Yamagishi, H.: Darn/Superdarn: A Global View of the Dynamics of High-Lattitude Convection, *Sp. Sci. Rev.*, **71**, 761–796, doi: doi:10.1007/BF00751350, 1995.

Grocott, A., Yeoman, T., Nakamura, R., Cowley, S., Frey, H., Rème, H., and Klecker, B.: Multi-instrument observations of the ionospheric counterpart of a bursty bulk flow in the near-Earth plasma sheet, *Ann. Geophys.*, **22**, 1061–1075, 2004.

Grocott, A., Yeoman, T. K., Milan, S. E., Amm, O., Frey, H. U., Juusola, L., Nakamura, R., Owen, C. J., Rème, H., and Takada, T.: Multi-scale observations of magnetotail flux transport during IMF-northward non-substorm intervals, *Ann. Geophys.*, **25**, 1709–1720, 2007.

Gustafsson, G., André, M., Carozzi, T., I.Eriksson, A., Fälthammar, C.-G., Grard, R., Holmgren, G., Holtet, J. A., Ivchenko, N., Karlsson, T., Khotyaintsev, Y., Klimov, S., Laakso, H., Lindqvist, P.-A., Lybekk, B., Marklund, G., Mozer, F., Mursula, K., Pedersen, A., Popielawska, B., Savin, S., Stasiewicz, K., Tanskanen, P., Vaivads, A., and Wahlund, J.-E.: First results of electric field and density observations by Cluster EFW based on initial months of operation, *Ann. Geophys.*, **19**, 1219–1240, 2001.

Haerendel, G.: Disruption, ballooning or auroral avalanche - On the cause on substorms, in Substorms 1, Proceedings of the First International Conference on Substorms (ICS-1), Eur. Space Agency Spec. Publ., 1992.

Harris, E. G.: On a plasma sheet separating regions of oppositly directed magnetic field, *Nuovo Cimento*, **23**, 151–121, 1962.

Harvey, C. C.: Spatial gradients and the volumetric tensor, in Analysis Methods for Multi-Spacecraft Data, edited by G. Paschmann and P. W. Daly, pp. 307–348, ISSI, 1998.

Hasegawa, H., Sonnerup, B. U. Ö., Klecker, B., Paschmann, G., Dunlop, M. W., and Rème, H.: Optimal reconstruction of magnetopause structures from Cluster data, *Ann. Geophys.*, **23**, 973–982, 2005.

Hau, L.-N. and Sonnerup, B. U. Ö.: Two-dimensional coherent structures in the magnetopause: Recovery of static equilibria from single-spacecraft data, *J. Geophys. Res*, **104**, 6899–6918, doi: doi:10.1029/1999JA900002, 1999.

Henderson, M. G., Reeves, G. D., and Murphree, J. S.: Are north-south aligned auroral structures an ionospheric manifestation of bursty bulk flows?, *Geophys. Res. Lett.*, **25**, 3737–3740, doi: doi:10.1029/98GL02692, 1998.

Hones, Jr., E. W.: Plasma sheet behavior during substorms, *Washington DC American Geophysical Union Geophysical Monograph Series*, pp. 178–184, 1984.

Hoyle, F.: Some recent researches in solar physics., Cambridge [Eng.] University Press, 1949., 1949.

Huang, C. Y. and Frank, L. A.: A statistical study of the central plasma sheet - Implications for substorm models, *Geophys. Res. Lett.*, **13**, 652–655, 1986.

Huang, C. Y. and Frank, L. A.: Reply to Cattell and Elphic, *Geophys. Res. Lett.*, **14**, 776–778, 1987.

Johnstone, A. D., Alsop, C., Burge, S., Carter, P. J., Coates, A. J., Coker, A. J., Fazakerley, A. N., Grande, M., Gowen, R. A., Gurgiolo, C., Hancock, B. K., Narheim, B., Preece, A., Sheather, P. H., Winningham, J. D., and Woodliffe, R. D.: PEACE: a Plasma Electron And Current Experiment, *Sp. Sci. Rev.*, **79**, 351–398, 1997.

Kauristie, K., Sergeev, V. A., Kubyshkina, M., Pulkkinen, T. I., Angelopoulos, V., Phan, T., Lin, R. P., and Slavin, J. A.: Ionospheric current signatures of transient plasma sheet flows, *J. Geophys. Res.*, **105**, 10 677–10 690, doi: doi:10.1029/1999JA900487, 2000.

Keiling, A., Parks, G. K., Rème, H., Dandouras, I., Wilber, M., Kistler, L., Owen, C., Fazakerley, A. N., Lucek, E., Maksimovic, M., and Cornilleau-Wehrlin, N.: Energy-dispersed ions in the plasma sheet boundary layer and associated phenomena: Ion heating, electron acceleration, Alfvén waves, broadband waves, perpendicular electric field spikes, and auroral emissions, *Ann. Geophys.*, **24**, 2685–2707, 2006.

Khan, H. and Cowley, S. W. H.: Observations of the response time of high-latitude ionospheric convection to variations in the interplanetary magnetic field using EISCAT and IMP-8 data, *Ann. Geophys.*, **17**, 1306–1335, 1999.

Kivelson, M. G. and Russell, C. T.: Introduction to Space Physics, UK: Cambridge University Press, 1995.

Knight, S.: Parallel electric fields, *Planet. Sp. Sci.*, **21**, 741–750, doi: doi:10.1016/0032-0633(73)90093-7, 1973.

Kokubun, S. and McPherron, R. L.: Substorm signatures at synchronous altitude, *J. Geophys. Res*, **86**, 11 265–11 277, 1981.

Lester, M., Chapman, P., Cowley, S., Crooks, S., Davies, J., Hamadyk, P., McWilliams, K., Milan, S., Parsons, M., Payne, D., Thomas, E., Thornhill, J., Wade, N., Yeoman, T., and Barnes, R.: Stereo CUTLASS - A new capability for the SuperDARN HF radars, *Ann. Geophys.*, **22**, 459–473, 2004.

Liou, K. and Ruohoniemi, J. M.: A case study of relationship between substorm expansion and global plasma convection, *Geophys. Res. Lett.*, **33**, L02 105, doi: doi:10.1029/2005GL024736, 2006a.

Liou, K. and Ruohoniemi, J. M.: Correction to "A case study of relationship between substorm expansion and global plasma convection", *Geophys. Res. Lett.*, **33**, L10 101, doi: doi:10.1029/2006GL025990, 2006b.

Liou, K., Meng, C.-I., Lui, A. T. Y., Newell, P. T., and Wing, S.: Magnetic dipolarization with substorm expansion onset, *J. Geophys. Res.*, **107**, 1131–1142, doi: doi:10.1029/2001JA000179, 2002.

Liou, K., Meng, C.-I., and Wu, C.-C.: On the interplanetary magnetic field B_y control of substorm bulge expansion, *J. Geophys. Res.*, **111**, 9312–9319, doi: doi:10.1029/2005JA011556, 2006.

Liu, W. W.: Physics of the explosive growth phase: Ballooning instability revisited, *J. Geophys. Res.*, **102**, 4927–4931, doi: doi:10.1029/96JA03561, 1997.

Liu, W. W., Liang, J., Donovan, E. F., Trondsen, T., Baker, G., Sofko, G., Jackel, B., Wang, C.-P., Mende, S., Frey, H. U., and Angelopoulos, V.: Observation of isolated high-speed auroral streamers and their interpretation as optical signatures of Alfvén waves generated by bursty bulk flows, *Geophys. Res. Lett.*, **35**, L04 104, doi: doi:10.1029/2007GL032722, 2008.

Luhr, H.: The IMAGE Magnetometer Network, in STEP International, vol. 4, pp. 4–6, USSCO, 1994.

Lui, A. T. Y.: A synthesis of magnetospheric substorm models, *J. Geophys. Res.*, **96**, 1849–1856, 1991.

Lui, A. T. Y.: Current disruption in the Earth's magnetosphere: Observations and models, *J. Geophys. Res.*, **101**, 13 067–13 088, doi: doi:10.1029/96JA00079, 1996.

Lui, A. T. Y.: Tutorial on geomagnetic storms and substorms, *IEEE Transactions on Plasma Science*, **28**, 1854–1866, doi: doi:10.1109/27.902214, 2000.

Lui, A. T. Y., Chang, C.-L., Mankofsky, A., Wong, H.-K., and Winske, D.: A cross-field current instability for substorm expansions, *J. Geophys. Res.*, **96**, 11 389–11 401, 1991.

Lundin, R. and Sandahl, I.: Some characteristics of the parallel electric field acceleration of electrons over discrete auroral arcs as observed from two rocket flights, Tech. rep., ESA, 1978.

Lyons, L. R., Blanchard, G. T., Samson, J. C., Lepping, R. P., Yamamoto, T., and Moretto, T.: Coordinated observations demonstrating external substorm triggering, *J. Geophys. Res*, **102**, 27 039–27 052, doi: doi:10.1029/97JA02639, 1997.

Lyons, L. R., Nagai, T., Blanchard, G. T., Samson, J. C., Yamamoto, T., Mukai, T., Nishida, A., and Kokobun, S.: Association between Geotail plasma flows and auroral poleward boundary intensifications observed by CANOPUS photometers, *J. Geophys. Res.*, **104**, 4485–4500, doi: doi:10.1029/1998JA900140, 1999.

McComas, D. J., Bame, S. J., Russell, C. T., and Elphic, R. C.: The near-earth cross-tail current sheet - Detailed ISEE 1 and 2 case studies, *J. Gephys. Res.*, **91**, 4287–4301, 1986.

McComas, D. J., Bame, S. J., Barker, P., Feldman, W. C., Phillips, J. L., Riley, P., and Griffee, J. W.: Solar Wind Electron Proton Alpha Monitor (SWEPAM) for the Advanced Composition Explorer, *Sp. Sci. Rev.*, **86**, 563–612, doi: doi:10.1023/A: 1005040232597, 1998.

McPherron, R. L.: Growth phase of magnetospheric substorms., *J. Geophys. Res.*, **75**, 5592–5599, 1970.

McPherron, R. L.: Magnetospheric Substorms, *Rev. Geophys.*, **17**, 657–681, doi: doi: 10.1029/RG017i004p00657, 1979.

McPherron, R. L., Russell, C. T., and Aubry, M. P.: Satellite studies of magnetospheric substorms on August 15, 1968. 9. Phenomenological model for substorms., *J. Geophys. Res.*, **78**, 3131–3149, 1973.

McWilliams, K. A., Yeoman, T. K., Sigwarth, J. B., Frank, L. A., and Brittnacher, M.: The dayside ultraviolet aurora and convection responses to a southward turning of the interplanetary magnetic field, *Ann. Geophys.*, **19**, 707–721, 2001.

Mende, S. B., Heetderks, H., Frey, H. U., Lampton, M., Geller, S. P., Abiad, R., Siegmund, O. H. W., Tremsin, A. S., Spann, J., Dougani, H., Fuselier, S. A., Magoncelli, A. L., Bumala, M. B., Murphree, S., and Trondsen, T.: Far ultraviolet imaging from the IMAGE spacecraft. 2. Wideband FUV imaging, *Sp. Sci. Rev.*, **91**, 271–285, 2000a.

Mende, S. B., Heetderks, H., Frey, H. U., Lampton, M., Geller, S. P., Habraken, S., Renotte, E., Jamar, C., Rochus, P., Spann, J., Fuselier, S. A., Gerard, J.-C., Gladstone, R., Murphree, S., and Cogger, L.: Far ultraviolet imaging from the IMAGE spacecraft. 1. System design, *Sp. Sci. Rev.*, **91**, 243–270, 2000b.

Mende, S. B., Heetderks, H., Frey, H. U., Stock, J. M., Lampton, M., Geller, S. P., Abiad, R., Siegmund, O. H. W., Habraken, S., Renotte, E., Jamar, C., Rochus, P., Gerard, J.-C., Sigler, R., and Lauche, H.: Far ultraviolet imaging from the IMAGE spacecraft. 3. Spectral imaging of Lyman-α and OI 135.6 nm, *Sp. Sci. Rev.*, **91**, 287–318, 2000c.

Milan, S. E., Cowley, S. W. H., Lester, M., Wright, D. M., Slavin, J. A., Fillingim, M., Carlson, C. W., and Singer, H. J.: Response of the magnetotail to changes in the open flux content of the magnetosphere, *J. Geophys. Res.*, **109**, A04 220, doi: doi:10.1029/2003JA010350, 2004.

Milan, S. E., Hubert, B., and Grocott, A.: Formation and motion of a transpolar arc in response to dayside and nightside reconnection, *J.Geophys. Res.*, **110**, A01 212, doi: doi:10.1029/2004JA010835, 2005.

Milan, S. E., Wild, J. A., Grocott, A., and Draper, N. C.: Space- and ground-based investigations of solar wind magnetosphere ionosphere coupling, *Adv. Sp. Res.*, **38**, 1671–1677, doi: doi:10.1016/j.asr.2005.08.009, 2006a.

Milan, S. E., Wild, J. A., Hubert, B., Carr, C. M., Lucek, E. A., Bosqued, J. M., Watermann, J. F., and Slavin, J. A.: Flux transport and tail dynamics during a prolonged substorm interval, in Cluster and Double Star Symposium, vol. 598 of *ESA Special Publication*, 2006b.

Nagai, T.: Observed magnetic substorm signatures at synchronous altitude, *J. Geophys. Res.*, **87**, 4405–4417, 1982.

Nakagawa, T. and Nishida, A.: Southward magnetic field in the neutral sheet produced by wavy motions propagating in the dawn-dusk direction, *Geophys. Res. Lett.*, **16**, 1265–1268, 1989.

Nakamura, R., Baumjohann, W., Brittnacher, M., Sergeev, V. A., Kubyshkina, M., Mukai, T., and Liou, K.: Flow bursts and auroral activations: Onset timing and foot point location, *J. Geophys. Res.*, **106**, 10 777–10 790, doi: doi:10.1029/2000JA000249, 2001a.

Nakamura, R., Baumjohann, W., Schödel, R., Brittnacher, M., Sergeev, V. A., Kubyshkina, M., Mukai, T., and Liou, K.: Earthward flow bursts, auroral streamers, and small expansions, *J. Geophys. Res.*, **106**, 10 791–10 802, doi: doi:10.1029/2000JA000306, 2001b.

Nakamura, R., Baumjohann, W., Mouikis, C., Kistler, L. M., Runov, A., Volwerk, M., Asano, Y., Vörös, Z., Zhang, T. L., Klecker, B., Rème, H., and Balogh, A.: Spatial scale of high-speed flows in the plasma sheet observed by Cluster, *Geophys. Res. Lett.*, **31**, L09 804, doi: doi:10.1029/2004GL019558, 2004.

Nakamura, R., Amm, O., Laakso, H., Draper, N. C., Lester, M., Grocott, A., Klecker, B., McCrea, I. W., Balogh, A., Rème, H., and André, M.: Localized fast flow disturbance observed in the plasma sheet and in the ionosphere, *Ann. Geophys.*, **23**, 553–566, 2005a.

Nakamura, R., Baumjohann, W., Zhang, T. L., Carr, C. M., Balogh, A., Fornacon, K.-H., Georgescu, E., Rème, H., Dandouras, I., Takada, T., Volwerk, M., Asano, Y., Runov, A., Eichelberger, H., Klecker, B., Mouikis, C., Kistler, L. M., and Amm, O.: Cluster and Double Star observations of dipolarization, *Ann. Geophys.*, **23**, 2915–2920, 2005b.

Østgaard, N., Mende, S. B., Frey, H. U., Immel, T. J., Frank, L. A., Sigwarth, J. B., and Stubbs, T. J.: Interplanetary magnetic field control of the location of substorm onset and auroral features in the conjugate hemispheres, *J. Geophys. Res.*, **109**, 7204–7215, doi: doi:10.1029/2003JA010370, 2004.

Parker, E. N.: Dynamics of the Interplanetary Gas and Magnetic Fields., *Astrophysical Journal*, **128**, 664–676, 1958.

Paschmann, G. and Daly, P. W., eds.: Analysis Methods for Multi-Spacecraft Data, ISSI/ESA, 1998,2000.

Petrukovich, A. A., Zhang, T. L., Baumjohann, W., Nakamura, R., Runov, A., Balogh, A., and Carr, C.: Oscillatory magnetic flux tube slippage in the plasma sheet, *Ann. Geophys.*, **24**, 1695–1704, 2006.

Pontius, Jr., D. H. and Wolf, R. A.: Transient flux tubes in the terrestrial magnetosphere, *Geophys. Res. Lett.*, **17**, 49–52, 1990.

Popov, V. A., Papitashvili, V. O., and Watermann, J. F.: Modeling of equivalent ionospheric currents from meridian magnetometer chain data, *Earth, Planets, and Space*, **53**, 129–137, 2001.

Raj, A., Phan, T., Lin, R. P., and Angelopoulos, V.: Wind survey of high-speed bulk flows and field-aligned beams in the near-Earth plasma sheet, *J. Geophys. Res.*, **107**, 3–1, doi: doi:10.1029/2001JA007547, 2002.

Rème, H., Aoustin, C., Bosqued, J. M., Dandouras, I., Lavraud, B., Sauvaud, J. A., Barthe, A., Bouyssou, J., Camus, T., Coeur-Joly, O., Cros, A., Cuvilo, J., Ducay, F., Garbarowitz, Y., Medale, J. L., Penou, E., Perrier, H., Romefort, D., Rouzaud, J., Vallat, C., Alcaydé, D., Jacquey, C., Mazelle, C., D'Uston, C., Möbius, E., Kistler, L. M., Crocker, K., Granoff, M., Mouikis, C., Popecki, M., Vosbury, M., Klecker, B., Hovestadt, D., Kucharek, H., Kuenneth, E., Paschmann, G., Scholer, M., Sckopke, N., Seidenschwang, E., Carlson, C. W., Curtis, D. W., Ingraham, C., Lin, R. P., McFadden, J. P., Parks, G. K., Phan, T., Formisano, V., Amata, E., Bavassano-Cattaneo, M. B., Baldetti, P., Bruno, R., Chionchio, G., di Lellis, A., Marcucci, M. F., Pallocchia, G., Korth, A., Daly, P. W., Graeve, B., Rosenbauer, H., Vasyliunas, V., McCarthy, M., Wilber, M., Eliasson, L., Lundin, R., Olsen, S., Shelley, E. G., Fuselier, S., Ghielmetti, A. G., Lennartsson, W., Escoubet, C. P., Balsiger, H., Friedel, R., Cao, J.-B., Kovrazhkin, R. A., Papamastorakis, I., Pellat, R., Scudder, J., and Sonnerup, B.: First multispacecraft ion measurements in and near the Earth's magnetosphere with the

identical Cluster Ion Spectrometry (CIS) experiment, *Ann. Geophys.*, **19**, 1303–1354, 2001.

Robert, P., Dunlop, M. W., Roux, A., and Chanteur, G.: Accuracy of current density determination, in Analysis Methods for Multi-Spacecraft Data, edited by G. Paschmann and P. W. Daly, pp. 395–418, ISSI, 1998.

Rostoker, G.: Current flow in the magnetosphere during magnetospheric substorms., *J. Geophys. Res.*, **79**, 1994–1998, 1974.

Runov, A., Nakamura, R., Baumjohann, W., Zhang, T. L., Volwerk, M., Eichelberger, H.-U., and Balogh, A.: Cluster observation of a bifurcated current sheet, *Geophys. Res. Lett.*, **30**, 8–1, 2003.

Runov, A., Sergeev, V. A., Baumjohann, W., Nakamura, R., Apatenkov, S., Asano, Y., Volwerk, M., Vörös, Z., Zhang, T. L., Petrukovich, A., Balogh, A., Sauvaud, J.-A., Klecker, B., and Rème, H.: Electric current and magnetic field geometry in flapping magnetotail current sheets, *Ann. Geophys.*, **23**, 1391–1403, 2005.

Runov, A., Sergeev, V. A., Nakamura, R., Baumjohann, W., Apatenkov, S., Asano, Y., Takada, T., Volwerk, M., Vörös, Z., Zhang, T. L., Sauvaud, J.-A., Rème, H., and Balogh, A.: Local structure of the magnetotail current sheet: 2001 Cluster observations, *Ann. Geophys.*, **24**, 247–262, 2006.

Ruohoniemi, J. M. and Baker, K. B.: Large-scale imaging of high-latitude convection with Super Dual Auroral Radar Network HF radar observations, *J. Geophys. Res.*, **103**, 20 797–20 811, doi: doi:10.1029/98JA01288, 1998.

Ruohoniemi, J. M. and Greenwald, R. A.: Statistical patterns of high-latitude convection obtained from Goose Bay HF radar observations, *J. Geophys. Res.*, **101**, 21 743–21 764, doi: doi:10.1029/96JA01584, 1996.

Russell, C. T., Mellott, M. M., Smith, E. J., and King, J. H.: Multiple spacecraft observations of interplanetary shocks Four spacecraft determination of shock normals, *J. Geophys. Res.*, **88**, 4739–4748, 1983.

Russell, C. T., Snare, R. C., Means, J. D., Pierce, D., Dearborn, D., Larson, M., Barr, G., and Le, G.: The GGS/POLAR magnetic fields investigation, *Sp. Sci. Rev.*, **71**, 563–582, doi: doi:10.1007/BF00751341, 1995.

Safargaleev, V. V. and Mal'Tsev, Y. P.: Internal gravitational waves in a plasma sheet., *Geomagnetism and Aeronomy*, **26**, 270–274, 1986.

Schwartz, S. J.: Shock and discontinuity normals, mach numbers, and related parameters, in Analysis Methods for Multi-Spacecraft Data, edited by G. Paschmann and P. W. Daly, pp. 249–270, ISSI, 1998.

Sergeev, V., Angelopoulos, V., Carlson, C., and Sutcliffe, P.: Current sheet measurements within a flapping plasma sheet, *J. Geophys. Res*, **103**, 9177–9188, doi: doi:10.1029/97JA02093, 1998.

Sergeev, V., Runov, A., Baumjohann, W., Nakamura, R., Zhang, T. L., Volwerk, M., Balogh, A., Rème, H., Sauvaud, J. A., André, M., and Klecker, B.: Current sheet flapping motion and structure observed by Cluster, *Geophys. Res. Lett.*, **30**, 60–1, 2003.

Sergeev, V., Liou, K., Newell, P., Ohtani, S., Hairston, M., and Rich, F.: Auroral streamers: characteristics of associated precipitation,convection and field-aligned currents, *Ann. Geophys.*, **22**, 537–548, 2004a.

Sergeev, V., Runov, A., Baumjohann, W., Nakamura, R., Zhang, T. L., Balogh, A., Louarnd, P., Sauvaud, J.-A., and Reme, H.: Orientation and propagation of current sheet oscillations, *Geophys. Res. Lett.*, **31**, L05 807, doi: doi:10.1029/2003GL019346, 2004b.

Sergeev, V. A., Angelopoulos, V., Gosling, J. T., Cattell, C. A., and Russell, C. T.: Detection of localized, plasma-depleted flux tubes or bubbles in the midtail plasma sheet, *J. Geophys. Res.*, **101**, 10 817–10 826, doi: doi:10.1029/96JA00460, 1996.

Sergeev, V. A., Sauvaud, J.-A., Popescu, D., Kovrazhkin, R. A., Liou, K., Newell, P. T., Brittnacher, M., Parks, G., Nakamura, R., Mukai, T., and Reeves, G. D.: Multiple-spacecraft observation of a narrow transient plasma jet in the Earth's plasma sheet, *Geophys. Res. Lett.*, **27**, 851–854, 2000.

Sergeev, V. A., Sormakov, D. A., Apatenkov, S. V., Baumjohann, W., Nakamura, R., Runov, A. V., Mukai, T., and Nagai, T.: Survey of large-amplitude flapping motions in the midtail current sheet, *Ann. Geophys.*, **24**, 2015–2024, 2006.

Shiokawa, K., Baumjohann, W., and Haerendel, G.: Braking of high-speed flows in the near-Earth tail, *Geophys. Res. Lett.*, **24**, 1179–1182, doi: doi:10.1029/97GL01062, 1997.

Shiokawa, K., Baumjohann, W., Haerendel, G., Paschmann, G., Fennell, J. F., Friis-Christensen, E., Lühr, H., Reeves, G. D., Russell, C. T., Sutcliffe, P. R., and Takahashi, K.: High-speed ion flow, substorm current wedge, and multiple Pi 2 pulsations, *J. Geophys. Res.*, **103**, 4491–4508, doi: doi:10.1029/97JA01680, 1998a.

Shiokawa, K., Haerendel, G., and Baumjohann, W.: Azimuthal pressure gradient as driving force of substorm currents, *Geophys. Res. Lett.*, **25**, 959–962, doi: doi:10.1029/98GL00540, 1998b.

Sitnov, M. I., Guzdar, P. N., and Swisdak, M.: On the formation of a plasma bubble, *Geophys. Res. Lett.*, **32**, 16 103, doi: doi:10.1029/2005GL023585, 2005.

Slavin, J. A., Tanskanen, E. I., Hesse, M., Owen, C. J., Dunlop, M. W., Imber, S., Lucek, E. A., Balogh, A., and Glassmeier, K.-H.: Cluster observations of travelling compression regions in the near-tail, *J. Geophys. Res.*, **110**, A06 207, doi: doi:10.1029/2004JA010878, 2005.

Smith, C. W., L'Heureux, J., Ness, N. F., Acuña, M. H., Burlaga, L. F., and Scheifele, J.: The ACE Magnetic Fields Experiment, *Sp. Sci. Rev.*, **86**, 613–632, doi: doi:10.1023/A:1005092216668, 1998.

Snekvik, K., Haaland, S., Østgaard, N., Hasegawa, H., Nakamura, R., Takada, T., Juusola, L., Amm, O., Pitout, F., Rème, H., Klecker, B., and Lucek, E. A.: Cluster observations of a field aligned current at the dawn flank of a bursty bulk flow, *Ann. Geophys.*, **25**, 1405–1415, 2007.

Sonnerup, B. U. O. and Cahill, Jr., L. J.: Magnetopause structure and attitude from Explorer 12 observations, *J. Geophys. Res.*, **72**, 171–183, 1967.

Sonnerup, B. U. O. and Scheible, M.: Minimum and maximum variance analysis, in Analysis Methods for Multi-Spacecraft Data, edited by G. Paschmann and P. W. Daly, pp. 185–220, ISSI, 1998.

Speiser, T. W. and Ness, N. F.: The Neutral Sheet in the Geomagnetic Tail: Its Motion, Equivalent Currents, and Field Line Connection through It, *J. Geophys. Res.*, **72**, 131–141, 1967.

Stone, E. C., Frandsen, A. M., Mewaldt, R. A., Christian, E. R., Margolies, D., Ormes, J. F., and Snow, F.: The Advanced Composition Explorer, *Sp. Sci. Rev.*, **86**, 1–22, doi: doi:10.1023/A:1005082526237, 1998.

Tsyganenko, N. A.: Global quantitative models of the geomagnetic field in the cislunar magnetosphere for different disturbance levels, *Planet. Sp. Sci.*, **35**, 1347–1358, doi: doi:10.1016/0032-0633(87)90046-8, 1987.

Tsyganenko, N. A.: A magnetospheric magnetic field model with a warped tail current sheet, *Planet. Sp. Sci.*, **37**, 5–20, doi: doi:10.1016/0032-0633(89)90066-4, 1989.

Tsyganenko, N. A. and Stern, D. P.: Modeling the global magnetic field of the large-scale Birkeland current systems, *J. Geophys. Res.*, **101**, 27 187–27 198, doi: doi:10.1029/96JA02735, 1996.

Tsyganenko, N. A., Singer, H. J., and Kasper, J. C.: Storm-time distortion of the inner magnetosphere: How severe can it get?, *J. Geophys. Res.*, **108**, 1209, doi: doi:10.1029/2002JA009808, 2003.

Untiedt, J. and Baumjohann, W.: Studies of Polar Current Systems Using the IMS Scandinavian Magnetometer Array, *Sp. Sci. Rev.*, **63**, 245–390, doi: doi:10.1007/BF00750770, 1993.

Viljanen, A. and Häkkinen, L.: Image magnetometer network, in ESA SP-1198: Satellite-Ground Based Coordination Sourcebook, edited by M. Lockwood, M. N. Wild, and H. J. Opgenoorth, pp. 111–118, 1997.

Volwerk, M., Glassmeier, K.-H., Runov, A., Nakamura, R., Baumjohann, W., Klecker, B., Richter, I., Balogh, A., Rème, H., and Yumoto, K.: Flow burst-induced large-scale plasma sheet oscillation, *J. Geophys. Res.*, **109**, A11 208, doi: doi:10.1029/ 2004JA010533, 2004.

Wells, H. G.: War of the Worlds, London: Heinemann, 1898.

Wolf, R. A.: The quasi-static (slow-flow) region of the magnetosphere, in Solar-terrestrial physics: Principles and theoretical foundations; Proceedings of the Theory Institute, Chestnut Hill, MA, August 9-26, 1982 (A84-33851 15-46). Dordrecht, D. Reidel Publishing Co., 1983, p. 303-368., edited by W. H. Matthaeus, pp. 303–368, 1983.

Zhang, T. L., Baumjohann, W., Nakamura, R., Balogh, A., and Glassmeier, K.-H.: A wavy twisted neutral sheet observed by CLUSTER, *Geophys. Res. Lett.*, **29**, 5–1, 2002.

Zhang, T. L., Nakamura, R., Volwerk, M., Runov, A., Baumjohann, W., Eichelberger, H. U., Carr, C., Balogh, A., Sergeev, V., Shi, J. K., and Fornacon, K.-H.: Double Star/Cluster observation of neutral sheet oscillations on 5 August 2004, *Ann. Geophys.*, **23**, 2909–2914, 2005.